PROCEEDINGS OF THE KECK GEOLOGY CONSORTIUM

Volume 36
2023-2024 Projects

Dr. Cameron Davidson and Dr. Karl Wirth, Editors
Co-Directors, Keck Geology Consortium

Theresa Klauer
Keck Geology Consortium Administrative Assistant
Macalester College

Keck Geology Consortium
Macalester College
1600 Grand Ave, St. Paul, MN 55105
(651) 696-6108, Info@KeckGeology.org

ISSN# 1528-7491
doi: 10.18277/AKRSG.2024.36

Funding Provided by:
Keck Geology Consortium Member Institutions
The National Science Foundation Grant NSF-REU 2050697

PROCEEDINGS OF THE KECK GEOLOGY CONSORTIUM

2023-2024 Projects

Cameron Davidson Editor and Co-Director Carleton College	Keck Geology Consortium Macalester College 1600 Grand Ave. St Paul, MN 55105	Karl Wirth Editor and Co-Director Macalester College

Keck Geology Consortium Member Institutions:

Amherst College, Beloit College, Carleton College, Colgate University, The College of Wooster, The Colorado College, Franklin & Marshall College, Macalester College, Pomona College, Trinity University, Union College, Washington & Lee University, Whitman College

2023-2024 GATEWAY PROJECTS

GEOCHEMICAL CONTROLS ON URANIUM CONTAMINATION OF GROUNDWATER IN THE CENTRAL VALLEY AND HIGH PLAINS AQUIFER SYSTEMS
Faculty: BRADY ZIEGLER, Trinity University
Peer Mentor: MARK NICKELS, Trinity University
Students: YARELY CONTRERAS-JOYA, Hamilton College; ANNA HEIKES, Trinity University; HOLLY MIRALES, Hamilton College; AMBER NELSON, Amherst College

THE IMPACT OF LARGE FLOODS ON FLUVIAL SYSTEMS IN NORTHERN YELLOWSTONE NATIONAL PARK
Faculty: LYMAN PERSICO, Whitman College
Peer Mentor: SARAH HOFFMAN, Whitman College
Students: KATALYN DENBY, Washington and Lee University; YOEL IZAGUIRRE, Carleton College; ANDREA KAUFER, Union College; SOPHIA POWERS, Macalester College; MIA SANCHEZ, Amherst College

2023-2024 ADVANCED PROJECTS

STRUCTURAL EVOLUTION OF A SEGMENTED NORMAL FAULT TRANSFER ZONE, SEVIER FAULT, SOUTHERN UTAH
Faculty: BEN SURPLESS, Trinity University
Students: PIERCE HAYTON, Colorado College; AUDREY JENNINGS, Trinity University; JACK MRACHEK, Purdue University; MORGAN SHARP, Whitman College

YOUNG EYES ON OLD ROCKS: EVALUATING TECTONIC MODELS FOR NEOARCHEAN(?) BASIN FORMATION IN THE METAMORPHIC CORE OF THE BLACK HILLS, SOUTH DAKOTA
Faculty: TREVOR WALDIEN, South Dakota School of Mines
Students: REBECCA BRAUN, South Dakota School of Mines; LIAM FRY, Eckerd College; WILLA OBRINGER, Lake Superior State University; ALEXANDRA ROBINSON, Pomona College

2023-2024 ADVANCED PROJECTS – continued

INTEGRATED STRATIGRAPHIC AND PALEOENVIRONMENTAL STUDY OF THE MIDDLE-LATE DEVONIAN CARBONATE TO BLACK SHALE TRANSITION IN THE MICHIGAN BASIN
Faculty: JAY ZAMBITO, Beloit College; PETER VOICE, Western Michigan University
Students: TIFFANY BARKER-EDWARDS, University of Texas at San Antonio; MIKAYLA GIEHLER, Macalester College; JACK GUGINO, Miami University – Oxford; ISABEL JOHNSON, Beloit College; HOLIDAY O'BRYAN, Macalester College; CONNOR QUIROZ, California State University, Monterey Bay; LAM TRUONG, California State University Long Beach; AINSLEY WIESNER, The College of Wooster; MARCELLA WINGET, Hamilton College

Conference Presentations – California Gateway Project

Contreras-Joya, Y., Heikes, A., Nickels, M., Mirales, H., Nelson, A., Mine, A., and Ziegler, B., 2023, Spatial and statistical analysis of uranium in the High Plains aquifer in comparison to the Central Valley aquifer, *in* Geological Society of America Abstracts with Programs. Vol. 55, No. 6, doi:10.1130/abs/2023AM-390307.

Mirales, H., Nelson, A., Heikes, A., Contreras-Joya, Y., Ruiz, S., Mine, A., and Ziegler, B., 2023, Evaluating geochemical and microbial influences on uranium mobilization in Central Valley, California, *in* Geological Society of America Abstracts with Programs. Vol. 55, No. 6, doi:10.1130/abs/2023AM-390308.

Conference Presentations – Yellowstone Gateway Project

Denby, K., Izaguirre, Y., Kaufer, A., Powers, S., Sanchez, M., Hoffman, S., and Persico, L., 2024, A tale of two floods: comparing peak discharges of the 1918 and 2022 northern Yellowstone National Park floods, *in* Geological Society of America Abstracts with Programs. Vol. 56, No. 4, doi:10.1130/abs/2024CD-399418.

Hoffman, S., and Persico, L.P., 2024, Reconstructing peak discharge variability of the June 2022 flood in northern Yellowstone National Park, *in* Geological Society of America Abstracts with Programs. Vol. 56, No. 4, doi:10.1130/abs/2024CD-399728.

Persico, L.P., and Meyer, G., 2024, Exploring variability in peak discharge and erosion caused by the June 2022 atmospheric river flood in northern Yellowstone National Park, *in* Geological Society of America Abstracts with Programs. Vol. 56, No. 4, doi:10.1130/abs/2024CD-399897.

Short Contributions – Utah Advanced Project

TESTING MODELS OF NORMAL FAULT PROPAGATION AND DAMAGE ZONE DEVELOPMENT
BENJAMIN SURPLESS, Trinity University

THE ROLE OF FAULT DAMAGE ZONES IN STRUCTURALLY CONTROLLED LANDSCAPE EVOLUTION, SEVIER FAULT ZONE, SOUTHERN UTAH
PIERCE HAYTON, Colorado College
Project Advisors: Tyler Grambling, Sarah Schanz

COMPUTER MODELING OF NORMAL FAULT-RELATED DAMAGE ZONES: IMPLICATIONS FOR ESTIMATING GEOTHERMAL ENERGY POTENTIAL
AUDREY JENNINGS, Trinity University
Project Advisor: Benjamin Surpless

GEOLOGICAL TIMELINE & EXTENSION OF MARTIAN FAULTING IN THE ALBA MONS REGION OF MARS
JACK MRACHEK, Purdue University
Project Advisor: Michael Eddy

DAMAGE ZONE DEVELOPMENT AND CROSS-FAULT ASYMMETRY ON THE MT. CARMEL SEGMENT OF THE SEVIER NORMAL FAULT, SOUTHWEST UTAH
MORGAN SHARP, Whitman College
Project Advisor: Kevin Pogue

Short Contributions – Black Hills Advanced Project

POLYPHASE DEFORMATION OF NEOARCHEANPALEOPROTEROZOIC ROCKS IN THE BLACK HILLS, SOUTH DAKOTA
TREVOR WALDIEN, South Dakota School of Mines and Technology

DEFORMATION TEMPERATURE AND KINEMATICS OF THE DAKOTA TECTONIC ZONE WITHIN THE LITTLE ELK GRANITE IN THE BLACK HILLS, SOUTH DAKOTA, NEAR NEMO, SOUTH DAKOTA
REBECCA BRAUN, South Dakota School of Mines and Technology
Project Advisor: Trevor Waldien

KINEMATIC ANALYSIS OF SHEAR ZONES IN THE LITTLE ELK GRANITE, BLACK HILLS, SOUTH DAKOTA
LIAM T. FRY, Eckerd College
Project Advisor: Laura Wetzel

ELUCIDATION OF AN UNDEFINED RELATIONSHIP: A STUDY OF THE BOXELDER CREEK QUARTZITE AND LITTLE ELK GRANITE TO DECIPHER PALEOPROTEROZOIC BASIN DEVELOPMENT IN THE BLACK HILLS, SOUTH DAKOTA
WILLA OBRINGER, Lake Superior State University
Project Advisors: Paul Kelso and Derek Wright

U-PB ZIRCON DATING OF NEOARCHEAN ROCKS IN THE LITTLE ELK TERRANE, BLACK HILLS, SOUTH DAKOTA
ALEX ROBINSON, Pomona College
Project Advisor: Nicole Moore

Short Contributions – Michigan Basin Advanced Project

INTEGRATED STRATIGRAPHIC AND PALEOENVIRONMENTAL STUDY OF THE MIDDLE-LATE DEVONIAN CARBONATE TO BLACK SHALE TRANSITION IN THE MICHIGAN BASIN
JAMES J. ZAMBITO IV, Beloit College; PETER J. VOICE, Western Michigan University

CORRELATING THE TRAVERSE GROUP LIMESTONE FROM SUBSURFACE TO OUTCROP, MICHIGAN BASIN
MARCELLA M. WINGET, Hamilton College
Project Advisor: Catherine C. Beck

DIAGENESIS OF A PYRITIZED CONTACT OF THE MIDDLE TO LATE DEVONIAN TRANSITION FROM CARBONATE TO BLACK SHALE
HOLIDAY R. O'BRYAN, Macalester College
Project Advisors: Kelly R. Macgregor and Jeff T. Thole

AN ANALYSIS OF STRATIGRAPHIC, PALEOECOLOGIC, AND GEOCHEMICAL VARIABILITY IN THE "SQUAW BAY FORMATION," MICHIGAN BASIN
AINSLEY S. WIESNER, The College of Wooster
Project Advisor: Shelley A. Judge

GEOCHEMICAL ANALYSIS OF THE MIDDLE TO UPPER DEVONIAN ANTRIM SHALE, KROCKER 1-17 CORE, MICHIGAN BASIN
MIKAYLA C. GIEHLER, Macalester College
Project Advisor: Kelly R. Macgregor

EXPLORING THE SUITABILITY OF THE MIDDLE-LATE DEVONIAN ANTRIM SHALE, MICHIGAN BASIN, FOR ORGANIC CARBON ISOTOPIC ANALYSIS
JACK P. GUGINO, Miami University
Project Advisor: Brian S. Currie

MAGNETIC SUSCEPTIBILITY OF SEDIMENTARY STRATA IN THE LATE DEVONIAN ANTRIM FORMATION OF THE MICHIGAN BASIN
TIFFANY BARKER-EDWARDS, University of Texas at San Antonio
Project Advisors: Peter J. Voice and James J. Zambito IV

CHARACTERIZING THE SEDIMENT SOURCE OF THE ELLSWORTH FORMATION OF THE MICHIGAN BASIN USING LITHOSTRATIGRAPHY AND CHEMOSTRATIGRAPHY
ISABEL R. JOHNSON, Beloit College
Project Advisor: James J. Zambito IV

MODELING MARINE PALEOENVIRONMENTS OF THE ELLSWORTH PRODELTA DURING THE LATE DEVONIAN IN THE MICHIGAN BASIN
CONNOR J. QUIROZ, California State University, Monterey Bay
Project Advisors: Peter J. Voice and James J. Zambito IV

GEOLOGIC MAPPING OF ALPENA COUNTY, MICHIGAN
LAM T. TRUONG, California State Long Beach University
Project Advisors: Peter J. Voice and James J. Zambito IV

KECK Geology Consortium
Learning Science Through Research
Published by the Keck Geology Consortium
Short Contributions
Keck Geology Consortium
Volume 36
May 2024
doi: 10.18277/AKRSG.2024.36.01

TESTING MODELS OF NORMAL FAULT PROPAGATION AND DAMAGE ZONE DEVELOPMENT

BENJAMIN SURPLESS, Trinity University

INTRODUCTION

Because seismic hazard assessment and natural resource development rely on prediction of fault behavior, structural geologists commonly model the evolution of fault systems to better understand their long-term evolution. Researchers have established that faults perturb local stress fields as they propagate, influencing the formation of minor faults and intense fracturing in an envelope, or "damage zone", around them (Fig. 1) (e.g., Peacock and Sanderson, 1996; Shipton and Cowie, 2003; Kim et al., 2004; Choi et al., 2016). These damage zones increase rock permeability, which enhances groundwater flow rates (e.g., Rowley, 1998), hydrocarbon migration (e.g., Morley et al., 1990), ore mineralization (e.g., DeWitt et al., 1986), and geothermal energy production potential (e.g., Siler et al., 2018; Shervais et al., 2024).

In addition, although researchers have long recognized that fault zones are segmented, as opposed to continuous, planar surfaces (e.g., Tchalenko, 1970; Schwartz and Coppersmith, 1984), researchers have made significant advances in the role that segmentation plays in overall fault system evolution (e.g., Long and Imber, 2011; Siler et al., 2018; Surpless and Thorne, 2021) as well as how interacting faults affect damage zone development (e.g., Kim et al., 2004; Choi et al., 2016). Where two adjacent normal fault segments interact, fracturing is commonly amplified, increasing the volume of rock damaged relative to two separate, isolated faults (e.g., Stock and Hodges, 1990; Hudson, 1992; Faulds, 1996).

In this Keck Utah Advanced Project, students investigated the evolution of normal fault networks, using their results to learn how faults and their damage zones evolve through time. Four students investigated different aspects of the central Sevier fault zone in southern Utah (Fig. 2), a well-studied, steeply west-dipping normal fault system with ~400 – 800 m dip-

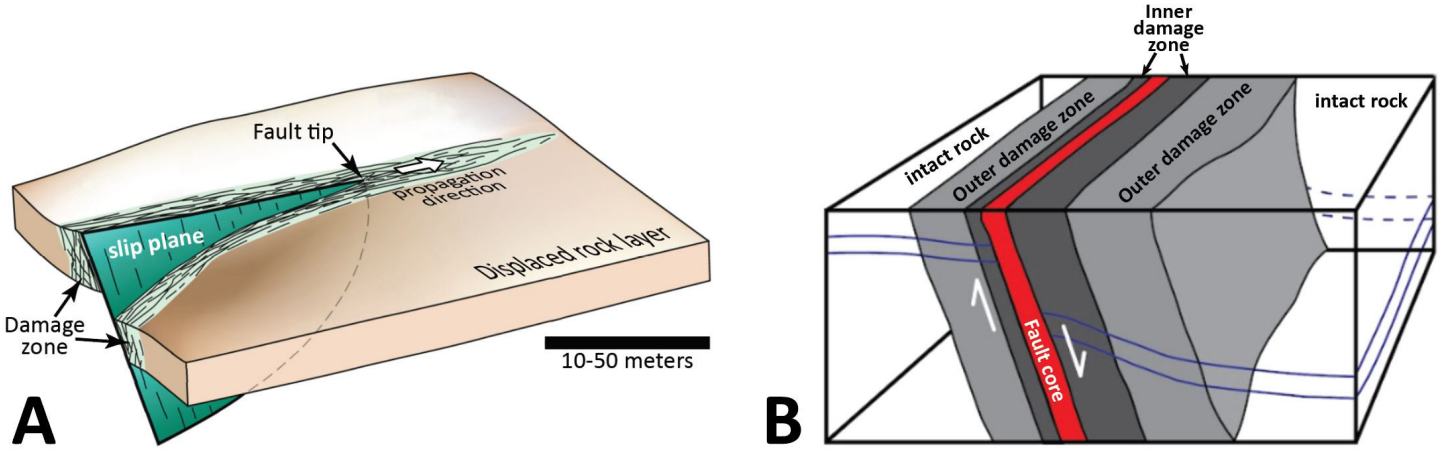

Figure 1. Development of a fault damage zone during normal fault propagation and displacement. A. damage zone development ahead of a propagating, elliptical fault tip and parallel to the fault plane (adapted from Fossen, 2016). B. Damage zone architecture and terminology (adapted from Laio et al., 2020).

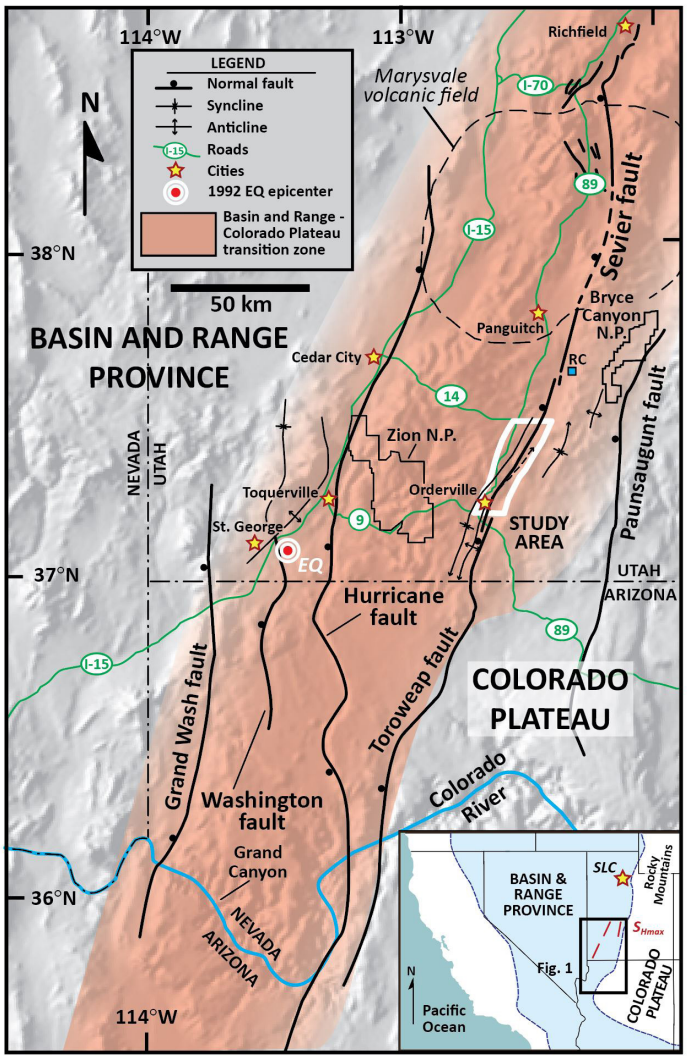

Figure 2. The Sevier fault zone study area within the Basin and Range-Colorado Plateau transition zone [see inset, with the location of Salt Lake City (SLC) indicated with a star]. The red lines on the inset figure are orientations of the maximum horizontal stress field (SHmax) as constrained by Lundstern and Zoback (2020). The Sevier-Toroweap fault, the Grand Wash fault, the Washington fault, the Hurricane fault, and the Paunsaugunt fault accommodate extension across the transition zone. Ball is on the hanging wall of faults. The epicenter of the 1992 M5.8 St. George earthquake is indicated by the red and white symbol, labeled "EQ" (Christenson et al., 1995). Approximate areal distribution of the Marysvale volcanic field is outlined by dashed lines. Blue box indicates the location of Red Canyon (RC), where Hecker (1993) constrained slip rate along the Sevier fault. Study area boxed in white. Fold data are from Doelling et al. (1989), Bowers (1991), and Stewart and Taylor (1996). Digital shaded relief modified from Thelin and Pike (1991). Figure modified from Hecker (1993), Reber et al. (2001), Surpless and McKeighan (2022), and Taylor et al. (in press).

slip displacement (e.g., Scheifelbein, 2002; Taylor et al., in press), and one student studied spectacularly well-exposed normal fault systems in the Tharsis region of Mars to investigate the structural evolution of a normal fault systems across a range of scales.

STUDY AREAS

The Sevier normal fault, considered one of the most important structures in the Basin and Range province (e.g., Davis, 1999; Lund et al., 2008), is part of the Toroweap-Sevier fault system, which extends for more than 300 km from northern Arizona to southern Utah (Fig. 2). The fault has accommodated extension across the transition zone from the Basin and Range province to the relatively stable Colorado Plateau since the Miocene (e.g., Reber et al., 2001; Lund et al., 2008), and previous workers have noted the potential of the fault to produce significant earthquakes (Anderson and Rowley, 1987; Doelling and Davis, 1989; Anderson and Christenson, 1989; Christenson, 1995; Lund et al., 2008). It is likely that many segments of the Sevier fault reactivate older high-angle, Laramide-age contractional structures (e.g., Stewart and Taylor, 1996; Schiefelbein and Taylor, 2000), which may explain why the steeply-west-dipping fault zone is segmented in map view, with variations in the geometry of linkages between normal fault segments (e.g., Davis, 1999; Reber et al., 2001; Schiefelbein, 2002; Doelling, 2008).

In this project, students focused their investigations on a particularly complex portion of the Sevier fault zone, termed the Orderville geometric bend (e.g., Reber et al., 2001) (Fig. 2). The Orderville bend displays a range of geometries associated with the interactions of three fault segments, which include the Mt. Carmel segment, the Orderville segment, and the Spencer Bench segment (Taylor et al., in press). The interaction of these 3 fault segments is likely responsible for the formation of the minor faults (displayed in white) and relay ramps shown adjacent to Red Hollow Canyon and Stewart Canyon (Fig. 2); these features likely evolved within the perturbed stress field associated with the transfer zones between dominant fault segments (Fig. 3).

STUDENT PROJECTS

The excellent vertical and lateral exposure of the Jurassic Navajo sandstone at the two primary study areas, at Red Hollow Canyon and Elkheart Cliffs (Fig. 2), provided students opportunity to directly observe faults and fractures within this well-studied lithology

(e.g., Rogers et al., 2004; Schultz et al., 2010; Solom et al., 2010). The Elkheart Cliffs exposure (Fig. 2) displays the simplest fault geometry because the Mt. Carmel segment accommodates all E-W extension. In contrast, at Red Hollow Canyon and Stewart Canyon (Fig. 3), extensional strain is accommodated by a more complex system.

To address fundamental questions about how rock volumes respond to the evolution of complex, segmented, normal fault systems, students applied a variety of approaches, including analysis of field data, 3D digital modeling and analysis of photographic data, development of a 3D retrodeformable model of the fault network based on previously published cross-sections and map data, 3D stress-strain software modeling of fault and fracture formation and propagation, and remote-sensing analysis of a complex, segmented fault system in the Tharsis region of Mars. Their work improves our understanding of the 3D evolution of faults and fracture networks in complex normal fault zones, which has important implications for natural resource exploration.

Demi Durham (Trinity University) used the Move2022 modeling suite (by Petex) to develop a viable 3D model of the complexly-segmented Sevier fault zone based on previously published geologic maps and cross-sections. She focused primarily on the fault network displayed in Fig. 3, focusing especially on the fault network north of the south tip of the Spencer Bench segment. With previously published geologic maps and cross-sections (Schiefelbein, 2002) as a base, she digitized geologic unit contacts and fault planes to build a 3D model of the fault network. She used this model to test the validity of initial cross-sectional interpretations, because earlier subsurface interpretations in cross-sections were based on surface mapping rather than direct documentation of subsurface fault and layer geometries.

Demi identified inconsistencies in cross-section interpretations based on misaligned unit horizons and fault surfaces. She revised these cross sections to integrate more accurate fault dips, include new fault planes, where they projected across lines of section, and changed the thicknesses of units, where those thicknesses were inconsistent across fault blocks. Demi also added new cross-sections where the density of published and revised sections was not sufficient to constrain the interaction of faults at depth. Her resulting model was a more accurate depiction of the Sevier system, which included complex but viable

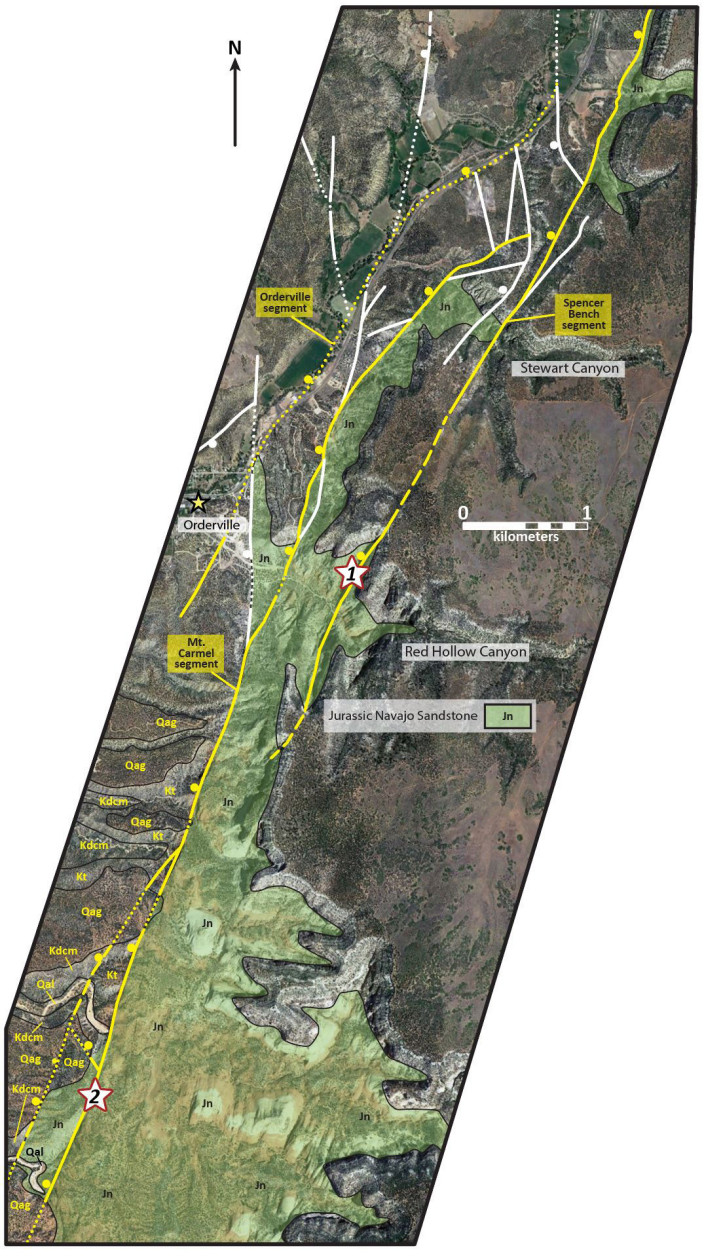

Figure 3. Simplified structural map of the steeply WNW-dipping central Sevier fault zone. Yellow faults represent the primary segments of the fault zone, and the white faults are subsidiary faults that help accommodate extension across the fault network. The green shaded areas represent exposures of the Jurassic Navajo Sandstone, and outlined areas labeled with yellow abbreviations are lithologies in the hanging wall of the Mt. Carmel segment, including: Kt (Cretaceous Tropic Shale), Kdcm (Cretaceous Dakota and Cedar Mountain Formations), Qag (older alluvial gravels), and Qal (modern alluvium). The white stars represent the locations of field and modeling studies performed by Pierce Hayton (1) and Morgan Sharp (2). Demi Durham focused her modeling investigation on the region north of the tip of the Spencer Bench segment.

structural geometries. This final model constrains both the subsurface orientations of faults and the geometric relationships between them. Although it was beyond the scope of her research, future researchers should be able to use her model investigate what retrodeformation of extension tells us about the evolution of the overall network.

Importantly, this three-dimensional model of the complexly segmented normal fault network can be applied to other fault zones with similar subsurface geometries across the Basin and Range Province, where heat flows are high. Because fault damage zones adjacent to faults usually create zones of higher permeability, the geometric relationships between these faults can be used to target zones with high geothermal energy potential in similar segmented systems.

Pierce Hayton (Colorado College) used field data and Structure-from-Motion (SfM) model analysis to investigate how a propagating fault affects the rock around it. As a propagating fault fractures the rock around it, subsequent weathering and erosion will strongly affect how the local landscape evolves. Pierce focused on the Spencer Bench segment, which displaces the Jurassic Navajo Sandstone (Fig. 3). Because the Navajo Sandstone is located on both sides of the fault, he was able to hold lithology constant to evaluate differences in damage zone distribution and resulting impacts on erosional processes. In addition, the headward erosion process permitted him to use cross-drainage profiles from the northernmost exposure of the segment in Red Hollow Canyon to the main drainage as temporal snapshots of profile evolution to evaluate how damage zone fracturing affects valley evolution.

Pierce found that the hanging wall of the steeply dipping fault was far wider than the footwall of the fault, consistent with previous studies of normal fault damage zones (e.g., Berg and Skar, 2005; Liao et al., 2020). In addition, he found a weak correlation between the intensity of damage zone fracturing and topographic evolution. Pierce also found that erosion rates were higher in the hanging wall compared to the footwall of the system, consistent with the idea that deformation can impact landscape evolution.

Audrey Jennings (Trinity University) analyzed stress, strain, and fracture evolution using the Fault Response Modeling module of the Move 2022 software suite (by Petex). She created 3D models of a single-fault system and investigated how the hanging wall and footwall of the normal fault accommodated strain using different models of fault evolution (the constant length model vs. the propagating model). Audrey found that the spatial distribution of strain was most strongly controlled by accumulated displacement, stage of lateral propagation, pore fluid pressure, and depth relative to the centroid of the fault, assuming a relatively elliptical slip model. Her findings can be applied to poorly exposed fault systems in high heat flow regions, where an understanding of fault damage zone distribution is important.

Jack Mrachek (Purdue University) investigated the evolution of an unusual circumferential fault network within and adjacent to the Alba Mons volcano-tectonic complex of the Tharsis region of Mars. He analyzed high-resolution orbital imagery to investigate the cross-cutting relationships between fluvial systems, normal faults, and volcanic lava flows. He also documented fault segment lengths and associated heave and throw values to compare displacement-length relationships on Mars relative to similar fault networks on Earth.

Jack confirmed the results of previous researchers, learning that lava flows pre-dated both fluvial systems and faulting, while faults across the region cut fluvial systems, establishing those features as the youngest across the Alba Mons region. Jack also documented the total extension accommodated by the circumferential system along an approximately East-West line of section, with 21 faults accommodating 5.5% extension. He also measured 200 faults' displacements and lengths and derived a power-law relationship between the variables that suggested a different relationship relative to similar displacement - length data on Earth. Jack hypothesized that this discrepancy might be the result of differing crustal thicknesses for the two planets.

Morgan Sharp (Whitman College) used field data and Structure-from-Motion (SfM) model analysis to investigate how fault- damage zones develop (Fig. 1) in response to fault propagation and accumulated

displacement. He focused on multiple exposures of the damage zone associated with the Mt. Carmel segment of the Sevier fault zone; because displacements along that fault vary along strike, Morgan was able to compare damage zone development at different stages of fault slip. He also compared how hanging wall fracture data compared with footwall fracture data, revealing asymmetry in damage zone development.

Morgan's results are consistent with those of Savage and Brodsky's (2011) hypothesis that normal fault damage zones evolve in two phases, including a first phase, when damage zone width increases proportionally with displacement, and a second phase, when above a critical displacement value, the rate of damage zone width increase slows and is not linked as strongly to displacement. Morgan's data show that footwall damage zone width varies on the meter scale for displacements that vary by hundreds of meters, which is consistent with the second phase of normal fault displacement suggested by Savage and Brodsky (2011).

His work also reveals asymmetry in both fracture orientations and damage zone widths in the hanging wall and footwall. The damage zone width in the hanging wall is significantly wider than the footwall, and fractures in the hanging wall are dominated by fault-perpendicular fractures in contrast with fault-parallel fractures in the footwall.

ACKNOWLEDGEMENTS

This material is based upon work supported by the Keck Geology Consortium and the National Science Foundation under Grant No. 2050697. It was also supported by NSF Award 2042114 to PI Surpless. Finally, funding was provided by the Geosciences Department at Trinity University, including funding from the Roy and Tinker Funds to support undergraduate student research.

REFERENCES

Anderson, R.E., and Christenson, G.E., 1989, Quaternary faults, folds, and selected volcanic features in the Cedar City 1°x2° quadrangle, Utah: Utah Geological and Mineral Survey Miscellaneous Publication 89-6, 29 p.

Anderson, J.J., and Rowley, P.D., 1987, Geologic map of the Panguitch NW quadrangle, Iron and Garfield Counties, Utah: Utah Geological and Mineral Survey Map 103, 8 p. pamphlet, scale 1:24,000.

Berg, S., and T. Skar, 2005, Controls on damage zone asymmetry of a normal fault zone: Outcrop analyses of a segment of the Moab fault, SE Utah: Journal of Structural Geology, 27, 1803–1822, doi: 10.1016/j.jsg.2005.04.012.

Bowers, W.E., 1991, Geologic map of Bryce Canyon National Park and vicinity, southwestern Utah: United States Geological Survey Miscellaneous Investigations Series Map 2180, 1:24,000.

Choi, J-H., Edwards, P., Ko, K., and Kim, Y-S., 2016, Definition and classification of fault damage zones: a review and a new methodological approach: Earth Science Reviews, v. 152, p. 70-87.

Christenson, G.E., ed., 1995, The September 2, 1992 ML 5.8 St. George earthquake, Washington County, Utah: Utah Geological Survey Circular 88, 41 pp.

Davis, G., 1999, Structural geology of the Colorado Plateau region of southern Utah, with special emphasis on deformation bands: Geological Society of America Special Paper 342.

DeWitt, E., Thompson, J., and Smith, R., 1986, Geology and gold deposits of the Oatman district, northwestern Arizona: U.S. Geologic Survey Open-File Report 86-0638, 34 p.

Doelling, H.H., 2008, Geologic map of the Kanab 30'x60' quadrangle, Kane and Washington Counties, Utah, and Coconino and Mohave Counties, Arizona, 1:100,000-scale: Utah Geological Survey, MP-08-2DM.

Doelling, H.H., and Davis, F.D., 1989, The geology of Kane County, Utah, with sections on petroleum and carbon dioxide by Cynthia J. Brandt: Utah Geological and Mineral Survey Bulletin 124, 192 p., scale 1:100,000, 10 plates.

Faulds, J., 1996, Geologic map of the Fire Mountain 7.5' quadrangle, Clark County, Nevada, and Mohave County, Arizona: Nevada Bureau of Mines and Geology Map 106, scale 1:24,000 (with accompanying text).

Fossen, H., 2016, Structural Geology: Cambridge

University Press, Cambridge, UK, 510 p.
Hecker, S., 1993, Quaternary tectonics of Utah with emphasis on earthquake-hazard characterization: Utah Geological Survey Bulletin 127, p. 1-31.
Hudson, M., 1992, Paleomagnetic data bearing on the origin of arcuate structures in the French Peak – Massachusetts Mountain area of southern Nevada: Geological Society of America Bulletin, v. 104, p. 581 – 594.
Kim, K.-S., Peacock, D., and Sanderson, D., 2004, Fault damage zones: Journal of Structural Geology, v. 26, p. 503–517.
Liao, Z., Hu, L., Huang, X., Carpenter, B.M., Marfurt, K.J., Vasileva, S., and Zhou, Y., 2020, Characterizing damage zones of normal faults using seismic variance in the Wangxuzhuang oilfield, China: Interpretations v. 8, p. 1- 24.
Long, J., and Imber, J., 2011, Geological controls on fault relay zone scaling: Journal of Structural Geology, v. 33, p. 1790 – 1800.
Lund, W.R., Knudsen, T.R., and Vice, G.S., 2008, Paleoseismic reconnaissance of the Sevier fault, Kane and Garfield Counties, Utah: Utah Geologic Survey Special Study 122, Paleoseismology of Utah, v. 16, 31 p.Lowe, D., 2004, Distinctive image features from scale invariant keypoints: International Journal of Computer Vision, v. 60, p. 91–110, doi: 10 .1023 /B: VISI .0000029664 .99615.94.
Lundstern, J-E., and Zoback, M.D., 2020, Multiscale variations of the crustal stress field throughout North America: Nature Communications, v. 11:1951, https://doi.org/10.1038/s41467-020-15841-5.
Morley, C., Nelson, R., Patton, T., and Munn, S., 1990, Transfer zones in the East African Rift system and their relevance to hydrocarbon exploration in rifts: American Association of Petroleum Geologists Bulletin, v. 74, p. 1234 – 1253.
Peacock, D.C.P., and Sanderson, D.J., 1996, Effects of propagation rate on displacement variations along faults: Journal of Structural Geology, v. 18, p. 311 –320.
Reber, S., Taylor, W., Stewart, M., and Schiefelbein, I., 2001, Linkage and Reactivation along the northern Hurricane and Sevier faults, southwestern Utah, In XXX, Eds., The Geologic Transition, High Plateaus to Great Basin – A Symposium and Field Guide, The Mackin Volume: Utah Geological Association Publication 30, Pacific Section American Association of Petroleum Geologists Publication GB78, p. 379 – 400.
Rowley, P., 1998, Cenozoic transverse zones and igneous belts in the Great Basin, Western United States: Their tectonic and economic implications In Faulds, J.E., and Stewart, J.H., Eds., Accommodation zones and transfer zones: the regional segmentation of the Basin and Range province: Geological Society of America Special Paper No. 343, p. 195-228.
Savage, H.M., and Brodsky, E.E., 2011, Collateral damage: Evolution with displacement of fracture distribution and secondary fault strands in fault damage zones: Journal of geophysical research, v. 116, doi:10.1029/2010jb007665.
Schiefelbein, I., 2002, Fault segmentation, fault linkage, and hazards along the Sevier fault, southwestern Utah [M.S. thesis]: Las Vegas, University of Nevada at Las Vegas, 132 p.
Schiefelbein, I., and Taylor, W., 2000, Fault development in the Utah transition zone and High Plateaus subprovince: Abstracts with Programs, v. 32, No. 7, p. 431.
Schwartz, D.P., and Coppersmith, K.J., 1984, Fault behavior and characteristic earthquakes – Examples from the Wasatch and San Andreas fault zones: Journal of Geophysical Research, v. 89, p. 5681 – 5698.
Shipton, Z.K., and Cowie, P.A., 2003, A conceptual model for the origin of fault damage zone structures in high-porosity sandstone: Journal of structural geology, v. 25, p. 333–344, doi:10.1016/s0191-8141(02)00037-8.
Siler, D., Hinz, N., and Faulds, J., 2018, Stress concentrations at structural discontinuities in active fault zones in the western United States: Implications or permeability and fluid flow in geothermal fields: Geological Society of America Bulletin, v. 130, No 7, p. 1273 – 1288.
Shervais, J. et al., 2024, Geothermal play fairway analysis, part 1: Example from the Snake River Plain, Idaho, v. 117, p. 1 – 18.
Stewart, M., and Taylor, W., 1996, Structural analysis and fault segment boundary identification along the Hurricane fault in southwestern Utah: Journal

of Structural Geology, v. 18, p. 1017 – 1029.
Stock, J., and Hodges, K., 1990, Miocene to recent structural development of an extensional accommodation zone, northeastern Baja California, Mexico: Journal of Structural Geology, v. 12, p. 312 – 328.
Surpless, B.E., and McKeighan, C., 2022, The role of dynamic fracture branching in the evolution of fracture networks: an outcrop study of the Jurassic Navajo Sandstone, southern Utah: Journal of Structural Geology, v. 161. DOI: 10.1016/j.jsg.2022.104664.
Surpless, B., and Thorne, S., 2021, Segmentation of the Wassuk Range normal fault system, Nevada (USA): implications for earthquake rupture and Walker Lane dynamics: Geological Society of America Bulletin, v. 134, p. 39-59, DOI: 10.1130/B35756.1
Taylor, W., Surpless, B., and Schiefelbein, I., in press, Complex segment linkage along the Sevier normal fault, southwestern Utah: Lithosphere.
Tchalenko, J.S., 1970, Similarities between shear zones of different magnitudes: Bulletin of the Geological Society of America, v. 81, p. 1625–1640.
Thelin, G.P., and Pike, R.J., 1991, Landforms of the Conterminous United States - A Digital Shaded-Relief Portrayal: U.S.G.S. Geologic Investigations Series I – 2720.

KECK Geology Consortium
Learning Science Through Research
Published by the Keck Geology Consortium
Short Contributions
Keck Geology Consortium
Volume 36
May 2024
doi: 10.18277/AKRSG.2024.36.02

THE ROLE OF FAULT DAMAGE ZONES IN STRUCTURALLY CONTROLLED LANDSCAPE EVOLUTION, SEVIER FAULT ZONE, SOUTHERN UTAH

PIERCE HAYTON, Colorado College
Project Advisors: Tyler Grambling, Sarah Schanz

INTRODUCTION

The relationships between fault systems, weathering, and erosion strongly affect how local landscapes evolve. As a fault propagates it creates a damage zone, characterized by intense fracturing in the lithology surrounding the fault. Fault damage zones associated with normal faults can develop asymmetrically, further influencing the regional and local fault geometry, as well as the underlying structural geology. Damage zone asymmetry often presents as both an asymmetry in damage zone width and sometimes as an asymmetry in the fracture distribution and density. The damage zone within hanging walls can be much wider than the within the footwall (Berg and Skar, 2005; Choi et al., 2016), resulting in a much larger volume of rock being affected by fracturing and fracture networks. Damage zones can often be divided into a more intense inner zone and less intense outer zone. Fracture networks and damage zones can sometimes influence fluid flow and drainage patterns, which, in turn, influence weathering and erosion of the highly fractured rock.

This study investigates the relationship between damage zone development and the morphology of fault-controlled landscapes, specifically along the Spencer Bench fault segment of the Sevier Fault. The results shed light on the style of topographic evolution in fault-controlled landscapes. Exploring this phenomenon along an active fault splay will lead to a broader understanding of the linkage between tectonic stress, strain, and physical landscapes.

STUDY AREA

The Sevier Fault is in the transition zone between the Basin and Range Province and the Colorado Plateau physiographic provinces. The Sevier Fault is a sequence of six separate fault segments that have linked to form an interconnected fault network. The fault network now acts as one large, laterally continuous fault due to the linkages that formed across segments (Taylor et al., 2024). This study focuses on a fault-parallel side drainage into Red Hollow Canyon near Orderville, UT (Figure 1). Within the side drainage, the Spencer Bench fault segment almost exclusively displaces the Navajo Sandstone. The drainage trends NE-SW, parallel to fault strike, and displays approximately 10m of displacement at the northern tip and decreases to about 5m at the southern end. The western slope is comprised of the hanging wall of the fault segment, while the eastern slope consists of the footwall. Despite lithologic consistency across the fault, the slope of the hanging wall is significantly shallower than the slope of the footwall. This drainage exhibits headward, apparently fault-controlled, erosion that has resulted in younger exposures being located at the northeast tip of the canyon and older exposures at the mouth to the southwest. As a result, the northern end has undergone the least erosion while the southern end has experienced the greatest amount of erosion.

METHODS

Field Methods

While in the field, we measured fracture orientation and position along each scanline. We determined strike, dip, and dip direction of fractures using Brunton Compasses and we measured position using a handheld meter tape, which we then collated with

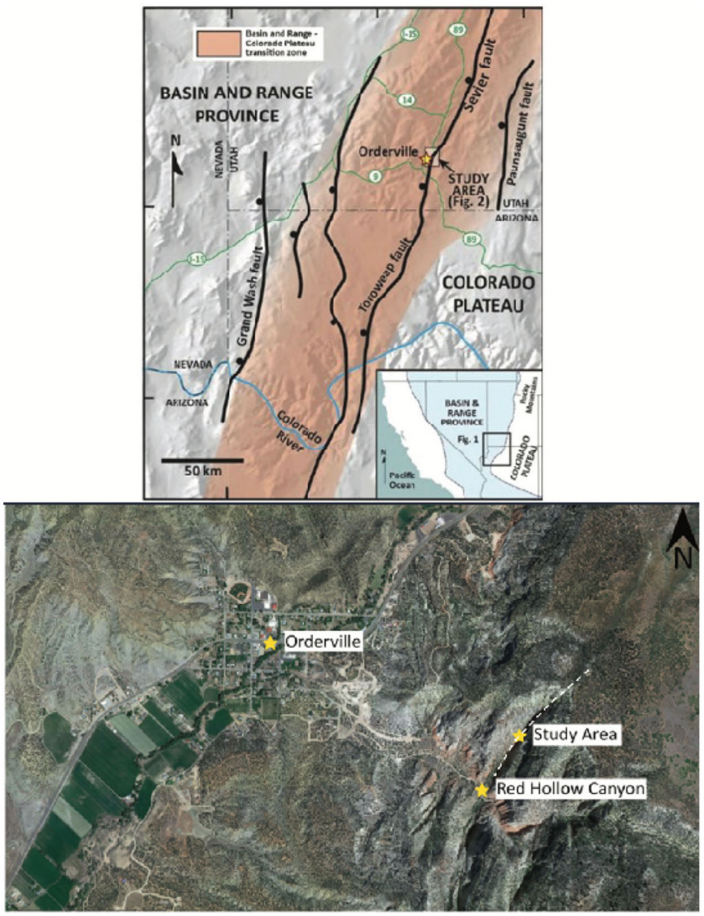

Figure 1. Location of our greater study area, Orderville, UT, and my specific study area. The trace of the Spencer Bench fault segment is highlighted by the dashed, white line in the lower map.

structural data from previous years. We recorded UTM coordinates of start- and end-points of all scanlines using handheld GPS units. We used scanline data to calculate statistics such as fracture intensity. Large portions of the landscape and fault trace were inaccessible by foot, so we used an unmanned aerial vehicle (UAV) to record video of inaccessible outcrops.

3D Structure from Motion (SfM)

While video of inaccessible outcrops is useful, producing georeferenced 3D models allows for quantitative interpretation of outcrop characteristics. UAV video was imported into Agisoft Metashape Professional to create 3D models by finding overlapping points between captured video frames. Although it is difficult to use SfM models are not high enough resolution to measure fracture orientation, such as strike and dip, it is possible to measure the fracture spacing within these regions. I georeferenced precise locations on each model using coordinates gathered in Google Earth Pro to ensure that I could measure real-world distances and accurately measure spacing between visible fractures. We then used these data to calculate fracture density.

Cross-Sectional Topographic Profiles

Due to the drainage exhibiting headward erosion, I constructed seven, down-drainage cross-sectional topographic profiles to compare potential asymmetry in rates of erosion within the hanging wall compared to the footwall. Because the northernmost profiles are the youngest, and the southernmost are the most mature, any asymmetry in erosion rates should become more prevalent moving south the drainage. The northernmost profiles should display the least slope asymmetry, due to having had the least amount of time to erode. These profiles were constructed using ArcGIS Pro and 1m digital elevation models.

RESULTS

Fracture Intensity and Spacing

I calculated the average fracture intensity and the damage zone width within the hanging wall and footwall of the Spencer Bench fault segment. This was done from both the data measured in the field and from the 3D SfM models. As shown in Table 1, the damage zone width within the hanging wall is significantly larger (190m) than it is within the footwall (94m). The average fracture spacing, standard deviation, and median of fracture spacing also display this asymmetry; the hanging wall displays a higher fracture intensity than the footwall. The damage zone extends nearly twice as far into the hanging wall than it does into the footwall. Although there is a lack of consensus on how to best define the outer boundary of damage zone (Choi et al., 2016), I defined the outer boundary of the damage zone as the point at which the frequency of deformation becomes equal to the value found further from the fault trace, as described by Choi et al. (2016).

Down-drainage Cross-sectional Topographic Profiles

I constructed seven cross-sectional profiles in the canyon to assess any asymmetry in slope and the

Table 1. Observed and calculated values for the Spencer Bench fault segment.

	Hanging Wall	Footwall
Damage Zone Width (m)	191.4	94.4
Number of Observations	86	35
Mean Fracture Spacing (m)	1.4	9.1
Fractures per meter	0.71	0.11
Fracture Spacing STDev (m)	2.0	8.0
Fracture Spacing Median (m)	0.7	6.8

effects of fault-driven landscape evolution. Figure 2 shows the location of these profiles, and Figure 3 shows these profiles graphed. These profiles are graphed at their respective elevations and normalized to one datum in order to qualify morphological changes throughout the profiles down drainage. Although the hanging wall slope is visibly shallower than the footwall, there is no discernable pattern in profile slope along strike. The slopes of the hanging wall maintain a consistent shape and do not seem to shallow out as the profiles move south.

Following the construction of these profiles, I averaged them over 25 m and 50 m intervals extending from the fault trace (Figure 4). I chose a 25 m interval to assess the landscape immediately surrounding the fault trace and the 50 m interval to constrain how the landscape evolves over a wider portion of the canyon. I was hesitant to average over the entirety of the profiles because: 1) some of these profiles extend onto adjacent topography and 2) some of these profiles begin to include terrain from the nearby plateau, or extend over a ridge into another canyon. As can be seen in Figure 4, the profiles in the 25 m interval continue to display little to not pattern, but the semblance of a pattern begins to emerge in the 50 m interval. Profiles 1 and 2 seem to decrease in slope difference, with differences of 32º and 15º respectively. Profiles 3 through 7 exhibit a gentle but steady pattern of increase in slope difference. Profile 3 only has a difference in slope of 11º which steadily grows to a difference of 18º by Profile 7.

Figure 2. Location of seven cross-sectional down-drainage profiles, each profile is color coded across Figure 3.

DISCUSSION

Damage Zone Width and Fracture Intensity

Field data indicate that the damage zones within the hanging wall and footwall are asymmetrical, with a difference in width of nearly 100m. This agrees with previous research from the nearby Moab Fault by Berg and Skar (2005), who found that the damage zone can be upwards of three times as wide in the hanging wall than it is within the footwall. This asymmetry is also found in fracture intensity data, as the average fracture spacing within the hanging wall is 1.4m compared to 9.1m in the footwall. This difference in fracture density could be attributed to the lack of an inner damage zone. As the name suggests, this is the inner most region of the damage zone, sometimes found within the footwall of a fault. Although Berg and Skar (2005) state that it is possible for these damage zones to form without an inner damage zone, it is possible that one exists. If there is a more intense inner damage zone, it would display a much higher degree deformation, and therefore the fracture intensity within the footwall reported here is not completely accurate.

Berg and Skar (2005) attribute the asymmetric damage zone development to a difference in lithology across the fault. This study provides a new perspective on this problem, as the damage zones studied here are comprised exclusively of the Navajo Sandstone. My findings suggest that damage zone distribution may be affected by something other than lithology. One alternative option for damage zone width control is

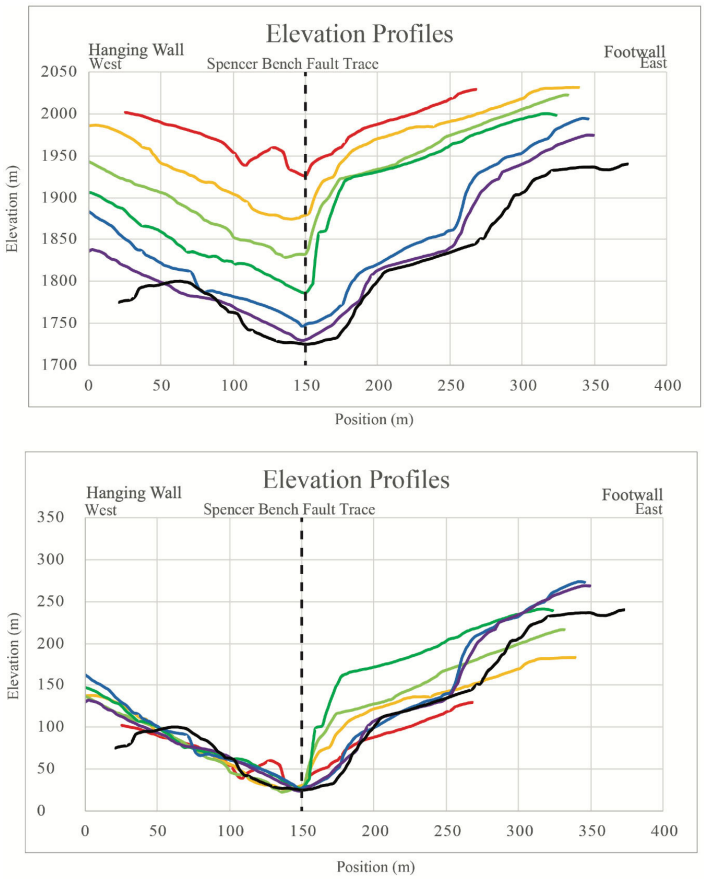

Figure 3. Topographic profiles from Figure 2. The graph on top has these profiles at their respective elevation, while the lower graph has them normalized to one elevation toreveal patterns.

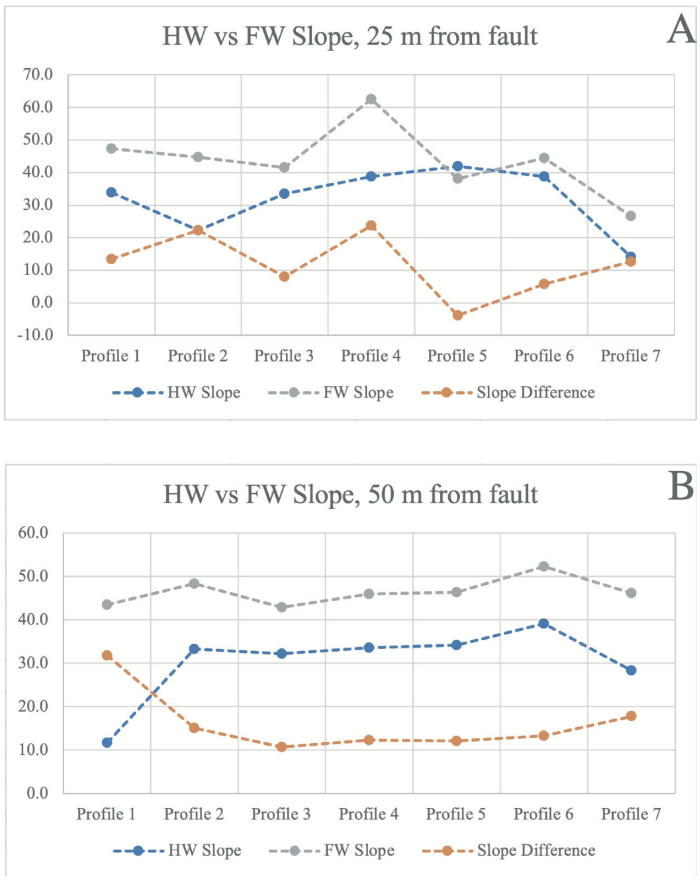

Figure 4. Average slope of the hanging wall, footwall, and difference between the two over A) 25 m interval and B) 50 m interval from the fault trace.

the density of microfractures across the fault blocks. While we did not measure microfracture density at this study site, we do know that microfracture distribution can be asymmetrical (Faulkner et al., 2011). Investigating microfracture density and distribution in the future could help to explain differences seen in slope across the fault trace.

We did not find an inner damage zone within our study area, and while this is not directly at odds with previous research, it is potentially a point of contrast that requires a more detailed assessment of the fault zone than was possible in this work. Regardless, the formation, propagation, and accumulation of displacement along the Spencer Bench fault segment has caused a variable deformation response between the hanging wall and footwall.

Topography Across the Fault

My initial hypothesis was that the northernmost profiles (red lines in Figs. 3, 4) would display the greatest amount of symmetry between the hanging wall and footwall, as fracture-enhanced weathering and erosion would not have had sufficient time to present. As the profiles moved south, I expected the western, hanging wall side of the canyon to shallow out more quickly than the footwall. Thus, the profiles would become more asymmetric as they moved south as exposures increased in age and accumulated strain. As can be seen in the normalized graph in Figure 3, this pattern is not visible, and slope does not have a strong correlation with exposure age across a 25 m swath.

In the 50 m profiles (Figure 4), there is a weak correlation between slope and spatiotemporal distribution along strike, although it is still not as strong as I initially hypothesized. If the northernmost profiles were the most symmetric, then we would expect the slope difference to be close to zero and would increase as the profiles moved south. The difference in slope in the 25 m interval seems to jump around erratically. In the 50 m interval though, Profiles 3 through 7 display a gradual increase in

slope difference from a difference of 11º in Profile 3 to 18º by Profile 7. Profiles 1 and 2 decrease in slope difference, rather than increasing as observed in the southernmost profiles.

The difference in Profiles 1 and 2 may be because Profiles 1 and 2 may extend into the White Throne member of the Temple Cap sandstone in the highest elevations of the canyon. Although this drainage is comprised almost exclusively of the Navajo Sandstone, there are a few meters of the White Throne member at the top of the canyon. We unfortunately do not have a measurement of this member here, but it may be possible that Profiles 1 and 2 extend into this member. If this is the case, the White Throne member may have difference lithologic and physical properties driving erosion to manifest differently in these two profiles. Another potential explanation is that these profiles may be young enough that drainage networks and variations in precipitations have not had sufficient time to normalize like they have in the older, more mature profiles. It is also possible that the adjacent plateau may be close enough to have an effect on rates of erosion. Irregularity of slope difference at a 25 m interval and in the uppermost extent of the canyon may indicate that there is a threshold length and rate at which enhanced fault damage zone erosion correlates with topographic response.

CONCLUSIONS

This drainage into Red Hollow Canyon is an excellent location to study the relationships between fracture intensity and landscape evolution. The studied portion of the Spencer Bench fault segment allows us to isolate the role of landscape response to faulting, as lithology and climate are consistent across the fault trace. Understanding how underlying structures can influence local or regional landscape evolution is key to mitigating secondary, fault-related hazards and provide better understanding of the relationship between fracturing and landscape evolution. This is especially important as land use in structurally controlled regions becomes more prevalent.

Throughout this section of the Spencer Bench segment, the damage zone is asymmetric across the fault. This is in line with previous research on normal faults in the transition zone between the Basin and Range and Colorado Plateau physiographic provinces (Berg and Skar, 2005). The fracture networks are also more intense within the hanging wall than within the footwall. This points towards a greater partitioning of strain into the hanging wall than the footwall. These findings are in line with previous research describing damage zone asymmetry. Furthermore, these findings indicate that such asymmetry is not controlled by a lithologic contrast and may result from the distribution of stress across fault zones.

While the damage zone and fracture network are asymmetrical there is a spatiotemporal dependence to this asymmetry. There is little to no pattern in slopes between the hanging wall and footwall along the 25 m profile lines. The slopes vary greatly from one profile to the next, with no clear trend, which may be due to the interval being too small to draw meaningful conclusions from. A pattern does emerge in the 50 m interval in Profiles 3 through 7. This pattern of gentle increase in slope difference as the profiles move south was my initial hypothesis. The slope difference increases from 11º in Profile 3 to 18º in Profile 7. Profiles 1 and 2 do not follow this pattern, potentially due to the duration of surface exposure or a lithologic contrast in the distal portions of the canyon.

Following these results, there is a weak correlation between underlying geological structures and landscape evolution. Berg and Skar (2005) attribute damage zone asymmetry to a lithology asymmetry across a fault. This study presents evidence that damage zones are asymmetric within normal fault systems even when lithology is consistent. Within this singular lithology, erosion rates have been accelerated within the hanging wall compared to the footwall. We also found an asymmetry in damage zone intensity and distribution; they extend ~100 m further and present more intensely in the hanging wall than the footwall. While further study is needed to explore mechanisms dictating this behavior, it is apparent that asymmetric damage zones are typical of upper crustal normal faults.

ACKNOWLEDGEMENTS

This material is based upon work supported by the

Keck Geology Consortium and the National Science Foundation under Grant No. 2050697. Funding was also provided by NSF Award No. 2042114 to PI Benjamin Surpless. Special thanks to Dr. Ben Surpless for leading this project, and to my advisors Dr. Tyler Grambling and Dr. Sarah Schanz.

REFERENCES

Berg, S., and Skar, T., 2005, Controls on damage zone asymmetry of a normal fault zone: oyutcrop analysises of a segment of the Moab Fault, SE Utah: Journal of Structural Geology, v. 27, p. 1803–1822, doi:https://doi.org/10.1016/j.jsg.2005.04.012.

Choi, J.-H., Edwards, P., Ko, K., and Kim, Y.-S., 2016, Definition and classification of fault damage zones: a reivew and a new methodological approach: Earth-Science Reviews, v. 152, p. 70–87, doi:https://doi.org/10.1016/j.earscirev.2015.11.006.

Faulkner, D.R., Mitchell, T.M., Jensen, E., and Cembrano, J., 2011, Scaling of fault damage zones with displacement and the implications for fault growth processes: Journal of Geophysical Research, v. 116, p. B05403, doi:10.1029/2010JB007788.

Taylor, W.J., Surpless, B., and Schiefelbein Kerscher, I.M., 2024, Complex Segment Linkage Along the Sevier Normal Fault, Southwestern Utah: Lithosphere, v. 2024, doi:10.2113/2024/lithosphere_2023_332.

KECK Geology Consortium
Learning Science Through Research
Published by the Keck Geology Consortium
Short Contributions
Keck Geology Consortium
Volume 36
May 2024
doi: 10.18277/AKRSG.2024.36.03

COMPUTER MODELING OF NORMAL FAULT-RELATED DAMAGE ZONES: IMPLICATIONS FOR ESTIMATING GEOTHERMAL ENERGY POTENTIAL

AUDREY JENNINGS, Trinity University
Project Advisor: Benjamin Surpless

INTRODUCTION

In the 21st century, many nations have sought to diversify their energy resources to promote energy security and slow climate change impacts (e.g., Boden, 2017). New renewable energy resources, such as geothermal energy, can help achieve this. To be productive at the utility-scale, geothermal energy systems require high subsurface heat flow and connected fluid pathways. Fault damage zones are conducive to geothermal energy production due to the high stresses and strain created by faulting, which can increase subsurface permeability due to intense fracturing (e.g., Micale et al., 2014; Faulds and Hinz, 2015; Shervais et al., 2024). Thus, further investigating damage zone formation in normal fault zones is a crucial step in expanding geothermal energy production in the United States.

However, field-based geothermal exploration can be prohibitively expensive, making lower-cost exploration options like 3D computer modeling appealing (e.g., Micale et al., 2014; Shervais et al., 2024). Therefore, this study utilized 3D modeling to assess the influence of different geologic variables (including fault displacement, fault propagation, and pore fluid pressure) on damage zone development in a simple normal fault system. Through this work, I aim to answer a range of research questions, including:

1. How do stress, strain, and fracturing evolve as faults propagate, and how do different fault propagation models impact the evolution of deformation?

2. What effects do fault-related stress and strain fields have on fracturing orientations and intensities within the rock volume?

3. How does the distribution of fault-related fracturing vary with depth and accumulated displacement?

4. Can we use 3D modeling results to aid in the identification of locations with especially high permeability and thus geothermal potential?

BACKGROUND

Geothermal energy production

Production sites for geothermal energy development must provide both elevated heat flows and high permeabilities. Traditional strategies for permeability identification, such as drilling into the subsurface to look for the presence of heated, mobile fluids (e.g., Boden, 2017), can be effective but typically require upfront financial investment that may not be recouped if they fail to locate the desired setting (e.g., Micale et al., 2014).

Further investigation of damage zones can be helpful for geothermal system locations because zones tend to form in predictable patterns, with the greatest intensity of fracture and shear-related deformation near the fault center. (e.g., Berg and Skar, 2005; Savage and Brodsky, 2011; Choi et al., 2016). Damage zones also often form asymmetrically, with the width and intensity of deformed regions differing between the hanging wall (HW) and footwall (FW) (e.g., Berg and Skar, 2005; Choi et al., 2016; Liao et al., 2020). Furthermore, faults propagate laterally and accumulate displacement over their life, causing damage zones to potentially vary based on stage of fault growth.

However, patterns of fault propagation are not entirely understood. The fault propagation (FP) model posits that a fault lengthens horizontally as it accumulates vertical displacement, such that the fault is growing horizontally and vertically at the same rates (e.g., Cowie et al., 2000; Kim and Sanderson, 2005; Rotevatn et al., 2019). In contrast, the constant length (CL) model describes an initial rapid accumulation of horizontal length and then an accumulation of dip-slip displacement (e.g., Cowie, 1998; Nicol, 2005; Rotevatn et al., 2019). However, neither conceptual model has emerged as a more accepted model of fault growth (Rotevatn et al., 2019). Because fault propagation and associated displacement accumulation are the most significant sources of stress, strain, and fracturing within normal fault systems, better understanding the implications of both models for the evolution of stress, strain, and fracture development is critical for evaluating damage zones associated with faults at locations with high geothermal potential.

METHODS

Model construction

To investigate damage zone development in normal fault zones, I utilized the Fault Response Modeling (FRM) module of Move 2022 (by Petex). This module calculates 72 distinct geologic variables based on user-designed 3D fault scenarios. It also utilizes boundary element modeling (BEM), calculating specified variables only at defined observation points across the model in order to reduce computing power but maintain accuracy (Petex, 2020). Such calculations are based on the movement and flexure of blocks of material relative to the fault plane. I constructed three different sets of fault models, calculating the resulting values for variables of interest ((maximum Coulomb shear stress, E1 (strain value in the orientation of maximum strain), and strain dilation (increase in volume related to rock deformation)) at the meter scale across 3 different depths (0.5 km, 2 km, and 3 km). Using the FRM module I also generated predictions of fracture orientation and intensity across each model. Data is shown via heatmaps for each variable, with warmer colors indicating higher variable values and larger dots representing more intense fracturing. In addition to these heatmaps, I also exported the raw numerical data for each variable and graphed it across defined cross-fault profiles in order to visualize spatial changes in stress and strain.

Each model consists of a single, 5 km-long fault segment dipping at 70 degrees from the horizontal (Fig. 1). I also set every observation surface to mimic the lithological properties of the Navajo sandstone, including a Young's Modulus of 30,000 MPa, a Poisson's Ratio of 0.25, and a density value of 2,495 kg/m^3 (Schultz, 2010). The Navajo sandstone is present throughout much of the Basin and Range province (e.g., Fossen et al., 2011), a promising region for geothermal development due to the intense faulting and high heat flow found throughout (e.g., Faulds and Hinz, 2015). By defining the properties of our observation surfaces to be like the Navajo Sandstone, results can be better applied to real world geothermal potential. I also defined pore fluid pressures of 5.2 MPa for the 0.5 km-depth surface, 20.6 MPa for the 2 km-depth surface, and 36.0 MPa for the 3 km-depth surface of every model, as well as a model with a pore fluid pressure value of 0 MPa for each observation surface depth, serving as a control model to compare stress, strain, and fracturing results across fluid conditions.

To model the potential impacts of the fault propagation (FP) model on damage zone development, I constructed three different normal fault segment models which mimic a simultaneous increase in vertical displacement and lateral increase in fault length. To simulate fault development according to the constant length (CL) propagation model, I kept the fault segment at 6 km of length across all three models and gradually increased the vertical displacement in

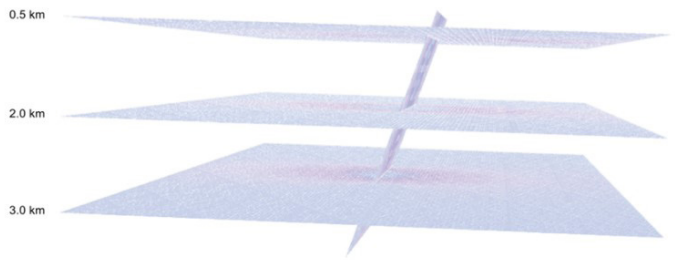

Figure 1. Fault model geometry in sideview. The topmost observation layer is located at 0.5 km-depth beneath the surface; the middle observation layer is located at 2.0 km-depth; and the bottommost layer is located at 3.0 km-depth. The fault plane dips at 70 degrees from the horizontal.

the same manner as the FP models: first 10 m of slip, then 50 m, and finally 200 m (Fig. 2).

DATA AND RESULTS

Damage zone distributions

In every scenario, the locations of MCSS and E1 maximums and minimums are nearly identical, indicating that stress and strain vary in an identical manner within a given model. Near the fault center, the predicted variable values are greater than for the same variable at the fault tips. I also used the same set of fault displacements (10, 50, and 200 meters) for all models. In all models, greater fault displacement is associated with proportionally higher predictions of MCSS, E1, and dilation values. However, the location and width of elevated stress and strain values (i.e. damage zones) for each model remains consistent, regardless of increasing vertical displacement. Fracture intensity is also greatest where stress and strain values are highest, and decreases away from damage zones (Fig. 3).

Depth

The top observation surface in each model predicts greater areas of elevated E1 and MCSS values (i.e. damage zones) within the hanging wall, relative to the footwall. But, as depth increases, the location of major damage zones shifts towards the fault plane, such that they occur in the footwall at depth. The numerical values of MCSS, E1, and dilation predicted by the models also change between observation surfaces; within the same model, the middle observation surface (2 km depth) predicts the highest values, with the bottom layer displaying slightly lower values, and the top observation surface demonstrating the lowest (Fig. 4).

Fault growth models (FP vs. CL)

For the different fault propagation models, the relative location of MCSS, E1, and dilation maximums and minimums for each observation surface remains consistent, with the highest values observed near the fault center, and decreasing values associated with the fault tips. However, this pattern is shortened proportionally to the fault plane in the start and middle stages of the FP model. Numerically, the fault propagation models at every stage generate greater predicted E1, MCSS, and dilation values than for the constant length models experiencing the same vertical displacement, in the same material, and measured at the same depth (Fig. 5).

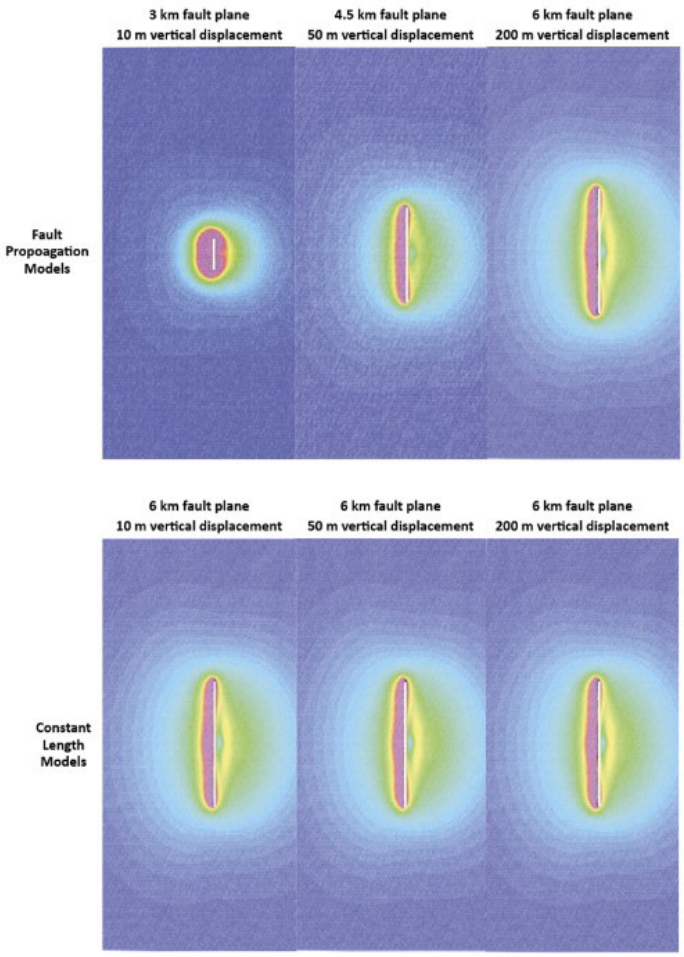

Figure 2. Fault Propagation and Constant Length fault growth models. Constructed models simulating the Fault Propagation (top) and Constant Length (bottom) theories of fault growth. Models are shown from the top, with fault lengths represented by white lines. The hanging wall lies to the left of each fault plane, and the footwall lies on the right. Fault models are overlain by MCSS predictions for a 6 km fault plane (shown at 0.5km of depth) experiencing 200 m of displacement, approximating the CL End model. Warmer values indicate greater MCSS values.

Pore fluid pressure

The location and volumetric extent of damage zones between models with different pore fluid pressures remain consistent. However, the specific values predicted for MCSS, E1, and dilation vary such that models with a set PFP value of 0 MPa predict lower MCSS and E1 values at a given point, relative to an equivalent model with realistic pore fluid pressures.

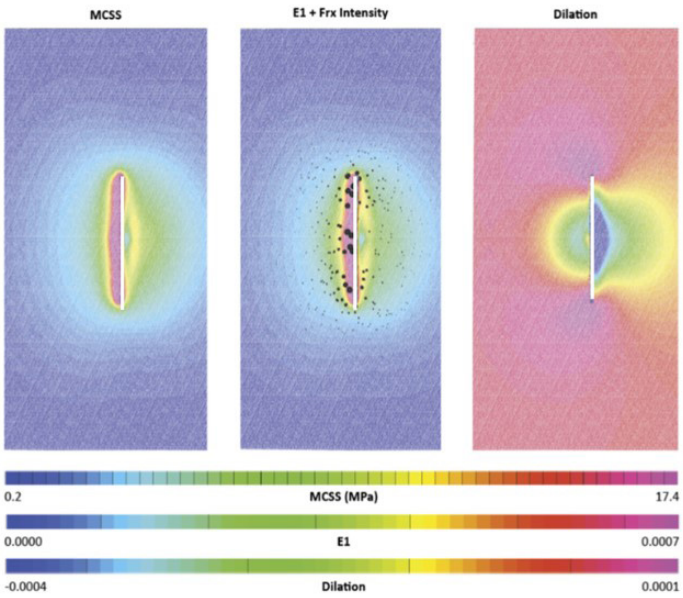

Figure 3. Distribution of damage zones. Predicted MCSS (left), E1 (middle), and dilation (right) values for the 0.5 km depth surface of a model experiencing 200 meters of vertical displacement along a 6 km fault plane. This model represents the Constant Length model with realistic pore fluid pressures included. Warmer colors represent higher values; cooler colors represent lower values. Fracture intensity is also depicted on the E1 surface, with larger black dots representing greater fracture intensity at a given point.

For example, the maximum MCSS value predicted in the CL End model with 0 MPa of PFP is just over 600 MPA; in the same model but with realistic PFP values, the maximum MCSS value predicted is about 800 MPa.

DISCUSSION

Damage zone distributions

In all models, the greatest values of stress and strain occur adjacent to the fault plane and decrease with distance. This trend is also well-documented in field studies, with the frequency of fault-related deformation greatest near the fault (e.g., Choi, 2016; Childs et al., 2009). The width of damage zones also appears consistent between models, even as displacement increases, mirroring a consistent damage zone model proposed by Ferrill and Morris (2001). However, previous field studies, as summarized by Houwers et. al. (2015), suggest increasing fault displacement corresponds to widening damage zones. Because the FRM module does not account for pre-existing weaknesses and thus negates the potential deformational influence of early fracturing, I cannot offer insight into which of these patterns is more realistic, though this represents a potential area for future research.

Furthermore, the higher predicted stress and strain values present away from the fault plane in the hanging wall of the 0.5 km observation surface of the models, relative to the footwall, suggest that damage zones form asymmetrically across normal fault planes. Such asymmetry has been documented in a field study of the same lithology (Navajo sandstone), with a narrower damage zone in the footwall (70 m) of the normal fault versus the hanging wall (210 m) (Berg and Skar, 2005).

Change in damage zone distributions with depth

Every model demonstrates damage zone asymmetry, though the direction varies with depth. I have not found studies that provide a satisfying cause for this switch in damage zone location with depth. However, fault slip tapering and related propagation direction may play a role. Fault slip tapering refers to displacement which is greatest at the fault center and decreases to 0 at fault tips, as observed in field studies. This fault slip distribution is represented in my modeling. Because displacement accumulates, the fault plane above the centroid represents an area on the fault plane that experiences upward propagation of accumulating displacement, and the fault plane below represents an area that experiences downward propagation of displacement. The fault dips at an angle and strain-related fracturing propagates in an orientation that is more energetically favorable, especially based on propagation direction (e.g., Sharon and Fineberg, 1996; Zhou et al., 2018; Fineberg and Bouchbinder, 2015; Surpless and McKeighan, 2022); thus, propagation direction may explain damage zone asymmetry.

Fault growth models: fault propagation vs. constant length

By comparing the damage zone extents between my Fault Propagation and Constant Length models, it is clear that damage zones tend to follow the same distribution of high stress and strain around the fault plane, regardless of propagation model or stage. However, the sizes of these damage zones

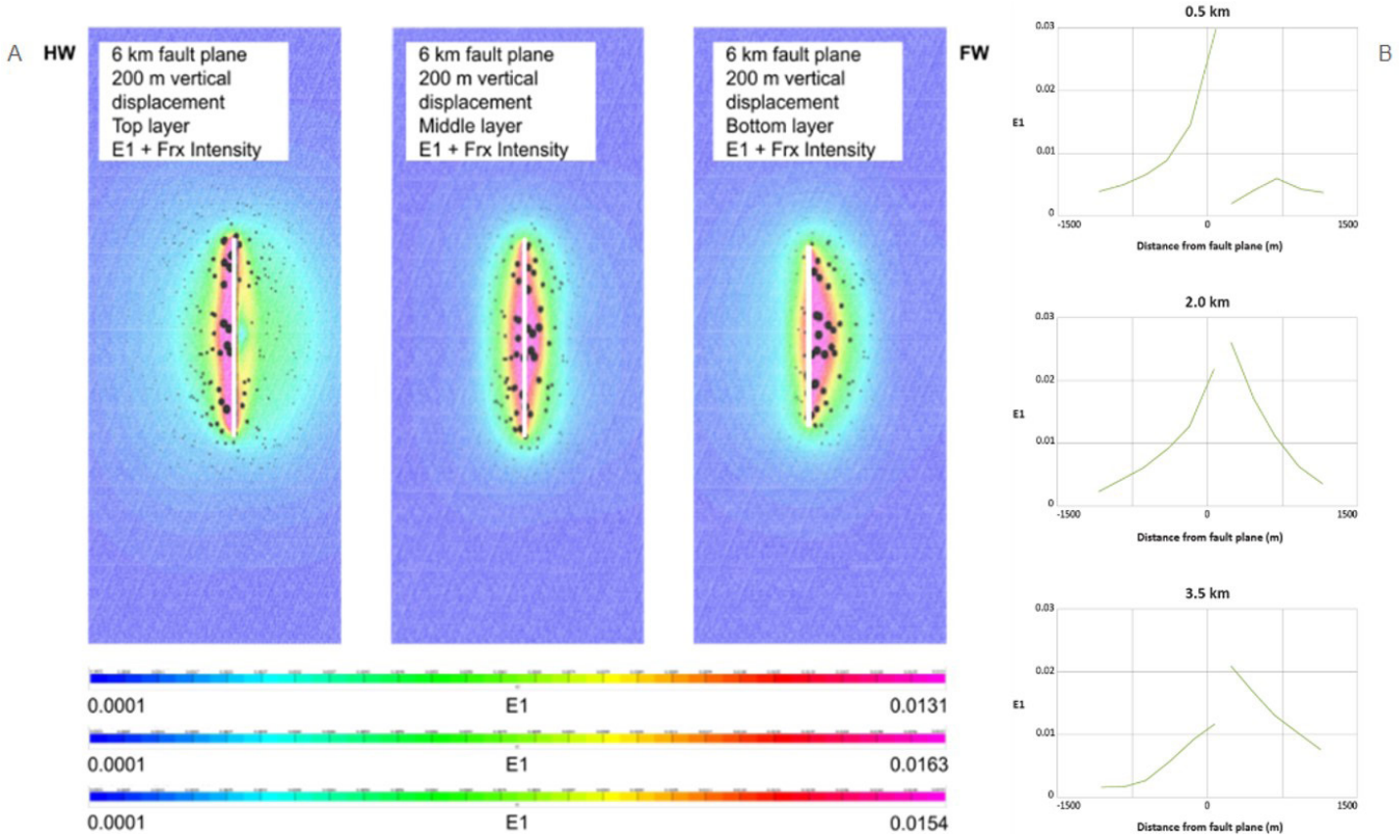

Figure 4. A) Damage zone distribution with depth. Predicted E1 values and fracture intensities for the 0.5 km-depth surface (left), 2 km-depth surface (middle), and 3.5 km-depth surface (right) of a 6 km fault plane experiencing 200 m of vertical displacement. These models represent 3 different depths of the CL End stage of the Constant Length growth model. Warmer colors represent higher values; cooler colors represent lower values. Fracture intensity is also depicted on the E1 surface, with larger black dots representing greater fracture intensity at a given point. B) Graphical representations of E1 values at 0.5 km (top), 2.0 km (middle), and 3.5 km (bottom) depths around a 6 km fault plane experiencing 200 m of vertical displacement. These models represent 3 different depths of the CL End stage of the Constant Length growth model. As depth increases, elevated E1 values shift from the hanging wall side of the graph (0.5 km depth) to the footwall side of the graph (3.0 km depth).

vary with fault propagation model stage such that the shorter fault planes of early-stage FP models generated proportionally shorter damage zones in the fault-parallel direction. Still, both the FP model set and the CL model set concluded with a 6 km fault plane experiencing 200 m of vertical depth, and the associated stress and strain variable predictions for these final stages of each model set produced essentially identical damage zone distributions. Such a discrepancy in damage zone area between early-stage FP and CL models indicates that damage zones would form differently based on the relationship between fault propagation and displacement accumulation; however, fault zones with the same fault length and amount of displacement may ultimately have similar damage zone distributions regardless of growth history.

Influence of pore fluid pressure

My models also indicate that systems with realistic pore fluid pressures (PFPs) record higher MCSS and E1 values than systems with PFP values of 0. When considering the Mohr Coulomb failure envelope, failure in material occurs if the shear and normal stress values are such that the Mohr circle intersects the failure envelope. Higher pore fluid pressure shifts the Mohr circle towards the left, meaning that failure is far more likely to occur. The elevated strain values observed in models with realistic PFP values, relative to in models with no PFP, thus likely reflect the leftwards shift towards failure and a potential for increased permeability.

Fracturing intensity and orientation

Understanding fracture intensity and orientation

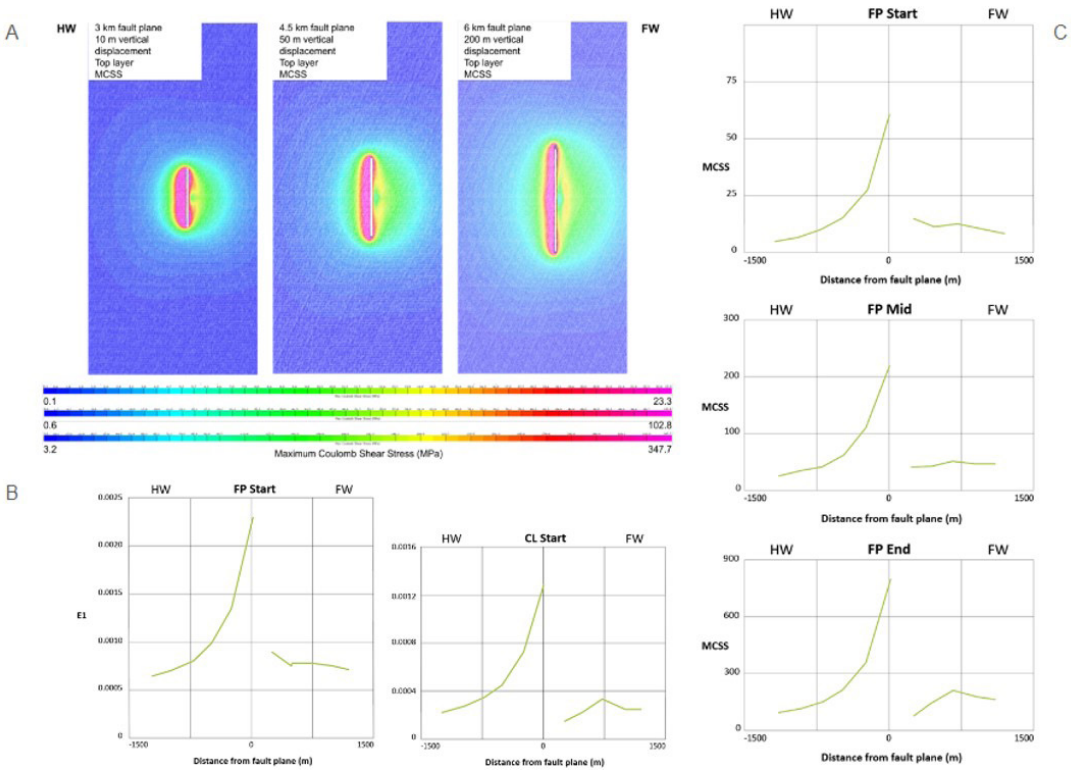

Figure 4. A) Fault propagation (FP) model of fault growth. Predicted MCSS for the 0.5 km depth surface of a 3 km fault plane experiencing 10 m of vertical displacement, representing the FP start model (left); a 4.5 km fault plane experiencing 50 m of vertical displacement, representing the FP Mid model (middle); and a 6 km fault plane experiencing 200 m of vertical displacement, representing the FP End stage of the Fault Propagation model of fault growth. Models include realistic pore fluid pressures. Warmer colors represent higher values; cooler colors represent lower values. B) Graphical representations of E1 predicted for a 3 km fault plane experiencing 10 m of vertical displacement, representing the FP Start stage of the Fault Propagation model (left) and a 6 km fault plane experiencing 10 m of vertical displacement, representing the CL Start stage of the Constant Length fault growth model. For the same stage (starting vs. ending) in the FP fault growth model (left) and the CL fault growth model (right), predicted MCSS and E1 values are higher in the FP models compared to the CL models. C) Graphical representations of MCSS values for the FP model shown in A. As fault propagation within the Fault Propagation conceptual model of fault growth continues, predicted MCSS values increase.

predictions is especially important for assessment of geothermal potential because increases in permeability created by fracturing and dilation create the primary pathways for circulating geothermal fluids in fault systems. My modeling results indicate that fracture intensities are greatest in regions of elevated stress and strain, meaning that the locations of high intensity fracturing in each model are subject to the same trends observed in damage zone locations.

CONCLUSION

Implications for geothermal energy

Based on my model results and published field studies, the location and nature of damage zone development around a normal fault system can vary, depending on factors like 1) amount of vertical displacement experienced by the fault, 2) stage of fault propagation; 3) pore fluid pressure; and 4) depth (in relation to the slip-tapering centroid). The high fracture intensities and dilation values (and thus likely high permeability) observed in the damage zones of my models provide insights into damage zone development that can be used to better understand geothermal energy potential in normal fault zones and for constraining potential targets for future field-based geothermal exploration. Given that geothermal energy is one of the most promising renewable energy resources of the 21st century, with the potential to generate 2-4 times as much electricity as wind or solar energy at the same installed capacity, finding ways to minimize the cost of geothermal exploration will be crucial for promoting green energy and developing resilient electricity through resource diversification (U.S. Department of Energy, 2019). 3D modeling, which can be done in advance of expensive field studies, represents a potential method for better identifying damage zones that can support utility-scale geothermal energy

production.

ACKNOWLEDGMENTS

This material is based upon work supported by the Keck Geology Consortium and the National Science Foundation under Grant No. 2050697.

REFERENCES

Berg, S.S., and Skar, T., 2005, Controls on damage zone asymmetry of a normal fault zone: outcrop analyses of a segment of the Moab fault, SE Utah: Journal of Structural Geology, v. 27, p. 803-1822.

Boden, D.R., 2017, Geologic Fundamentals of Geothermal Energy: Boca Raton, Florida, CRC Press, 399 p.

Childs, C., Manzocchi, T., Walsh, J.J., Bonson, C.G., Nicol, A., Schoepfer, M.P.J., 2009, A geometric model of fault zone and fault rock thickness variations, Journal of Structural Geology, v. 31, p. 117 - 127.

Choi, J.H., Edwards, P., Ko K., and Kim, Y.S., 2016, Definition and classification of fault damage zones: A review and a new methodological approach: Earth-Science Reviews, v. 152, p. 70 – 87.

Cooke, M., unpublished, Numerical Methods – Boundary Element Modeling, 3p.

Cowie, P.A., and Shipton, Z.K., 1998, Fault Tip Displacement Gradients and Process Zone Dimensions, Journal of Structural Geology, v. 20, p. 983 - 997.

Crider, J., and Pollard, D., 1998, Fault linkage: Three-dimensional mechanical interaction between echelon normal faults, Journal of Geophysical Research, v. 103, p. 24.373 - 24.391.

Faulds, J., and Hinz, N., 2015, Favorable Tectonic and Structural Settings of Geothermal Systems in the Great Basin Region, Western USA: Proxies for Discovering Blind Geothermal Systems, in Proceedings, World Geothermal Congress, Melbourne: Australia, Nevada Bureau of Mines and Geology (https://www.osti.gov/servlets/purl/1724082).

Ferrill, D.A., and Morris, A.P., 2001, Displacement gradient and deformation in normal fault systems, Journal of Structural Geology, v.23, p. 619 – 638.

Fineberg, J., and Bouchbinder, E., 2015, Recent developments in dynamic fracture: Some perspectives, International Journal of Fracture, v.196, 33 – 57.

Fossen, H., and Rotevatn, A., 2015, Fault linkage and relay structures in extensional settings- A review, Earth Science Reviews.

Fossen, H., 2016, Structural Geology: 2nd edition, Cambridge: Cambridge University Press.

Houwers, M.E., Heijnen, L.J., Becker, A., Rijkers, R., 2015, A Workflow for the Estimation of Fault Zone Permeability for Geothermal Production: A General Model Applied on the Roer Valley Graben in the Netherlands, in Proceedings, World Geothermal Congress, Melbourne: Australia.

Kim, Y.S., Peacock, D., Sanderson, D, 2004., Fault damage zones: Journal of Structural Geology v. 26. P. 503 - 517. DOI: 10.1016/j.jsg.2003.08.002.

Kim, Y.S., and Sanderson, D., 2005, The relationship between displacement and length of faults: A review, Earth Science Reviews, v. 68, p. 317 – 334.

Liao, Z., Hu, L., Huang, X., Carpenter, B.M., Marfurt, K.J., Vasileva, S., and Zhou, Y., 2020, Characterizing damage zones of normal faults using seismic variance in the Wangxuzhuang oilfield, China: Interpretations v. 8, p. 1- 24.

Micale, V., Oliver, P., and Messent, F., 2014, The Role of Public Finance in Deploying Geothermal: Background Paper, in San Giorgio Group Report, Climate Policy Initiative, p. 1 - 15.

Nicol, A., Childs, C., Walsh, J.J., Manzocchi, T., Schopfer, M.P.J., 2017, Interactions and growth of faults in an outcrop-scale system, Geological Society of London Special Publications, v. 439, p. 23 – 39.

Petex, 2020, Move 2020 Tutorial 33: Fault Response Modeling.

Rotevatn, A., Jackson, C.A.L., Tvedt, A.B.M, Bell, R.E., Blaekkan, I., 2019, How do normal faults grow? Journal of Structural Geology, v. 125, p. 174 – 184.

Savage, H.M., Brodsky, E.E., 2011, Collateral damage: Evolution with displacement of fracture distribution and secondary fault strands in fault damage zones, v. 116, p. 1 – 14.

Schultz, R., 2010, Porosity and Grain Size Controls

on Compaction Band Formation in Jurassic Navajo Sandstone: American Geological Union geophysical Research Letters v. 37, 22.

Sharon, E., Fineberg, E., 1996, Microbranching instability and the dynamic fracture of brittle materials: Physics Reviews, v. B54, p. 7128–7139.

Shervais, J. et al., 2024, Geothermal play fairway analysis, part 1: Example from the Snake River Plain, Idaho, v. 117, p. 1 – 18.

Surpless, B.E., and McKeighan, C., 2022, The role of dynamic fracture branching in the evolution of fracture networks: an outcrop study of the Jurassic Navajo Sandstone, southern Utah: Journal of Structural Geology, v. 161. DOI: 10.1016/j.jsg.2022.104664.

U.S. Department of Energy, 2019, Geovision: Harnessing the Heat Beneath our Feet: https://www.energy.gov/sites/prod/files/2019/06/f63/GeoVision-full-report-opt.pdf (accessed September 2023)

Zhou, S., Zhuang, X., Zhu, H., Rabczuk, T., 2018, Phase field modeling of crack propagation -Branching Coalescence Rocks: Theoretical Applications of Fracture Mechanics, v. 96, p. 174–192.

KECK Geology Consortium
Learning Science Through Research
Published by the Keck Geology Consortium
Short Contributions
Keck Geology Consortium
Volume 36
May 2024
doi: 10.18277/AKRSG.2024.36.04

GEOLOGICAL TIMELINE & EXTENSION OF MARTIAN FAULTING IN THE ALBA MONS REGION OF MARS

JACK MRACHEK, Purdue University
Project Advisor: Michael Eddy

INTRODUCTION

Alba Mons is a Martian volcano-tectonic complex that lies to the north of the Tharsis region (Tanaka, 1990). This area has the thickest Martian crust at 90 km (Kim et al., 2023). Alba Mons is one of the largest volcanic complexes in the Tharsis region, far larger than any volcano on Earth, with a diameter of roughly 1400 km (East-West) by 1000 km (North-South) with a collapsed caldera at the center (Öhman & McGovern, 2014). Alba Fossae is located to the northwest of Alba Mons, where extensive normal faulting has taken place. Excellent exposure of volcanic rocks, ancient fluvial systems, and fault scarps makes this region an ideal place to explore the geologic history of the Alba Mons volcanic edifice (Tanaka, 1990).

To better understand the geologic history of the Alba Fossae region, I analyzed high-resolution orbital imagery using a mosaic (released April 2023) constructed from images taken by the CTX camera aboard the Mars Reconnaissance Orbiter. This exercise involved determining cross-cutting relationships between volcanic flows, ancient fluvial systems, and fault scarps. The sequence of geologic events in this area has been previously studied (Karimova, 2017), but hasn't been revisited with the new data from the Mars CTX Camera. I also explored the overall extensional aspect of Alba Fossae by investigating fault displacement to length relationships and determined the degree of extension in the Alba Fossae region. To determine these relationships, I measured each fault segment length using Google Mars and then measured the fault's heave and throw values. This same process was used to determine the degree of extension along a single transect perpendicular to the faults in the Alba Fossae region. After the calculations were completed, I then assembled displacement vs. length graphs for comparison to these relationships in terrestrial faults. For context, it is important to note the difference between Alba Mons and large volcanoes on Earth. Alba Mons spans 5.7 million square kilometers (Cattermole, 1990). Mauna Loa, Earth's largest volcano, spans just 5,271 square kilometers (USGS survey). The size difference is significant and must be considered when comparing terrestrial and martian volcanoes.

BACKGROUND

Alba Mons is a large shield volcano on Mars with a diameter of roughly 1400 km (East-West) by 1000 km (North-South) that was volcanically active during the early to middle Amazonian period (3.0 Gya to 2.5 Gya) (Öhman & McGovern, 2014 ; Ivanov & Head, 2006). The summit of Alba Mons reaches a height of around 7 km (Ivanov & Head, 2006).

The volcano has regions of circumferential faulting along its outer edges, including the Alba Fossae region which is located northwest of the collapsed caldera complex at the center of the volcano (Fig. 1). These large fault systems are a result of applied lithospheric forces from the Tharsis region (Carr, 1980 ; Tanaka et al., 1991), and they've been influential in the evolution and history of Alba Mons (Ivanov & Head, 2006). As Alba Mons became inactive, it relaxed, and the lithospheric stress began to manifest itself via faulting around the volcanic region. The mass of Alba Mons is large enough that it loaded the lithosphere and caused the formation of circumferential faults. The Alba Fossae fault zone is also home to lava flows and fluvial

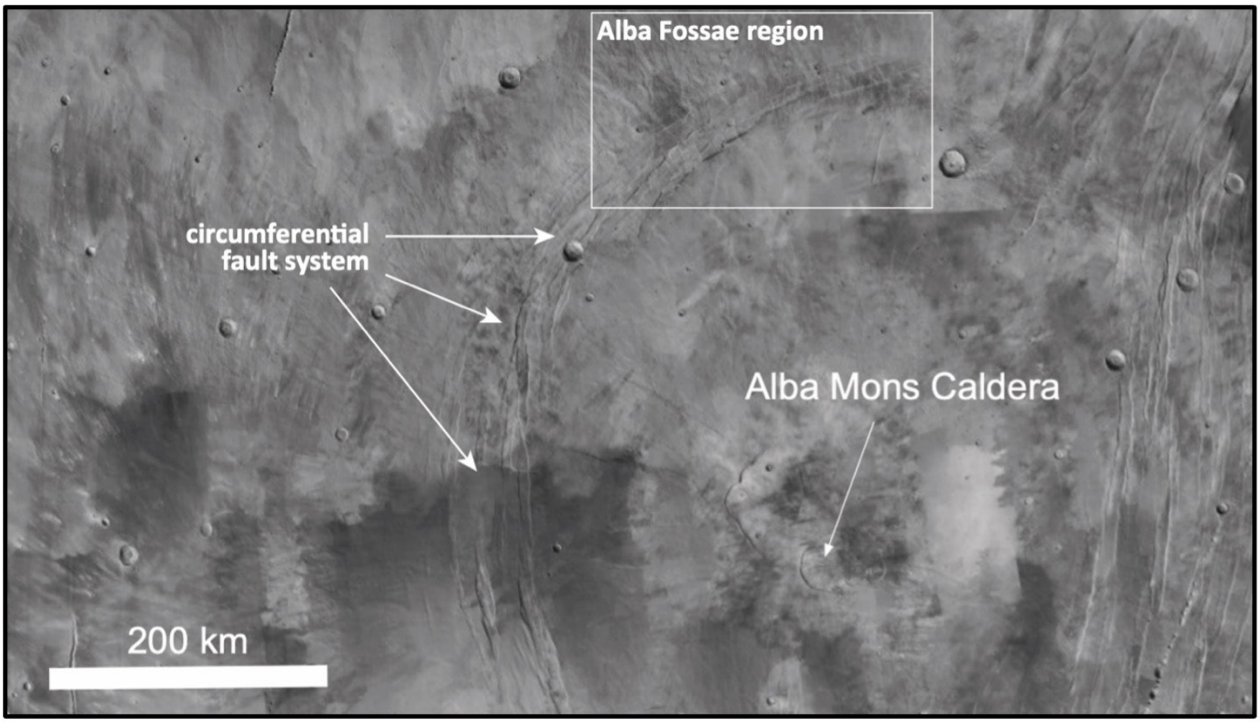

Figure 1. Snapshot from the CTX mosaic which shows the Alba Mons Caldera and the Alba Fossae region where the analysis was conducted, and the circumferential faults can be seen.

systems that interact with various fault segments.

The north-south trending faults formed as a result of tectonic effects from the Tharsis volcano complex stretching the surface as the volcano arose. This set of faults interacted with the circumferential faults on the outskirts of Alba Mons (Ivanov & Head, 2006). The graben of the Alba Fossae system both cut through and were cut by lava flows on the flanks of the volcano (Ivanov & Head, 2006). This is one of the relationships explored within this region. The faulting history of Alba Fossae spans a long period of time. The graben systems were active at certain points from the Hesperian (3.5-3.7 Gya) to the early Amazonian (2.5-2.6 Gya) periods (Ivanov & Head, 2006). The faults and fluvial systems play a major role in the geologic history of this region on Mars and Alba Mons is a small portion of that history (Tanaka, 1990). The fluvial systems in the region of Alba Fossae are thought to have been active both before and after the volcano's activity (Karimova, 2017). The last event is believed to be the formation of the circumferential faulting which outlines the northwestern portion of Alba Mons (The region of study). The timeline of events is disputed by different studies that have examined the region (Karimova, 2017 ; Ivanov & Head, 2006). Using the new CTX camera mosaic I explored the region in greater detail to establish an accurate timeline of geologic events.

Exploring the relationship between displacement and fault segment length has been done several times on Earth in large surveys of faults (Walsh & Watterson, 1988). The relationship between the displacement and length can be expressed through an equation: D = cLn. Where D is the displacement value, length is L, n is some scaling value of the relationship, and c is the rock strength value. The values of n range from about 0.5 to 2 for normal faults on Earth. In a study done in 2022, the relationship equation was determined to be D = 0.3L0.92 and this was based on a survey containing data from 4,059 normal faults from 66 sources around the world (Lathrop et al., 2022). Several factors are taken into consideration when conducting surveys of this nature. Different fault segment lengths will have different length vs. displacement relationships. This survey measured both inactive and active faults. The circumferential faults in Alba Fossae are thought to have been inactive for the past 500 million years (Ivanov & Head, 2006).

It has been suggested that fault displacement and fault length relationships don't follow a linear model, but instead propagate to its near maximum length and then, over time, displace with little tip propagation

(Walsh et al., 2002). Faults most likely grow following the hybrid model which has two distinct phases. The first phase accounts for about 20% to 30% of the fault's life. In this phase, the fault reaches the near maximum propagation length and about 10% to 60% of the fault's displacement occurs. The second phase has almost no propagation and this is where 40% to 90% of the displacement occurs (Rotevatn et al., 2019). Different times during the fault's lifespan will correspond to different length vs. displacement relationships. This is why exploring inactive faults on Earth and comparing them with the circumferential faults in Alba Fossae is critical. The fault must be at maximum displacement when measuring the fault length and examining the length vs. displacement relationship.

METHODS

I used several methods to investigate the evolution of faulting in the Alba Fossae region. I performed image analysis using the mosaic made from images taken by the CTX camera. The images from the CTX camera were the primary source of imagery data that I used when analyzing the geologic timeline of events of the Alba Fossae region. I compared some of the specific faults and areas back to Google Mars to examine the elevation data. Google Mars also had wonderful 3D interaction features. Using the mosaic, I located the geologic features that were present and made note of them.

I identified faults, fluvial systems, and lava flows. I looked at locations within Alba Fossae where there was an interaction between two features. The analysis of these interactions allowed me to determine the geologic timeline of the region. If one feature cuts through another feature, for example, a fault cutting through a lava flow, the fault is younger than the lava flow. I found instances where normal faults cut through fluvial systems, fluvial systems cut through lava flows, and normal faults cut through lava flows. I also found locations where north-south running faults were cut by circumferential faults. I took images of the sites where interactions occurred and then made diagrams/figures that properly illustrate the feature interactions in a simplified view. With the diagrams and the photo evidence, I was able to provide the rough geologic timeline of Alba Fossae. I also used Google Mars to measure 253 total fault segment lengths in the Alba Fossae region. I measured the displacement values of 200 out of the 253 faults. I calculated the overall extension percentage of the region, which required a line to be drawn from the interior of the circumferential faults to the exterior faults. This process was done within Google Mars and the line is shown in Figure 2. The line intersected with 21 different faults. I calculated each fault's heave and throw values. I made graphs to describe the relationship between the fault segment lengths, and the heave, throw, and displacement. The heave and throw values were gathered by capturing elevation profile data along each fault at the highest displacement point on the fault shown in Figure 3.

I calculated the displacement values using the Pythagorean theorem. I measured the throw values of each fault by taking an elevation profile like the one above and subtracting the value denoted by the intersection of the red slope line and the blue line (3) by the value denoted by the intersection of the red slope line and the blue line (4). The heave was measured similarly, first taking an elevation profile like the one above and subtracting the value denoted by the intersection of the red slope line and the orange line (2) by the value denoted by the intersection

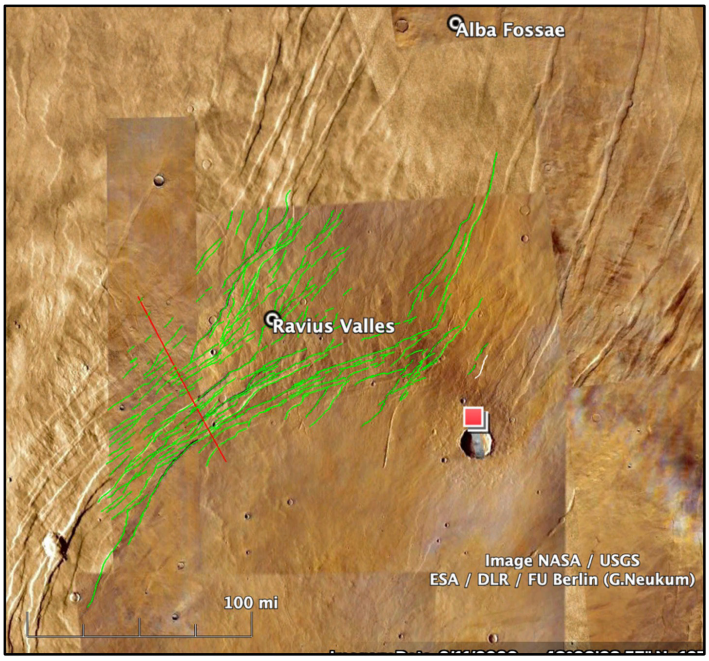

Figure 2. Screenshot from Google Mars of the Alba Fossae region. All 253 faults are traced by the green lines. The red line denotes the reference line used to calculate percent extension.

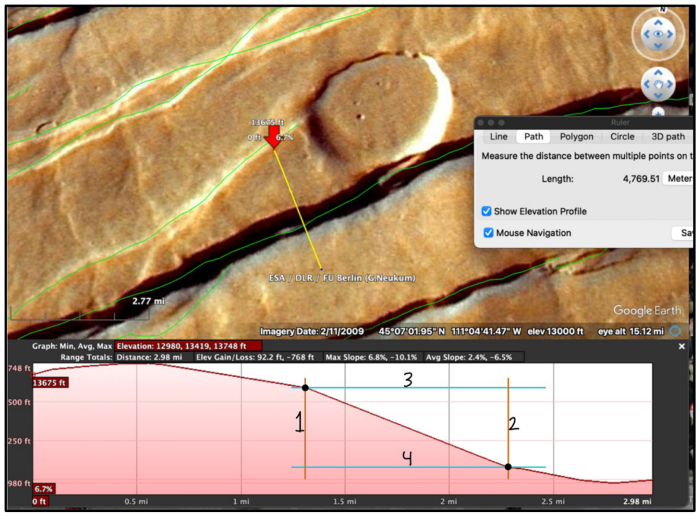

Figure 3. An example of how the heave and throw values were calculated for each fault segment in Google Mars.

of the red slope line and the orange line (1). After calculating the heave and the throw values I was able to calculate the dip separation via the Pythagorean theorem if you assume the slope as a hypothenuse of a triangle. The length vs. displacement relationship of Martian faults was compared to the same relationship for Earth faults. The total length of the extension line was measured. The 21 faults along the transect used to determine the magnitude of extension in this region had their heave values added up to get a total extension value. By taking the length of the transect and dividing it by the summed heaves then multiplying by 100, the fractional extension was determined.

Human error as well as inaccuracies in the Google Mars data set appear in the data. Measuring the individual faults by tracing them out on a computer may affect the data. Google Mars was interacting with Google Earth which left the elevation data intertwined during some measurements. These uncertainties must be accounted for when discussing the overall accuracy of the measurements and calculations that were made.

RESULTS

Based on the imagery analysis, the lava flows are the oldest features in the Alba Fossae region. The fluvial systems followed, supported by evidence that fluvial systems have eroded lava flows in multiple locations. The faults were the last feature, as they displaced both the lava flows and the fluvial systems. A diagram of these interactions and evolutions is shown in Figure 4. The diagrams show lava flows being cut by fluvial systems, circumferential faults cutting through north-south faults, and circumferential faults cutting through lava flows. The timeline is consistent with previous studies of the region (Öhman & McGovern, 2014 ; Karimova, 2017 ; Ivanov & Head, 2006) and the sporadic nature of the volcano's activity through time. Alba Mons has a long history of volcanic eruptions with uncertainty as to when volcanism initiated and terminated. The next step was measuring the 200 faults' displacement and length values which can be seen in Graph A of Figure 5, my data was plotted and is inconsistent with the results seen on Earth through the survey of 4,059 normal faults. The equation that expresses the relationship between fault displacement and fault length is as follows: D = 0.3L0.92 (Lathrop et al., 2022). The Mars data had an equation of D = 12.2L0.31. The difference between these equations arises because Mars faults have longer lengths than displacement values than normal faults on Earth. Graph B in Figure 5 demonstrates the inconsistency between the faults on Earth and Alba Fossae, but the graphs appear to line up. When taking a greater look at the equations that reflect the two different data sets you can see the clear differences between the two, fault displacement to length relationships. The final step was computing the percent extension accommodated by circumferential faulting. The line

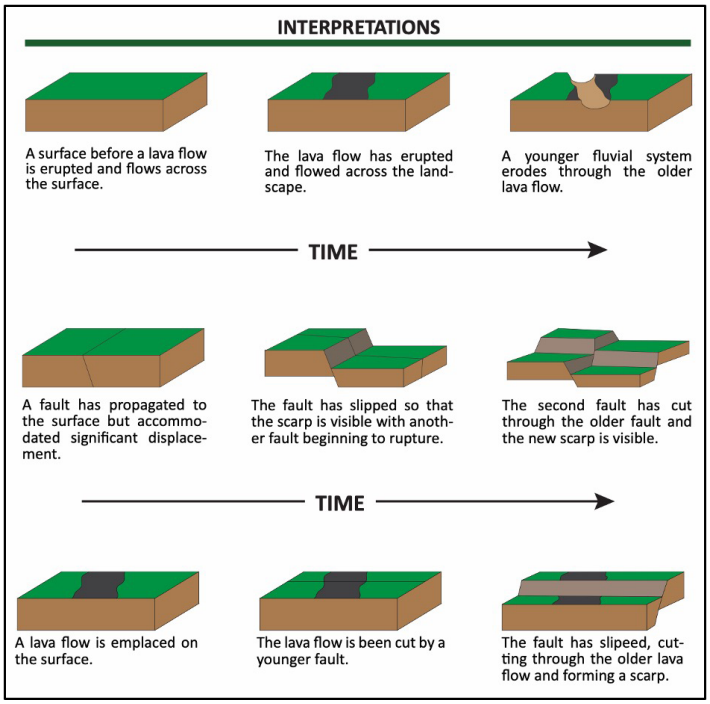

Figure 4. Diagram explaining the morphology, evolution, and overall relationship between geologic features in Alba Fossae.

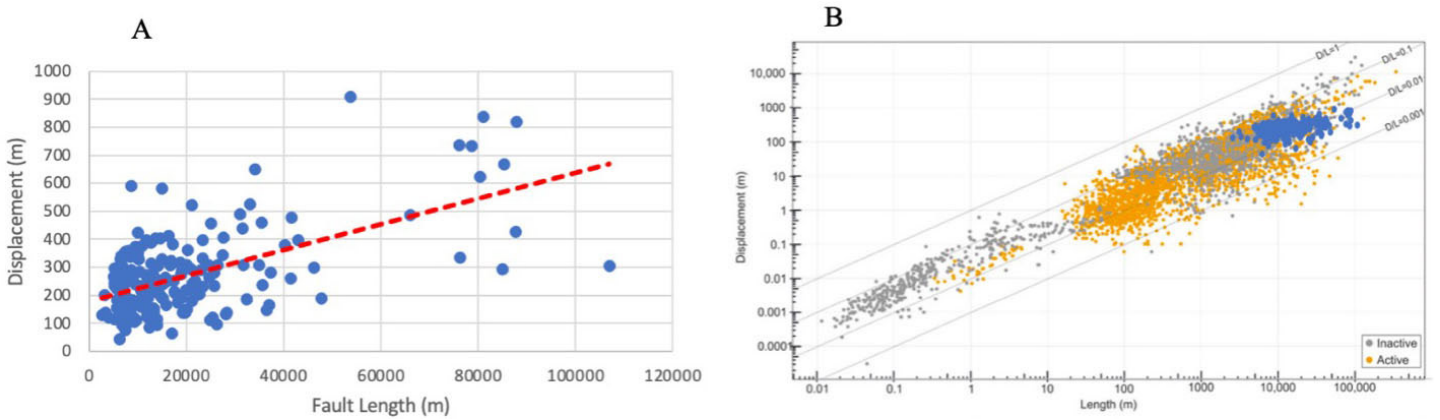

Figure 5. A. 200 faults plotted on a graph where fault length is the x-axis and displacement is the y-axis, both shown in meters. The red dashed line is the average slope that was determined with an R^2 value of 0.339. The relationship equation calculated was $D = 12.2L^{0.31}$. B. All 4059 faults (Lathrop et al., 2022) are plotted on a logarithmic graph overlaid by my 200 faults measured from the Alba Fossae region on Mars. Active vs Inactive faults are specified by the orange and grey dot colors, respectively, and the blue dots being the inactive Martian faults. Remember the equation that describes the fault length vs. displacement relationship on Earth: $D = 0.3L^{0.92}$.

of section is 127 km in length. By adding up each fault's heave value that intersected with the extension line, the total came out to be 7.02 km of extension. By dividing the extension line length by the overall extension and then multiplying by 100, the percent of the extension comes out to 5.53% extension.

DISCUSSION

The circumferential faults within Alba Fossae were formed after the Alba Mons volcanic edifice had been constructed. A large chunk of my research which contained analysis of the geologic timeline of the Alba Fossae region is reinforced by previous timelines laid out (Karimova, 2017) & (Ivanov & Head, 2006). The overall timeline of events is consistent with the volcanic history spanning several time periods, and having a complicated history that is poorly understood. The lava flows were the first feature to form. Erosional features can be seen via fluvial flows cutting through the lava flows and the youngest geologic features are the circumferential faults. The CTX mosaic allowed us to take a deeper and more detailed look into the exact relationships of the region and it was important to confirm the previous studies' results. The volcanic edifice was active and once the volcano went dormant, the stress that was applied to the lithosphere was so large that faults were created to accommodate for the lithospheric load applied by the collapsed caldera. The discrepancy between Earth's fault displacement vs. length relationship and Mars' fault displacement vs. length relationship could be a result of the difference in crustal thickness between the two planets. The overall conclusion that can be made from this research study is that further research is necessary. Many factors need to be accounted for when comparing fault relationships between two planets as well as analyzing a geologic timeline of the region with a complex past. This type of research needs to be done over several years. During this process, it is critical to take into account a wide range of variables to make acute measurements.

ACKNOWLEDGMENTS

This material is based upon work supported by the Keck Geology Consortium and the National Science Foundation under Grant No. 2050697. Funding was also provided by NSF Award 2042114 to PI Benjamin Surpless. A special thanks is extended to Dr. Surpless of Trinity University and Dr. Eddy of Purdue University. Thank you to all of my research teammates who made this possible. Thank you, TW and TS.

REFERENCES

California Institute of Technology, Jay Dickson, Full map of Mars: The Global CTX Mosaic of Mars, Mars Reconnaissance Orbiter & Mars Orbiter Laser Altimeter

Carr, M. H. (1980). The morphology of the Martian surface. Space Science Reviews, 25(3), 231-284. https://doi.org/10.1007/bf00221929

Cattermole, P. (1990). Volcanic flow development

at Alba Patera, Mars. Icarus, 83(2), 453–493. https://doi.org/10.1016/0019-1035(90)90079-o

Ivanov, M. A., & Head, J. W. (2006). Alba Patera, Mars: Topography, structure, and evolution of a unique late Hesperian–early Amazonian shield volcano. Journal of Geophysical Research, 111(E9). https://doi.org/10.1029/2005je002469

Karimova, R. (2017). Fault Populations on Alba Mons, Mars, and their Age Relationships to Volcanic, Fluvial, and Glacial Processes. European Planetary Science Congress; EPSC Abstracts. Vol. 11, p. 1-2 http://meetingorganizer.copernicus.org/EPSC2017/EPSC2017-207-1.pdf

Kim, D., Durán, C., Giardini, D., Plesa, A., Stähler, S. C., Boehm, C., Philippe Lognonné, McLennan, S. M., Ceylan, S., Clinton, J., Davis, P. M., Khan, A., Knapmeyer□Endrun, B., Panning, M. P., Wieczorek, M. A., P. Lognonné, & B. Banerdt. (2023). Global Crustal Thickness Revealed by Surface Waves Orbiting Mars. Geophysical Research Letters, 50(12). https://doi.org/10.1029/2023gl103482

Lathrop, B. A., C. A-L. Jackson, Bell, R. E., & A. Rotevatn. (2022). Displacement/Length Scaling Relationships for Normal Faults; a Review, Critique, and Revised Compilation. Frontiers in Earth Science, 10. https://doi.org/10.3389/feart.2022.907543

Öhman, T., & McGovern, P. J. (2014b). Circumferential graben and the structural evolution of Alba Mons, Mars. Icarus, 233, 114–125. https://doi.org/10.1016/j.icarus.2014.01.043

Rotevatn, A., Jackson, C. A.-L. ., Tvedt, A. B. M., Bell, R. E., & Blækkan, I. (2019). How do normal faults grow? Journal of Structural Geology, 125, 174–184. https://doi.org/10.1016/j.jsg.2018.08.005

Tanaka, K. L. (1990). Tectonic History of the Alba Patera-Ceraunius Fossae Region of Mars. SAO/NASA Astrophysics Data System. Lunar and Planetary Science Conference, p. 515-523. https://articles.adsabs.harvard.edu//full/1990LPSC...20..515T/0000522.000.html

Tanaka, K. L., Golombek, M. P., & Banerdt, W. B. (1991). Reconciliation of stress and structural histories of the Tharsis region of Mars. Journal of Geophysical Research: Planets, 96(E1), 15617–15633. https://doi.org/10.1029/91je01194

USGS. (2024). Mauna Loa. Www.usgs.gov. https://www.usgs.gov/volcanoes/mauna-loa

Walsh, J. J., Nicol, A., & Childs, C. (2002). An alternative model for the growth of faults. Journal of Structural Geology, 24(11), 1669–1675. https://doi.org/10.1016/s0191-8141(01)00165-1

Walsh, J. J., & Watterson, J. (1988). Analysis of the relationship between displacements and dimensions of faults. Journal of Structural Geology, 10(3), 239–247. https://doi.org/10.1016/0191-8141(88)90057-0

KECK Geology Consortium
Learning Science Through Research
Published by the Keck Geology Consortium
Short Contributions
Keck Geology Consortium
Volume 36
May 2024
doi: 10.18277/AKRSG.2024.36.05

DAMAGE ZONE DEVELOPMENT AND CROSS-FAULT ASYMMETRY ON THE MT. CARMEL SEGMENT OF THE SEVIER NORMAL FAULT, SOUTHWEST UTAH

MORGAN SHARP, Whitman College
Project Advisor: Kevin Pogue

INTRODUCTION

Most fault zones are made up of a core, bounded on either side by damage zones. Damage zones are volumes of rock distinct from the fault core where the host rock is fractured at higher densities than the background level, but indicators of concentrated shear are rarely present (Fossen, 2016). Damage zones can be important conduits for subsurface fluid flow (Kim and Sanderson, 2010) and can have significant impacts on the geomorphology of fault zones (Kirkpatrick et al., 2020). Both key damage zone attributes are controlled by the characteristics of fracturing within the damage zone. Damage zones are important because of their implications for groundwater flow, hydrocarbon migration, geothermal fluid dynamics, and the evolution of topography around faults.

There are multiple models for the relationship between damage zone width and accumulation of displacement on a fault (Shipton and Cowie, 2003). One model proposes that the damage zone forms at an initial width and its width increases as displacement is accumulated on the fault (Shipton and Cowie, 2001). In another model, once the damage zone reaches maturity, its width remains relatively constant even as the fault continues to accumulate displacement (Savage and Brodsky, 2011).

A combination of ground-based scanline surveys and Structure-from-Motion (SfM) modeling was used to collect data on fracture characteristics, such as fracture spacing, orientation, and intensity, in various structural settings. The width of the damage zone was compared between locations along the fault with varying amounts of displacement. Areas where very little displacement has been accommodated by the fault represent locations where the damage zone had less time to develop, and areas that accommodate hundreds of meters of displacement represent longer periods of damage zone development. By comparing the width of the damage zone between these two settings, the model of damage zone development which best represents the damage zones on the Sevier fault can be determined. Additionally, hanging wall fracture data was compared with footwall fracture data, which revealed asymmetries in the fracture characteristics of the two fault blocks.

BACKGROUND

The Sevier fault (called the Toroweap fault in Arizona) has a surface trace of ~ 100 km, trends N30°E, and dips to the west (e.g., Reber et al., 2001). This fault, and other large, sub-parallel normal faults are in the transition zone between the Basin and Range Province to the west and the Colorado Plateau to the east, where they accommodate extension between the two regions (Fig. 1). The Sevier fault has a maximum displacement of ~ 790 m and cuts rocks that are Precambrian to Quaternary in age (Reber et al., 2001). The recent rate of slip on the Sevier fault has been estimated at 0.018 mm/yr (Schiefelbein, 2002). The Sevier fault system is made up of numerous fault segments which meet and interact at salients, forming complex assemblages of linked faults and relay ramps (Taylor et al., in press).

The area of study was in Lower Sand Wash, a drainage where multiple segments of the Sevier fault are well-exposed just east of the town of Mt. Carmel Junction, UT. Rocks exposed in the area are primarily of the Jurassic Navajo Sandstone, which is aeolian in origin.

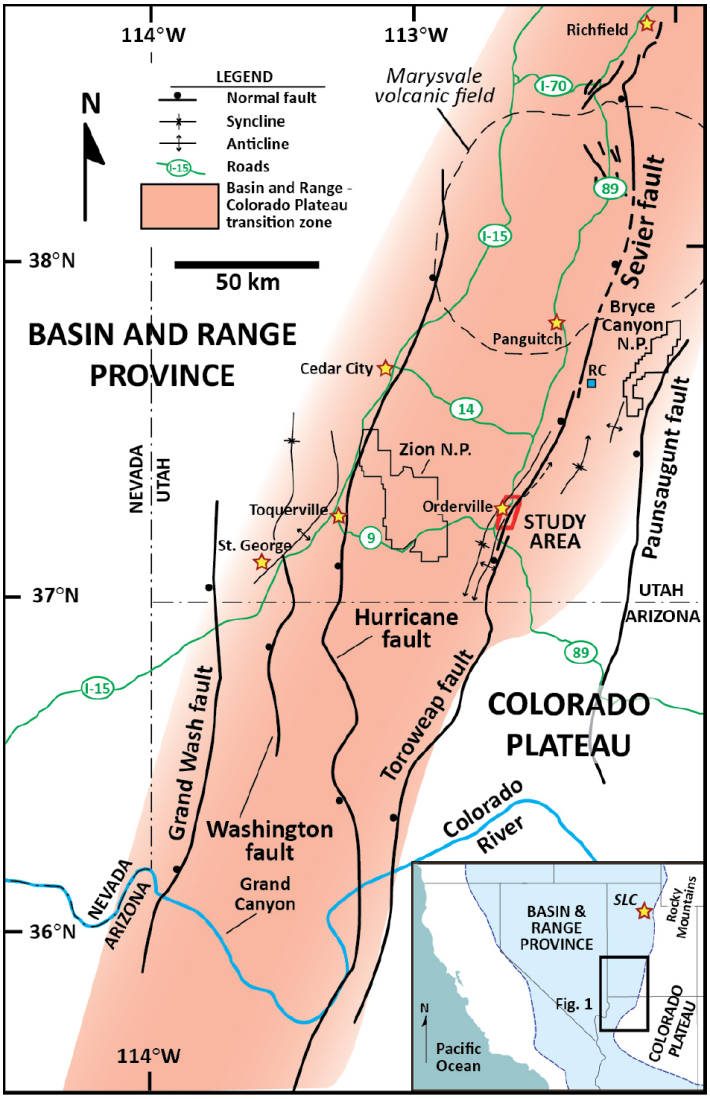

Figure 1. Overview map of the Basin and Range-Colorado Plateau transition zone showing the major faults that accommodate extension in the area. See inset for regional location of main figure map. Note the location of the study area denoted by the red box to the east of the community of Orderville. Ball symbols are on the hanging wall side of fault traces. Figure is modified from Taylor et al., in press.

Lower Sand Wash was selected due to its well-exposed bedrock outcrops as well as its accessibility for ground-based surveys.

METHODS

Field Methods

On well-exposed and continuous outcrops, scanlines were established perpendicular to the dominant fracture plane orientation, and the dip and dip direction of each continuous fracture on the scanline was measured along with the spacing between fractures (Fig. 2). The positions of scanline start and end points and other locations of interest (fault plane exposures, slickenline exposures, etc.) were recorded with a Trimble Geo XH handheld global positioning system receiver (30 cm accuracy). Location data were compiled in a GIS database. Scanline measurements were complimented by field photographs, descriptions, and detailed sketches of important structural features.

A DJI Phantom 4 drone was flown along the Mt. Carmel fault segment and adjacent areas to record high resolution video of the land surface. Flights were conducted during the midday hours for improved contrast and image quality. UAV surveys provided imagery of areas such as canyon walls, cliff faces, and remote uplands which were inaccessible on foot.

3D Model Construction

VLC Media Player was used to extract still images from UAV-captured video at a rate of one image per second, providing the image-to-image overlap needed for model construction. Images were imported into Agisoft Metashape Professional version 2 (Agisoft) to construct spatially accurate, georeferenced Structure from Motion (SfM) models of the land surface. In

Figure 2. Geologists measuring the attitude of and spacing between fractures along a scanline in Lower Sand Wash.

Agisoft, images were aligned, and a point cloud, mesh and model texture were built. Models were georeferenced by selecting identifiable ground control points (GCPs) in Google Earth Pro and placing markers on corresponding points on the models using Agisoft's georeferencing tool. Finally, map view orthomosaics of georeferenced models were generated in Agisoft.

Fracture Mapping and Analysis

Agisoft's markup tools were used to annotate all fractures visible in the orthomosaic. Once fractures were annotated, scanlines were established perpendicular to the dominant fracture orientation (strike) on well-exposed outcrops and spacing between fractures was measured.

For all scanlines, both model-based and field-based, fracture intensity was calculated as the number of fractures per meter along the scanline. The regularity of fracture spacing was calculated using Cv', defined as $Cv' = \sigma / M$, where σ = the standard deviation of fracture spacings in a scanline and M = the median fracture spacing in the scanline. Cv' = 1 is the cutoff above which fracture spacing is more clustered than random and below which it is more regular than random (Hooker et al., 2023). Stereonet plots of fracture orientations were also created from scanline data.

The width of the damage zone was measured using aerial imagery to make a visual estimate of where fracturing reduced to background levels. Footwall and hanging wall damage zone widths were measured at Lower Sand Wash, and footwall width was measured at the location of maximum displacement on the Mt. Carmel segment, ~ 3 km north of Lower Sand Wash.

RESULTS

Footwall damage zone width measurements in the Jurassic Navajo Sandstone show that at the point of maximum displacement along strike of the Mt. Carmel fault segment (Surpless, unpub.), throw is ~ 790 m and the footwall damage zone is ~ 54 m wide. In Lower Sand Wash, throw is ~ 150-220 m and the footwall damage zone is ~ 44 m wide. The hanging wall damage zone width in Lower Sand Wash is ~102 m (Fig. 3).

Fractures in the footwall generally fall into a wide-ranging set with strikes ranging from ~ 330° to ~ 30° (Fig. 4). The 30° end of this range is roughly parallel to the main strand of the Mt. Carmel fault segment in this location, while the 330° end of the range aligns with the prominent gullies cutting into the footwall (two are visible in Figure 4). Fractures in the hanging wall cluster into two dominant sets (Fig. 4). One has strikes ranging from ~ 260° to ~ 330° and is roughly perpendicular to the strike of the fault. The other set has strikes ranging from ~ 30° to ~ 60° and is roughly fault-parallel.

Cv' and fracture intensity data plots show no clear trends separating values in the hanging wall and the footwall (Fig. 5). Footwall scanlines have a Cv' range of 0.76 - 3.41 and a fracture intensity range of 0.57 - 2.45 fractures / meter. Hanging wall scanlines have a Cv' range of 0.73 - 4.12 and a fracture intensity range of 1.18 - 3.83 fractures / meter.

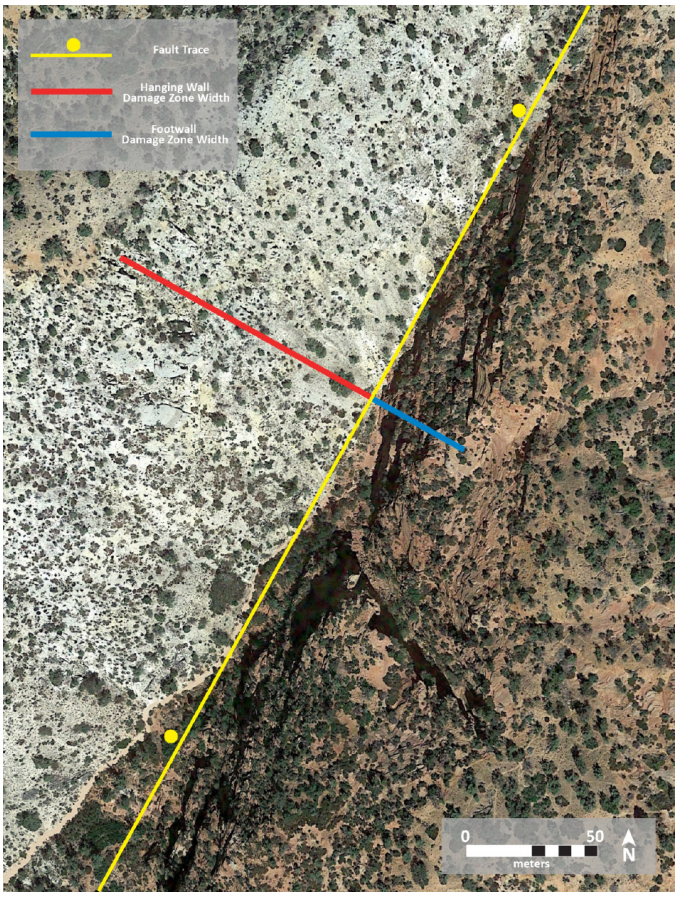

Figure 3. Detail map of the upper canyon in Lower Sand Wash annotated with the fault trace as well as the measured widths of the damage zones in the footwall (blue) and hanging wall (red). Ball symbols are on the hanging wall side of the fault trace.

DISCUSSION

Damage Zone Width Across Displacements

The fact that footwall damage zone width varies only on the meter scale over a range of displacements that vary on the scale of hundreds of meters suggests that a simple scaling model cannot be used to explain the relationship between footwall damage zone width and displacement. The constant width model is likely a more accurate representation of the damage zone width development style occurring on the Mt. Carmel segment of the Sevier fault.

Savage and Brodsky (2011) divide the "lifespan" of a normal fault into two phases: in the first, damage zone width increases proportionally to displacement on the fault, and in the second, at displacements greater than ~150 m, damage zone width increase slows and is not strongly tied to displacement accumulation. At both locations where footwall damage zone width was measured, displacements were greater than ~150 m, thus the displacement and displacement-damage zone width relationship observed at these two locations align with Savage and Brodsky's (2011) descriptions of the second phase of a fault's "lifespan" in which displacement accumulation and damage zone width are not strongly related.

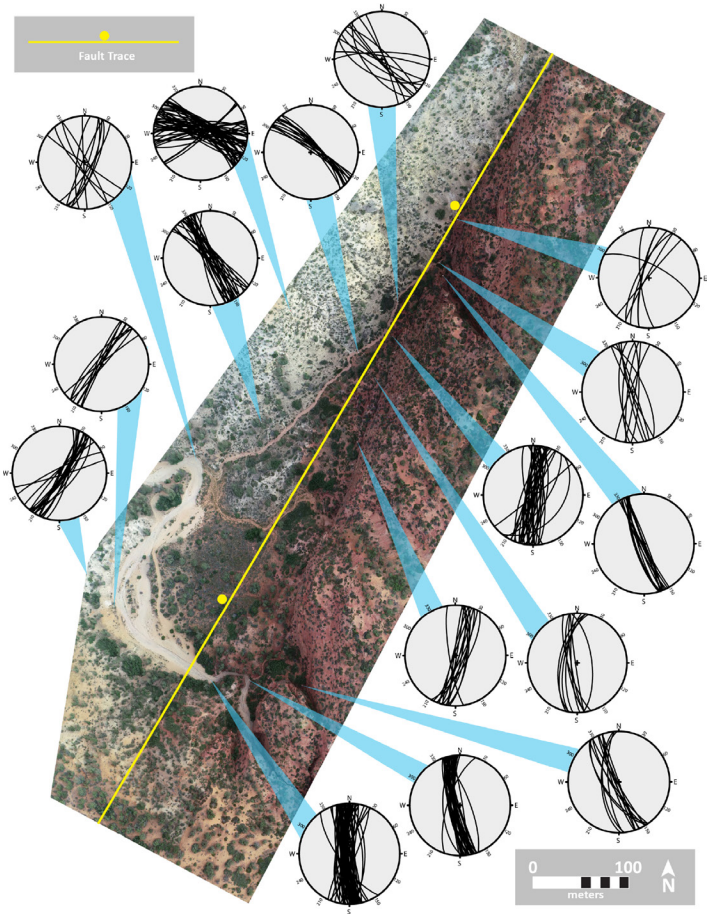

Figure 4. Orthomosaic of Lower Sand Wash annotated with the fault trace and stereonets showing the fracture orientations of each scanline and where each scanline was measured in the field. Stereonets representing scanlines measured in the footwall are displayed to the right of the orthomosaic and those representing scanlines measured in the hanging wall are displayed to the left. Ball symbols are on the hanging wall side of the fault trace.

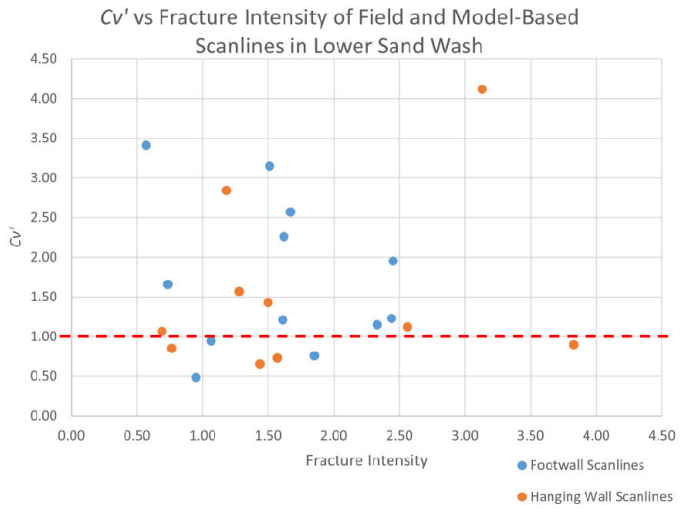

Figure 5. Scatter plot of the Cv' and fracture intensity values of field-based as well as model-based scanlines in Lower Sand Wash, with fracture intensity on the x-axis and Cv' on the y-axis. Scanlines measured in the footwall are represented by blue points and those measured in the hanging wall are represented by orange points. The red dashed line represents the cutoff (Cv' = 1) above which fracture spacing is more clustered than random.

Asymmetry Between Fault Blocks

Fracture orientation data show asymmetry between the hanging wall and footwall. While the set of roughly fault-parallel fractures striking ~ 30° is present in both the footwall and the hanging wall (Fig. 4), the scanlines in the hanging wall that contain this fracture set are farther from the fault and closer to a secondary fault strand than the other hanging wall scanlines. Due to their proximity to the secondary fault strand, these fault-parallel fractures may be formed by stresses in the footwall of the secondary strand. If this is the case, this fracture set fits into the overall trend shown in the data, with roughly fault-parallel fractures in the footwall and roughly fault-perpendicular fractures in the hanging wall. Strain modeling done on the Sevier fault by Jennings (2024) also found fracture orientation asymmetries between fault blocks. In their modeling, the same footwall-hanging wall fracture

orientation trend occurs at 3 km depth (Jennings, 2024). This suggests that the rock presently exposed at the surface may have been at a significant depth at the time of faulting.

Cross-fault asymmetry in damage zone width has been documented in normal fault systems by previous studies (Berg and Skar, 2005; Liao et al., 2020). Berg and Skar (2005) favor an asymmetrical stress field as the primary control on this asymmetry. Differing lithology in the two fault blocks due to fault-offset is another potential control on asymmetrical damage zone characteristics. In the case of Lower Sand Wash, the Navajo Sandstone is exposed in both the hanging wall and the footwall, so cross-fault lithological variation is not likely a significant control on these asymmetries.

Cv' and fracture intensity data do not reveal cross-fault asymmetries (Fig. 5). Given the asymmetries shown in the other cross-fault datasets, either 1) the factors controlling the observed asymmetries do not impact fracture clustering and intensity or 2) the collected fracture clustering and intensity data are insufficient to reflect these asymmetries due to small sample size or topographic relief limitations on data collection.

CONCLUSIONS

Analysis of scanline and SfM data from the Mt. Carmel segment of the Sevier fault in southwest Utah supports a "constant width" model of damage zone development and displays distinct asymmetries between the hanging wall and footwall.

Observations of damage zones in the footwall show very similar widths (~ 44 m and ~ 54 m) across a wide range of fault displacements (~ 150 m to ~ 790 m). This suggests that damage zone development in Lower Sand Wash is better represented by a "constant width" model – in which damage zone width is not strongly controlled by displacement – than a scaling model.

Differing fracture orientations and damage zone widths in the hanging wall and footwall suggest asymmetries in strain between the two fault blocks. Specifically, the footwall is dominated by fault-parallel fractures, the hanging wall is dominated by fault-perpendicular fractures, and the hanging wall damage zone is more than two times wider than that of the footwall. The data do not show asymmetries in fracture intensity or clustering between the two fault blocks.

ACKNOWLEDGEMENTS

This material is based upon work supported by the Keck Geology Consortium and the National Science Foundation under Grant No. 2050697. Funding was also provided by NSF Award 2042114 to PI Surpless and by the Trinity University Department of Geosciences. Thank you to my advisors, Drs. Ben Surpless and Kevin Pogue for their guidance and feedback. Thanks also to the field crew: Audrey, Demi, Pierce, and Jack.

REFERENCES

Fossen, H., 2016, Structural Geology: Cambridge, England, Cambridge University Press.

Hooker, J.N., Marrett, R., and Wang, Q., 2023, Rigorizing the use of the coefficient of variation to diagnose fracture periodicity and clustering: Journal of structural geology, v. 168, p. 104830, doi:10.1016/j.jsg.2023.104830.

Jennings, A., 2024, Computer Modeling of Normal Fault-Related Damage Zones: Implications for Estimating Geothermal Energy Potential: Trinity University B.S. Thesis, 63 p.

Kim, Y.-S., and Sanderson, D.J., 2010, Inferred fluid flow through fault damage zones based on the observation of stalactites in carbonate caves: Journal of structural geology, v. 32, p. 1305–1316, doi:10.1016/j.jsg.2009.04.017.

Kirkpatrick, H.M., Moon, S., Yin, A., and Harrison, T.M., 2020, Impact of fault damage on eastern Tibet topography: Geology, v. 49, p. 30–34, doi:10.1130/G48179.1.

Liao, Z., Hu, L., Huang, X., Carpenter, B.M., Marfurt, K.J., Vasileva, S., and Zhou, Y., 2020, Characterizing damage zones of normal faults using seismic variance in the Wangxuzhuang oilfield, China: Interpretations v. 8, p. 1- 24.

Reber, S., Taylor, W.J., Stewart, M., and Schiefelbein, I.M., 2001, Linkage and reactivation along the northern Hurricane and Sevier faults, southwestern Utah: Utah Geological Association

Publication 30 and Pacific Section American Association of Petroleum Geologists Guidebook GB 78, p. 379-400.

Savage, H.M., and Brodsky, E.E., 2011, Collateral damage: Evolution with displacement of fracture distribution and secondary fault strands in fault damage zones: Journal of geophysical research, v. 116, doi:10.1029/2010jb007665.

Schiefelbein, I., 2002, Fault segmentation, fault linkage, and hazards along the Sevier Fault, southwestern Utah [M.S. thesis]: Las Vegas, University of Nevada.

Shipton, Z.K., and Cowie, P.A., 2003, A conceptual model for the origin of fault damage zone structures in high-porosity sandstone: Journal of structural geology, v. 25, p. 333–344, doi:10.1016/s0191-8141(02)00037-8.

Shipton, Z.K., and Cowie, P.A., 2001, Damage zone and slip-surface evolution over μm to km scales in high-porosity Navajo sandstone, Utah: Journal of structural geology, v. 23, p. 1825–1844, doi:10.1016/s0191-8141(01)00035-9.

Surpless, B., unpublished, Geologic cross-section of the Mt. Carmel segment of the Sevier fault zone, southern Utah.

Taylor, W., Surpless, B., and Schiefelbein, I., 2024, Complex segment linkage along the Sevier normal fault, southwestern Utah: Geosphere (in press).

KECK Geology Consortium
Learning Science Through Research
Published by the Keck Geology Consortium
Short Contributions
Keck Geology Consortium
Volume 36
May 2024
doi: 10.18277/AKRSG.2024.36.06

POLYPHASE DEFORMATION OF NEOARCHEAN-PALEOPROTEROZOIC ROCKS IN THE BLACK HILLS, SOUTH DAKOTA

TREVOR WALDIEN, South Dakota School of Mines and Technology

INTRODUCTION

The crystalline core of the Black Hills of western South Dakota exposes Neoarchean and Paleoproterozoic plutonic and metamorphic rocks that record processes related to the assembly of Laurentia (e.g., Lisenbee, 1988; Whitmeyer and Karlstrom, 2007; Redden and Dewitt, 2008). Whereas early analysis of the Black Hills Precambrian interpreted that the Black Hills conincide with the Trans-Hudson orogeny–the suture between the Wyoming and Superior cratons that forms the core of the Laurentian continent (Redden et al., 1990), exposure of Wyoming craton Archean orthogneisses along the eastern side of the Black Hills (e.g., Gosselin et al., 1988; McCombs et al., 2004) complicates this picture (Fig. 1). Subsequent work has partially reconciled this issue by reinterpreting the location of the eastern margin of the Wyoming Craton (Worthington et al., 2016), recognizing an earlier phase of continental rifting that could have displaced fragments of the Wyoming craton prior to assembly or Laurentia (Dahl et al., 2006; Van Boening and Nabelek, 2008), or considering that Black Hills metamorphic rocks may not represent the Trans-Hudson orogen (Dahl et al., 2010).

Little Elk Creek in the northeastern edge of the Black Hills crystalline core is an isolated erosional window that provides nearly continuous exposure of deformed Archean and Paleoproterozoic rocks along a ~7 km across-strike transect (Fig. 2). The Black Hills Keck group aimed to better characterize the formation and deformation features of rocks along Little Elk Creek to better understand how genetic relationships and shared deformation features among these rocks inform the various tectonic models.

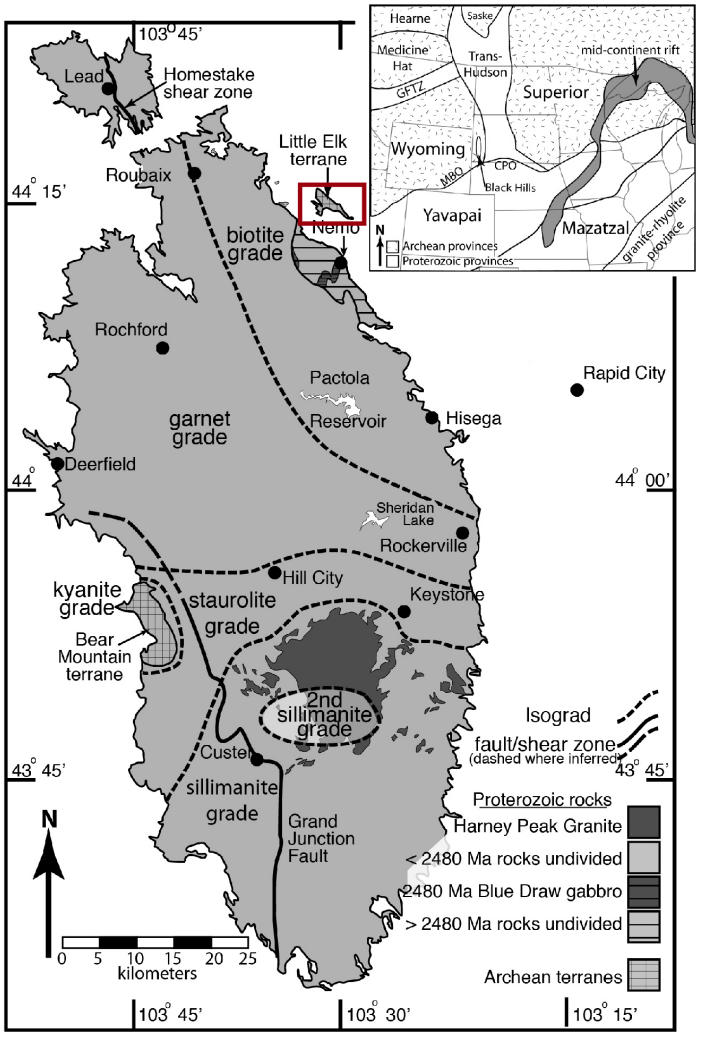

Figure 1. Generalized geologic map of the Black Hills crystalline core with cities (black circles) and regionally important structures. The study area and map units relevant to the proposed study are outlined in red. Inset: Regional map of Laurentian cratonic blocks and sutures between blocks relative to state borders. Note the location of the Black Hills within the Trans-Hudson domain. CPO–Central Plains Orogen; MBO–Medicine Bow Orogen. Modified from Allard and Portis, (2013).

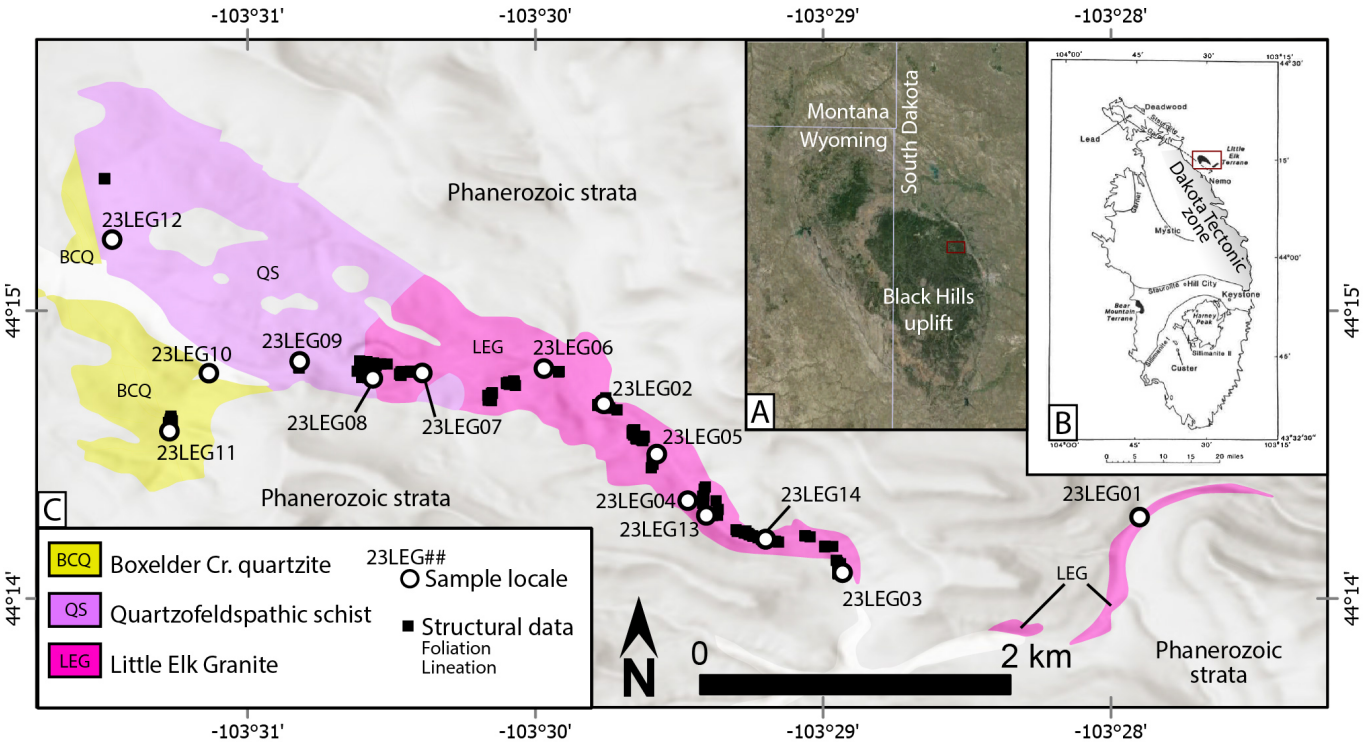

Figure 2. A) Google Earth image showing the location of the Black Hills (dark green region) relative to political borders. The Little Elk Creek area is outline by the red rectangle. B) Metamorphic isograd map of the Black Hills Precambrian core from Gosselin et al. (1988). Black shaded regions represent Archean rocks. The Little Elk Creek area is outline by the red rectangle. C) Geologic map of the Little Elk Creek area showing sample and structural data locations. Modified from Redden and DeWitt (2008).

GEOLOGIC CONTEXT

Precambrian crystalline rocks in the Black Hills are exposed in the core of a doubly plunging Laramide anticline, wherein syn- and post-Laramide erosion cut through Phanerozoic platform strata into the Precambrian core (Lisenbee, 1988). Much of the metamorphic core of the range consists of Paleoproterozoic metasedimentary rocks, which represent an ocean basin that was closed during Proterozoic suturing of the Superior and Wyoming cratons during the Trans-Hudson orogeny (Redden and DeWitt, 2008). Four generations of structures have been documented to record deformation and metamorphism during closure of the ocean basin: (1) N-vergent tight-to-isoclinal, recumbent folding estimated to have taken place at ca. 1883-1775 Ma prior to regional metamorphism (Dahl et al., 2005a). Fabrics associated with this folding (S1/F1) may be locally preserved as inclusion trails in porphyroblasts (Dahl et al., 2005b) (2) N-NW trending upright, isoclinal folding (F2) with a strongly developed axial planar cleavage (S2) at ca. 1760-1747 Ma (Dahl and Frei, 1998); (3) Vertically plunging folds (F3) and sinistral mylonite zones that deform S2 at ca. 1736-1719 Ma (Morelli et al., 2010). (4) Doming and associated folding (F4) related to emplacement of the Harney Peak granite in the southern Black Hills, which is dated at 1717-1715 Ma (Redden et al., 1990). The earliest evidence of regional metamorphism is associated with the F2 folding event (Nabelek et al., 2006), which persisted until crustal melting resulted in emplacement of the Harney Peak granite at ca. 1715 Ma (Redden et al., 1990).

Rocks exposed in Little Elk Creek consist of the Little Elk granite, quartzofeldspathic schist, and the Boxelder Creek quartzite (Fig. 2). The Little Elk granite is an augen gneiss that has been dated at 2559 ± 6 Ma (McCombs et al., 2004). A variably developed shear fabric defines the contact between the Little Elk granite, quartzofeldspathic schist, and the Boxelder Creek quartzite, which masks the original relationship among the rock units. Some previous work envisions the Little Elk granite as intruded into the quartzofeldspathic schist (e.g., Redden and DeWitt, 2008) (Fig. 2), whereas other work argues that the quartzofeldspathic schist is a high strain equivalent to the Little Elk granite (Nicosia and Allard, 2014). South of Little Elk Creek, the Boxelder

Creek quartzite is intruded by a suite of 2480 ± 6 Ma metagabbro bodies (Dahl et al., (2006), which brackets the age of the metasedimentary rocks to be earliest Proterozoic or Archean. Although the the Little Elk granite is interpreted to have been a source area for the Boxelder Creek quartzite (e.g., Redden and DeWitt, 2008), the lack of granite clasts in the quartzite have so far left the proposed genetic relationship tenuous.

METHODS

The Black Hills Keck group performed field work in August, 2023 with the goals of documenting potential genetic relationships and deformation phases among the rock types exposed in Little Elk Creek. We collected field data and samples along an east-west transect through Little Elk Creek. Along the profile, students worked together to 1) collect structural measurements with the FieldMove application on Apple iPad; 2) collect oriented samples for thin section microstructural analysis; 3) photograph cross cutting relationships; 4) collect large samples for geochronology; and 5) write field notes that give appropriate context to the samples and measurments. At the end of the field season, students used the facilities at the South Dakota School of Mines and Technology to cut thin section billets and perform rock crushing/mineral separation for geochronology. Thin section billets were sent to Wagner Petrographic to produce polished thin sections. Mineral separates were sent to the Arizona Laserchron Center for mounting and eventual analysis by a subset of the Keck group.

STUDENT PROJECTS

Four students (Fig. 3) from four colleges performed research projects focused on determining the identity and deformation history of rocks in Little Elk Creek. Their work elucidates processes that took place during the formation of the oldest rocks in the Black Hills and subsequent deformation phases that juxtaposed them.

Liam Fry (Eckerd College) performed a kinematic analysis of shear zones within the Little Elk Granite. Liam found that shear zones in the granite can be split into two groups based on their fabric types. The type 1 fabric is a high temperature augen gneiss fabric

Figure 3. Students of the Black Hills Keck group. Back: Alex Robinson (left) and Liam Fry (right). Front: Rebecca Braun (left) and Willa Obringer (right).

characterized by plastically deformed feldspar crystals up to ~5 cm in diameter. Asymmetry within the augen gneiss fabric suggests top-down shear sense along a moderately SW-dipping foliation. The type 2 fabric crosscuts the type 1 fabric and is characterized by fracturing of the preexisting feldspar augens within a low-temperature mylonitic fabric. Opposing strike-slip shear sense indicators and a steeply plunging stretching lineation suggest that the type 2 fabric formed in a pure shear dominated transpression zone. Liam's data collectively demonstrate that the Little Elk granite records at least two deformation events that are distinguishable with detailed field observations. The first event likely formed late in the intrusion history of the Little Elk granite at ca. 2560 Ma, and the second event likely formed late in the suturing of the Wyoming and Superior cratons around ca. 1720 Ma.

Rebecca Braun (South Dakota School of Mines and Technology) performed petrography and microstructural analysis on a suite of oriented thin

sections of mylonitized orthogneiss (Liam's type 2 fabric). Rebecca found that the microstructures in thin section, like the outcrop, show opposing shear sense indicators, suggesting a significant component of pure shear deformation in addition to the strike-slip motion. Fractures between feldspar crystals are filled with polygonal quartz and quartz in the main shear fabric displays undulatory extinction. Rebecca used the contrasting deformation textures in quartz and feldspar to bracket the deformation temperature of the mylonite to 300-450ºC. Rebecca's data collectively show that the late mylonitic fabric in the Little Elk granite represents a greenschist facies pure shear dominated transpression zone.

Willa Obringer (Lake Superior State University) performed a combined structural and geochronological analysis of the Boxelder Creek Quartzite juxtaposed along the western margin of the Little Elk granite. Willa's structural data show that the quartzite was deformed by a combination of flattening and left lateral simple shear. Detrital zircon U-Pb data from the quartzite contain ages consistent with derivation from Wyoming craton sources, including a distinctive ca. 2550 Ma age population that overlaps the age of the Little Elk granite. Willa also leveraged a newly acquired Scanning Electron Microscope at her home institution to show that the Boxelder Creek quartzite is endowed in Cr and Ag. Willa's data collectively show that the Boxelder Creek quartzite may represent a ca. 2550-2480 Ma syn-rift depocenter that formed along the eastern margin of the Wyoming craton and was sybsequently deformed along with the Little Elk Granite from which it was likely derived.

Alex Robinson (Pomona College) performed U-Pb dating of samples mapped as "Little Elk granite" and "biotite-feldspar gneiss" (Fig. 2) to test whether the biotite-feldspar gneiss may represent a mylotinized version of the Little Elk granite (as supported by Liam and Rebecca's analyses). Alex found that zircons grains from the two samples yielded unimodal distributions of ages centered on ca. 2550 Ma, with few analyses that span back to ca. 2800 Ma. The U-Pb data support the field data and suggest that the biotite-feldspar gneiss is best interpreted as a portion of the Little Elk granite that has experienced intense deformation, resulting in grain size reduction and the development of mylonitic shear zones.

ACKNOWLEDGEMENTS

This material is based upon work supported by the Keck Geology Consortium and the National Science Foundation under Grant No. 2050697.

REFERENCES

Allard, S. T., & Portis, D. H. (2013). Paleoproterozoic transpressional shear zone, eastern Black Hills, South Dakota: Implications for the late tectonic history of the southern Trans-Hudson Orogen. Rocky Mountain Geology, 48(2), 73-99.

Dahl, P. S., & Frei, R. (1998). Step-leach Pb-Pb dating of inclusion-bearing garnet and staurolite, with implications for Early Proterozoic tectonism in the Black Hills collisional orogen, South Dakota, United States. Geology, 26(2), 111-114.

Dahl, P. S., Hamilton, M. A., Jercinovic, M. J., Terry, M. P., Williams, M. L., & Frei, R. (2005a). Comparative isotopic and chemical geochronometry of monazite, with implications for U-Th-Pb dating by electron microprobe: An example from metamorphic rocks of the eastern Wyoming Craton (USA). American Mineralogist, 90(4), 619-638.

Dahl, P. S., Hamilton, M. A., Wooden, J. L., Foland, K. A., Frei, R., McCombs, J. A., & Holm, D. K. (2006). 2480 Ma mafic magmatism in the northern Black Hills, South Dakota: a new link connecting the Wyoming and Superior cratons. Canadian Journal of Earth Sciences, 43(10), 1579-1600.

Dahl, P. S., Terry, M. P., Jercinovic, M. J., Williams, M. L., Hamilton, M. A., Foland, K. A., Clement, S.M., & Friberg, L. M. (2005b). Electron probe (Ultrachron) microchronometry of metamorphic monazite: Unraveling the timing of polyphase thermotectonism in the easternmost Wyoming Craton (Black Hills, South Dakota). American Mineralogist, 90(11-12), 1712-1728.

Gosselin, D. C., Papike, J. J., Zartman, R. E., Peterman, Z. E., & Laul, J. C. (1988). Archean rocks of the Black Hills, South Dakota: Reworked basement from the southern extension of the Trans-Hudson orogen. Geological Society

of America Bulletin, 100(8), 1244-1259.
Lisenbee, A. L. (1988). Tectonic history of the Black Hills uplift. AAPG Field trip guide to the Powder River Basin.
McCombs, J. A., Dahl, P. S., and Hamilton, M. A., 2004, U-Pb ages of Neoarchean granitoids
from the Black Hills, South Dakota, USA: Implications for crustal evolution in the Archean Wyoming Province: Precambrian Research, v. 130, p. 161–184.
Morelli, R. M., Bell, C. C., Creaser, R. A., & Simonetti, A. (2010). Constraints on the genesis of gold mineralization at the Homestake Gold Deposit, Black Hills, South Dakota from rhenium–osmium sulfide geochronology. Mineralium Deposita, 45(5), 461-480.
Nabelek, P. I., Labotka, T. C., Helms, T., & Wilke, M. (2006). Fluid-mediated polymetamorphism related to Proterozoic collision of Archean Wyoming and Superior provinces in the Black Hills, South Dakota. American Mineralogist, 91(10), 1473-1487.
Nicosia, C. & Allard, S., (2014), Petrologic and Geochemical Characterization of Archean Gneisses in the Little Elk Terrane, Black Hills, South Dakota. Student Research and Creative Projects 2014-2015. 11.
Redden, J. A., & DeWitt, E. (2008). Maps Showing Geology Structure and Geophysics of the Central Black Hills South Dakota (Vol. 2777, pp. 44-p). US Geological Survey Scientific Investigations Map, 1:100,000 scale; 2 sheets.
Redden, J. A., Peterman, Z. E., Zartman, R. E., DeWitt, E., 1990, U-Th-Pb geochronology and preliminary interpretation of Precambrian tectonic events in the Black Hills, South Dakota, in Lewry, J. F., and Stauffer, M. R., eds., The Early Proterozoic Trans-Hudson Orogen of North America: Geological Association of Canada Special Paper 37, p. 229–251.
Van Boening, A. M., & Nabelek, P. I. (2008). Petrogenesis and tectonic implications of Paleoproterozoic mafic rocks in the Black Hills, South Dakota. Precambrian Research, 167(3-4), 363-376.
Whitmeyer, S. J., & Karlstrom, K. E. (2007). Tectonic model for the Proterozoic growth of North America. Geosphere, 3(4), 220-259.
Worthington, L. L., Miller, K. C., Erslev, E. A., Anderson, M. L., Chamberlain, K. R., Sheehan, A. F., ... & Siddoway, C. S. (2016). Crustal structure of the Bighorn Mountains region: Precambrian influence on Laramide shortening and uplift in north-central Wyoming. Tectonics, 35(1), 208-236.

KECK Geology Consortium
Learning Science Through Research
Published by the Keck Geology Consortium
Short Contributions
Keck Geology Consortium
Volume 36
May 2024
doi: 10.18277/AKRSG.2024.36.07

DEFORMATION TEMPERATURE AND KINEMATICS OF THE DAKOTA TECTONIC ZONE WITHIN THE LITTLE ELK GRANITE IN THE BLACK HILLS, SOUTH DAKOTA, NEAR NEMO, SOUTH DAKOTA

REBECCA BRAUN, South Dakota School of Mines and Technology
Project Advisor: Trevor Waldien

ABSTRACT

Precambrian rocks in the Black Hills record multiple tectonic processes, including suturing of the Wyoming and Superior cratons from ca. 1.740-1.715 Ga. One of these structures active during this time is the Dakota Tectonic Zone (DTZ), which is a strike-slip shear zone. We examined intracrystalline deformation and associated microstructures in oriented thin sections of the Little Elk Granite (2.560 Ga gneiss) within the DTZ to further document how the strike-slip deformation fits into the Precambrian structural evolution of the Black Hills. At the outcrop scale, the Little Elk Granite contains two types of fabrics. Fabric type 1 is an augen gneiss fabric characterized by alignment of ~1-5 cm K-feldspar crystals that is interpreted to have formed during emplacement of the Little Elk Granite. Fabric type 2 cross-cuts the augen gneiss fabric and is characterized by comminution of the large K-feldspar grains within mylonitic shear zones. Whereas the type 1 fabric is folded throughout the field area, the type 2 shear fabric is consistently oriented at ~150/70°SW and contains a down-dip stretching lineation. Oriented thin sections cut perpendicular to foliation and parallel to lineation contain broken feldspar crystals that in some cases also exhibit undulose extinction. Domains between paired fragments of broken feldspar crystals are filled in with equant polycrystalline quartz aggregates and are regularly oriented at a high angle (>45°) to the shear foliation. Quartz-rich domains in the type 2 fabric generally display undulose extinction and dynamic recrystallization textures. Kinematic indicators from asymmetric strain shadows associated with feldspar porphyroclasts and asymmetrically folded micas yield dominantly top-to-the-right shear sense, but top-to-the-left shear sense is also common. These data from the Little Elk Granite suggests that the DTZ is an upper greenschist facies (~300-450°C) right-lateral pure shear dominated transpression zone that likely formed late in the suturing of the Wyoming and Superior cratons.

INTRODUCTION

The metamorphic core of the Black Hills uplift exposes poly-deformed Precambrian metamorphic rocks (Redden and DeWitt, 2008) (Fig. 1). Multiple folding events have been identified in the Precambrian core of the Black Hills; two of these folding events are thought to be associated with the suturing of the Wyoming and Superior cratons from ca. 1.740-1.715 Ga (Norwood, Brown, and Hawkins, 2013; Allard and Portis, 2013). These folding events show shortening deformation in F1 and F2 recumbent folds associated with thrust faults. A third deformation event, D3/F3, is characterized by vertically plunging isoclinal folds, which deform D2/F2 features and thus likely form late in the suturing process (Redden and DeWitt, 2008; Allard and Portis, 2013). The F3 folds are spatially associated with strike-slip shear zones, and the deformation zone along the northeastern boundary of the metamorphic core has collectively been called the Dakota Tectonic Zone (DTZ) (Allard and Portis, 2013) (Fig. 1B).

Previous research on the DTZ has focused on the kinematics of deformation at various locations throughout the Black Hills. This research builds upon the previous work by using oriented samples

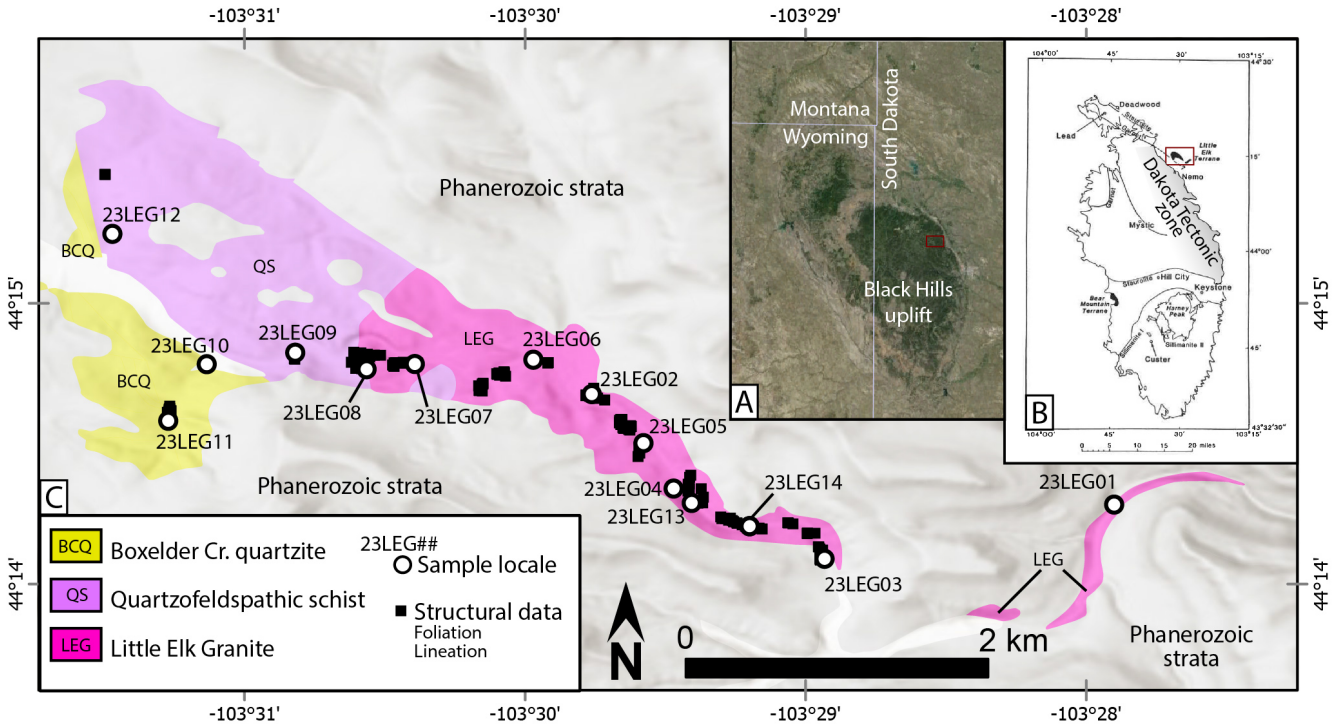

Figure 1. A) Google Earth image showing the location of the Black Hills (dark green region) relative to political borders. The Little Elk Creek area is outline by the red rectangle. B) Metamorphic isograd map of the Black Hills Precambrian core from Gosselin et al. (1988). Black shaded regions represent Archean rocks. The Little Elk Creek area is outline by the red rectangle. C) Geologic map of the Little Elk Creek area showing sample and structural data locations. Modified from Redden and DeWitt (2008).

to document microstructures along Little Elk Creek in a systematic transect across the shear zone. The results from this analysis bear on the kinematics and temperature of DTZ deformation in the northeastern Black Hills.

GEOLOGIC SETTING

The oldest rocks in the Black Hills are in the Little Elk (Fig. 1) and Bear Mountain terranes, which are dated at 2559 ± 6 Ma and 2596 ± 11 Ma, respectively (McCombs et al., 2004) (Fig. 1B). Other Precambrian rocks in the Black Hills consist of Paleoproterozoic metasedimentary rocks that are interpreted as deposited on top of the Archean rocks (Redden and DeWitt, 2008). This includes the Nemo Group, which is a package of quartzite, metaconglomerate, and iron formation exposed in a thrust sheet near Nemo, SD (Allard and Portis, 2013). These Paleoproterozoic rocks are generally interpreted to have been deposited within a continental rift that stretched between the Black Hills and Sudbury, Ontario, Canada (Dahl et al., 2006).

Deformation of Precambrain rocks in the Black Hills records four folding events that are interpreted to have formed during convergence between the Wyoming craton to the west and other cratonic blocks to the south and east (e.g., Norton and Redden, 1990; Redden et al., 1990; Terry and Friberg, 1990; Helms and Labotka, 1991; Dahl et al., 1999, 2005a, 2005b; Nabelek et al., 1999, 2006; Redden et al., 2008). D1, the earliest folding event, is thin-skinned, nappe-style, deformation that produced north-vergent recumbent folds that affected all rocks older than 2480 Ma (Redden et al., 1990, 2008). D1 had an associated folding event, F1, that is represented by local east-northeast-trending, tight-to-isoclinal folds in bedding, S0, and axial planes that dip shallowly to the south-southeast (Redden et al., 1990, 2008). The F2 folds, that are associated with D2, refold the F1 structures into upright, north-northwest-trending isoclinal synforms and antiforms with subhorizontal hinge lines (Redden et al., 1990, 2008). F2 folds are associated with an axial-planar cleavage fabric, S2, that is north-northwest-striking and subvertical (Redden et al., 1990, 2008). D3 is associated with "cross folds", F3, that refold the S2 fabric from D2 into upright, vertically plunging folds (Dahl et al., 1999; Redden et al., 1990, 2008). The DTZ (D3) is associated with F3, which can be distinguished from S2 near F3 fold hinges where it cross-cuts the S2 fabric (Redden et

al., 1990, 2008). D4 occurred after the DTZ and is characterized by recumbent folding along the margins of the the Harney Peak Granite in the southern Black Hills (Fig. 1B) and is interpreted to record vertical flattening following intrusion at ca. 1715 Ma (Dahl et al., 1999; Redden et al., 1990).

MATERIALS AND METHODS

Fieldwork was done in the Nemo, SD, area, looking at outcrops of the Little Elk Granite. The fieldwork consisted of going to the outcrops and using the FieldMove application on an Apple iPad to measure strike and dip of the shear foliation and the trend and plunge of the stretching lineation. A Brunton compass was used when the outcrop surface was too small for the iPad. Notes were taken in a notebook about the outcrop characteristics, such as outcrop scale deformation features. Pictures of all the outcrops were taken using the FieldMove app and annotated to record the observations. A rock hammer and chisels were used to collect seven oriented samples, about 10cm to 15cm in diameter. Because the Little Elk Granite is primarily an augen gneiss with K-feldspar crystals up to 3 cm in diameter, the samples were selected to have crystals smaller than the thin section glass slide so the section would contain more than a single crystal.

After the fieldwork was completed, the samples were brought to the Mineral Industries building on the South Dakota School of Mines and Technology campus to be cut into billets using a rock saw. The samples were cut into billets 0.5 x 2.7 x 4.6 cm proportions. The billets were cut perpendicular to the foliation and parallel to the lineation, and oriented with a notch in the down-plunge direction. After this process was complete, the billets were sent to Wagner Petrographic to be made into thin sections.

When thin sections were returned petrography was performed using a Nikon Eclipse LV100 POL model microscope. The thin sections have allowed for the identification of grain boundaries, undulatory extinction, strain shadows, and other microstructures. Structures that recorded the shear zone kinematics were documented and tallied.

RESULTS

At outcrop scale, the Little Elk Granite has two different fabrics (Fig. 2). Fabric type 1 is an augen gneiss fabric characterized by alignment of ~1-5 cm K-feldspar crystals that is interpreted to have formed during emplacement of the Little Elk Granite. Fabric type 2 cross-cuts the type 1 augen gneiss fabric and is characterized by comminution of the large K-feldspar grains within mylonitic shear zones. The type 1 fabric is folded throughout the field area, whereas the type 2 shear fabric is consistently oriented at ~150/70°SW and contains a steeply plunging lineation with a rake of ~70°. The microstructural analysis focused on the type 2 fabric.

In the thin section reference frame (cut parallel to the steeply plunging lineation), both top-right and top-left shear sense indicators are present. These structures are recorded by asymmetric pressure shadows associated with feldspar porphyoclasts and simple shear folding (Fig. 3). The quantity of microstructures showing each shear sense is similar, with 14 structures exhibiting top away from the notch and 12 structures exhibiting top towards the notch among all analyzed samples. The subtle predominance of top-away-from-notch

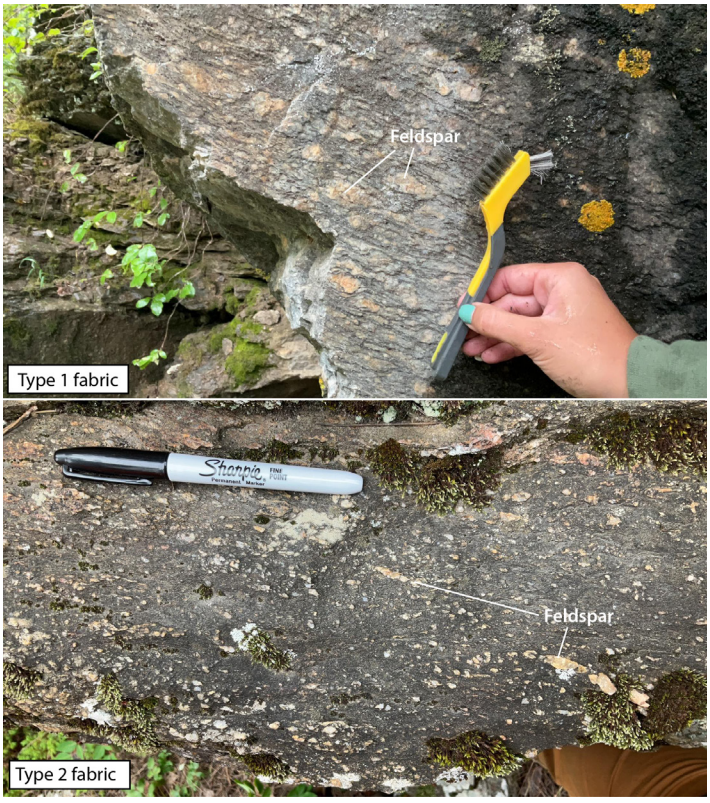

Figure 2. Field photographs of the the two fabric types in the Little Elk granite.

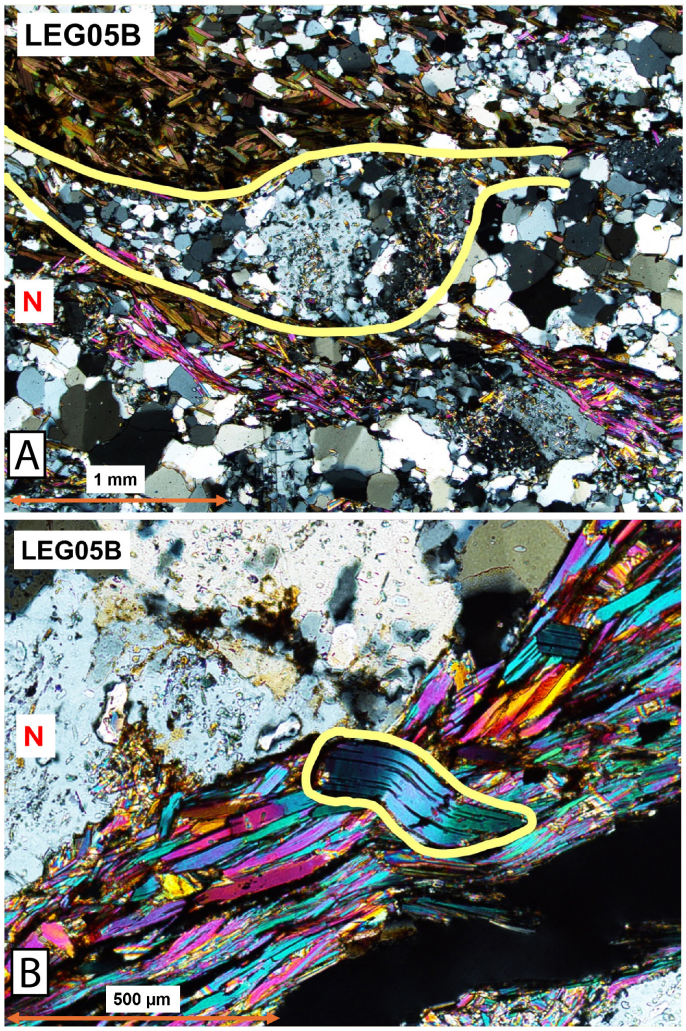

Figure 3. A) Photomicrograph showing top-to-the-right asymmetric pressure shadow on feldspar porhyroclast. B) Asymmetric fold in mica grain giving top-to-the-left shear sense. N–notch.

shear sense corresponds to oblique thrust-dextral shear sense in the geographic reference frame. Other characteristics that were exhibited in the thin sections are indicated in Table 1.

Most thin sections contain large (~1 mm) broken feldspar grains with polygonal quartz in the spaces in between feldspar fragments (Fig. 4). These fractures are regularly oriented at a high angle (>45°) to the shear foliation. Some thin sections contain isolated K-feldspar porphyroclasts with no obvious paired fragments. All thin sections contain quartz grains with undulose extinction. Some thin sections also have feldspar and mica grains with undulose extinction. Many thin sections have dynamic recrystallization textures, which are indicated by both quartz and feldspar grains having sinuous boundaries (Fig. 4). In some instances, the feldspar grains with sinuous boundaries follow the sinuous grain boundaries of the quartz.

DISCUSSION

Deformation Kinematics

The transect through the Little Elk Granite along Little Elk Creek offers the opportunity to walk across the DTZ with nearly continuous outcrop. These outcrops show both left- and right-lateral kinematics, which are also recorded at the thin section scale (Fig. 3). Based on the data collected here, the two types of structures are almost equal in population, which suggests that the rotation direction of the mineral grain during deformation is controlled by the orientation of the long crystallographic axis prior to deformation (Fossen and Tikoff, 1993). This process is common in deformation conditions where the incremental shortening axis is

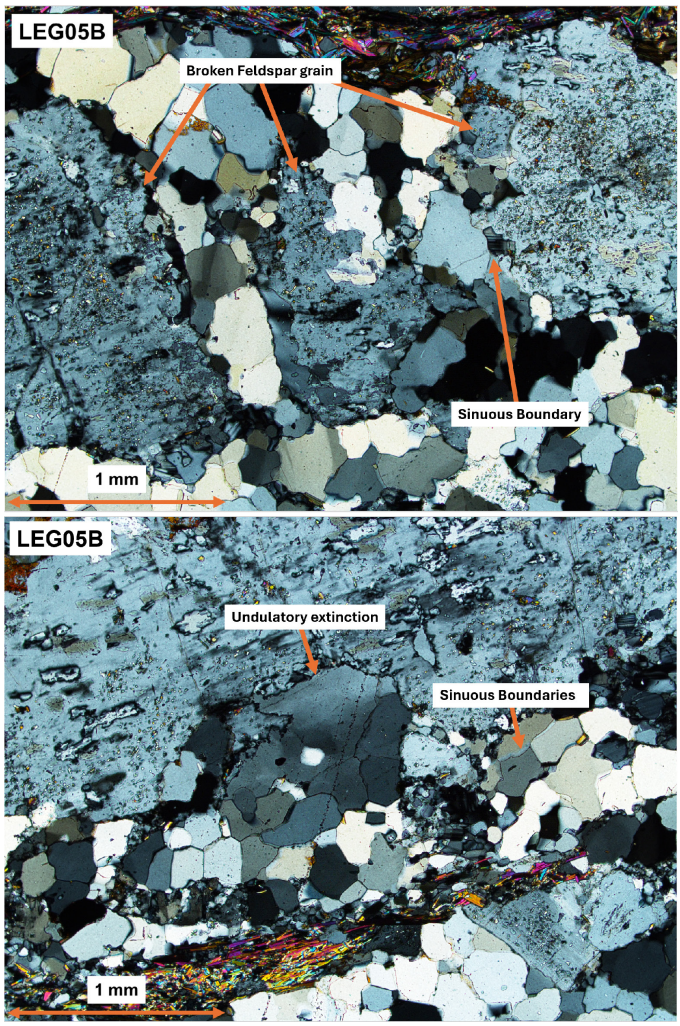

Figure 4. Photomicrogaphs illustrating deformation textures in quartz and feldspar grains including: broken feldspar, undulose extinction, and high surface area grain boundaries.

Table 1: Thin section observations

	Sample number								
Feature/ Structure	23LEG02A	23LEG02B	23LEG05A	23LEG05B	23LEG07A	23LEG07B	23LEG10A	23LEG12A	23LEG12B
Majority right-lateral	X					X		X	X
Majority left-lateral				X					
Equal right and left lateral							X		
Broken fsp	X		X	X	X		X		
Polygonal qz in cracks	X		X	X	X		X		
Undulos fsp	X		X		X		X		
Undulos qz	X	X	X	X	X	X	X	X	X
Sinuous qz boundaries	X	X	X		X	X	X	X	X
Sinuous fsp boundaries		X							
Polygonal qz	X	X	X	X	X	X	X	X	X
Polygonal fsp									
Twinning fsp	X	X	X	X					
Very Small grains (<200µm)	X	X	X	X	X	X	X	X	X
Small grains (201µm-600µm)	X	X	X	X	X	X	X	X	X
Medium grains (601µm - 1,000µm)	X		X	X	X	X	X		
Large grains (>1,000µm)			X	X	X		X		

oriented at a high (>45°) angle to the fabric, such as pure shear (Fossen and Tikoff, 1993). At the outcrop scale, the evidence of pure shear deformation is significant with a strong foliation and stretching lineation. Evidence for simple shear in outcrop consists of asymmetric pressure shadows associated with feldspar prophyroclasts, and local S-C-C' fabrics (Allard and Portis, 2013). Together, these data imply that the bulk deformation involved components of both pure shear and simple shear. The slight predominance of top-up-plunge shear sense indicators in thin section and the obliquity of the stretching lineation in outcrop suggest that oblique dextral-reverse kinematics predominate for DTZ deformation at this location. The combination of strike-slip shear sense observed in map view, conflicting shear sense indicators, and nearly down-dip stretching together suggest that the bulk deformation fits a pure shear dominated transpression model (Fossen and Tikoff, 1993; Twiss and Moores, 2007). This interpretation is consistent with other studies of the DTZ; however, the slight predominance of right-lateral shear observed here contrasts with previous work emphasizing left-lateral shear (e.g., Allard and Portis, 2013).

Deformation Temperature

The contrasting quartz and feldspar microstructures allow for an estimation of the DTZ deformation temperature. At typical crustal strain rates, feldspar deforms by plastic deformation mechanisms at temperatures above 450°C, and quartz deforms by plastic deformation mechanisms at temperatures above 300°C (Fossen and Cavalcante, 2017). At temperatures below 300°C, both the feldspar and quartz grains would deform by brittle mechanism, whereas if the deformation temperature was above 450°C, then both minerals would deform by crystal-plastic deformation mechanisms. In the DTZ at Little Elk Creek, large feldspar grains are broken, forming cracks between the broken pieces that are filled with polygonal quartz (Fig. 4). Quartz grains exhibiting undulatory extinction indicate deformation by crystal-plastic processes. Quartz, and sometimes feldspar, grains commonly display sinuous grain boundaries that interact with the grains around them, which records grain boundary migration by plastic deformation mechanisms (Passchier and Truow, 2005) (Fig. 4). These observations together suggest that the quartz was deforming by plastic deformation while the feldspar was deforming by brittle deformation, which together bracket the deformation temperature to 300-450°C. This interpretation is supported by samples from gabbroic dikes within the Little Elk Granite that display reaction rims of syn-kinematic actinolite pseudomorphing hornblende in thin section. These observations collectively indicate that the DTZ at the location of the Little Elk Creek deformed at upper greenschist facies temperatures.

The interpretation of greenschist facies deformation within the DTZ at the Little Elk Creek contrasts with

observations of the DTZ farther south in the Black Hills where it is documented to be a higher-grade shear zone (e.g., Hill, 2006). This along-strike change in deformation temperature could be explained by the DTZ in the Little Elk Creek being a preserved higher crustal level of the shear zone or the heat source of the metemorphisim being in the southern area of the hills. If the DTZ along Little Elk Creek is a preserved higher crustal level of the shear zone, it could indicate that the Precambrian basement of the Black Hills has been tilted to the north, allowing for preservation of the higher crustal in the north. If the heat source of the metamorphism in the hills was in the south, this could indicate that deformation in the DTZ overlapped in time with the emplacement of the Harney Peak Granite.

CONCLUSION

The DTZ is part of the D3 event recorded in the Precambrian basement of the Black Hills. This event is associated with flattening and strike-slip shear that is primarily focused along the eastern side of the Black Hills metamorphic core. This deformation is shown clearly in the Little Elk Granite through quartz and feldspar grains. The quartz and feldspar grains show both left- and right-lateral shear sense at outcrop and thin-section scales, with right-lateral structures marginally dominating both. This opposing shear sense, along with steeply plunging stretching lineation, suggests that the DTZ is a pure-shear-dominated transpression zone. Feldspar grains within the shear zone deformed by brittle mechanisms while quartz deformed by cystal-plastic mechanisms. This relationship indicates that the DTZ at the location of Little Elk Creek is an upper greenschist facies shear zone.

ACKNOWLEDGMENTS

This material is based upon work supported by the Keck Geology Consortium and the National Science Foundation under Grant No. 2050697. Thank you to Trevor Waldien for helping and guiding this research. Thank you to South Dakota School of Mines and Technology for allowing the use of their materials, equipment, and spaces for this research.

REFERENCES

Allard, S.T., and Portis, D.H., 2013, Paleoproterozoic transpressional shear zone, eastern Black Hills, South Dakota: Implications for the late tectonic history of the southern Trans-Hudson Orogen: Rocky Mountain Geology, v. 48, p. 73–99, doi:10.2113/gsrocky.48.2.73.

Dahl, P. S. and four others, 1999, New constraints on the timing of Early Proterozoic tectonism in the Black Hills (South Dakota), with implications for docking of the Wyoming Province with Laurentia: Geological Society of America Bulletin, v. 111, p. 1335–1349.

Dahl, P. S. and five others, 2005a, Comparative isotopic and chemical geochronometry of monazite, with implications for U-Th-Pb dating by electron microprobe: An example from metamorphic rocks of the eastern Wyoming craton (USA): American Mineralogist, v. 90, p. 619–638.

Dahl, P. S., and seven others, 2005b, Electron probe (Ultrachron) microchronometry of metamorphic monazite: Unraveling the timing of polyphase thermotectonism in the easternmost Wyoming craton (Black Hills, South Dakota): American Mineralogist, v. 90, p. 1712–1728.

Dahl, P. S., and six others, 2006, 2480 Ma mafic magmatism in the northern Black Hills, South Dakota: A new link connecting the Wyoming and Superior cratons: Canadian Journal of Earth Sciences, v. 43, p. 1579–1600.

Fossen, H., and Cavalcante, G.C.G., 2017, Shear zones - A review: Earth Science Reviews, v. 171, p. 434–455, doi:10.1016/j.earscirev.2017.05.002.

Fossen, H., and Tikoff, B., 1993, The deformation matrix for simultaneous simple shearing, pure shearing and volume change, and its application to transpression-transtension tectonics: Journal of Structural Geology, v. 15, p. 413–422, doi:10.1016/0191-8141(93)90137-y. (accessed October 2023)

Helms, T. S., and Labotka, T. C., 1991, Petrogenesis of Early Proterozoic pelitic schists of the southern Black Hills, South Dakota: Constraints on regional low-pressure metamorphism: Geological Society of America Bulletin, v. 103, p. 1324–1334.

McCombs, J. A., Dahl, P. S., and Hamilton, M. A., 2004, U-Pb ages of Neoarchean granitoids from the Black Hills, South Dakota, USA: Implications for crustal evolution in the Archean Wyoming Province: Precambrian Research, v. 130, p. 161–184.

Nabelek, P. I., and three others, 2006, Fluid-mediated polymetamorphism related to Proterozoic collision of Archean Wyoming and Superior Provinces in the Black Hills, South Dakota: American Mineralogist, v. 91, p. 1473–1487.

Nabelek, P. I., Sirbescu, M., and Liu, M., 1999, Petrogenesis and tectonic context of the Harney Peak Granite, Black Hills, South Dakota: Rocky Mountain Geology, v. 34, p. 165–181

Norton, J. J., and Redden, J. A., 1990, Relations of zoned pegmatites to other pegmatites, granite, and metamorphic rocks in the southern Black Hills, South Dakota: American Mineralogist, v. 75, p. 631–655.

Norwood, B., Brown, M., and Hawkins, R., 2013, Structural and Kinematic Analysis of the Nemo Shear Zone, Documents the Final Suturing of Wyoming and Superior Provinces in the Black Hills, SD in Proceedings, Student Research and Creative Projects 2014-2015: Winona State University Geoscience. 2 p.(accessed October 2023).

Passchier, C. W., & Trouw, R. A. (2005). Microtectonics. Springer Science & Business Media.

Redden, J. A., and three others, 1990, U-Th-Pb geochronology and preliminary interpretation of Precambrian tectonic events in the Black Hills, South Dakota, in Lewry, J. F., and Stauffer, M. R., eds., The Early Proterozoic Trans-Hudson Orogen of North America: Geological Association of Canada Special Paper 37, p. 229–251.

Redden, J. A., and 12 others, 2008, Maps showing geology, structure, and geophysics of the central Black Hills, South Dakota: U.S. Geological Survey Scientific Investigations Map 2777, scale1:100,000, 2 sheets, 44 p.

Redden, J.A., and DeWitt, E., 2008, Maps Showing Geology, Structure, and Geophysics of the Central Black Hills, South Dakota: U.S. Geological Survey Scientific Investigations Map 2777, 44-p. pamphlet, 2 sheets, https://pubs.usgs.gov/sim/2777/ (accessed September 2023).

Terry, M. P., and Friberg, L. V. M., 1990, Pressure– temperature–time path related to the thermotectonic evolution of an Early Proterozoic metamorphic terrane, Black Hills, South Dakota: Geology, v. 18, p. 786–789.

Tikoff, B., and Fossen, H., 1993, Simultaneous pure and simple shear: the unifying deformation matrix: Tectonophysics, v. 217, p. 267–283, doi:10.1016/0040-1951(93)90010-h. (accessed October 2023)

Twiss, R. J., & Moores, E. M. (2007). Structural Geology (2nd ed.). W.H. Freeman., 444 and 445 p.

KECK Geology Consortium
Learning Science Through Research
Published by the Keck Geology Consortium
Short Contributions
Keck Geology Consortium
Volume 36
May 2024
doi: 10.18277/AKRSG.2024.36.08

KINEMATIC ANALYSIS OF SHEAR ZONES IN THE LITTLE ELK GRANITE, BLACK HILLS, SOUTH DAKOTA

LIAM T. FRY, Eckerd College
Project Advisor: Laura Wetzel

ABSTRACT

The Black Hills of western South Dakota and eastern Wyoming were uplifted as a result of the Laramide orogeny occupying the suture between the Wyoming and Superior cratons. Two exposures of Archean orthogneiss, the Bear Mountain Terrane and the Little Elk Granite (LEG), represent the oldest rocks exposed in the Precambrian core of the Black Hills and offer the opportunity to study tectonic processes involved in forming the Laurentian craton. This study presents new structural field data (orientation of foliation planes, stretching lineations, and cross cutting relations; n=270 measurements) along a ~5 km transect that record the deformation history of the LEG. Two dominant fabric types were found in outcrop: augen gneiss (type 1) and mylonitized granite (type 2). The type 1 fabric is characterized by 1-5 cm K-feldspar crystals aligned to give top-down or "normal" sense of shear, small-scale folding of the fabric, and is cross-cut by aplite dikes at multiple sites. The type 2 mylonitic fabric overprints the type 1 fabric and intensifies from east to west along the transect, resulting in a loss of the type 1 fabric. The stretching lineation in the type 2 fabric plunges down dip with shear sense indicators observable in outcrop. Both fabrics display a southeast-striking and ~70°SW dipping foliation at every site. Yet, subtle folding of the type 1 fabric at some sites causes it to be crosscut by the type 2 fabric. Based on the high-temperature deformation features in the type 1 fabric and the cross-cutting relationship with aplite dikes, we interpret that the type 1 fabric formed during emplacement of the granite. Assuming the LEG has not experienced significant tilting since emplacement, the top-down shear sense recorded by alignment of K-feldspar may suggest emplacement of the LEG into an extensional setting. Our observations of the type 2 fabric, including down-plunge stretching lineations and opposing shear sense indicators support previous interpretations of transpressional deformation within the LEG and metasedimentary rocks sheared along its western margin. With the new data describing shear zone kinematics in the LEG, we interpret that the type 1 fabric formed prior to suturing of the Wyoming and Superior Cratons and the type 2 fabric formed during craton suturing.

INTRODUCTION

Precambrian rocks present in the Black Hills, South Dakota form a domal core due to regional uplift during the Laramide Orogeny (Redden et al., 1990). The Archean Little Elk Granite (LEG) and Bear Mountain Granite (BMG) are present on the edges of the exposed Precambrian core (Fig. 1), which was metamorphosed and deformed during the Early Proterozoic (Redden et al., 1990). Laying in the southeastern portion of the Wyoming Craton, Paleoproterozoic and Neoarchean rocks of the Black Hills underwent multiple tectonic events affiliated to the collision of the Wyoming and Superior Cratons (Dahl et al., 2006). In association with large-scale folds, Paleoproterozoic, north-northwest-trending, axial planar foliation was found preserved in east-northeast-trending fold nappes within the Black Hills (Dahl et al., 2006). These structures can be seen as a result accretion of the norther Yavapai island-arc terrane and more importantly the approximate east-west shortening associated with the suturing of the Wyoming and Superior crtatons (Dahl et al., 2006). These events formed a northwest-southeast-striking foliation in the Precambrian rocks throughout the Black Hills (Redden et al., 1990).

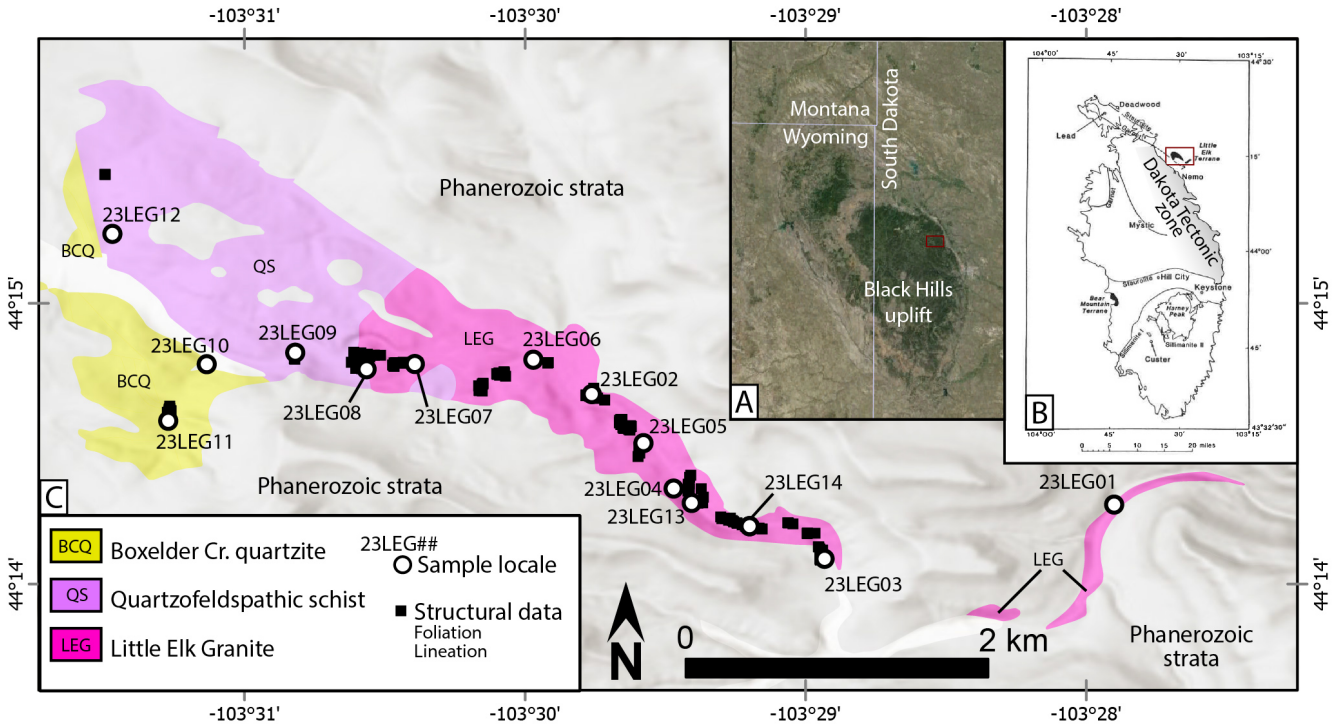

Figure 1. A) Google Earth image showing the location of the Black Hills (dark green region) relative to political borders. The Little Elk Creek area is outline by the red rectangle. B) Metamorphic isograd map of the Black Hills Precambrian core from Gosselin et al. (1988). Black shaded regions represent Archean rocks. The Little Elk Creek area is outline by the red rectangle. C) Geologic map of the Little Elk Creek area showing sample and structural data locations. Modified from Redden and DeWitt (2008).

Exposure of the LEG is limited to two windows in the Paleozoic sedimentary rocks over an area of ~2 square miles (Zartman & Stern, 1967) (Fig. 1). The LEG is feldspathic, displaying a dominant porphyritic, coarse grained texture with well-developed augen structure (Redden et al., 1990). The gneissic LEG occupying the valley of Little Elk Creek is well banded consisting of mica flakes parallel to well-defined layers between quartz and feldspar bands (Runner, 1934). Thin section analysis from Runner (1934) displays a composition of microcline, orthoclase, and albite feldspar, 60%; quartz 25%; biotite and muscovite, 15%; along with minor content of apatite, tourmaline, zircon, and pyrite. Large fractured quartz and feldspar grains were among the first essential minerals to form in the Little Elk gneissic granite. Subsequent of initial crystallization of these minerals is formation of mylonitic zones, micaceous layers, and veinlets. These developed along fractures in the quartz and feldspar grains (Taylor, 1935). Aplite dikes are seen to frequently cut through the main mass along with small quartz-rich veins. Cross cutting features intrude along and across structural planes of the main granite, but they do not display some of the same metamorphic characteristics of the granite. Previously observed in Runner (1934), the folding in this region consists of a doubly plunging isoclinal antiform that is overturned toward the northeast.

The aims of this study are to assess the kinematics and deformation history of the LEG. Through the assessment of field measurements, kinematic analysis of LEG shear zones can assist in further interpretation of metamorphism of the Archean basement and the LEG.

METHODS

The LEG was observed during August 2023, which involved structural-kinematic analysis in the field and sampling for analytical work. Ten days were spent in the field collecting structural measurements and field samples of exposed outcrops of the LEG. Outcrops were observed and analyzed along a transect along Dalton Lake Road (Fig. 1). Site observation started east of Dalton Campground with site 23LEG01 and continued west to 23LEG12 (Fig. 1). An application on iPad Mini, FieldMove, was utilized to measure strike and dip of foliation planes, contact planes of dikes, localized shear zones, and fault planes. Trend and plunge of mineral lineation were measured using the same instrumentation. With

the use of Allmendinger's Stereonet 11 program, field measurements were plotted on stereonets and a map of the studied area to assess patterns in the orientations among the sites.

RESULTS

Fabric observations

Two fabric types are present in LEG outcrops as: an augen gneiss fabric (type 1) and a mylonitized granite fabric (type 2). Cross-cutting aplite dikes display different deformation characteristics visible in each fabric. Preservation of type 1 fabric to decreases to the west as the type 2 fabrics intensifies. West of site 23LEG08 (Fig. 1), type 1 fabric is not preserved. East of 23LEG14 (Fig. 1), type 2 fabric is not present.

Type 1, augen gneiss

Type 1 fabric consists of deformed feldspar augens up to ~5 cm in diameter (Fig. 2a). Throughout the transect, augens in type 1 fabric predominately display top-down, or hanging wall-down shear sense along a dipping fabric, recorded by asymmetric pressure shadows associated with the augens (Fig. 2a inset). Aplite dikes are observed to crosscut the type 1 fabric, and do not experience any deformation associated with the type 1 fabric (Fig. 2b).

Type 2, mylonitic fabric

The type 2 fabric lacks the large feldspar augens that characterize the type 1 fabric (Fig. 3a). Based on outcrop scale deformation textures, feldspar in the type 2 fabric deforms by fracturing of augens from the type 1 fabric. In the type 2 fabric, rotation of fractured grains, asymmetric pressure shadows, and local S-C fabrics record both dextral and sinistral shear sense (Fig. 3a, b). Aplite dikes that crosscut the type 1 fabric are deformed along with the type 2 fabric (Fig. 3c).

Stereonet observations

Foliation plane, lineation, joint, and fold axis measurements were collected at a total of 16 sites along the transect. Table 1 displays the number and type of measurements taken at each site. A threshold of ≥5 measurements was used to determine notable sites. The sites that were deemed notable to use for further analysis are: 23LEG – 02, 03, 05, 06, 07, 08, 10, and 13 (Fig. 4). Sites that contain the type 1 fabric have a relatively consistent trend of southeast-striking and southwest-dipping foliation (Fig. 4). Sites that contain the type 2 fabric display similar trends in orientation to those with type 1 fabric of a generally southeast-striking and southwest dipping fabric. Among the notable sites, 23LEG13 is the sole location in which the general orientation of the foliation planes differs. Type 1 fabric at LEG13 is consistent with the type 1 fabrics at other sites, but the type 2 foliation planes at this site are strike north-south and have variable dip direction (Fig. 4). All lineations corresponding to both fabrics display a plunge moderately to the southwest, congruent with a down dip relationship to the foliation planes with little variation.

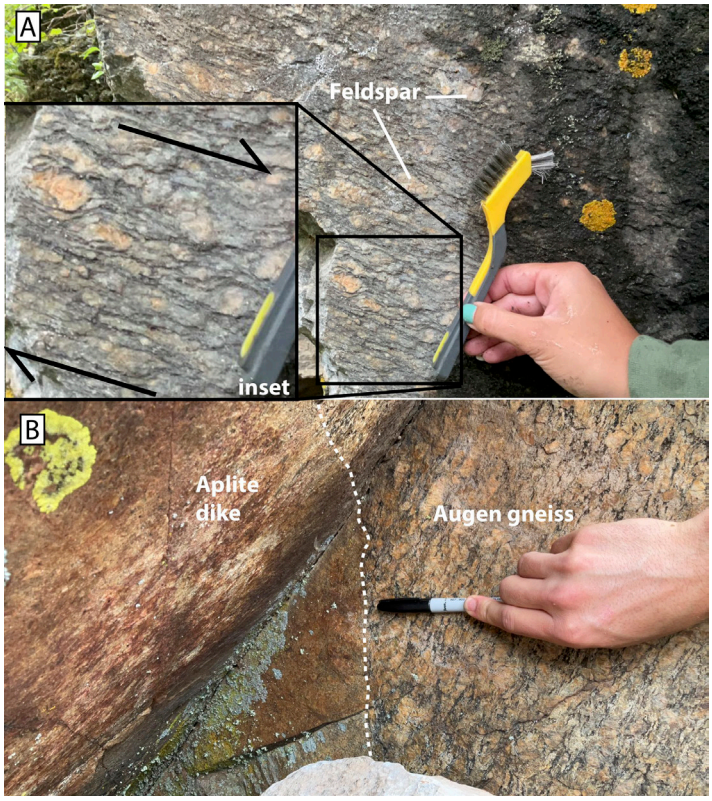

Figure 2. A) Outcrop photo of type 1 fabric (augen gneiss) foliation plane at site 23LEG03. Inset: Asymmetric shear on large, orange-pink, feldspathic augens indicate top-down shear sense. B) Augen gneiss fabric crosscut by undeformed aplite dike at 23LEG02.

DISCUSSION

The identification of two different fabric types provides insight to the deformation history of the LEG. The presence of large feldspar augens in the

Figure 3. A) Outcrop photo of well-developed type 2 fabric (mylonitic granite) indicating top-to-the-left shear sense. B) S-C structure in type 2 fabric indicating top-to-the-right shear sense. C) Aplite dike stretched within the type 2 fabric. D) incipient development of the type 2 fabric overprinting and localized within the type 1 augen gneiss fabric.

type 1 fabric may indicate a metamorphic process that was hotter, resulting in plastic deformation of the feldspar grains (Fig. 2). The type 2 fabric, however, is characterized by smaller feldspar grains that display brittle deformation features, indicating a colder metamorphic process during deformation. The type 2 fabric is observed to develop along the type 1 fabric (Fig. 3d) and deform aplite dikes that crosscut the type 1 fabric (Fig. 3c). Moreover, the westward intensification of type 2 fabric in combination with loss of type 1 fabric suggests that shearing related to the type 2 fabric resulted in the lithologic boundary along the western margin of the LEG (Fig. 1) (Allard and Portis, 2013). These data together indicate that the deformation features observed in the LEG record an evolution from higher temperature to lower temperature, wherein the higher temperature fabrics predate the intrusion of aplite dikes. Although one sample of undeformed aplite dike (sampled from

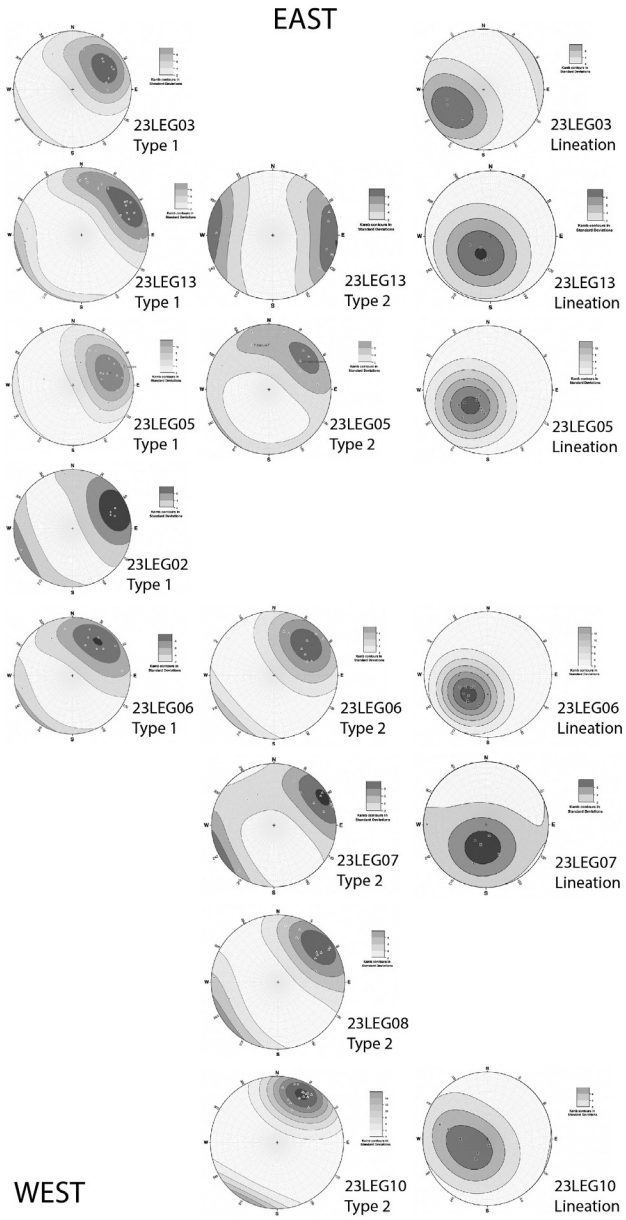

Figure 4. Structural data for notable sites organized from east to west along the transect. Planar data (fabric types 1 and 2) are plotted as poles to the foliation. Kamb contours in standard deviation are associated with the data to aid in visualization.

Table 1. Little Elk Granite Structural data

Station ID	Type 1	Type 2	Dike margin	Stretching Lineation	Fold axis
23LEG01	4	0	0	3	0
23LEG03	16	0	0	5	1
23LEG14	3	1	0	1	0
23LEG13	22	10	0	4	0
23LEG04	1	0	0	0	0
23LEG05	20	12	7	12	0
23LEG02	6	1	4	1	0
23LEG06	12	9	5	13	0
23LEG07	2	12	0	6	5
23LEG08	0	15	3	2	0
23LEG09	0	3	0	1	0
23LEG10	0	16	0	7	0
23LEG15	7	2	0	1	0
23LEG16	7	7	0	0	0

Fig. 2b) did not yield zircon for dating, the common interpretation that aplite dikes form late in the emplacement history of igneous bodies and the high temperature implied by the plastic deformation of feldspar in the type 1 fabric together suggest that the type 1 fabric may have formed during emplacement of the LEG.

Both similarities and difference appear by incorporating the deformation textures with the orientation and kinematic information of each fabric type. Although the orientation of the type 1 fabric is modified by overprinting (Fig. 4), sites that preserve the type 1 fabric commonly display top-down shear sense in asymmetric augen porphyroclasts along a moderately-steeply southwest dipping foliation (Figs 2a, 4). The top-down shear sense is accompanied by a moderately developed stretching lineation that plunges nearly down dip (Fig. 4). The type 2 fabric displays spatially variable development of opposing strike-slip shear sense indicators (Fig. 3a, b, d) combined with a stretching lineation that plunges nearly down dip. Strike-slip shear zones with opposing shear sense and a steeply plunging stretching lineation have been widely documented and are generally thought to form by a combination of pure shear and simple shear deformation in a strain regime called "transpression" (Fossen and Tikoff, 1993).

Incorporating the deformation textures, structural geometries, and kinematic information together yields insight to the deformation history of the LEG and the processes that led to deformation. Interpreting the type 1 high temperature augen gneiss fabric to have formed during emplacement of the LEG implies that emplacement took place in an active tectonic setting. Although there is little/no information to test whether the type 1 fabric is presently in the orientation at which it formed, the current geometric-kinematic information suggests that the fabric formed in an extensional environment. Interestingly, the age of the LEG (2559 ± 6 Ma: McCombs et al., 2004) was closely followed by the breakup of supercontinent Kenorland (Bekker and Eriksson, 2003). Thus, the interpretation of the type 1 fabric forming in an extensional environment is permissible with the present data. The transpressional features displayed by the type 2 fabric have been documented elsewhere in the Black Hills and are interpreted to represent a left-lateral transpression zone called the "Dakota Tectonic Zone" that formed late in the suturing of the Wyoming and Superior cratons along the Trans-Hudson Orogeny (Allard and Portis, 2013). The timing of Dakota Tectonic zone deformation is not well bracketed, but is interpreted to precede, or slightly overlap with emplacement of the Harney Peak granite at ca. 1715 Ma (Redden et al., 1990; Allard and Portis, 2013).

CONCLUSIONS

Through observing shear zones of the LEG, some of the most notable discoveries are the differing fabrics and their foliation and lineation orientations. The LEG contains two fabrics: an older, high temperature augen gneiss fabric (type 1), and a younger low-temperature mylonitic fabric (type 2). The type 2 fabric formed subparallel to the type 1 fabric and locally crosscuts it. Synthesizing kinematic information from each fabric with the regional geologic framework suggests that the type 1 fabric formed in an extensional environment after ca. 2560 Ma and that the type 2 fabric formed in a transpressional environment prior to 1715 Ma.

ACKNOWLEDGEMENTS

This material is based upon work supported by the Keck Geology Consortium and the National Science Foundation under Grant No. 2050697. We thank Trevor Waldien (South Dakota School of Mines & Technology) for providing resources, knowledge, and guidance throughout the research project. We thank Laura Wetzel (Eckerd College) for assisting with organization and progression of the project at my home institution (Eckerd College). I thank my student research partners, Willa Obringer (Lake Superior State University), Rebecca Braun (South Dakota School of

Mines & Technology), and Alex Robinson (Pomona College) for assistance and excellent collaboration in the field and laboratory setting.

REFERENCES

Allard, S. T., Portis, D. H., 2013, Paleoproterozoic transpressional shear zone, eastern Black Hills, South Dakota; implications for the late tectonic history of the southern Trans-Hudson Orogen. Rocky Mountain geology. 48(2):73–99.

Allmendinger, R. W., Cardozo, N., and Fisher, D., 2012, Structural geology algorithms: Vectors and tensors in structural geology: Cambridge University Press (book to be published in early 2012).

Bekker, A., & Eriksson, K. A. (2003). A Paleoproterozoic drowned carbonate platform on the southeastern margin of the Wyoming Craton: a record of the Kenorland breakup. Precambrian Research, 120(3-4), 327-364.

Dahl P.S., Hamilton M.A., Wooden J.L., Foland K.A., Frei R., McComba J.A., Holm D.K., 2006, 2480 Ma mafic magmatism in the northern Black Hills, South Dakota; a new link connecting the Wyoming and Superior Cratons. Canadian Journal of Earth Sciences. 43(10):1579–1600.

Fossen, H., and Tikoff, B., 1993, The deformation matrix for simultaneous simple shearing, pure shearing and volume change, and its application to transpression-transtension tectonics: Journal of Structural Geology, v. 15, p. 413–422, doi:10.1016/0191-8141(93)90137-y.

Gosselin, D. C., Papike, J. J., Shearer, C. K., Peterman, Z. E., & Laul, J. C., 1990, Geochemistry and origin of Archean granites from the Black Hills, South Dakota. Canadian Journal of Earth Sciences, 27(1), 57–71.

Redden, J. A., Peterman, Z. E., Zartman, R. E., DeWitt, E., Lewry, J. F., & Stauffer, M. R., 1990, U-Th-Pb geochronology and preliminary interpretation of Precambrian tectonic events in the Black Hills, South Dakota. The early Proterozoic Trans-Hudson Orogen of North America. Geol Assoc Can Spec Pap, 37, 229-251.

Runner, J. J., 1934, Pre-Cambrian geology of the Nemo District, Black Hills, South Dakota. The American Journal of Science. 5(167):353-372.

Taylor, G. L., 1935, Pre-Cambrian granites of the Black Hills. The American Journal of Science. 29(171):278-291.

Zartman, R. E., Stern, T. W., 1967, Isotopic age and geologic relationships of the Little Elk Granite, northern Black Hills, South Dakota. USGS Prof. Paper D. 575, 157-163.

KECK Geology Consortium
Learning Science Through Research
Published by the Keck Geology Consortium
Short Contributions
Keck Geology Consortium
Volume 36
May 2024
doi: 10.18277/AKRSG.2024.36.09

ELUCIDATION OF AN UNDEFINED RELATIONSHIP: A STUDY OF THE BOXELDER CREEK QUARTZITE AND LITTLE ELK GRANITE TO DECIPHER PALEOPROTEROZOIC BASIN DEVELOPMENT IN THE BLACK HILLS, SOUTH DAKOTA

WILLA OBRINGER, Lake Superior State University
Project Advisors: Paul Kelso and Derek Wright

INTRODUCTION

The Black Hills of South Dakota, located on the southeastern edge of the Wyoming Province, are host to an extensive range of complex tectonic events, from the breakup of supercontinent Kenorland to the Trans-Hudson and Laramide orogenies (Whitmeyer & Karlstrom, 2007). In the Late Cretaceous, the Laramide Orogeny uplifted the Black Hills, providing excellent exposure of Archean and Proterozoic terranes (Lisenbee,1988). Two Archean domains are exposed in the Black Hills, the Bear Mountain Domain (BMD) and the Little Elk Granite (LEG) Domain, the latter of which is central to this study. The location of the LEG alone spawns several questions, as it is geographically separated from other Neoarchean rocks of the Wyoming craton (Fig. 1).

Several tectonic models have been proposed to explain the distribution of Neoarchean rocks in the Black Hills. One model suggests that the LEG formed by arc magmatism and represents one of the easternmost exposures of Neoarchean magmatism in the Wyoming Province (Karlstrom & Houston, 1984). In this model, the LEG and BMD formed along the edge of the craton during crustal accretion (Karlstrom & Houston, 1984). The generation of crust in these domains is due to plate convergence between the Superior and Wyoming Cratons and is considered to represent the final assembly of supercontinent Kenorland between 2,590 and 2450 Ma (McCombs et al., 2004). A focal point of this model is the Blue Draw Metagabbro (BDM), variably thought to be evidence of arc magmatism (Van Boening & Nabelek, 2008) or a product of continental breakup and rifting between the Wyoming and Superior cratons at ca. 2.48 Ga (Dahl et al., 2006). The latter theory is associated with conflicting tectonic models, which stand on the premise that subduction was not involved in the tectonic evolution of the Black Hills, but rather rifting events catalyzed by a mantle plume (Van Boening & Nabelek, 2008). One model for the rifting event suggests that two rifting periods exposed Archean domains and formed a basin where Proterozoic sediments were later deposited (Redden et al., 1990). This model suggests that sediment deposition occurred in an extensional setting within the Wyoming craton, with western-sourced sediments filling the basin to the east. This study aims to evaluate the relationship between the LEG and Boxelder Creek Quartzite (BCQ) where they are exposed in Little Elk Creek to assess the plausibility of these various tectonic models.

GEOLOGIC BACKGROUND

The BCQ, characterized as an orthoquartzite with stretched pebble metaconglomerate layers, is suggested to be sourced from Neoarchean crust, including the LEG, during a Paleoproterozoic rifting event (Redden & DeWitt, 2008). The LEG is an augen gneiss with an I-type granite protolith and a Pb-Pb age of 2,559 +/- 6 Ma (McCombs et al., 2004). The exact age of the BCQ has yet to be determined using modern analytical methods and has been bracketed between the LEG and BDM (Redden & DeWitt, 2008). The BCQ is juxtaposed against the LEG by a local shear zone, making the relationship between the two formations unclear. It is unknown whether the granites intrude or are buried by the BCQ.

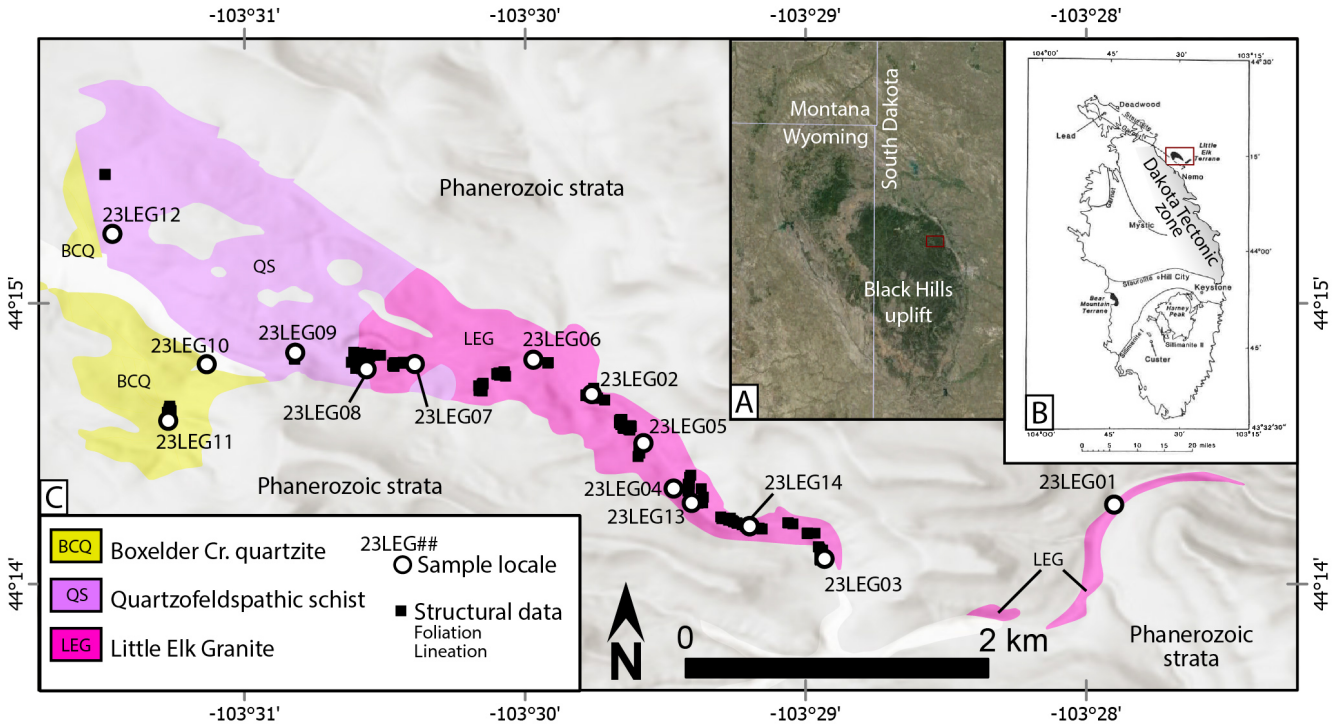

Figure 1. A) Google Earth image showing the location of the Black Hills (dark green region) relative to political borders. The Little Elk Creek area is outline by the red rectangle. B) Metamorphic isograd map of the Black Hills Precambrian core from Gosselin et al. (1988). Black shaded regions represent Archean rocks. The Little Elk Creek area is outline by the red rectangle. C) Geologic map of the Little Elk Creek area showing sample and structural data locations. Modified from Redden and DeWitt (2008).

METHODS

Structural Analysis

Orientations of foliations, clasts, and fold axes were measured using a Brunton Compass. By analyzing the morphology of porphyroclasts, shear sense was recorded. The lengths of maximum and minimum axes of elongated cobbles were collected from the BCQ outcrop in two dimensions, along strike and down-dip within the foliation. Cobble length measurements were entered into the EllipseFit 3.11 program (Vollmer, 2018) to create Hsu and Flinn-Ramsay plots.

Geochemistry

Scanning electron microscopy and micro X-ray fluorescence analysis offered geochemical insights into the BCQ. The back-scattered electron detector (BSD-C) was used to perform compositional analysis through energy dispersive spectroscopy (EDS). The accelerating voltage was set between 20-30 KeV, and a 40-60 probe count was used to observe samples in low vacuum mode. The rhodium X-ray tube with microcapillary optics was used for μXRF analysis, with a dwell time of 25 ms/pixel and a pixel size of 20 micrometers.

Geochronology

Zircon grains retrieved from the BCQ were dated using Laser Ablation-Inductively Coupled Plasma Mass Spectrometry (LA-ICPMS) at the LaserChron Lab at the University of Arizona. Samples were crushed, sieved to less than 250 micrometers, and panned using a miner's gold pan to remove dust and light minerals. Magnetic grains were removed using a hand magnet and Frantz LB-1 isodynamic separator. Lithium heteropolytungstate (LST), with a density of 2.85 g/cc, was used to separate dense non-magnetic minerals (e.g., zircon) from low-density, non-magnetic minerals such as quartz and feldspar.

Zircon grains were mounted with three zircon standards: the Duluth Gabbro (FC1; 1099 ± 2 Ma), Sri Lanka (SL; 563.5 ± 2.3 Ma), and R33 (419.3 ± 0.4 Ma) (Gehrels, 2010). Analysis spots were picked using backscattered electron and cathodoluminescence imaging. A 15 um beam was used, and the laser was set at a repetition rate of 8 Hz and fluence of 4 J/cm2, which ablated at a rate of 1 mm/s and yielded an average pit depth of 12 mm. An uncertainty of

2-sigma (%) is achieved. Data was filtered employing concordance using an 80% threshold. IsoplotR was utilized to generate kernel density estimate plots, calculate the weighted mean age of the youngest statistical population, and plot data on a Wetherill concordia diagram (Ludwig, 2008).

RESULTS

Structural Analysis

Outcrops of the BCQ have a steeply southwest-dipping foliation (126/70º SW) and steeply southwest plunging stretching lineation (Fig. 2A). Several moderately plunging folds are scattered throughout outcrops trending south/southeast (Fig. 2A) and deform the foliation. Conglomerate clasts form sigma porphyroclasts, which indicate top-to-the-left shear-sense parallel to foliation (Fig. 2B). Ramsay plots generated from clast length measurements indicate strain is predominantly in the field of flattening (Fig. 2C), yet the asymmetric porphyroclasts also require a simple shear component to the deformation. Observation of thin sections reveals both static quartz recrystallization textures and undulose extinction, with lesser amounts of bulging grain boundaries. Evidence of ductile shearing is prevalent within thin sections in asymmetric porphyroclasts and S-C fabrics. Asymmetric porphyroclasts and S-C fabrics both indicate top-to-the-left shear sense in thin section.

Geochemistry

SEM and µXRF analyses revealed abundant chromium, nickel, titanium, zinc, iron mineralization and lesser amounts of silver, copper, and rare earth element mineralization (Fig. 3). Chromium and titanium are concentrated in fuchsite and titanite, respectively, and concentrated within micaceous seams surrounding larger, quartz-dominated clasts. Iron and zinc mineralization show no spatial patterns; however, in some instances, iron is mineralized in ooids. Silver traces correlate with sulfur concentrations, suggesting silver is hosted within sulfide minerals such as acanthite. However, there are instances in which silver is associated with iron. Copper is associated with aluminum, silica, and iron within single grains, possibly in the for of aluminum ferrian chrysocolla. Uranium and thorium are prevalent within zircon grains.

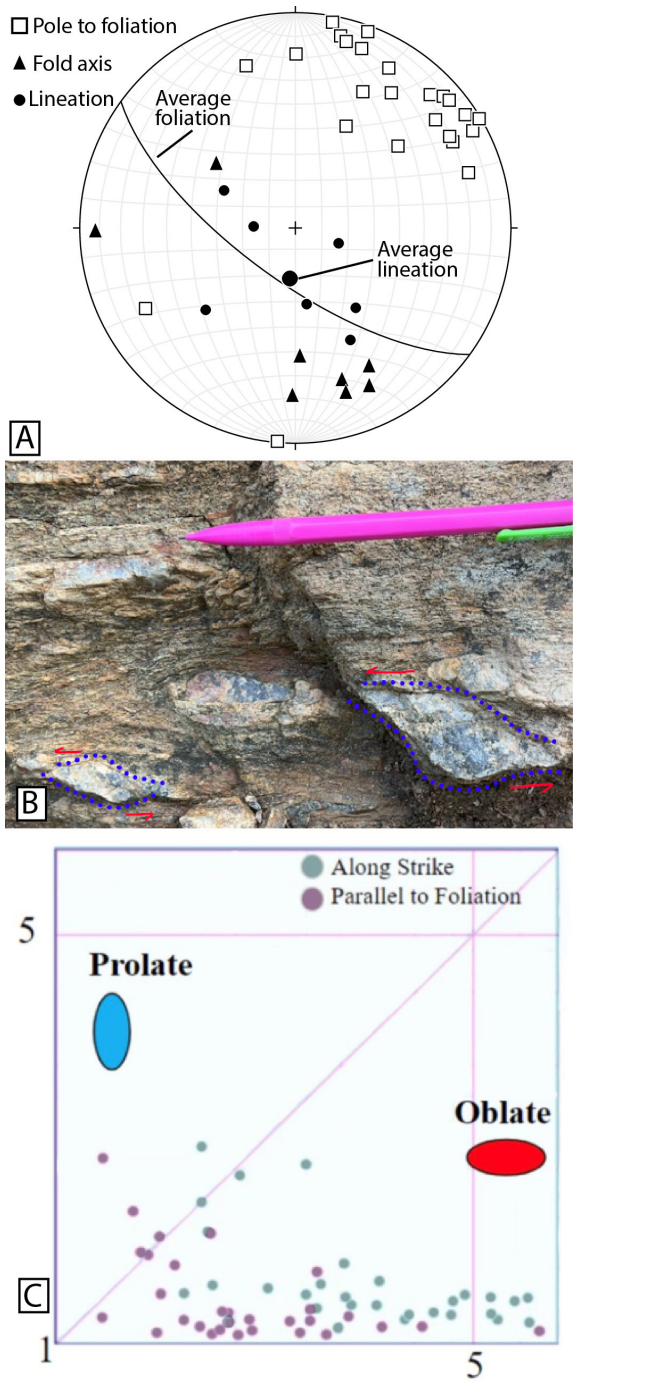

Figure 2. A) Equal area lower hemisphere stereonet showing structural data for the Boxelder Creek Quartzite. B) Outcrop photo showing sheared quartz clasts that indicate left lateral shear sense. C) Ramsay plot showing measurements from the quartz clasts indicating that they plot in the field of flattening.

Rare earth elements are found within monazite and zircon. The light rare earth elements (LREEs) cerium, lanthanum, and neodymium were most common, with only a few cases of ytterbium. LREEs are substituted in exchange for zirconium in zircon and phosphorus in monazite.

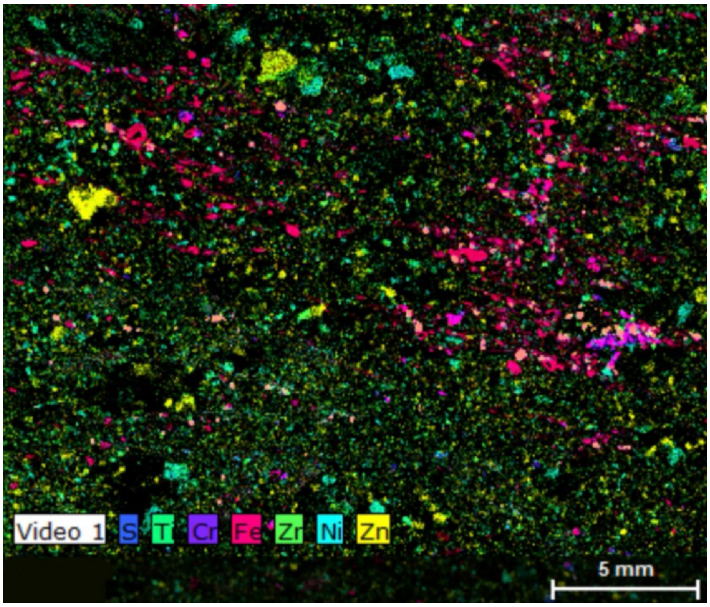

Figure 2. µXRF map displaying trace mineral and metal concentrations within the BCQ. The occurrence of transition metals such as Fe, Ni, and Zn suggests hydrothermal alteration.

Geochronology

Spot analyses (n=182) were generated for the single sample of the BCQ via LA-ICPMS. Sixty-nine of the analyses passed the filtering criteria. The concordia diagram shows both discordant and reverse discordant values (Fig. 4B). Discordant values associated with lead loss yield several ages younger than 2.48 Ga; these values are known to be inaccurate due to the intrusive relationship between the 2.48 Ga BDM and BCQ (Dahl et al., 2006). The KDE of the U-Pb data shows age populations at ca. 2560 Ma, 2700 Ma, 3000 Ma, and 3300 Ma (Fig. 4C). The maximum depositional age of the BCQ is 2552.1 ± 7.1 Ma (Fig. 4D), determined by taking the weighted mean of the youngest age population.

DISCUSSION

Structural Analysis

In field observations, the BCQ displays sheared clasts with top-left kinematics contained within the foliation (Fig. 2B). These clasts record left-lateral simple shear parallel to the foliation plane. This field data, combined with the flattening observed in the Ramsay diagram (Fig. 2C), suggests that these deformation features formed together in left-lateral transpression (e.g., Fossen and Tikoff, 1998). These deformation fabrics most likely record D3 deformation manifested

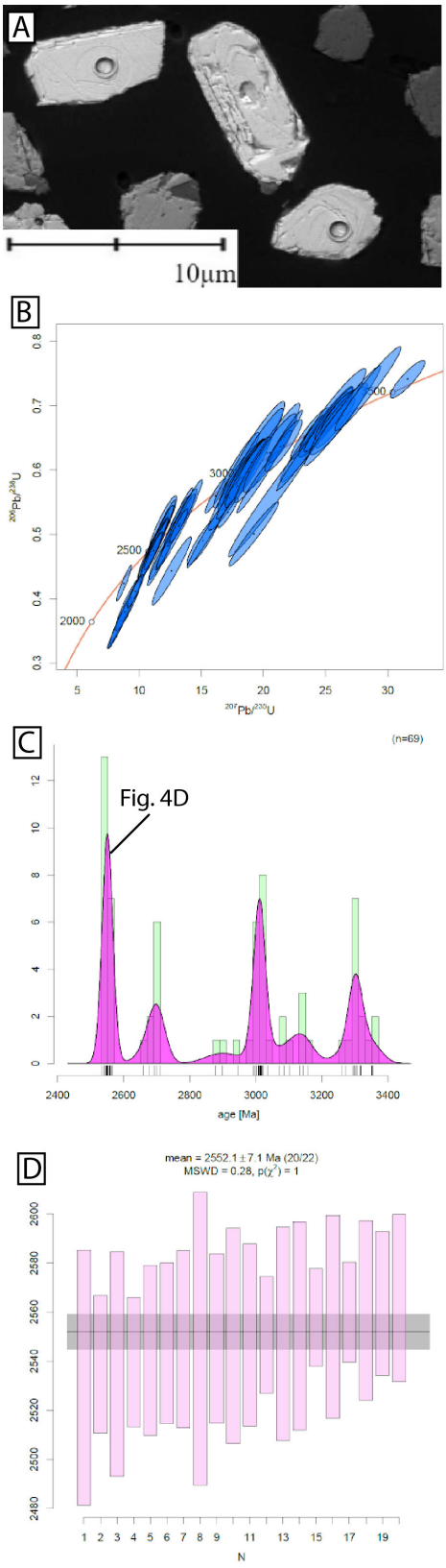

Figure 4. Geochronological data from the Boxelder Creek Quartzite. (A) BSE image of representative zircon grains with laser pits. (B) Wetherill concordia diagram showing the quality of the data that passed the filtering criteria. (C) Kernel density estimate plot showing age populations of detrital zircon grains in the Boxelder Creek Quartzite. (D) Weighted mean plot of the youngest detrital zircon dates in the Boxelder Creek Quartzite.

as a mylonitic sinistral transpression zone, which has also been documented in the LEG across strike of the BCQ (Allard & Portis, 2013).

Geochemistry and Mineralization

Transition metals such as nickel, zinc, copper, silver, and the accessory mineral pyrite are present within the BCQ and were likely mobilized by hydrothermal fluids. Pyrite is present alongside other detrital heavy metals in a mineral assemblage typical within paleoplacer deposits (e.g., Taylor & Anderson, 2010). The quartz pebble conglomerate lithology of the BCQ, along with its deposition within a clastic basin, and late Archean to early Proterozoic age, is observed among several paleoplacer deposits (Taylor & Anderson, 2010).

Sediment Provenance

The BCQ contains zircon age populations at ca. 2560, 2700, 3000, and 3300 Ma (Fig. 4C). The wide range of ages and implied sources for the BCQ is not unexpected, as it is hypothesized to be an alluvial fan and fluvial deposit sourced from the Wyoming craton (Gosselin, 1988; Redden & Dewitt, 2008). The Montana metasedimentary province and the Beartooth-Bighorn magmatic zone are subprovinces within the Wyoming craton with ages up to 3.5 Ga and contain detrital zircons dated up to 4 Ga (Mueller & Frost, 2006), making these a plausible source of the 3000 Ma and 3300 Ma zircon populations in the BCQ. Discordant values on the concordia diagram likely record lead loss from younger metamorphic events.

Discovery of ca. 2.56 Ga detrital zircons within the BCQ confirms that the LEG (2559 ± 6 Ma: McCombs et al., 2004) was a source for sediments within the BCQ. However, the lack of feldspars in thin section and the presence of ultramafic-derived materials spawns further questions. The absence of feldspars can be explained by distinctly different chemical weathering during the Archean. During this period, increased rainfall, higher temperatures, and higher atmospheric CO_2 (Hessler & Lowe, 2006) may have enhanced feldspar weathering relative to modern rates, leaving a quartz-dominated source for the BCQ. The abundance of heavier elements, including Cr (Fig. 3), suggests that the source terrain for the BCQ was not only granitic but likely included mafic-ultramafic sources as well. The presence of iron oxide clasts suggests that the Nemo Iron formation was a source alongside the LEG and other granitic material within the Wyoming craton.

Synthesis

This study establishes that the BCQ records basin formation between 2560 and 2480 Ma, aligning with the hypothesized breakup of the supercontinent Kenorland (McCombs et al., 2004). SEM and μXRF analyses reveal abundant chromium, nickel, titanium, zinc, iron, and smaller amounts of silver, copper, and rare earth elements. Exhumation and sedimentary recycling of mantle materials during this rifting event are possible sources of these elements. The prevalence of these transition metals could also suggest hydrothermal alteration linked to a rift environment (Redden, 1987; Taylor & Anderson, 2010). The Archean cratonic setting, age, lithology, and distinct mineralization of the BCQ support the hypothesis that the BCQ is a paleoplacer deposit (e.g., Redden, 1987). Ramsay diagrams show flattening as the primary strain, and sinistral kinematic indicators are abundant in outcrops and thin sections, indicating the BCQ deformed by sinistral transpressional shear. Fabrics in the BCQ are likely related to D3 in the Black Hills, which is shared with the LEG across strike of the shear zone (Allard & Portis, 2013). Conclusively, the data presented here support the interpretation that the BCQ formed in a rift environment that received detritus from the LEG and other parts of the Wyoming craton between 2560-2480 Ma. Following closure of the ocean basin in the Paleoproterozoic, left lateral transpression recorded in the BCQ is shared with the LEG, suggesting that the shear zone between them is a relatively minor structure that overprints a depositional relationship between the BCQ and LEG.

ACKNOWLEDGMENTS

This material is based upon work supported by the Keck Geology Consortium and the National Science Foundation under Grant No. 2050697. NSF 2215270 MRI: Acquisition of a low vacuum Scanning Electron Microscope (SEM) with EDS detector and STEM capability to advance research and undergraduate

research training. NSF 2320397 Equipment: MRI: Track 1 Acquisition of a Micro X-ray Fluorescence Spectrometer to Support Multidisciplinary Research and Education in the Upper Midwest. NSF-EAR 2050246 for support of the Arizona LaserChron Center. I want to thank my mentor, Dr. Trevor Waldien, for imparting extensive knowledge on all aspects of geology and preparing me for the professional world. Additionally, I express my appreciation to Dr. Paul Kelso and Dr. Derek Wright, professors at Lake Superior State, for their guidance, knowledge, and assistance.

REFERENCES

Allard, S. T., & Portis, D. H. (2013). Paleoproterozoic transpressional shear zone, eastern Black Hills, South Dakota: Implications for the late tectonic history of the southern Trans-HudsonOrogen. Rocky Mountain Geology, 48(2), 73-99.

Corrigan, David & Pehrsson, S. & Wodicka, N. & Dekemp, E. (2009). The Palaeoproterozoic Trans-Hudson Orogen: A prototype of modern accretionary processes. Geological Society, London, Special Publications. 327. 457–479. 10.1144/SP327.19.

Dahl, P. S., Hamilton, M. A., Wooden, J. L., Foland, K. A., Frei, R., McCombs, J. A., & Holm, D. K.(2006). 2480 Ma mafic magmatism in the northern Black Hills, South Dakota: a new link connecting the Wyoming and Superior cratons. Canadian Journal of Earth Sciences, 43(10),1579–1600.

Fossen, H. and Tikoff, B. (1998). Extended Models of Transpression and Transtension, and Application to Tectonic Settings. In: Holdsworth, R.E., Strachan, R.A. and Dewey, J.F., Eds., Continental Transpressional and Transtensional Tectonics. Geological Society of London, Special Publications, 135, 1–14.

Gehrels, G. (2010). U-Th-Pb analytical methods for Zircon. Arizona LaserChron Center. https://sites.google.com/laserchron.org/arizonalaserchroncenter/home.

Gosselin, D. C., Papike, J. J., Zartman, R. E., Peterman, Z. E., & Laul, J. C. (1988). Archean rocks of the Black Hills, South Dakota: Reworked basement from the southern extension of the Trans-Hudson orogen. Geological Society of America Bulletin, 100(8), 1244-1259.

Hessler, A. M., & Lowe, D. R. (2006). Weathering and sediment generation in the Archean: An integrated study of the evolution of siliciclastic sedimentary rocks of the 3.2Ga Moodies Group, Barberton Greenstone Belt, South Africa. Precambrian Research, 151(3–4), 185–210. https://doi.org/10.1016/j.precamres.2006.08.008

Karlstrom, K. E., & Houston, R. S. (1984). The Cheyenne Belt: Analysis of a Proterozoic suture in southern Wyoming. Precambrian Research, 25(4), 415-446.

Lisenbee, A. L. (1988). Tectonic history of the Black Hills uplift. AAPG Field trip guide to the Powder River Basin.

Ludwig, K. R. (2008). User's manual for Isoplot 3.70 (Vol. 4, pp. 76–80). Berkeley Geochronology Center Special Publication. https://doi.org/10.1111/j.1439-0272.2007.00823.x

McCombs, J.A., Dahl, P.S., & Hamilton, M.A. (2004). U–Pb ages of Neoarchean granitoids from the Black Hills, South Dakota, USA: implications for crustal evolution in the Archean Wyoming province. Precambrian Research, pp. 130, 161–184.

Nicosia, C. & Allard, S., (2014). Petrologic and Geochemical Characterization of Archean Gneisses in the Little Elk Terrane, Black Hills, South Dakota. Student Research and Creative Projects 2014-2015. 11.

Mueller, P.A. and C D Frost. 2006. The Wyoming Province: a distinctive Archean craton in Laurentian North America. Canadian Journal of Earth Sciences. 43(10): 1391-1397. https://doi.org/10.1139/e06-075

Redden, J.A. (1987)."Uraniferous Early Proterozoic Conglomerates of the Black Hills, South Dakota, USA." Geological Survey, Denver, Colorado, United States of America.

Redden, J. A., Peterman, Z. E., Zartman, R. E., DeWitt, E., (1990). U-Th-Pb geochronology and preliminary interpretation of Precambrian tectonic events in the Black Hills, South Dakota, in Lewry, J. F., and Stauffer, M. R., eds., The Early Proterozoic Trans-Hudson Orogen of North America: Geological Association of Canada Special Paper 37, p. 229–251.

Redden, J.A., and DeWitt, E. (2008). Maps Showing Geology, Structure, and Geophysics of the Central Black Hills, South Dakota: U.S. Geological Survey Scientific Investigations Map 2777, 44-p. pamphlet, 2 sheets, https://pubs.usgs.gov/sim/2777/ (accessed September 2023).

Taylor, R.D., and Anderson, E.D., (2010). Quartz-Pebble-Conglomerate Gold Deposits, Chapter P of Mineral Deposit Models for Resource Assessment, U.S. Geological Survey Scientific Investigations Report 2010–5070–P.

Van Boening, A. M., & Nabelek, P. I. (2008). Petrogenesis and tectonic implications of Paleoproterozoic mafic rocks in the Black Hills, South Dakota. Precambrian Research, 167(3-4), 363-376.

Vollmer, F.W., (2018). Automatic contouring of geologic fabric and finite strain data on the unit hyperboloid. Computers & Geosciences. http://dx.doi.org/10.1016/j.cageo.2018.03.006 .

Whitmeyer, S. J., & Karlstrom, K. E. (2007). Tectonic model for the Proterozoic growth of North America. Geosphere, 3(4), 220-259.

KECK Geology Consortium
Learning Science Through Research
Published by the Keck Geology Consortium
Short Contributions
Keck Geology Consortium
Volume 36
May 2024
doi: 10.18277/AKRSG.2024.36.10

U-PB ZIRCON DATING OF NEOARCHEAN ROCKS IN THE LITTLE ELK TERRANE, BLACK HILLS, SOUTH DAKOTA

ALEX ROBINSON, Pomona College
Project Advisor: Nicole Moore

ABSTRACT

Proterozoic metasedimentary rocks exposed in the core of the Black Hills, South Dakota, are generally interpreted to represent an ocean basin that closed during suturing of the Wyoming and Superior cratons. However, two Archean crystalline terranes are exposed at the western (Bear Mountain terrane) and eastern (Little Elk terrane) margins of the Black Hills Precambrian core and have an unclear relationship with the Proterozoic rocks. This study focuses on the Little Elk terrane, which has been mapped as two individual units: the Little Elk Granite and Biotite-Feldspar Gneiss. Previous work on the Little Elk terrane has argued either that these units are distinct entities based on structural features, or that they are variably deformed versions of the same granite body. We present U-Pb zircon data from each of the two units with the goal of determining whether the units are unique geologic features or have some genetic relationship. After LA-ICP-MS analyses on 315 zircons from each sample, the zircon U-Pb data were filtered for concordance (75-110%) and compared using concordia plots, kernel density estimate plots, weighted mean plots, and associated statistics. Both samples display significant discordance with a lower intercept at 0 Ma, suggesting simple Pb loss. The data that passed the filtering criteria display a normal unimodal distribution for each sample. The granite sample yielded a weighted mean age of 2545 ± 2.3 Ma (MSWD= 0.86, n= 139), and the gneiss sample yielded a weighted mean age of 2555 ± 2.3 Ma (MSWD= 0.7, n=149). Each sample contains few analyses older than ca. 2600 Ma. Given the normal distribution of the data, the under-dispersion of the analyses, and similarity between the mean ages, we interpret that the two units share an origin, and the Biotite-Feldspar Gneiss is a portion of the Little Elk Granite that experienced higher strain. Synthesizing our data with other recent work on the Little Elk Terrane reveals that a greenschist facies shear zone juxtaposes the western margin of the Little Elk Granite against Paleoproterozoic quartzites to the west. We interpret that the Biotite-Feldspar Gneiss represents the portion of that shear zone with Little Elk Granite protolith.

INTRODUCTION

The oldest rocks exposed in the Black Hills are Archean granites, and can be split into two terranes: the Little Elk in the east and the Bear Mountain in the west. Metasedimentary rocks are exposed between the two Archean granites, which have an unclear relationship to the Archean granites. Our focus here is on the Little Elk Terrane (LET), which consists of an Archean granite known as the Little Elk Granite (LEG), an Archean Biotite-Feldspar Gneiss (BFG), and a Proterozoic metasedimentary unit (Figure 1).

An early study of these units interpreted the BFG to be older than the LEG based on the presence of an older northeast-trending fabric only present in the BFG being crosscut by a younger northwest-trending fabric observed in both the BFG and LEG (Gosselin et al., 1988). However, this interpretation was challenged by more recent mapping that identified a northeast-trending fabric within the LEG and interpreted the shear fabrics, folding of the shear fabric, sinistral asymmetry, and grain-size reduction to argue for an east-side-up shear system responsible for both fabrics (Allard and Portis, 2013). The variation in the outcrop appearance of the LET, therefore, would be explained by strain-partitioning wihtin a single granitic body.

More recently, whole rock major and trace element

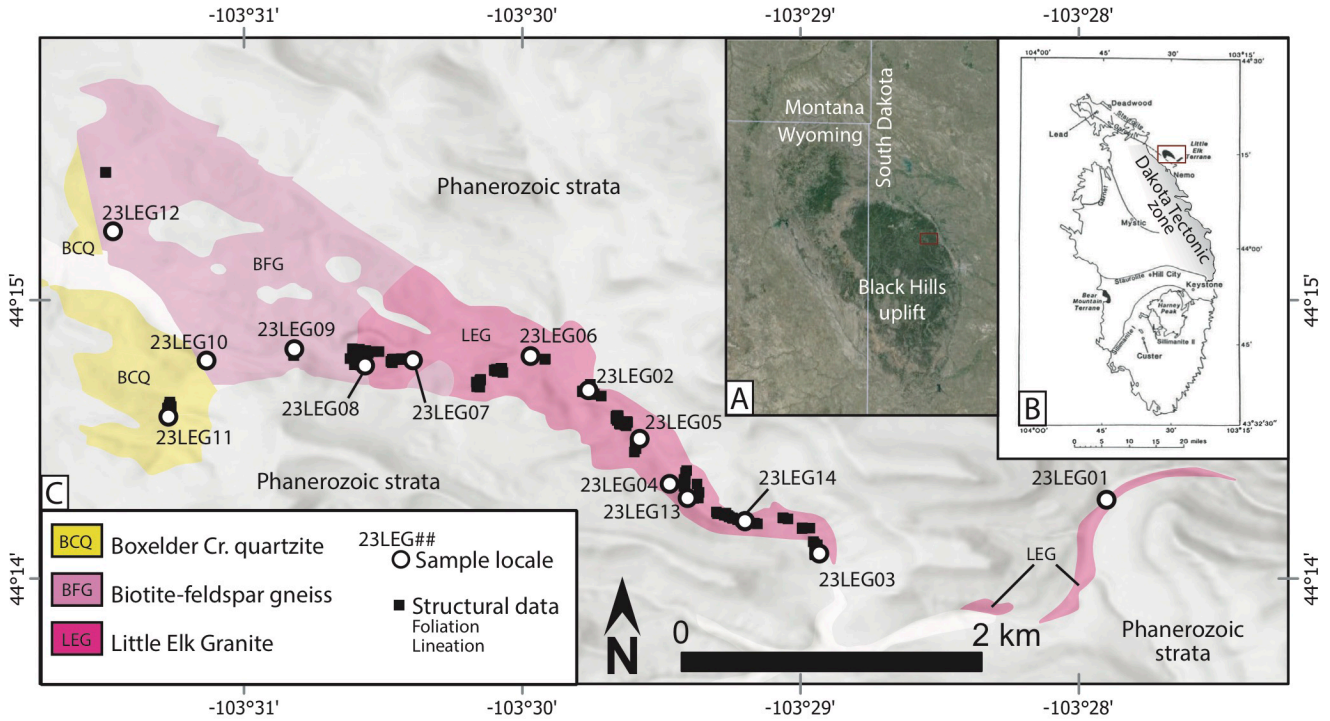

Figure 1. A) Google Earth image showing the location of the Black Hills (dark green region) relative to political borders. The Little Elk Creek area is outline by the red rectangle. B) Metamorphic isograd map of the Black Hills Precambrian core from Gosselin et al. (1988). Black shaded regions represent Archean rocks. The Little Elk Creek area is outline by the red rectangle. C) Geologic map of the Little Elk Creek area showing sample and structural data locations. Modified from Redden and DeWitt (2008).

geochemical data from both the LEG and BFG has been interpreted to record a single granitic origin for both units (Nicosia and Allard, 2014). This study aims to further test this interpretation through the use of U-Pb zircon dating to determine whether the BFG and LEG should continue to be regarded as separate units or if the BFG is a portion of the LEG that experienced intense deformation.

GEOLOGIC BACKGROUND

The Black Hills of South Dakota are commonly interpreted as a southern extension of the Trans-Hudson Orogeny, which involved the east-west convergence of the Superior and Wyoming cratons (Gosselin et al., 1988). The dome was uplifted during the Laramide Orogeny between ca 65 - 55 Ma, and exposes mainly Paleoproterozoic metasedimentary rocks, which are intruded by the ca. 1715 Ma Harney Peak Granite (Redden and Dewitt, 2008). These Paleoproterozoic metasedimentary are bound in the east and west by the Archean Little Elk and Bear Mountain terranes, respectively (Gosselin et al., 1988). The granites within these units are interpreted to have formed due to crustal accretion along the edge of the Wyoming craton (Gosselin et al., 1988).

The Little Elk terrane is exposed in Little Elk Creek approximately 8 km north of Nemo, South Dakota and has been interpreted as a fragment of the Wyoming Craton that has been displaced to the east (Gosselin et al., 1988). Rocks mapped as LEG are granitic and characterized by large (1-5 cm) K-feldspar crystals that are variably deformed by flattening and simple shear deformation (Figure 2; Allard and Portis, 2013). Rocks mapped as BFG exhibit highly variable texture ranging from gneissic banding to mylonitic textures (Figure 3). The dominant foliation in both units dips steeply (~60-80º) southwest (Redden and DeWitt, 2008). Previous geochronology on the Little Elk terrane targeted both the LEG and BFG and yielded multi-grain Thermal-Ionization Mass Spectrometry ages of 2549 ± 11 Ma (LEG) and single grain Secondary-Ion Mass Spectrometry ages of 2559 ± 6 Ma (LEG, 8 single grain analyses) and 2563 ± 6 Ma (BFG, 7 single grain analyses) (Gosselin et al., 1988; McCombs et al., 2004).

METHODS

Samples were collected from both the LEG and BFG, and then washed, crushed, sieved to less than 250 micrometers, and poured onto a Wilfley table to

Figure 2. Representative field photographs of the Little Elk granite at site 23LEG05 showing relatively undeformed granite (top) and gneissic texture that has been previously interpreted as a high strain zones in the granite (bottom).

remove light mineral grains. Magnetic grains were removed from the heavy grains using a hand magnet and Frantz LB-1 isodynamic separator. Lithium heteropolytungstate (LST) was used to separate the denser non-magnetic minerals, such as zircon, from the low-density, non-magnetic minerals. The zircon grains retrieved were mounted in 1" epoxy rounds, imaged using a scanning electron microscope, then dated using the Laser Ablation-Inductively Coupled Plasma Mass Spectrometry (LA-ICPMS) at the Arizona Laserchron Center.

Three well characterized zircon reference materials were mounted along with the sample grains, the Duluth Gabbro (FC1; 1009± 2 Ma), Sri Lanka (SL; 563.5 ± 2.3 Ma), and R33 (419.3 ± 0.4 Ma) (Gehrels et al., 2008). 315 analysis spots were handpicked manually on the TeamViewer platform for each sample. A 193 nm Photon Machine Excimer laser was then used to ablate the grains and isotopes were measured using a Thermo Element 2 HR ICP-MS. An uncertainty of ~2% for each analysis was achieved, and the data were then filtered with a concordance threshold of 75-110%. 142 data points from sample 23LEG05 and 151 data points from sample 23LEG10 passed the filtering criterion. With the filtered data, IsoplotR (Vermeesch, 2018) was used to create kernel density estimate (KDE) plots, calculate the weighted mean age of each sample, and plot data on a Wetherill Concordia diagram.

RESULTS

Using a Wetherill Concordia plot, the data from sample 23LEG05 (LEG) generally plot beneath the concordia curve, with the exception of six data points (Figure 4A). The KDE plot demonstrated a normal unimodal distribution with a slight positive skew (Figure 4B). The weighted mean of the 142 analyses yielded an age of 2545 ± 2.3 Ma, and a Mean Square Weighted Deviation (MSWD) of 0.86 (Figure 4C).

Using the same approach, the data from sample 23LEG10 (BFG) the data largely fell beneath the concordia curve, with the exception of 13 data points (Figure 5A), and one concordant date at ca. 1615 Ma. The KDE plot demonstrated a normal unimodal distribution (Figure 5B). The weighted mean of 151

Figure 3. Representative field photographs of the biotite-feldspar gneiss at site 23LEG10 showing mylonitic textuures (top) and gneissic texture that have been previously interpreted as variable deformation within the biotite-feldspar gneiss unit.

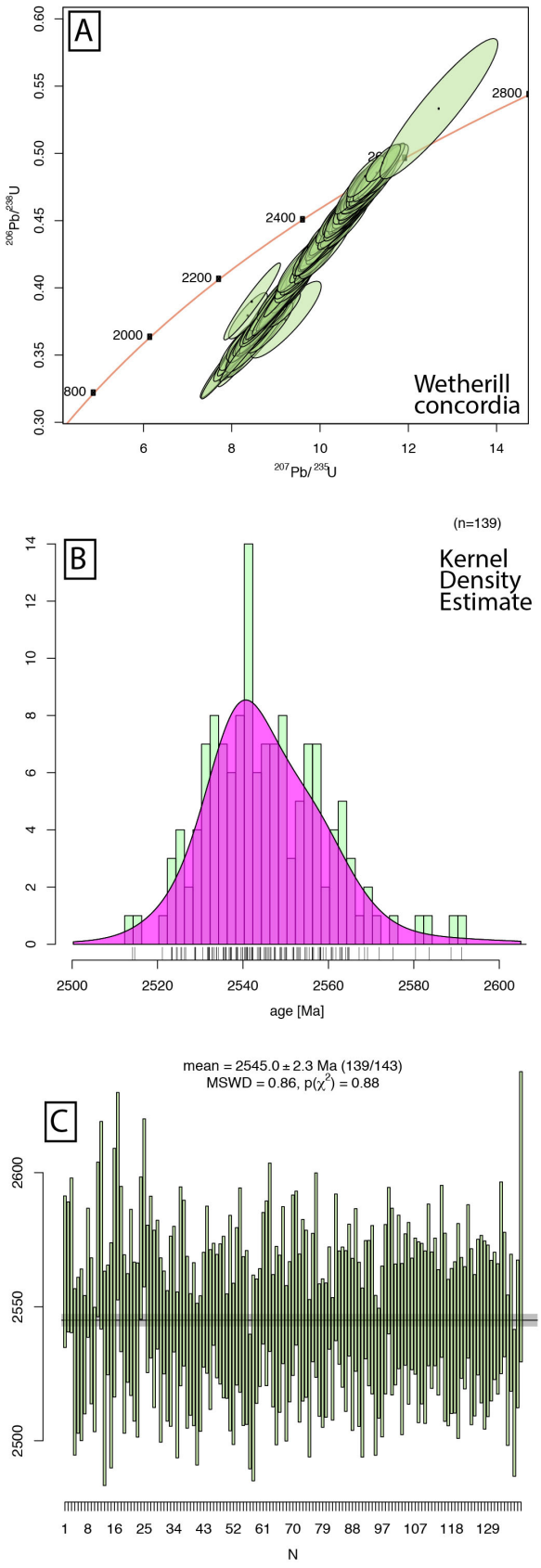

Figure 4. Geochronology plots for the granite sample (23LEG05). A) Wetherill Concordia plot of the data that passed the filtering criterion. B) Kernel Density Estimate plot (purple) and histogram (green). C) Weighted mean plot of the data that passed the filtering criterion and were not rejected by IsoplotR.

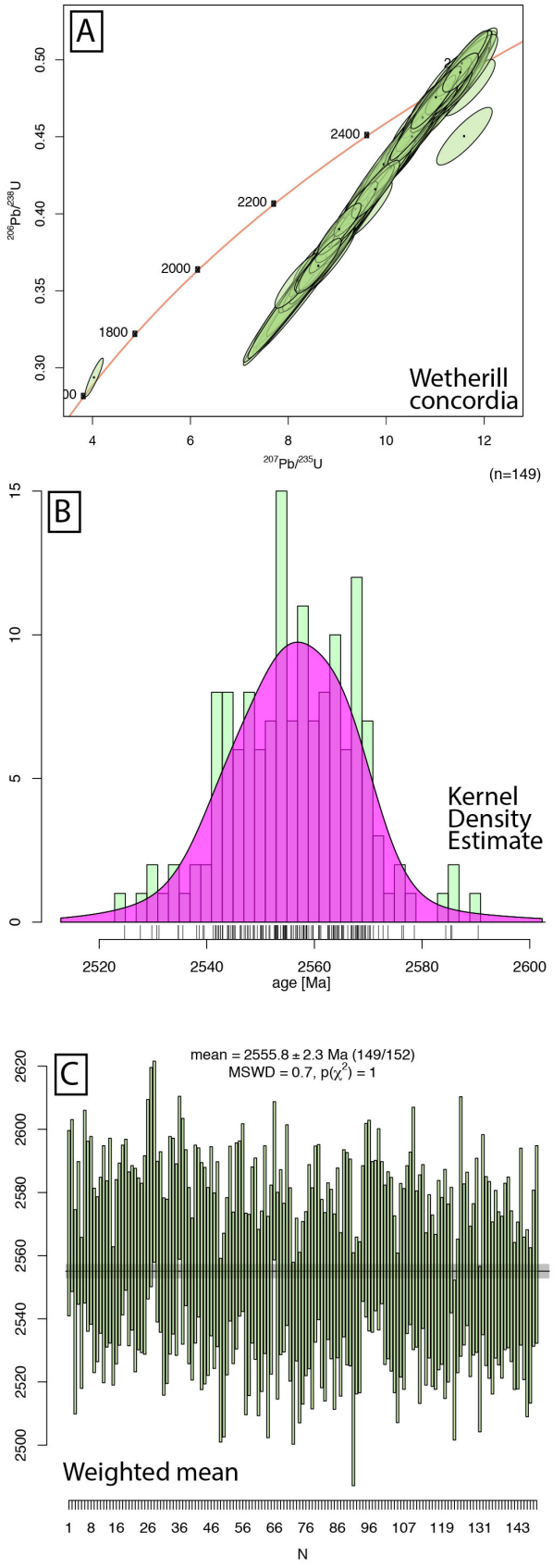

Figure 5. Geochronology plots for the gneiss sample (23LEG10). A) Wetherill Concordia plot of the data that passed the filtering criterion. B) Kernel Density Estimate plot (purple) and histogram (green). C) Weighted mean plot of the data that passed the filtering criterion and were not rejected by IsoplotR.

analyses yielded an age of 2555 ± 2.3 Ma, and an MSWD of 0.7 (Figure 5C).

DISCUSSION

The data show several similarities between samples 23LEG05 (LEG) and 23LEG10 (BFG). First, the MSWDs of both samples is less than 1, indicating that the analytical uncertainties are overestimated, and the data is underdispersed. However, the values near 1 suggest that the data can be interpreted as having a largely normal distribution, which is corroborated by the KDE plots (Figures 4 and 5). These interpretations together suggest that the U-Pb data from both samples can be interpreted as being derived from a single source. For the granite sample (23LEG05), this implies a simple zircon crystallization history related to emplacement of the pluton with minimal inheritance from the country rock. For the gneiss sample (23LEG10), this implies either that the quartzofeldspathic sedimentary protolith was derived from a single age source, or that the protolith is an igneous rock with a single zircon age population, such as the LEG. The ages of both samples, as calculated by the weighted mean plot, are comparable to previous age determinations for the LEG, which were 2549 ± 11 Ma (Gosselin et al., 1988) and 2559 ± 6 Ma (McCombs et al., 2004).

The weighted mean ages from both samples contribute additional information regarding potential linkages between the two samples. The weighted mean age of the granite (2545 ± 2.3 Ma) is slightly younger than that of the gneiss sample (2555 ± 2.3 Ma), which could imply that the gneiss is older than the granite. However, the LEG and BFG are nearly identical in whole rock major and trace element geochemical data (Nicosia and Allard, 2014), implying that the units are either variably deformed versions of the same granite body, or that the BFG was metamorphosed from a sedimentary protolith that was derived from the LEG and is therefore younger. We interpret the similarity in the weighted mean ages (Figures 4 and 5), and field observations suggesting a systematic intensification in deformation features from the LEG into the BFG unit (Fry et al., 2024), and geochemical data (Nicosia and Allard, 2014) together to record that the BFG unit is a portion of the LEG that experienced higher strain than exposures to the east that have been mapped as LEG.

Synthesizing the new geochronology data and associated interpretations with other work on the Little Elk Terrane reveals that the BFG unit occupies the position between the LEG in the east and Boxelder Creek conglomerate in the west (Figure 1). Deformation features in the Boxelder Creek conglomerate suggest that it was sheared along the western side of the BFG unit by a left-lateral shear zone (Obringer et al., 2024). We interpret that this evidence of ductile deformation along the western margin of the BFG unit and within the BFG unit that wanes to the east into the LEG (Fry et al., 2024) to record that the BFG unit is best interpreted as the portion of the LEG that was involved in the shear zone between relatively undeformed LEG and the Boxelder Creek conglomerate.

CONCLUSIONS

Previous research in the Black Hills mapped the BFG and LEG as two separate units, based on structural data that differentiated the two. More recent studies use structural and geochemical evidence to argue that the two units formed from a single granitic body, and that the differences in appearance are due to strain partitioning. After dating two samples from the Little Elk Terrane – one from the BFG and one from the LEG – using U-Pb zircon dating techniques for both samples, the mean ages of each sample were found to be very similar. The adjacency of the two ages in addition to field relationships supports the interpretation of a single origin for the two units. The BFG can be interpreted to be part of a greenschist facies shear zone along the western margin of the LEG, with the protolith being the LEG.

ACKNOWLEDGEMENTS

This material is based upon work supported by the Keck Geology Consortium and the National Science Foundation under Grant No. 2050697. A special thank you to my project director and advisor Trevor Waldien, and my home institution advisor Nicole Moore. I would also like to that the other students on the project with me for teaching me new things and making the research experience enjoyable, as well as

the Keck Geology Consortium for the great learning opportunity. Field work was completed in the Black Hills of South Dakota, the ancestral homelands of the Oceti Sakowin peoples.

REFERENCES

Allard, S.T., & Portis, D.H., 2013, Paleoproterozoic transpressional shear zone, eastern Black Hills, South Dakota: Implications for the late tectonic history of the southern Trans-Hudson Orogen. Rocky Mountain Geology, v. 48, no. 2, p. 73-99.

Fry, L.T., Wetzel, L.R., and Waldien, T.S., 2024, Kinematic analysis of Little Elk Granite shear zones, Black Hills South Dakota: Geological Society of America Abstracts with Programs. Vol. 56, No. 4.

Gehrels, G. E., Valencia, V. A., & Ruiz, J., 2008, Enhanced precision, accuracy, efficiency, and spatial resolution of U-Pb ages by laser ablation–multicollector–inductively coupled plasma–mass spectrometry. Geochemistry, Geophysics, Geosystems, 9(3).

Gosselin, D. C., and four others, 1988, Archean rocks of the Black Hills, South Dakota: Reworked basement from the southern extension of the Trans-Hudson Orogen: Geological Society of America Bulletin, v. 100, p. 1244– 1259.

Gosselin, D.C., and four others, 1990, Geochemical and origin of Archean granites from the Black Hills, South Dakota; Canadian Journal of Earth Sciences, v. 27, p. 57 - 71.

Nicosia, C., and Allard, S.T., 2014, Petrologic and geochemical characterization of Archean gneisses in the Little Elk Terrane, Black Hills, South Dakota: Student Research and Creative Projects 2014-2015.

Obringer, W., Waldien, T., & Kelso, P., 2024, Elucidation of an Undefined Relationship: A Study of the Little Elk Granite and Boxelder Creek Quartzite as to Decipher Precambrian Basin Development in the Black Hills, SD. Vol 56, Geological Society of America Abstracts with Programs.

Redden, J. A., and DeWitt, E., 2008, Maps showing geology, structure, and geophysics of the central Black Hills, South Dakota: US Geological Survey.

Vermeesch, P., 2018, IsoplotR: a free and open toolbox for geochronology. Geoscience Frontiers, v.9, p.1479-1493, doi: 10.1016/j.gsf.2018.04.001.

KECK Geology Consortium
Learning Science Through Research
Published by the Keck Geology Consortium
Short Contributions
Keck Geology Consortium
Volume 36
May 2024
doi: 10.18277/AKRSG.2024.36.11

INTEGRATED STRATIGRAPHIC AND PALEOENVIRONMENTAL STUDY OF THE MIDDLE-LATE DEVONIAN CARBONATE TO BLACK SHALE TRANSITION IN THE MICHIGAN BASIN

JAMES J. ZAMBITO IV, Beloit College
PETER J. VOICE, Western Michigan University

INTRODUCTION

Devonian climate trends have long been studied within the context of biological change. For example, the end-Devonian glaciation is typically thought to be related to CO_2-drawdown due to the evolution of forests during the Middle-Late Devonian (Algeo and Scheckler, 1998, and references therein). However, more recent paleoclimate reconstructions indicate that the Devonian climate story is more complex. Even though it has now been shown that the Middle Devonian was cooler than the end-Devonian and glacio-eustatic sea-level dynamics operated during the Middle Devonian (Fig. 1; Elrick et al., 2009, 2022; Joachimski et al., 2009), only Late and end-Devonian evidence for glaciation has been documented (Ettensohn et al., 2020). In order to better understand these long-term patterns, a current focus within the Devonian research community is the study of the repeated, short-duration, globally-recognized events that resulted in marine anoxia, extinctions, and carbon-cycle perturbations (Fig, 1; House, 2002; Becker et al., 2020; Brett et al., 2020), especially within the context of local environmental change and tectonics (Zambito et al., 2012; Chen et al., 2021).

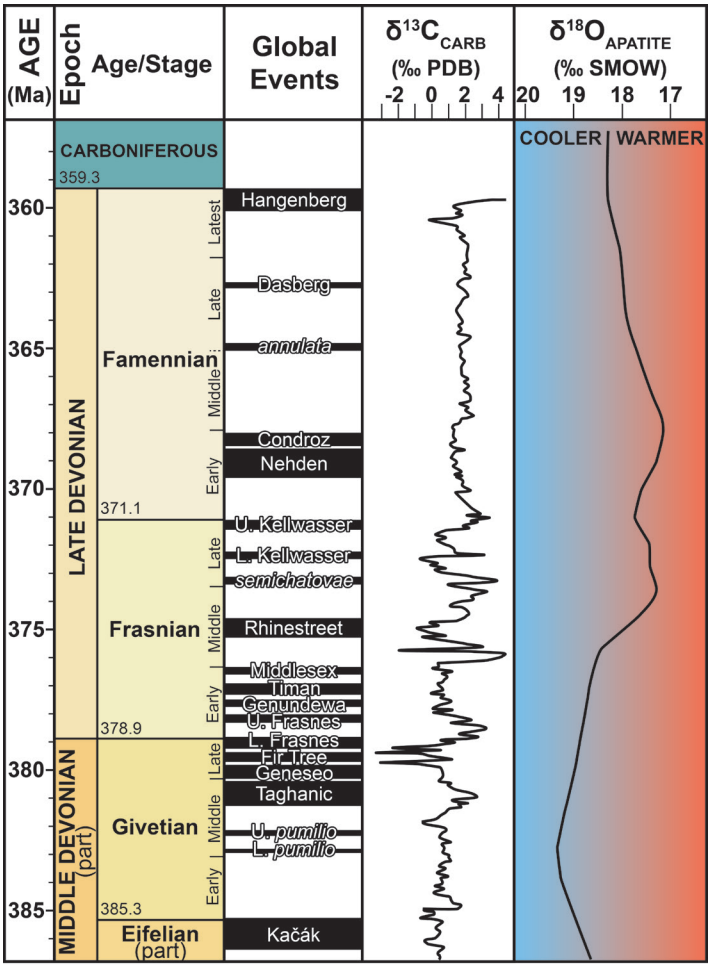

Figure 1. Middle (in part) and Late Devonian Time Scale showing the timing and duration of global events, carbonate carbon isotopic excursions, and generalized paleoclimate trends based on oxygen isotopic analysis of conodont apatite; Adapted from Becker et al., 2020.

This Keck Consortium project is focused on characterizing Middle-Late Devonian lithologies, geochemistry, and distribution of facies in the Michigan Basin in order to develop a local spatial and temporal framework within which future event stratigraphy can be undertaken. During this time interval, the overall depositional system transitioned from carbonate-dominated strata of the Traverse Group to siliciclastic-dominated strata, including organic-rich black shale, in the Squaw Bay Formation (herein "Squaw Bay Formation", a proposal for a formal name change to Birdsong Bay Formation is forthcoming, pers. comm. N. Stamm, 2024) and overlying Antrim Shale Formation and Ellsworth Shale Formation (Fig.

2).

GEOLOGIC SETTING

The Michigan Basin is one of three depocenters in the northeast and upper Midwest United States, the others being the foredeep Appalachian Basin adjacent to siliciclastic input from the Acadian Orogeny and the intracratonic Illinois Basin (Fig. 3). The intracratonic Michigan Basin contains ~5 km of strata that accumulated across a nearly-circular ~400 km diameter depocenter that is centered in the present-day state of Michigan (Gutschick and Sandberg, 1991a; Howell and Van Der Pluijm, 1999). There is little evidence for structural disruption in the Michigan Basin (Howell and van der Pluijm, 1999). Through the Middle to Late Devonian, the subsidence style in the Michigan Basin changed from basin-centered to eastward tilting (Howell and van der Pluijm, 1999), presumably due to substantial and renewed Acadian tectonism during the Middle-Late Devonian (see Ver Straeten, 2010, and references therein for detailed descriptions of Acadian tectophases). Along with these basin morphology changes, the Michigan Basin also shifted from carbonate-dominated deposition in the Middle Devonian Traverse Group to siliciclastic and organic matter dominated deposition in the Late Devonian (Fig. 2).

In the northern Appalachian Basin (New York State), Devonian strata are well exposed in an outcrop belt that is perpendicular to depositional strike of siliciclastic sediment input from the Acadian Mountains (Fig. 3); these strata are therefore not only better-studied than contemporaneous strata in the Michigan Basin, but New York strata are the type examples for which many global events are named (Fig. 1). However, the Appalachian Basin was also tectonically active at this time and local environmental change associated with basin subsidence and sediment supply often overprints global environmental changes (Fig. 1; Zambito et al., 2012). Conversely, the Middle-Upper Devonian transition from Traverse Group shallow marine carbonates through the transitional "Squaw Bay Formation" to the Antrim Formation anoxic black shale in the Michigan Basin is unlikely the result of continental-margin tectonism (Fig. 3), and more accurately reflects the signal of global

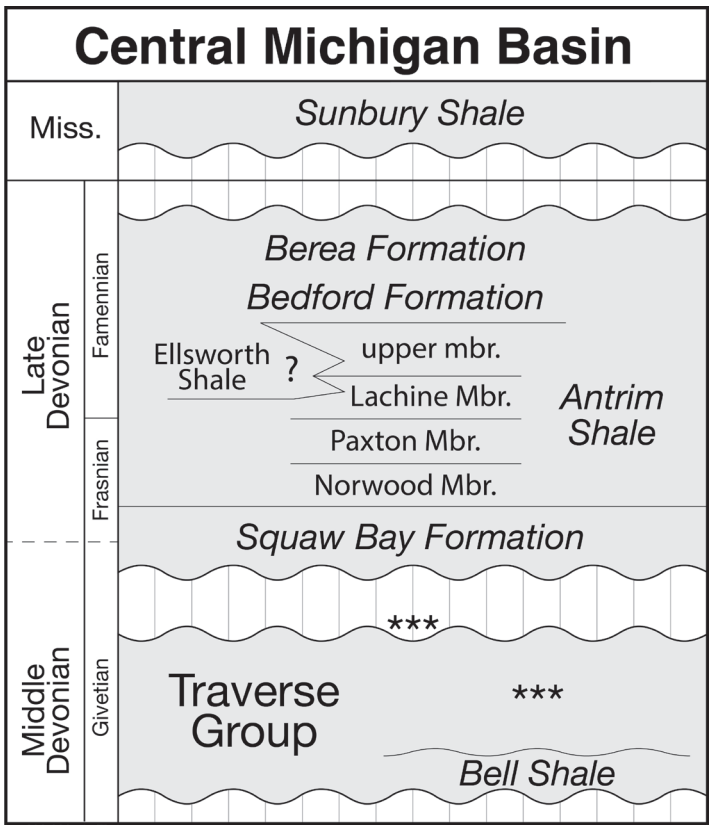

*Figure 2. Generalized lithostratigraphy of the Middle-Late Devonian stratigraphic succession, including the stratigraphic ranges of the cores studied (see Table 1; after Bultynck, 1976; Ells, 1978, 1979; Gutschick and Sandberg, 1991; Catacosinos et al., 2000; Wylie and Huntoon, 2003; Currie, 2016; Narkiewicz and Bultynck, 2016); *** Catacosinos et al. (2000) does not differentiate the Traverse Group in the subsurface, but see Wylie and Huntoon (2003) and Gutschick and Sandberg (1991a,b) for formation-level correlations in the subsurface and the interpretation that the age of the Traverse Group in the subsurface likely includes strata that are both older and younger than the strata of the Traverse Group at the Michigan Basin Margins.*

environmental change (Fig. 1). The studies discussed herein will provide a critical stratigraphic and paleoenvironmental framework within which future workers can identify global events in the Michigan Basin.

This project builds upon a long history of lithostratigraphic study and basin-wide correlation, though there is recognition that the stratigraphic nomenclature originally defined with the limited outcrops available at the northern basin margin is not easily applied to the subsurface (Fig. 2; Ehlers and Kesling, 1970; Kesling et al., 1974, 1976; Catacosinos et al., 2000; Wylie and Huntoon, 2003; Swezey et al., 2015). Furthermore, since Michigan Basin type-section outcrops are rare, stratigraphically short, and generally lack exposure of formation and member

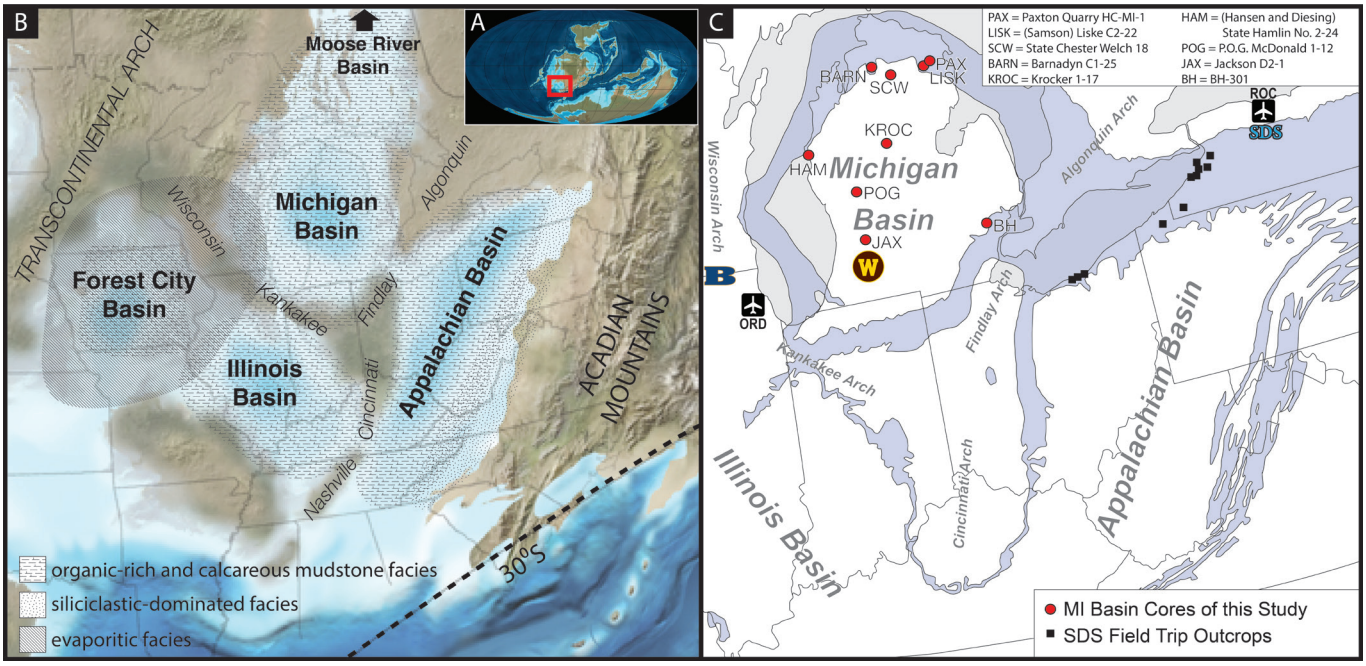

Figure 3. A) Devonian paleogeography (location of part B in red box). B) Paleogeography and generalized depositional settings of the Eastern and Midwest United States during the Middle-Upper Devonian. C) Outcrop belt (bluish gray) of Devonian strata in the study region (after Reed, 2004) and the location of Michigan Basin cores and SDS Field Trip stops examined as part of this study. Also shown is the location of sites where Keck research took place (Beloit College [B] and MGRRE at Western Michigan University [W]), the airports utilized, and the location of the SDS Meeting. Paleogeographic maps adapted from Blakey (2013).

contacts (Zambito and Voice, personal field notes), and a variety of cores exist as a result of active oil and gas exploration (Swezey et al., 2015), this project focuses on the study and sampling of the extensive drill core available at the Michigan Geological Repository for Research and Education (MGRRE) at Western Michigan University (see Figures 3 and 4 for details).

RESEARCH AND RESULTS

This Keck Consortium project involved research on core and outcrop as well as laboratory work (Fig. 3). The research group assembled at O'Hare International Airport and drove to the Michigan Geological Repository for Research and Education (MGRRE) at Western Michigan University for a project overview and to study and sample drill core. Then, the group traveled to Beloit College to conduct laboratory analyses. After initial laboratory work was complete, the research group drove to Cleveland where they joined a field meeting of the International Union of Geosciences Subcommission on Devonian Stratigraphy (SDS) to study the geologically contemporaneous Appalachian Basin Middle-Upper Devonian strata found in outcrops along the Lake Erie shoreline and creeks in Ohio, Pennsylvania, and New York State. This provided the opportunity to directly compare Michigan Basin subsurface observations to Devonian Global Event type example strata. Finally, this summer research experience culminated in a group poster presentation at the Subcommission on Devonian Stratigraphy Annual Meeting where students received constructive criticism from disciplinary experts on their project and preliminary data (Zambito et al., 2023). Students then departed from Rochester International Airport. Subsequent to the summer experience and after an academic year of research, group members presented the results of their research at the 2024 Joint North-Central and South-Central Section Meeting of the Geological Society of America on 21-23 April 2024 in Springfield, MO (Barker-Edwards et al., 2024; Giehler et al., 2024; Johnson et al., 2024; O'Bryan et al., 2024; Truong et al., 2024; Wiesner et al., 2024; Winget et al., 2024).

The lithostratigraphic successions studied, and the cores utilized in this project, are outlined in Figures 3 and 4 as well as Table 1. Most of the research conducted was on three cores: the basin margin State Chester Welch #18 core, the more basinal Krocker 1-17 core, and the Paxton Quarry core which was drilled at the stratigraphically important locality studied by Gutschick and Sandberg (1991b);

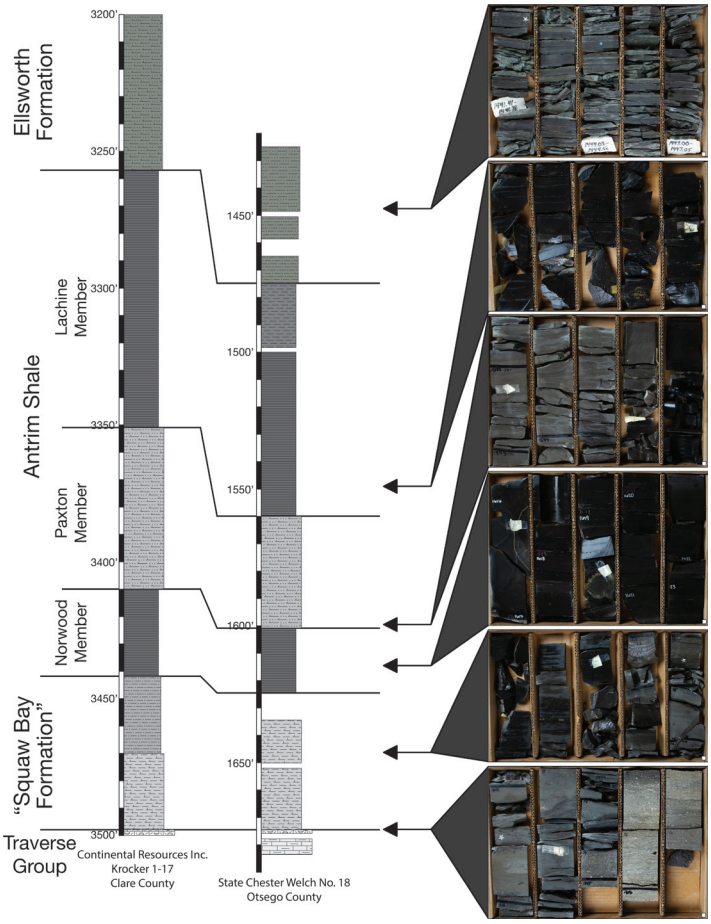

Figure 4. Lithostratigraphy and core photographs of the main studied successions. Lithostratigraphic columns for the Krocker 1-17 and State Chester Welch #18 cores are shown and correlated. Representative photographs of lithology for each unit studied are shown from the State Chester Welch #18 core.

unfortunately, the Paxton Quarry core was heavily sampled by previous researchers and therefore was not as ideal for geochemical sampling and the quarry itself has since flooded after decommissioning and is inaccessible. For this reason, most of the student projects undertaken focused on the State Chester Welch #18 and Krocker 1-17 cores.

The strata studied are shown in Figures 2 and 4. The base of the studied succession is the Traverse Group. Unconformably overlying the Traverse Group is the "Squaw Bay Formation," which transitions from a fossiliferous calcareous shale to a carbonaceous shale where it has a gradational contact with the black shale of the Norwood Member, the basal unit of the overlying Antrim Formation (Antrim Shale). The Norwood Member is relatively sharply overlain by the Paxton Member, a variably dolomitic, fossil-bearing gray mudstone. A sharp contact occurs between the Paxton and overlying Lachine Member, which is a black shale. The black shale of the Lachine gradationally transitions into the overlying Ellsworth Formation, which consists of interbedded light green-gray siltstone and dark gray to gray shale; the Ellsworth is the youngest unit observed in the cores studied. Regional gamma log correlation (Currie, 2016) suggests that the Ellsworth is overlain by the black shale of the upper member of the Antrim Formation across the basin, which is overlain by shale and sandstone of the Bedford and Berea formations and the Mississippian Sunbury Shale.

The research of **Winget** (this volume) was focused on the Traverse Group, specifically trying to identify the lithostratigraphic units described originally from scattered outcrops across the northern part of the lower peninsula within the cores studied herein. Winget (this volume) concluded that the strata of the Traverse Group in the State Chester Welch #18 core were most similar to previously collected hand samples from the type section of the Thunder Bay Formation.

The contact of the Traverse Group and overlying "Squaw Bay Formation" was studied petrographically and mineralogically by **O'Bryan** (this volume). Petrographic and scanning electron microscopy (SEM) and x-ray fluorescence scanning (μXRF) was used to decipher a complex paragenetic sequence of both early and late diagenetic mineralization (O'Bryan, this volume).

The lithology and paleontology of the "Squaw Bay Formation" was studied in detail by **Wiesner** (this volume). This study is an important step in the ongoing work of the USGS and the Michigan Geological Survey to better understand the subsurface expression of this unit in order to revise its inappropriate and hurtful name as well as lithologic characterization.

In order to gain a baseline understanding of detrital input into the Michigan Basin during the deposition of the "Squaw Bay" and Antrim formations to aid in interpretation of future organic carbon isotopic data within a global event stratigraphy framework (Fig. 1), **Giehler** (this volume) and **Gugino** (this volume) undertook chemostratigraphic analysis of the Krocker 1-17 and State Chester Welch #18 cores, respectively. Elemental proxies for detrital input were used to

Table 1. Sample Locations

NUMBER	NAME	LATITUDE	LONGITUDE
1	Paxton Quarry HC-MI-1	45.05346	-83.62996
2	(Samson) Liske C2-22	44.97927	-83.69924
3	State Chester Welch No. 18	44.90914	-84.49979
4	Barnadyn C1-25	45.05084	-84.87411
5	Krocker 1-17	43.95828	-84.82680
6	Hansen and Diesing State Hamlin No. 2-24	44.02325	-86.40055
7	Peninsular Oil and Gas McDonald 1-12	43.35304	-85.56642
8	Jackson D2-1	42.67055	-85.55842
9	BH-301	NA; Wayne County, Michigan	

constrain siliciclastic input into the basin, and how it changes across the basin and up section, through the "Squaw Bay" and the Antrim formations (Giehler, this volume; Gugino, this volume).

Another tool with implications for detrital influx as well as intra- and extrabasinal correlation is magnetic susceptibility. **Barker-Edwards** (this volume) utilized magnetic susceptibility of the "Squaw Bay" and Antrim formations to constrain detrital influx locally as well as correlate the strata of the Michigan Basin to a contemporaneous succession in the Illinois Basin that was studied previously.

The Ellsworth Formation is probably the least understood of the stratigraphic units addressed as part of this project. **Johnson** (this volume) undertook a detailed lithostratigraphic, chemostratigraphic, and mineralogical characterization of this unit in multiple cores, complemented by a high-resolution quantification and statistical analysis of Ellsworth Delta sedimentation (**Quiroz**, this volume).

Detailed study of multiple cores as part of this project, and a better understanding of the Michigan Basin stratigraphic framework (Fig. 2), meant that regional geologic mapping could also be revised. **Truong** (this volume) constructed a geologic map of Alpena County, Michigan that used lithologic observations from core to inform interpretation of driller's logs. Importantly, Truong (this volume) demonstrates that subdivisions of the Antrim Formation can be mapped confidently in the subsurface of the map area.

SUMMARY

The following short contributions outline new research endeavors to better understand the lithologies, geochemistry, and distribution of facies in the Michigan Basin. The results provide critical revisions to our collective understanding of the spatial and temporal stratigraphic framework of the Middle-Late Devonian Michigan Basin within which future research can be undertaken.

ACKNOWLEDGEMENTS

This material is based upon work supported by the Keck Geology Consortium and the National Science Foundation under Grant No. 2050697. Additional funding was provided by the Department of Geology at Beloit College. We are grateful for the time and insight provided by W. Harrison, L. Harrison, and J. Trout at MGRRE. Their extensive experience with the core collection facilitated the choice of cores to use and ensured the success of this project. J. Trout facilitated sampling the cores, working with the students to select intervals to sample and assisting with cutting billets and collecting samples. L. Harrison provided a welcoming environment for our students, making sure that they had everything they needed for working at MGRRE. W. Harrison provided insights in the geology of the Middle and Upper Devonian stratigraphy of the basin from his long experience with Michigan Basin rocks.

REFERENCES

Algeo, T.J., and Scheckler, S.E., 1998, Terrestrial-marine teleconnections in the Devonian: links between the evolution of land plants, weathering processes, and marine anoxic events (D. J. Beerling, W. G. Chaloner, & F. I. Woodward, Eds.): Philosophical Transactions of the Royal Society of London. Series B: Biological Sciences, v. 353, p. 113–130, doi:10.1098/rstb.1998.0195.

Barker-Edwards, T., Voice, P.J., and Zambito IV, J.J., 2024, Magnetic susceptibility of the Late Devonian Antrim Shale of the Michigan Basin: Geological Society of America Abstracts with Programs, v. 56, n. 3, doi: 10.1130/abs/2024NC-398895

Becker, R.T., Marshall, J.E.A., Da Silva, A.-C., Agterberg, F.P., Gradstein, F.M., and Ogg, J.G., 2020, The Devonian Period, in Gradstein, F.M., Ogg, J.G., Schmitz, M.D., and Ogg, G.M. eds., Geologic Time Scale 2020, Elsevier, p. 733–810, doi:10.1016/B978-0-12-824360-2.00022-X.

Blakey, R.C., 2013, Deep Time MapsTM – Maps

of Ancient Earth, https://deeptimemaps.com/ (accessed April 2022)

Brett, C.E., Zambito, J.J., McLaughlin, P.I., and Emsbo, P., 2020, Revised perspectives on Devonian biozonation and environmental volatility in the wake of recent time-scale revisions: Palaeogeography, Palaeoclimatology, Palaeoecology, v. 549, p. 108843, doi:10.1016/j.palaeo.2018.06.037.

Bultynck, P., 1976, Comparative Study of Middle Devonian Conodonts from Northern Michigan (U.S.A.) and the Ardennes (Belgium-France): The Geological Association of Canada Special Paper Number 15, p. 119–141.

Catacosinos, P.A., Harrison, W.B., Reynolds, R.F., Westjohn, D.B., and Wollensak, M.S., 2000, Stratigraphic Nomenclature For Michigan: Michigan Dept. of Environmental Quality Geological Survey Divisions and Michigan Basin Geological Society, http://www.dnr.state.mi.us/spatialdatalibrary/pdf_maps/geology/Stratigraphic_Column_Map.pdf.

Chen, B., Ma, X., Mills, B.J.W., Qie, W., Joachimski, M.M., Shen, S., Wang, C., Xu, H., and Wang, X., 2021, Devonian paleoclimate and its drivers: A reassessment based on a new conodont δ18O record from South China: Earth-Science Reviews, v. 222, p. 103814, doi:10.1016/j.earscirev.2021.103814.

Currie, B.J., 2016, Stratigraphy of the Upper Devonian-Lower Mississippian Michigan Basin: Review and Revision with an Emphasis on the Ellsworth Petroleum System [M.S. Thesis]: Western Michigan University, 148 p., https://scholarworks.wmich.edu/masters_theses/721/.

Ehlers, G.M., and Kesling, R.V., 1970, Devonian Strata of Alpena and Presque Isle Counties, Michigan: Museum of Paleontology, The University of Michigan, Miscellaneous Papers, 131 p., https://hdl.handle.net/2027.42/48601.

Ells, G.D., 1978, Stratigraphic Cross Sections Extending from Devonian Antrim Shale to Mississippian Sunbury Shale in the Michigan Basin: Michigan Department of Natural Resources, Geological Survey Division Michigan Department of Natural Resources, Geological Survey Division, Topical Report FE-2346-30, 208 p., https://doi.org/10.2172/6275903

Ells, G.D., 1979, Stratigraphic Cross Sections Extending from Devonian Antrim Shale to Mississippian Sunbury Shale in the Michigan Basin: Michigan Department of Natural Resources, Geological Survey Division Michigan Department of Natural Resources, Geological Survey Division, Report of Investigation 22, 186 p.

Elrick, M., Berkyová, S., Klapper, G., Sharp, Z., Joachimski, M., and Frýda, J., 2009, Stratigraphic and oxygen isotope evidence for My-scale glaciation driving eustasy in the Early–Middle Devonian greenhouse world: Palaeogeography, Palaeoclimatology, Palaeoecology, v. 276, p. 170–181, doi:10.1016/j.palaeo.2009.03.008.

Elrick, M., Gilleaudeau, G.J., Romaniello, S.J., Algeo, T.J., Morford, J.L., Sabbatino, M., Goepfert, T.J., Cleal, C., Cascales-Miñana, B., and Chernyavskiy, P., 2022, Major Early-Middle Devonian oceanic oxygenation linked to early land plant evolution detected using high-resolution U isotopes of marine limestones: Earth and Planetary Science Letters, v. 581, p. 117410, doi:10.1016/j.epsl.2022.117410.

Ettensohn, F.R., Clayton, G., Lierman†, R.T., Mason, C.E., Krause, F.F., DeBuhr, C., Brackman, T.B., Anderson, E.D., Dennis, A.J., and Pashin, J.C., 2020, Late Devonian lonestones, diamictites, and coeval black shales from the Appalachian Basin: Discerning relationships and implications for Late Devonian Appalachian history and glacially driven seafloor anoxia, in The Appalachian Geology of John M. Dennison: Rocks, People, and a Few Good Restaurants along the Way, Geological Society of America, p. 67–88, doi:10.1130/2020.2545(05).

Giehler, M.C., Gugino J.P., Voice, P.J., and Zambito IV, J.J., 2024, Lithological and geochemical analysis of the Middle to Upper Devonian Antrim Shale, Michigan Basin: insights into detrital input dynamics: Geological Society of America Abstracts with Programs, v. 56, n. 3, doi: 10.1130/abs/2024NC-398770

Gutschick, R.C., and Sandberg, C.A., 1991a, Late Devonian history of Michigan Basin, in Geological Society of America Special Papers, Geological Society of America, v. 256, p. 181–202, DOI: 10.1130/SPE256-p181.

Gutschick, R.C., and Sandberg, C.A., 1991b, Upper Devonian biostratigraphy of Michigan Basin, in Geological Society of America Special Papers, Geological Society of America, v. 256, p. 155–180, doi:10.1130/SPE256-p155.

House, M.R., 2002, Strength, timing, setting and cause of mid-Palaeozoic extinctions: Palaeogeography, Palaeoclimatology, Palaeoecology, v. 181, p. 5–25, doi:10.1016/S0031-0182(01)00471-0.

Howell, P.D., and Van Der Pluijm, B.A., 1999, Structural sequences and styles of subsidence in the Michigan basin: Geological Society of America Bulletin, v. 111, p. 974–991, doi:10.1130/0016-7606(1999)111<0974:SSASOS>2.3.CO;2.

Joachimski, M.M., Breisig, S., Buggisch, W., Talent, J.A., Mawson, R., Gereke, M., Morrow, J.R., Day, J., and Weddige, K., 2009, Devonian climate and reef evolution: Insights from oxygen isotopes in apatite: Earth and Planetary Science Letters, v. 284, p. 599–609, doi:10.1016/j.epsl.2009.05.028.

Johnson, I.R, Quiroz, C.J., Voice, P.J., and Zambito IV, J.J., 2024, Characterizing the Ellsworth Formation of the Michigan Basin using lithostratigraphy and chemostratigraphy: Geological Society of America Abstracts with Programs, v. 56, n. 3, doi: 10.1130/abs/2024NC-398769

Kesling, R.V., Johnson, A.M., and Sorensen, H.O., 1976, Devonian Strata of the Afton-Onaway Area, Michigan: Papers in Paleontology, Museum of Paleontology, The University of Michigan, v. 17, p. 1–149, https://hdl.handle.net/2027.42/48617.

Kesling, R.V., Segall, R.T., and Sorensen, H.O., 1974, Devonian Strata of Emmet and Charlevoix Counties, Michigan: Papers in Paleontology, Museum of Paleontology, The University of Michigan, v. 7, p. 1–187, https://hdl.handle.net/2027.42/48608.

Narkiewicz, K. and Bultynck, P., 2016, Taxonomy and biostratigraphic significance of Icriodus orri Klapper and Barrick and related Middle Devonian conodont species, Journal of Paleontology, v. 90(6), p. 1181-1196, doi: 10.1017/jpa.2016.41

O'Bryan, H.R., Thole, J., Voice, P., and Zambito IV, J., 2024, Diagenesis of a pyritized contact at the Middle to Late Devonian transition from carbonate to black shale in the Michigan Basin: Geological Society of America Abstracts with Programs, v. 56, n. 3, doi: 10.1130/abs/2024NC-398896

Reed Jr., J.C., 2004, Geology of the United States, Mexico, Central America, and the Antilles, and parts of Siberia, Colombia and Venezuela for the Geologic Map of Morth America, in: Reed, John C. Jr., Wheeler, John O., and Tucholke, Brian E., compilers, 2004, Geologic Map of North America: Decade of North American Geology Continental Scale Map 001, Boulder, Geological Society of America, 1:5000,000 scale.

Swezey, C.S., Hatch, J.R., East, J.A., Hayba, D.O., and Repetski, J.E., 2015, Chapter 2: Total Petroleum Systems of the Michigan Basin—Petroleum Geology and Geochemistry and Assessment of Undiscovered Resources, in U.S. Geological Survey Michigan Basin Province Assessment Team ed., Geologic assessment of undiscovered oil and gas resources of the U.S. portion of the Michigan Basin, U.S. Geological Survey, U.S. Geological Survey Digital Data Series DDS–69–T, p. 1–162, https://doi.org/10.3133/ds69T.

Truong, L.T., Voice, P.J., and Zambito IV, J.J., 2024, Preliminary geologic maps of Alpena County, Michigan: Geological Society of America Abstracts with Programs, v. 56, n. 3, doi: 10.1130/abs/2024NC-398768

Ver Straeten, C.A., 2010, Lessons from the foreland basin: Northern Appalachian basin perspectives on the Acadian orogeny, in Tollo, R.P., Bartholomew, M.J., Hibbard, J.P., and Karabinos, P.M., eds., From Rodinia to Pangea: The Lithotectonic Record of the Appalachian Region: Geological Society of America Memoir 206, p. 251–282, doi: 10.1130/2010.1206(12)

Wiesner, A.S., Judge, S., Voice, P.J., and Zambito IV, J.J., 2024, An Analysis of Stratigraphic and Paleoecologic Variability in the "Squaw Bay Formation," Michigan Basin: Geological Society of America Abstracts with Programs, v. 56, n. 3, doi: 10.1130/abs/2024NC-398913

Winget, M.M., Beck, C., Wegter, B., Voice, P.J., and Zambito IV, J.J., Comparing Lithologies and Geochemical Signals of the Middle Devonian

Thunder Bay Formation (Michigan Basin) in Core and at the Type Section: Geological Society of America Abstracts with Programs, v. 56, n. 3, doi: 10.1130/abs/2024NC-398920

Wylie, A.S., and Huntoon, J.E., 2003, Log-curve amplitude slicing: Visualization of log data and depositional trends in the Middle Devonian Traverse Group, Michigan basin, United States: AAPG Bulletin, v. 87, p. 581–608, doi:10.1306/12040201057.

Zambito IV, J.J., Brett, C.E., and Baird, G.C., 2012, The Late Middle Devonian (Givetian) Global Taghanic Biocrisis in Its Type Area (Northern Appalachian Basin): Geologically Rapid Faunal Transitions Driven by Global and Local Environmental Changes, in Talent, J.A. ed., Earth and Life, Dordrecht, Springer Netherlands, p. 677–703, doi:10.1007/978-90-481-3428-1_22.

Zambito IV, J.J., Voice, P.J., Barker-Edwards, T., Giehler, M.C., Gugino, J.P., Johnson, I.R., O'Bryan, H.R., Quiroz, C.J., Truong, L.T. 7, Wiesner, A.S., and Winget, M.M., 2023, Integrated stratigraphic and paleoenvironmental study of the Middle-Late Devonian Carbonate to black shale transition in the Michigan Basin, Subcommission on Devonian Stratigraphy Annual meeting, Geneseo, New York, Program and Abstracts p. 86-87.

KECK Geology Consortium
Learning Science Through Research
Published by the Keck Geology Consortium
Short Contributions
Keck Geology Consortium
Volume 36
May 2024
doi: 10.18277/AKRSG.2024.36.12

CORRELATING THE TRAVERSE GROUP LIMESTONE FROM SUBSURFACE TO OUTCROP, MICHIGAN BASIN

MARCELLA M. WINGET, Hamilton College
Project Advisor: Catherine C. Beck

INTRODUCTION

The Michigan Basin is a 400 km diameter structural basin with a geologic record spanning from the Ordovician through the Permian (Howell and van der Pluijm, 1991). Much of the basin's sedimentary record throughout the Devonian is correlated across the basin while other sections are difficult to recognize in both subsurface and outcrop, such as the Mid-Devonian Traverse Group. The Traverse Group is a series of limestones and calcareous shales that overlies the Dundee Formation and underlies the "Squaw Bay Formation" -Antrim Shale sequence (Gutschick and Sandberg, 1991). Over the years, terminology surrounding this group has been inconsistent and difficult to parse; some studies combine these limestones with the "Squaw Bay Formation" and classify the "Traverse Limestone" varyingly as a formation and group (Ehlers and Kesling, 1970; Gutschick and Sandberg, 1991, and references therein). Oil and gas logs simply refer to the topmost unit as the Traverse Limestone due to its lack of economic importance as a less significant hydrocarbon producer than the overlying Antrim Shale. Subsurface records only officially identify two units in the Traverse Group: the thinner Bell Shale and the overlying thick Traverse Limestone (Catacosinos et al. 2001). This simple division is not utilized in the outcrop belt which has been divided into a large number of units (see Wylie and Huntoon, 2003, and references therein). In addition to this, correlating these units is challenging because of a paucity of continuous exposure. Cores produced by oil and gas exploration have provided good subsurface data throughout the basin but Pleistocene glacial deposits have made good outcrops rare and difficult to fully correlate with the subsurface data. For instance, at the type section for the Thunder Bay Formation, upper and lower contacts of the unit are not visible, making thickness estimates very difficult (Ehlers and Kesling, 1970). Finally, the input of clay and clastic material from the Acadian Mountains to the east of the basin cause the facies observed across the basin to display different compositions and textures even when they should be the same temporal unit for correlation.

To gain a better understanding of the Traverse Group and its subsurface versus outcrop expression, this project describes and compares the Traverse Group in the State Chester Welch #18 (SCW-18) core to determine which outcrop unit it corresponds to. With its intact upper contact the SCW-18 core can provide a useful reference for future correlation in the Michigan Basin.

METHODS

To describe the subsurface Traverse Group limestone in detail, the SCW-18 core from a gas exploration well in north central Michigan was used (Figure 1). Prior to this study, the core was slabbed and included the upper 9 ft (2.75 m) of the Traverse Group to its contact with the "Squaw Bay Formation" (SB Formation.) For this project, the core was subdivided into facies based on the lithologic features and fossil assemblages. Fossil analysis was based on the content and preservation, and when possible, fossils were classified to the genus level. Next, hand samples taken from outcrops of the Traverse Group and SB Formation were assessed. These hand samples originated from across northern Michigan; one set of samples came from the Michigan Geologic Society 1949 field trip and the other set included samples from the Thunder Bay, Beebe School, Petoskey, and Whiskey Creek formations at their type sections collected by J. Zambito in the 2010s. These outcrop samples were

Figure 1. Map of locations of the SCW-18 core and the Thunder Bay Formation type section outcrop (Image from Google Earth).

also described based on their composition and fossil content. Published stratigraphic columns from the type areas of Michigan Basin units were also consulted for comparison, especially from Wylie and Huntoon (2003), Kesling et al. (1976) and Ehlers and Kesling (1976). Finally, the closest match to the lithology of the core sample was selected to identify its geologic unit from the type area descriptions and samples.

RESULTS

The lithology of the Traverse Group section of the SCW-18 core was dominantly a gray calcareous shale to limestone with abundant fossils (Figures 2 and 3). Throughout the core crinoid fossils were common as well as stylolites from post-deposition alteration. The lowest units A and B were matrix-supported mudstones with a higher portion of clay sediment than the overlying subsections. A stromatoporoid as well as pyrite were found in unit B. Bryozoans were most common in the lower three units. The middle of the core succession studied had the most abundant fossil material, with unit E approaching a packstone concentration recrystallized fossil material. Stromatoporoids and corals were found in the units C and E. After a gap of missing core, units G, H, and I have lower fossil abundance, but pyritized fossil material. This portion of the core was highly crystalline and the fossil material present was difficult to identify due to recrystallization, suggesting this segment was diagenetically altered near the upper contact with the SB Formation.

After consulting the literature and the hand samples from type areas around the Michigan Basin, it was determined that the SCW-18 core most closely resembles the Thunder Bay Formation. The hand samples from the Thunder Bay type area were similarly a gray calcareous shale to limestone with abundant crinoids, stylolites, and some stromatoporoids visible (Figure 2). The outcrop hand samples weren't highly crystalline like the upper units in the core samples, suggesting that it correlates best to calcareous shales and shaley limestones near the base of the core.

Compared to the Thunder Bay outcrop descriptions in the type areas published in Ehlers and Kesling (1976),

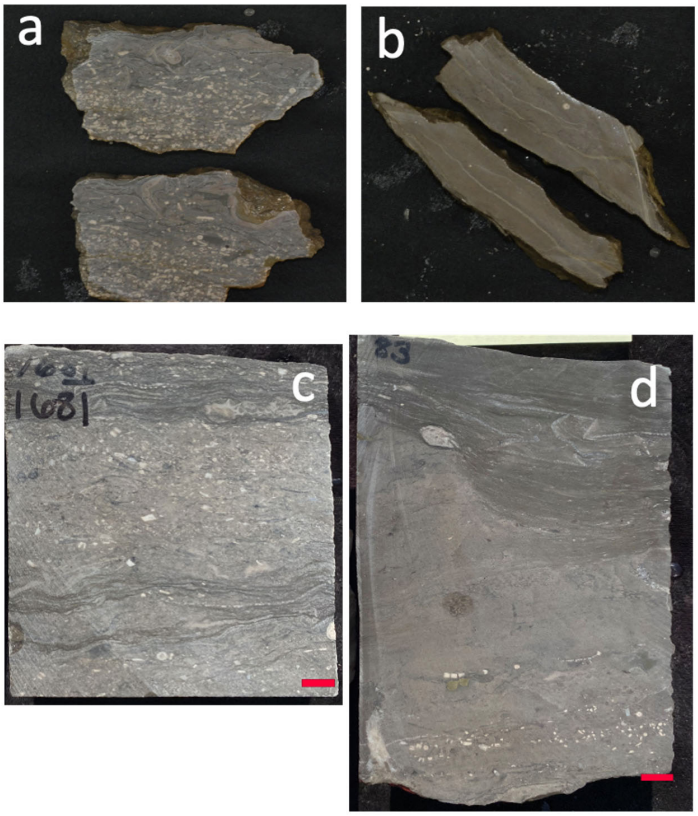

Figure 2. Examples of the SCW-18 core's texture compared to hand samples from the Thunder Bay type area. Fauna, color, and texture of hand sample a matches SCW-18 units C & E. Hand sample b resembles lower SCW-18 unit B. Red bar = 1 cm. 2a.) Thunder Bay outcrop sample with shaley limestone texture, packstone with crinoids and corals. Evidence of stylolites. 2b.) Thunder Bay outcrop sample. is a gray mudstone with stylolites and bryozoans. 2c.) SCW-18 core sample. This is a shaley limestone packstone with crinoids and coral.Several silhouettes surrounding bryozoan sheets are present. 2d.) SCW-18 core sample. This is a calcareous shale mudstone with sparse crinoid fossils and larger secondary stylolite features. Outcrop sample a and SCW-18 sample C closely resemble each other in fossil concentration and color while sample b and SCW-18 sample D have very similar textures.

the majority of the SCW-18 core closely resembles units 1 and 3 due to its fossil content and shaley limestone texture which grades into a crystalline limestone (Figure 3). There was no data on relative fossil abundance or the degree of crystallization at the outcrop but the overall texture, color, and fauna was the same. There was no pyrite recognized at the outcrop, possibly suggesting a higher level of diagenetic alteration in the subsurface.

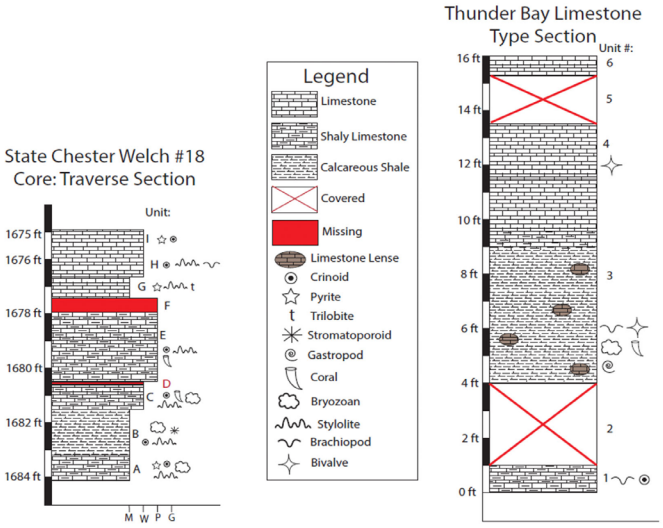

Figure 3. The SCW-18 core sequence of the Traverse Limestone compared to the Thunder Bay Formation type section in outcrop described by Ehlers and Kesling (1970). Lithology and fauna are similar, with the SCW-18 succession closely resembling units 1 & 3 of Ehlers and Kesling description.

DISCUSSION

Identifying the SCW-18 Traverse Group succession as the Thunder Bay Formation adds to the understanding of this relatively understudied unit by distinguishing differences between the subsurface and subaerial expressions of this unit and by establishing a reference for its contacts. Across the basin there appears to be variation in the extent of the Thunder Bay Formation. At the type area, the Thunder Bay had a total exposure of ~16 ft according to the literature and the hand samples from the area have ~19 ft of vertical distribution (Ehlers and Kesling, 1976). The SCW-18 core was drilled more centrally in the basin so although there was only 9 ft of the Thunder Bay Formation preserved in the core, a thicker package should be present in this part of the unit. If the core included the lower contact of the TB, there should be well over 20 ft of this lithology present.

Identifying the Thunder Bay Formation in this subsurface record can be used as a reference for the stratigraphic relationships in the Michigan Basin. Pleistocene glacial sedimentation has obscured much of the potential outcrop exposures around Michigan making comprehensive outcrops with conformable contacts uncommon. For instance, the type section for the Thunder Bay Formation has no visible contacts (Ehlers and Kesling, 1976). This makes the SCW-18 a useful reference section for study of the Thunder Bay Formation because it includes a clear upper contact with the overlying SB formation. Additionally, this identification bridges a gap between the subsurface and outcrop interpretations of the Traverse Group subdivisions. This correlation connects two regions that have had nomenclatural differences for the Traverse Group; in outcrops in North Central Michigan, the Thunder Bay Formation is not usually identified but in northeastern Michigan near the type area, the unit can be identified (Wylie and Huntoon, 2003). But given the lithological similarities between the eastern Michigan type area samples and the north-central Michigan, it is reasonable to suggest the Thunder Bay Formation could be a continuous unit across this portion of the basin.

To corroborate the identification of the Thunder Bay Formation in the subsurface, gamma ray logs from across the Michigan Basin were utilized. This data type assesses the level of natural gamma radiation from rocks lining the boreholes. High gamma values are typically associated with shaley rock textures with high organic carbon content. Wylie and Huntoon (2003) compiled a series of gamma ray logs from boreholes around the state that are near the sample localities used in this study; the Lake Horicon #1 borehole came from north-central Michigan near the SCW-18 core and the Cousineau “A” #1-16 data came from a location near the Thunder Bay type area. These logs revealed a trend of low gamma radiation in the upper most Traverse Group in the subsurface (Figure 4; Wylie and Huntoon, 2003). Typically crystalline limestones like the SCW-18 core interval should have low gamma levels, not the substantial peaks reflected in the Thunder Bay portion of the log. Based on these values, the core segment in this study is more likely the upper low-gamma Traverse Limestone rather than the true Thunder Bay unit that

is placed stratigraphically below it and separated by an unconformity. The lithologies of the samples from the type area were the sample texture, suggesting that a near-upper contact segment of the Traverse was successfully captured in the outcrop samples. Additionally, the package of this upper low-gamma section appears to be abbreviated in the eastern part of the basin near the outcrop. Rather than displaying two small peaks in the upper Traverse like in the basin-center samples (Lake Horicon #1), the outcrop area (Cousineau "A" #1-16) is condensed and does not include this full package of low-gamma lithology. Based on the distribution of these data points, the abbreviation of these profiles is probably due to the structure of the basin and difference in erosion from its center to the edge. Therefore it can be interpreted that the basin edge outcrop samples do not account for the full sequence observed in the subsurface core, even though the two don't include firm boundary indicators of both contacts.

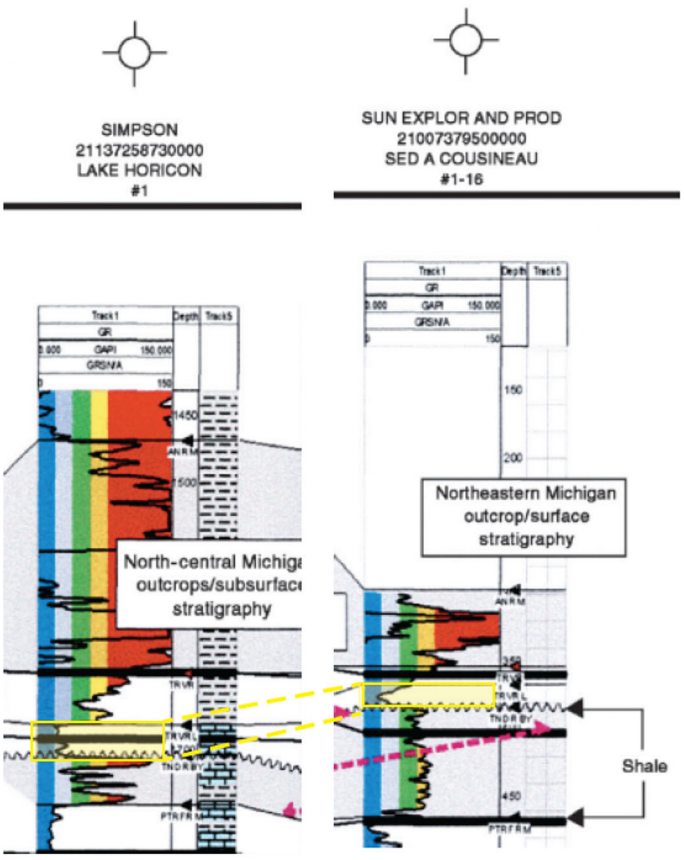

Figure 4. Gamma ray logs adapted from Wylie and Huntoon (2003). The Lake Horicon #1 bore hole was located near the SCW-18 drill site and the Cousineau "A" #1-16 bore hole is in northeastern Michigan near the Thunder Bay Formation type locality. Across the transect there is a peak in gamma radiation in the Thunder Bay unit over lain by a low gamma zone right near the upper contact of the Traverse with the SB.

CONCLUSIONS

By identifying the uppermost Traverse Group unit of the SCW-18 core, this study adds to the limited subsurface-to-outcrop correlation in the Michigan Basin and points to this core as a good reference for the contacts of the Thunder Bay Formation which have been difficult to study. Future studies could incorporate a temporal control on the subsurface and outcrop samples to establish relative distance from the contact with the SB formation in the type area. This work will help inform understanding of the relationships between regions of the Michigan Basin as well as its stratigraphic relationships which are essential to geologic research.

ACKNOWLEDGEMENTS

This material is based upon work supported by the Keck Geology Consortium and the National Science Foundation under Grant No. 2050697. I'd like to thank my advisors Jay Zambito and Peter Voice for their guidance and support. I'd also like to thank my research cohort for fostering a collaborative and fun work environment.

REFERENCES

Catacosinos, P.A., Harrison, W.B., III, Reynolds, R.F., Westjohn, D.B. & Wollensak, M.S. (2001) Stratigraphic Lexicon for Michigan. Geological Survey Division, Department of Environmental Quality and Michigan Basin Geological Society, Lansing, 56 p.

Ehlers, G.M., and Kesling, R.V., 1970, Devonian Strata of Alpena and Presque Isle Counties, Michigan: Museum of Paleontology, The University of Michigan, Miscellaneous Papers, 131 p., https://hdl.handle.net/2027.42/48601.

Gutschick, R.C., and Sandberg, C.A., 1991, Late Devonian history of Michigan Basin, in Geological Society of America Special Papers, Geological Society of America, v. 256, p. 181–202, DOI: 10.1130/SPE256-p181.

Howell, P.D., and Van Der Pluijm, B.A., 1999, Structural sequences and styles of subsidence

in the Michigan basin: Geological Society of America Bulletin, v. 111, p. 974–991, doi:10.1130/0016-7606(1999)111<0974:SSASOS>2.3.CO;2.

Kesling, R.V., Johnson, A.M., and Sorensen, H.O., 1976, Devonian Strata of the Afton-Onaway Area, Michigan: Papers in Paleontology, Museum of Paleontology, The University of Michigan, v. 17, p. 1–149, https://hdl.handle.net/2027.42/48617.

Wylie, A.S., and Huntoon, J.E., 2003, Log-curve amplitude slicing: Visualization of log data and depositional trends in the Middle Devonian Traverse Group, Michigan Basin, United States: AAPG Bulletin, v. 87, p. 581–608, doi:10.1306/12040201057.

KECK Geology Consortium
Learning Science Through Research
Published by the Keck Geology Consortium
Short Contributions
Keck Geology Consortium
Volume 36
May 2024
doi: 10.18277/AKRSG.2024.36.13

DIAGENESIS OF A PYRITIZED CONTACT OF THE MIDDLE TO LATE DEVONIAN TRANSITION FROM CARBONATE TO BLACK SHALE

HOLIDAY R. O'BRYAN, Macalester College
Project Advisors: Kelly R. MacGregor and Jeff T. Thole

INTRODUCTION

The geologic history of the Michigan Basin spans nearly the entire Paleozoic Era. Devonian outcrop and rock has been sampled extensively in cores across the state of Michigan as well as from the outcrop belts in the northern and southeastern Lower Peninsula. The mineralized contact between the "Squaw Bay Formation" and Traverse Group merits a greater degree of attention in order to differentiate early versus late diagenesis which has implications for the depositional environment and basin history, respectively. In every sample of this contact, where limestone of the Traverse Group is overlain by calcareous shale, pyrite occurs as nodules, framboids, and cubes. Petrographic and scanning electron microscopy (SEM) and x-ray fluorescence scanning (μXRF) were used to identify the mineralogies and define the microfacies present in these formations and at their contact. This work results in the reconstruction of a paragenetic sequence for the contact and both formations.

Paleogeographic Setting

The Michigan Basin represents 280 million years of geologic time, with around 4800 meters of preserved rock spanning nearly the entire Paleozoic (Milstein, 1987, Gutschick and Sandberg, 1991). During the Devonian, the Michigan Basin was a warm and tropical sea situated near or at the equator (Gutschick and Sandberg, 1991). Subsidence of the Traverse Group occurred conjointly with the Taghanic Onlap during the Middle-Late transition, and the "Squaw Bay Formation" is thought to have recorded the transition from carbonate platform to deep-water lime- and argillaceous mudstones (Gutschick and Sandberg, 1991).

The transition from the Middle to Late Devonian in the basin is marked by substantial development of a pycnocline and evidence of dys- to anoxic conditions on the seafloor (Gutschick and Sandberg, 1991). During the Late Devonian, the Acadian Orogeny influenced sediment supply and tectonic activity in the basin significantly. Erosion of the mountains led to an increase in fine sediment supply to the basin (Wylie and Huntoon, 2003). The Traverse Group was marked by basin centered subsidence, while the Antrim Shale (the shale unit overlying the "Squaw Bay Formation") was marked by eastern-tilted subsidence (Howell and van der Pluijm, 1999). In addition to basin subsidence, dys- to anoxic conditions have been identified, especially in Devonian carbonates and shales. Formolo et al. (2014) suggested that iron limitation led to increased sulfide accumulation and recycling and that the chemocline was subsequently pushed upwards in the water column.

METHODS

At the Michigan Geological Repository for Research and Education (MGRRE), drill cores from the Michigan Basin are housed, including cores through Upper Devonian strata. Both formations and the pyrite contact were identified from wire-line and gamma-ray log data as well as driller notes and measured sections of lithologies and contacts archived at MGRRE. Three cores were selected for sampling, each of which contained the pyritized contact. These were the State Chester Welch No. 18 core, the Krocker 1-17 core, and the BH-301 core (Fig. 1). Ten spots in the three

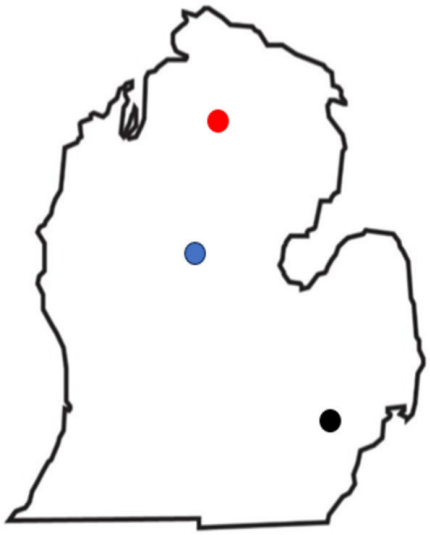

Core Name	Core Information			
Krocker 1-17 Well	***PN***	***API***	***Location***	***Included Formations***
	60134	21-035-60134-00-00	Clare County, MI	Ellsworth through "Squaw Bay" and Traverse Contact
	Lower Footage	***Upper Footage***	***Sampled Footages***	
	3497	3211	3463.8, 3494.3, 3497.5	
State Chester Welch No. 18	***PN***	***API***	***Location***	***Included Formations***
	33875	21-137-33875-00-00	Otsego County, MI	Norwood through Traverse
	Lower Footage	***Upper Footage***	***Sampled Footages***	
	1684	1435	1667.8, 1673.2, 1674.85, 1675.25	
BH-301	***PN***	***API***	***Location***	***Included Formations***
	None	None	Wayne County, MI	Norwood through Traverse
	Lower Footage	***Upper Footage***	***Sampled Footages***	
	120.5	60.5	110.1, 111.5, 117.5	

Figure 1. Locations and identification numbers of each core. The Krocker-17 Well is noted in blue, the State Chester Welch in red, and the BH301 in black. Abbreviations: PN = Permit Number, API = American Petroleum Institute Permit Number, MI = Michigan.

cores were sampled for thin sectioning, three of which were at the pyritized contact in each core. See Figure 1 for the locations of each well, footages selected from each core, and general information about the cores themselves. These billets were then sent to Wagner Petrographic of Lindon, Utah, and standard thickness (30µm) sections were prepared. The three samples which contained the pyritized contact were surface polished for microanalysis.

At Macalester College, a standard petrographic microscope with an attached CanonT5i DSLR camera was used to take pictures of all the thin sections at varying levels of magnification. Photographs were taken of not only the various minerals identified, but also of fossil structures and pyrite morphologies in the samples. High-resolution elemental abundance maps were collected on thin sections using the Bruker M-4 Tornado equipped with an Rh X-ray tube and thin-window silicon drift detector. Spatially-resolved X-ray maps display relative abundances of major elements including Mg, Al, Si, S, K, Ca, Fe, and Zn. Color intensities at each location represent semi-quantitative relative individual element abundance. Thin sections of the contact were analyzed with a JEOL JSM 6610LV scanning electron microscope equipped with a tungsten filament that was set to 15kV and operated under high vacuum. Select locations were imaged using backscattered electrons (BSE). The diameter of framboids in samples were measured using the SEM backscattered electron images and an average diameter for all framboids both in individual samples and all samples was calculated. This analysis was undertaken on the three thin sections of the contact. Using these findings, measures of framboid diameters are used to interpret the degree of oxygenation of the seawater these grains precipitated from based on work done by Chang et al. (2022).

RESULTS

Carbonates

Calcium is the most abundant element in all samples. In the "Squaw Bay Formation," lime mud is mixed with argillaceous muds in addition to other trace minerals. It is dispersed through the matrix of both formations and overlaps significantly with magnesium.

In the "Squaw Bay," calcite is mostly associated with fossil fragments and the clay matrix, but its altered form as dolomite is especially striking in the Traverse Limestone and within the pyritized contact. Dolomite crystals are abundant below the contact, and make up the entire matrix of the rock, showing significant overgrowth and deformation. Some twinning is present, especially in the lower (deeper) samples. Below the contact, crystals range from 0.5-3 microns in width and are relatively uniform in shape across this size range. Additionally, the dolomite crystals

have preserved original crystal structures as well as fossil debris, especially when in close proximity to the contact. In SEM photomicrographs, a visible difference in the saturation of the crystals themselves is present. There is a differentiation between low- and high-Mg calcite within crystals, and some show reaction rims (Figure 2).

Silicates

Silicon is the second most abundant element in all samples, with a much greater degree of incidence in the "Squaw Bay Formation" as identified by XRF scans (O'Bryan, 2024). Silica makes up a large part of the clay and silt matrix in the "Squaw Bay Formation," and mostly appears as chalcedony throughout the Traverse Limestone. Silica in the "Squaw Bay Formation" appears in three forms. It appears as part of the cement and mud in the matrix, as detrital quartz grains, and as biogenic silica. In the Traverse Limestone, silica is much less abundant, and significantly more concentrated in the areas it does appear. Chalcedony is the major mineral hosting silicon and appears associated with fossil debris or filling vug space.

Sulfides and Sulfates

Pyrite is often associated with fossils in these samples. Pyrite encrusted both fossil debris and other crystals,

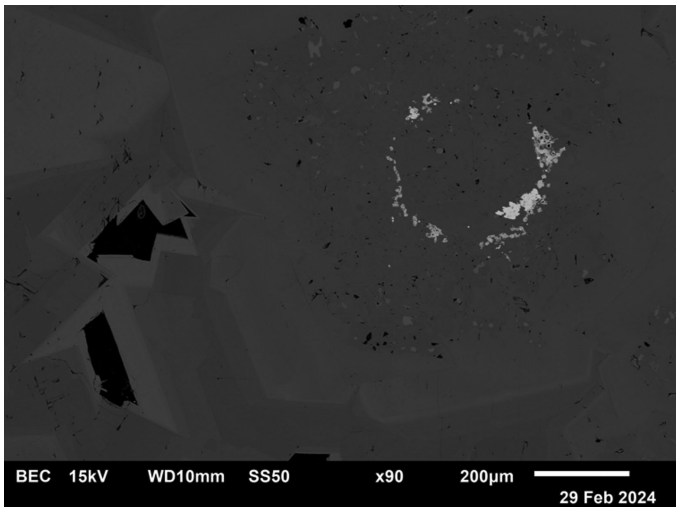

Figure 2. This is an SEM BSE image of calcite crystals found in the center of an echinoderm in the BH201-110 sample. High and low-Mg content differences are visible where lighter gray is lower-Mg calcite, darker gray is higher-Mg calcite, and white is pyrite. This zoning is indicative of multiple episodes of crystallization and dissolution.

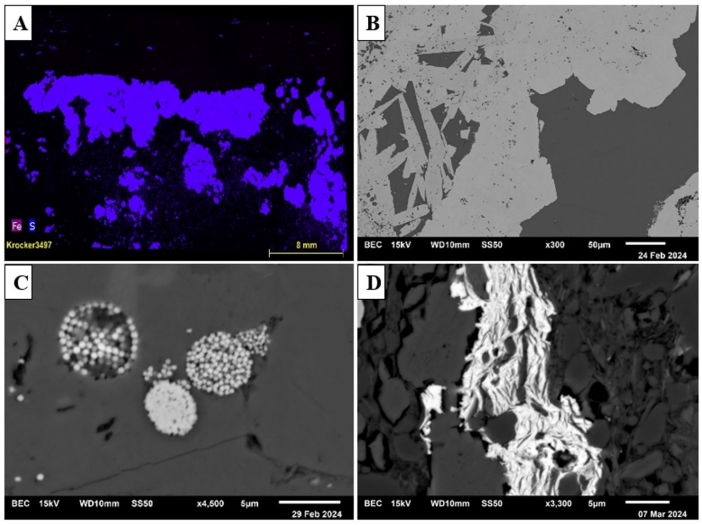

Figure 3. A) XRF Scan of the Krocker 3497 thin section showing abundance of pyrite (purple color created by the layering of Fe (violet) and S (royal blue). The upper limit of the pyrite is the contact between the "Squaw Bay Formation" and the Traverse Limestone. B) SEM BSE image of marcasite crystals (left center of image). Pyrite and marcasite are chemically indistinguishable from each other, but when viewed under reflected light, marcasite displays blue and green colors while pyrite is grayish gold. Here, marcasite is identified by its tabular crystal habit. C) SEM BSE image of framboids (light gray microaggregates) visible in the BH301-110 thin section. D) SEM BSE image of feathery barite (white) identified in the StChester 1674 thin section.

and original material was then dissolved and/or replaced while the pyrite remained. These pyritized fossil debris are especially helpful in determining the kind and abundance of marine life present in the samples and serve as an important indicator of the order of crystallization in some places.

In addition to being associated directly with organic content, pyrite exists in these samples as large masses or nodules, especially at the contact between the "Squaw Bay Formation" and the Traverse Limestone (Figure 3A). In the "Squaw Bay Formation," pyrite is more likely to occur as large nodules, and in the Traverse Limestone it is more likely to occur in association with fossils. Cubic pyrite is observed in all samples as well. Cubic crystals range from about 10 microns in length to about 2 millimeters.

The pyrite in these samples displays an additional uncommon morphology. Tabular crystals and rhombs of pyrite are visible at the margins of nodular masses and within the matrix of both the "Squaw Bay Formation" and the Traverse Limestone. Marcasite was identified, especially around the edges of the interior of the nodular masses. The elongate marcasite

crystals are about 100 microns in length from tip to tip, but few are larger than that, and most smaller (Figure 3B). The rhombic pyrite and marcasite were commonly associated with each other.

Framboidal pyrite is observed at the contact in varying sizes and shapes. Figure 3C shows framboids present in the BH301-110 thin section. Framboids across all samples averaged 9.5 microns in length with a standard deviation of 5.7 microns. Though framboids are not associated with anything spatially, they do commonly appear in conjunction with other sulfide minerals (barite and sphalerite) and with fossil debris.

Barite and sphalerite were also identified. The sphalerite exhibits similar crystal morphologies to pyrite, but does not occur as framboids, needles, or cubes. Sphalerite is associated directly with pyrite. Barite is a barium sulfate which is only observed in the contact between the "Squaw Bay" and Traverse formations in the State Chester Welch sample. Barite is often elongate and prismatic, but in this thin section it showed a curved and feathery form, which wove in and out of the sediment matrix and around pyrite framboids (Figure 3D).

Paragenetic Sequence

Based on all the above results, what follows is a paragenetic sequence for the contact. Additional paragenetic sequences for the Traverse Limestone and the "Squaw Bay Formation" can be found in O'Bryan (2024). The sequence presented here is based on extensive analysis of these samples but suffers from two major caveats. First, no absolute ages of any of the samples were determined, so all diagenetic processes described here are relative to each other. Second, thin sections were not stained nor subject to a pore analysis. While the lack of this information does not preclude the possibility of making conclusions about the sequence of diagenetic events, having it would certainly clarify spatial and temporal relationships.

Figure 4 shows the paragenetic sequence for the contact. At the contact between Traverse Limestone and "Squaw Bay Formation," there is extensive evidence for multiple episodes of pyritization, precipitation of minerals, and dissolution. Following the deposition of the Traverse Limestone, framboidal

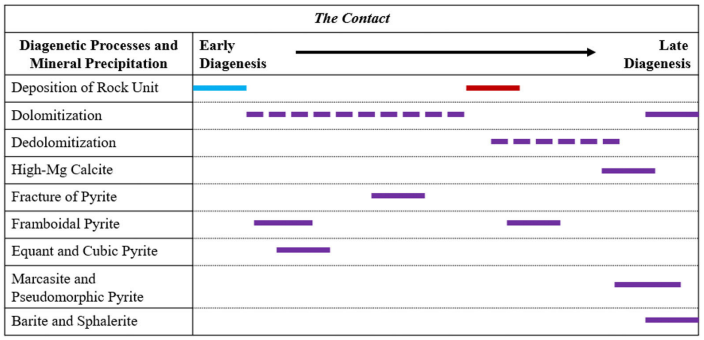

Figure 4. Paragenetic sequence of the contact between the "Squaw Bay Formation" and the Traverse Limestone. The deposition of the Traverse is blue, and the deposition of the "Squaw Bay" is red. Dashed lines represent uncertainty or otherwise continuous processes.

pyrite likely formed first in a bacterially-mediated setting, rich in organics and low in oxygen and this conclusion is supported by Chang et al. (2022) and He et al. (2022). These framboids, once formed and settled, gradually recrystallized into the nodular massive pyrite that dominates the samples. Secondary precipitation of framboids is supported by the measure of framboid diameters using the methods outlined in Chang et al. (2022); the framboids visible in the samples formed in dysoxic conditions, and precipitation occurred during early diagenesis. This was followed by the dolomitization of the Traverse Limestone. At some point between the initial precipitation of pyrite and the full dolomitization of the Traverse, the pyrite nodules underwent some stress and void space formed in cracks. Within these vugs grew large, well-formed dolomite rhombs as well as the elongate marcasite crystals. The marcasite formation and the formation of dolomite were likely closely related.

During the subsequent dedolomitization of the Traverse Limestone, which likely occurred sometime around when the "Squaw Bay Formation" was being deposited, pyrite replaced some of the dolomite rhombs, leading to the preservation of the initial crystal form with pyrite rather than dolomite. The second generation of framboidal pyrite also likely occurred around this time. The dedolomitization occurred before a precipitation of high-Mg calcite, filling the void space with clean, equant crystals. This final precipitation of high-Mg calcite preserved the pyrite rhombs. The precipitation of sphalerite and barite at the contact were the last minerals to have precipitated and were additionally accompanied by

a final dolomitization process. These were the latest diagenetic processes to take place and are likely related to the migration of deep basinal fluids into the subsurface.

DISCUSSION AND FUTURE WORK

Paragenetic Sequence

Two generations of pyrite and one generation of marcasite are noted in the paragenetic sequence of the contact. The first pyrite generation formed the massive, nodular pyrite that makes up the bulk of the pyrite present in these samples, followed by marcasite precipitation associated with the initial dolomitization of the Traverse. The second generation of pyrite produced the framboidal and replacement forms of pyrite that are especially visible at the bottom of the "Squaw Bay Formation" and at the edges of the original pyrite masses. This sequence is supported by theories of massive pyrite formation, bolstered by the work of Jorgensen et al. (2004), Sawlowicz (1993), and Chang et al. (2022). This first generation likely occurred before the "Squaw Bay Formation" was deposited and was likely initially mediated by bacteria.

Because it is assumed that the massive nodular pyrite was formed from the precipitation of framboids, the presence of well-formed framboids in the matrix of the "Squaw Bay Formation" is clear evidence of a second generation of pyrite. The exact chemistry of this relationship is unresolvable with the available data, but it is likely that pyrite formed both during a cessation of sediment supply to the basin (when the carbonate platform subsided) and when the "Squaw Bay Formation" began to be deposited and lithified. That said, the framboid diameter analysis results from Chang et al. (2022) suggest that the visible framboids in these samples were formed in early diagenetic processes, as precipitation of pyrite that occurred after burial of organics and was initially mediated by bacteria.

Rhombs are not a typical crystal form of pyrite. While it is not possible to determine exactly how these crystals formed, it is likely that pyrite forms as a pseudomorph of dolomite rhombs (Figure 5). The fluid that was responsible for the initial dolomitization of

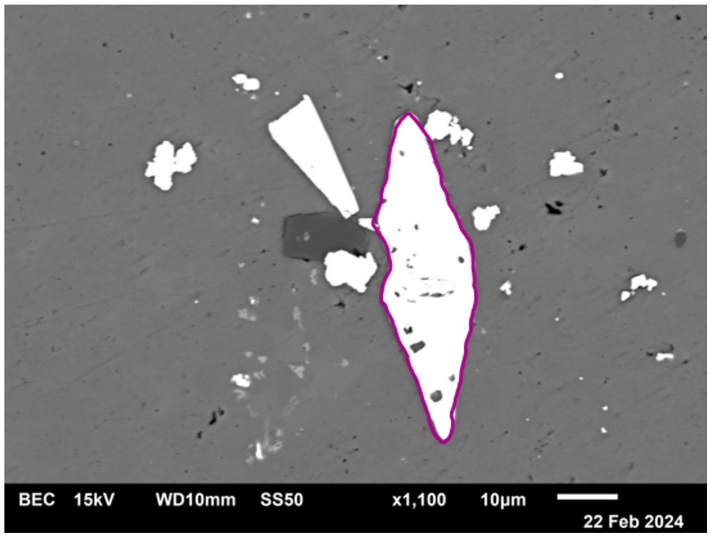

Figure 5. Pseudomorphic pyrite rhomb outlined in purple.

the Traverse allowed the growth of rhombic dolomite crystals in the available void space, which was created as a result of the initial dissolution in the Traverse Limestone. The process of dolomitization also resulted in the recrystallization or growth of marcasite on the initial pyrite nodules. What happened next is unclear. What we know is that dolomitization took place and that high-Mg calcite precipitated in void spaces, preserving both pyrite rhombs and elongate marcasite. The rhombs likely formed as a result of dolomite being leached out and pyrite filling in the pore left behind. The multiple dolomitization processes described above are supported by reaction rims of dolomite crystal, which grade between dolomite and high-Mg calcite.

Sphalerite, Barite, and MVT Mineralization

This study suggests the precipitation of sphalerite and barite along with a final dolomitization process were the latest diagenetic processes to occur. Both minerals are commonly associated with carbonate facies and other sulfide minerals (here pyrite) but how they came to appear in these samples is a larger question than simple alteration.

Mississippi Valley type deposits are concentrations of elements including zinc and barite, which manifest here as the minerals sphalerite and barite. Pyrite, dolomite, sphalerite, and barite specifically are all commonly associated with each other and with MVT deposits (Smith, 2021). MVT mineralization is hypothesized to occur as a result of tectonic activity

which directs hydrothermal ore-bearing fluid to flow through already lithified rock units. Regional hydrothermal systems play a large part in the occurrence of these deposits, and tectonic activity and bedrock chemistry is also a key variable associated with the availability of elements in host rocks (Paradis et al., 2007).

The fluids associated with MVT mineralization must be warm and chemically rich. The Michigan Basin is underlain by the failed Mid-Continental rift in North America. Volcanic bedrock formed in the Precambrian which underlies the north-western portion of the Basin likely formed the supply for Mg- and trace element rich fluids which dolomitized and precipitated sphalerite in the Krocker and State Chester wells (Heinrich, 1976). The fracture of Precambrian rock beneath the entire basin and the migration of deep, warm fluid through these fractures would provide the right amount of fluid with the correct composition to the Devonian subsurface. Importantly, barite was only identified in the BH-301 well, which is in the southeastern part of the basin.

Future Work

Limitations of the study include the limited number of samples available for analysis, which may have skewed results. Additionally, the complexity of dolomite and pyrite formation presents challenges in interpretation due to their rarity in modern environments and the variability of their forms. Future work would involve testing interpretations presented herein with isotopic data, performing point counting and porosity tests on samples, and conducting further SEM analysis with standardized chemical spectra to quantify the extent of diagenetic processes more accurately.

ACKNOWLEDGEMENTS

This material is based upon work supported by the Keck Geology Consortium and the National Science Foundation under Grant No. 2050697. I would like to thank my advisors, friends, and family, without whom this work would not have been possible.

REFERENCES

Chang, J., Li, Y., Lu, H., 2022, The morphological characteristics of authigenic pyrite formed in marine sediments: Journal of Marine Science and Engineering, vol. 10, no. 1533.

Formolo, M., Riedinger, N., Gill, B., 2014, Geochemical evidence for euxinia during the Late Devonian extinction events in the Michigan Basin (U.S.A.): Paleogeography, Palaeoclimatology, Palaeoecology, v. 414, p. 146-154.

Gutschick, R., and Sandberg, C., 1991, Late Devonian history of Michigan Basin: Geological Society of America, Special Paper 256.

He, R., et al. (2022) Devonian upper ocean redox trends across Laurussia: Testing potential influences of marine carbonate lithology on bulk rock I/Ca signals. Frontiers in Marine Science 9: 874759.

Heinrich, E., 1976, The Mineralogy of Michigan. Lansing, Mich.: Dept. of Natural Resources, Geological Survey Division.

Howell, P., van der Pluijm, B., 1999, Structural sequences and styles of subsidence in the Michigan Basin: Geological Society of America Bulletin, v. 111, p. 974-991.

Jorgensen, B., Bottcher, M., Luschen, H., Neretin, L., Volkov, I., 2004, Anaerobic methane oxidation and a deep H2S sink generate isotopically heavy sulfides in Black Sea sediments: Geochimica et Cosmochimica Acta, v. 68, no. 9, p. 2095-2118.

Milstein, R., 1989, Subsurface Stratigraphy of Cambrian rocks in the Southern Peninsula of Michigan: Michigan Basin, Geological Survey of Michigan, Bulletin 7, 12 p.

O'Bryan, H.R., 2024, Diagenesis of a pyritized contact of the Middle to Late Devonian transition from carbonate to black shale in the Michigan Basin, Honors Thesis, Macalester College, 98p.

Paradis, S., Hannigan, P., Dewing, P., 2007, Mississippi Valley-type lead-zinc deposits (MVT): Mineral Deposits of Canada, v. 5, 15 p.

Sawlowicz, Z., 1993, Pyrite framboids and their development: A new conceptual mechanism: Geologische Rundschau, v. 82, p. 148-156.

Smith, S., 2021, Investigations of Mississippi Valley-Type mineralizing fluids via analytical geochemistry, numerical modeling, and experimental geochemistry [P.h.D. thesis]:

University of Missouri-Columbia, 154 p.
Wylie, A. and Huntoon, J., 2003, Log-curve amplitude slicing: Visualization of log data and deposition trends in the Middle Devonian Traverse Group, Michigan Basin, United States: AAPG Bulletin, v., 87, no. 4, p. 581-608.

.

KECK Geology Consortium
Learning Science Through Research
Published by the Keck Geology Consortium
Short Contributions
Keck Geology Consortium
Volume 36
May 2024
doi: 10.18277/AKRSG.2024.36.14

AN ANALYSIS OF STRATIGRAPHIC, PALEOECOLOGIC, AND GEOCHEMICAL VARIABILITY IN THE "SQUAW BAY FORMATION," MICHIGAN BASIN

AINSLEY S. WIESNER, The College of Wooster
Project Advisor: Shelley A. Judge

INTRODUCTION

Since being named by Warthin and Cooper (1935) nearly 100 years ago from a single, poorly exposed outcrop, the stratigraphic term "Squaw Bay Formation" has been used inconsistently to describe subsurface rocks by both drillers and researchers in the Michigan Basin. Along with problems in consistency of use, in November 2021 the Secretary of the Interior, Deb Haaland, issued Secretarial Order 3404 with the subject of declaring a series of terms, including 'squaw,' "a derogatory term and implementing procedures to remove the term from federal usage" (Department of the Interior, 2021). Since Secretarial Orders 3404 was released, Michigan geoscientists were acutely aware of naming protocols within the state and with the Department of Interior press releases. Collaborating together in a Keck Geology Consortium advanced summer project provided a vehicle for additional research in these Devonian-aged units, one of which is subject to renaming because it uses the derogatory term "squaw" in its name.

Principle Aims

This research will use lithostratigraphy, paleoecology, and pXRF to characterize and determine the variability of the "Squaw Bay" succession in the Krocker 1-17 core from the northern Michigan Basin, informing the renaming efforts within the rules of the North American Stratigraphic Code. It is also important to note that this paper uses one core, the Krocker core, that best represents all of the trends and interpretations found and discussed in Wiesner (2024). Analysis of XRD and magnetic susceptibility data conducted in Wiesner (2024) is also excluded from this paper.

According to the Stratigraphic Code, renaming a formation necessitates an additional justification for the name replacement beyond the renaming of the geographic feature itself (North American Commission on Stratigraphic Nomenclature, 2021). Justifications for a name change could include boundary changes or the discovery of a duplicate name. Thus, the research presented in this paper will assist in the effort to rename this formation by better describing the various characteristics of the rocks in the area. The primary objectives are to: 1) conduct a lithostratigraphic analysis of the Krocker core to determine facies and depositional models; and 2) use multiple datasets to help define formational boundaries and member boundaries associated with the newly renamed "Squaw Bay Formation," which has the name Birdsong Bay Formation proposed for it by the U.S. Geological Survey.

STUDY AREA

The Michigan Basin is a relatively undeformed and roughly circular intracratonic basin filled with approximately 4,000 m of Paleozoic rocks (Howell and van de Pluijm, 1999; Gutschick and Sandberg, 1991). Gutschick and Sandberg (1991) write that the Michigan Basin was likely located on the equator during the Late Devonian but shifted south during the Frasnian and north during the Famennian (Figure 1). The Michigan Basin is surrounded by the Wisconsin Arch to the west, the Wisconsin highlands to the north, the Canadian shield to the northeast, the Algonquin arch to the east, the Findlay arch to the southeast, and the Kankakee arch to the southwest (Figure 1; Ells, 1979; Currie, 2016). For further information on the geologic setting and basin history see Zambito and

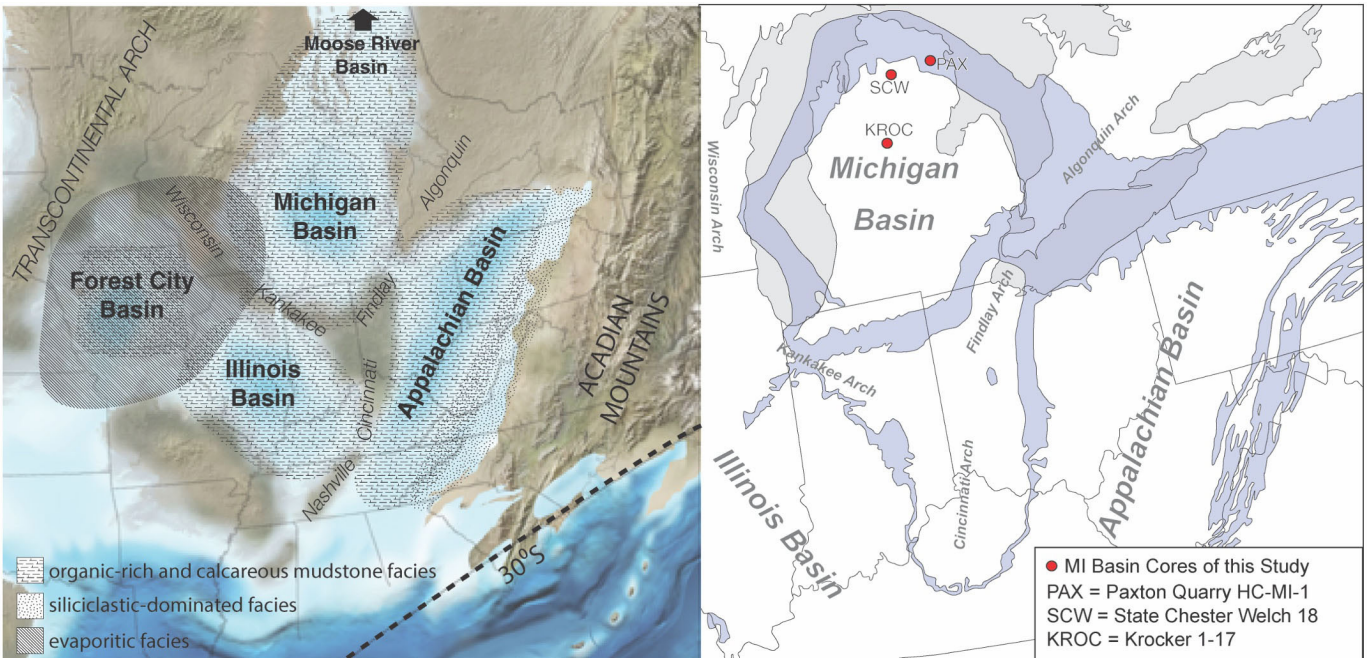

Figure 1. Left: Regional paleogeographic map showing the location of the Michigan Basin in relation to other tectonic basins of the Devonian. Right: Generalized map outlining the Devonian outcrop belt (purple) within the Michigan, Appalachian, and Illinois basins. The location of the three core localities (red dots) studied by Wiesner (2024), including the Krocker 1-17 core, are shown in the Michigan Basin. Paleogeographic maps are adapted from Blakey (2013) and Zambito and Voice (this volume). Devonian outcrop belt map adapted from Zambito and Voice (this volume).

Voice (this volume) and Wiesner (2024).

Data collection was conducted at the Michigan Geological Repository for Research and Education (MGRRE) at Western Michigan University in Kalamazoo, Michigan. This facility houses about 530,000 linear feet of drill core collected as a product of "oil, gas, and mineral exploration; environmental research; and geological mapping projects" (Western Michigan University, 2023).

Core Localities

Three cores, illustrated in Figure 1, were chosen not only because they encompass the entire "Squaw Bay Formation" in their respective areas, but also because they represent the observed variability in the lithologic facies from the center of the Michigan Basin to the margin. While Wiesner (2024) examines all three cores seen in Figure 1, this paper will only discuss the Krocker core. Additional information about the core localities can be found in Wiesner (2024).

METHODS

Lithostratigraphy and Paleoecology

This project analyzes a core through the "Squaw Bay Formation" in the northern Michigan Basin, with a focus on lithostratigraphic and paleoecologic characteristics. The raw data was collected at MGRRE by taking detailed notes and measurements every foot of the Krocker 1-17 core (Figure 2). Observations were taken on the entire "Squaw Bay Formation," including a few feet of the underlying Traverse Group and the overlying Norwood Member of the Antrim Shale. Fossils were identified to the class level and where possible to the genus level. Facies descriptions were compiled and include observation of the distribution of fossils (isolated fossils floating in matrix versus shell beds), sedimentary structures, and other characteristics. For detailed methodology and data collected see Wiesner (2024) and Appendix A therein. With the notes taken while at MGRRE, a stratigraphic column was constructed using Adobe Illustrator.

pXRF

Additional chemostratigraphic data was collected by pXRF analysis (see methods in Zambito et al., 2016). This data was collected by T. Barker-Edwards, M. Giehler, J. Gugino, and I. Johnson at Beloit

College. Further information providing context and demonstrating the significance of each dataset to the stratigraphic interval of study can be found in Wiesner (2024). The relevant data points were graphed and compiled with the stratigraphic column. pXRF data can be found in Appendix B of Wiesner (2024).

RESULTS

Lithology and Paleoecology

The "Squaw Bay Formation" in the Krocker core is bracketed by the underlying Traverse Group limestone and the dominantly carbonaceous black shale of the overlying Norwood Member of the Antrim Shale. There are six distinct lithofacies present in the examined section of the Krocker core (Figure 3). General lithofacies trends can be divided into two units with the first unit, between the depths of about 3,497ft-3,470ft, being a gray calcareous shale with two fossiliferous beds. The second unit

Figure 2. An engineering ruler was used to measure the dimensions of fossils and fossil beds. In addition, changes in sediment color were described as well as the size and location of features, such as pyrite and concretions.

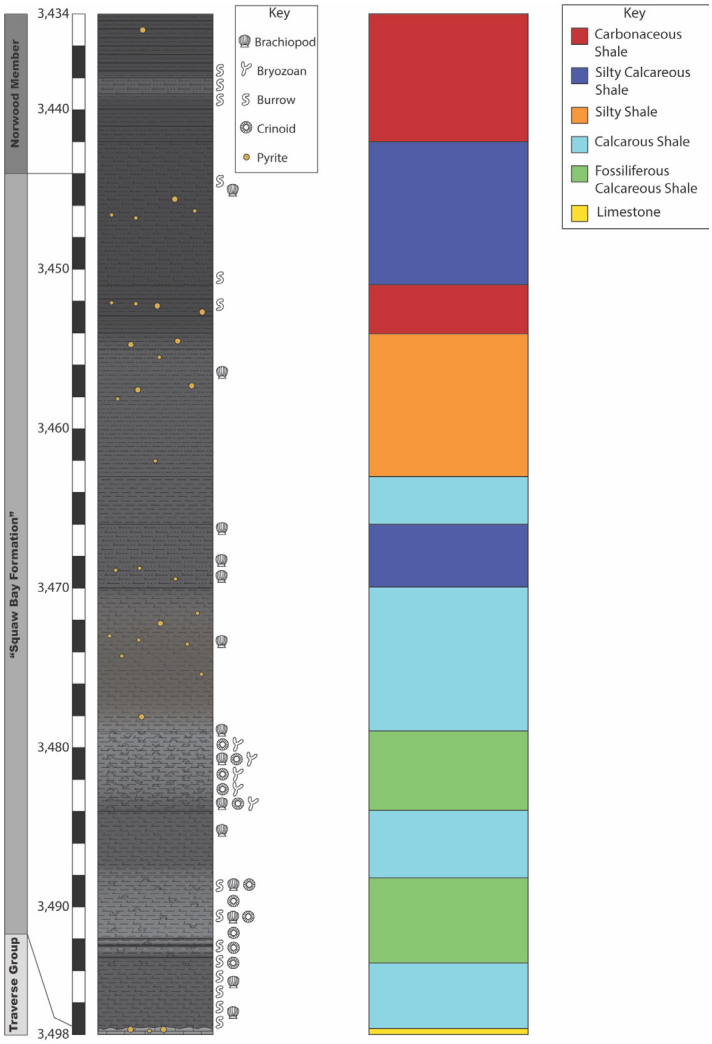

Figure 3. Stratigraphic column of the Krocker 1-17 core oriented next to a simplified column of the lithofacies present in the core. Lithologic symbols are taken from the FGDC Digital Cartographic Standard for Geologic Map Symbolization Section 37 (U.S. Geological Survey, 2006).

of the core, from about 3,470ft-3,444ft, illustrates a gradational change from gray calcareous shale to the black carbonaceous shale of the overlying Norwood Member. This second section of the core consists of mostly carbonaceous and silty black to dark gray shales. Additionally, there is an abundance of bioturbation at the bottom of the core below 3,488ft, with none in the middle of the core. Bioturbation reappears in the top 10ft of the "Squaw Bay" and continues into the Norwood Member.

The two concentrations of pyrite nodules consist of a group of generally smaller nodules (1cm or less in diameter) between 3,478-3,468ft, and a group of larger nodules (larger than 1cm in diameter) between 3,458-3,452ft. Additionally, the fossil distribution is dominantly within the bottom section of the core, with

several isolated brachiopods throughout the middle section of the core.

pXRF

This paper examines Potassium (K), Aluminum (Al), Silicon (Si), Calcium (Ca), and Magnesium (Mg) concentrations from the interval between 3,435ft-3,497ft in the Krocker core. Trendlines in Figure 4 show general increasing amounts of K, Al, and Si up the core. Conversely, amounts of Ca and Mg show a general decreasing trend up section, with Ca having a more pronounced decreasing slope. It is also important to note that the shape of the graphs of K, Al, and Si are similar, and that the shape of the Ca graph is inversely related those elements. One characteristic that is shared by all five graphs is that below a depth of 3,470ft, the data tends to deviate from the trendline more, while above 3,470ft it tends to deviate less.

DISCUSSION

Lithostratigraphic Analysis

When looking at the "Squaw Bay Formation" in the lithofacies column in Figure 3, the underlying boundary with the Traverse Group is a sharp, easily identifiable contact featuring abundant pyrite nodules. Similar sharp boundaries with a drastic change in lithology and primary sedimentary structures, frequently indicate a significant change in water depth of the depositional environments (Adducci, 2015). The upper contact with the Norwood Member of the Antrim Shale is gradational, alternating between calcareous and carbonaceous shales. The change from

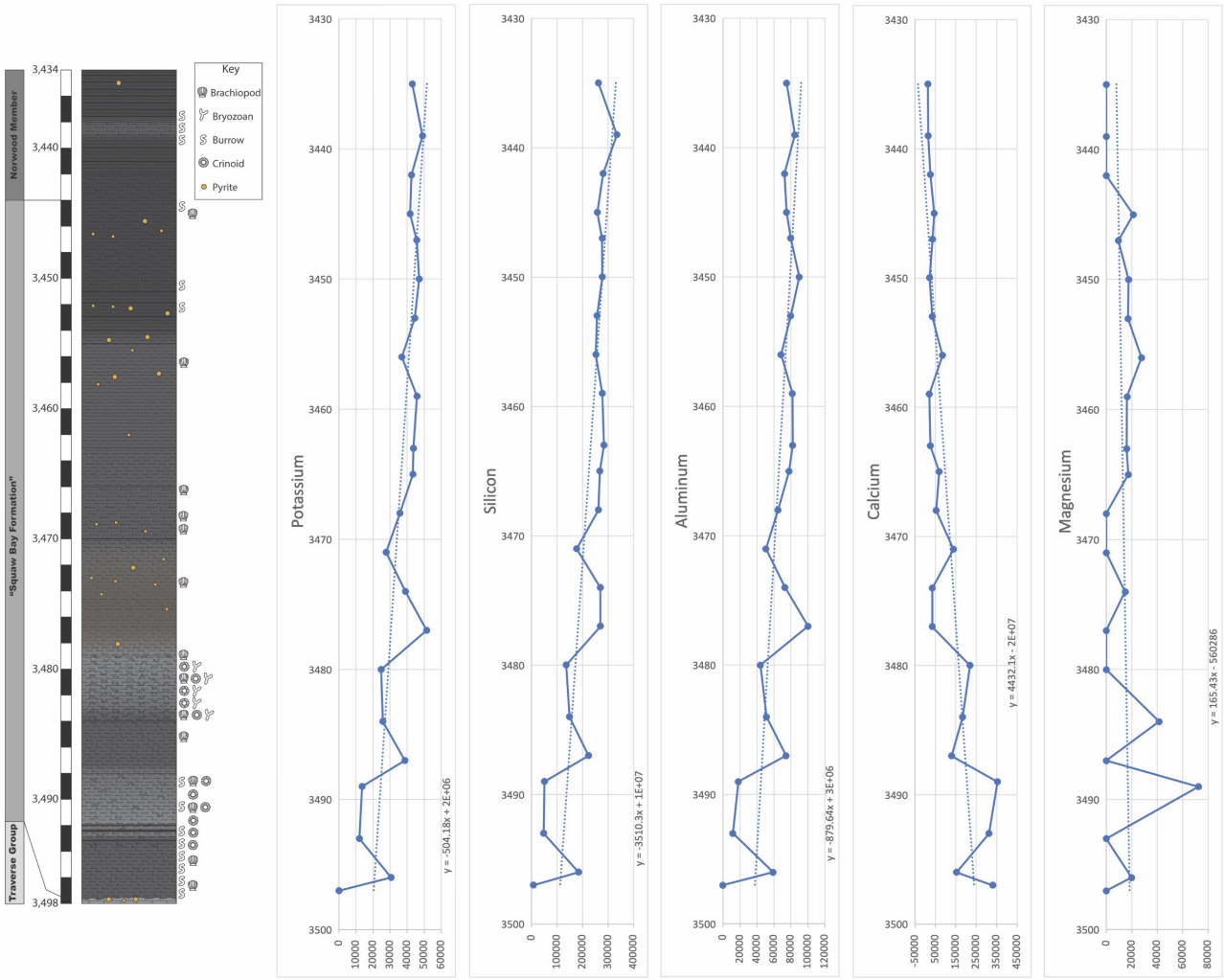

Figure 4. Stratigraphic column of the Krocker 1-17 core aligned with elemental profiles for key elements collected from pXRF analysis. Depth in the core is measured in feet and located on the Y-axis of the graphs, while concentrations of the elements are measured in ppm and located on the X-axis. Note that the trendlines in these graphs encompass most of the core, not just the "Squaw Bay Formation." All five graphs show a notable behavior change around the depth 3,470ft where they all transition from deviating more and frequently from the trendline, to following the trendline more closely.

calcareous to carbonaceous shale shows a deepening upward sequence, marking a transition in depositional environment from shallow marine carbonate deposition to deeper marine sedimentation (Currie, 2016).

A shallow marine carbonate environment interpretation for the lower half of the formation is further evidenced by more abundant fossils. The brachiopod, crinoid, and bryozoan fossils of the core were frequently broken but identifiable, indicating that the environment likely experienced moderate wave or current action that mechanically weathered the fossils (Adducci, 2015) and had sufficient energy and nutrients to sustain filter feeders. The top half of the "Squaw Bay Formation," while being a gradational contact, is mostly black carbonaceous shale. McGregor (1954) states that black shale depositional environments must allow for the preservation of organic matter with the deposited sediment and are often characterized by poor circulation and a lack of oxygen. This description supports a deep marine depositional environment.

The lithofacies patterns in the core also assist in potentially dividing the formation into two members. A division of the formation would feature a lower "Squaw Bay" that is characterized predominantly by gray calcareous shale and higher fossil content that both suggest a shallow marine depositional environment. An upper "Squaw Bay" member is characterized by predominantly black carbonaceous shale and fewer fossils that both suggest a deeper marine depositional environment that is less well circulated and is more dysoxic.

Geochemical Analysis

The pXRF data gathered shows increasing trendlines upsection on the K, Si, and Al graphs and decreasing trendlines upsection on the Ca and Mg graphs (Figure 4). Not only do K, Si, and Al have the same general trendline, their graphs also behave similarly with synchronized excursions in the data. The pattern displayed by these three elements indicates a higher concentration of clay minerals in the cores. Abundances of Al can also be an important indicator of clastic supply to an area (Mastalerz et al., 2019). Thus the increasing levels of Al in the Krocker core indicate an increase in clastic input. Ca and Mg, on the other hand, are good indicators of the carbonate minerals present. There are slightly lower levels of Mg, pointing to higher levels of calcite than dolomite in the shales (Mastalerz et al., 2019). Additionally, the opposite fluctuations in the Ca and Si graphs could indicate that there is a repeating cycle of clastic and carbonate sedimentation in the basin (Currie, 2016).

Within the pXRF graphs for all elements, there is only one easily distinguishable boundary. While contacts between the "Squaw Bay" and the over- and underlying formations were fairly visible in the lithostratigraphic analysis, there is no obvious contact in the pXRF graphs either because there is no data for that section of the core or because there is simply no notable change in the behavior of the graph. However, at around 3,470ft in the Krocker core, the graphs transition from more frequent deviations from the trendline at the bottom of the formation, to more closely following the trendline at the top of the formation, indicating a place where the formation could be subdivided into members. The location of this division corresponds to the changes in lithology and the potential split of the formation proposed during the lithostratigraphic analysis.

CONCLUSIONS

The "Squaw Bay Formation" is not only poorly described, but also its name contains a derogatory term that, following a U.S. Department of Interior secretarial order in 2021, needs to be changed. The goals of the research were to help inform this renaming process by determining the variability of the formation and locating boundaries between over- and underlying formations through analysis of lithostratigraphic, paleoecologic, and geochemical data.

This research worked to determine facies and depositional models in the "Squaw Bay Formation." The combination of datasets available for this analysis indicates that the lower "Squaw Bay" was a shallow marine carbonate environment, further supported by the relatively higher concentrations of Ca and Mg. Up section these features change and K, Si, and Al concentrations all increase, indicating rising sea levels

and a transition to a deep marine environment that is less oxygenated in the upper "Squaw Bay" and Antrim Shale.

This research also aimed to use all datasets to determine formational and member boundaries associated with the "Squaw Bay Formation." The lithostratigraphic analysis indicates a prominent and easily distinguished boundary between the Traverse Group and the "Squaw Bay Formation." This boundary is characterized by an abrupt transition from limestone to calcareous shale, with abundant pyrite nodules and crusts on this surface. However, no dataset examined in the research provided a clear delineation of the "Squaw Bay Formation" from the overlying Norwood Member due to the gradational nature of their contact.

Part of determining the contacts associated with the "Squaw Bay Formation" included determining any subdivisions in the member. Lithostratigraphic and pXRF data supports dividing the formation into two members around 3,470ft in the Krocker core. This division would split the rocks into a lower section of fossiliferous gray calcareous shale with pXRF values that vary more frequently with respect to the trendline, and an upper section of predominantly black calcareous shale with few fossils and pXRF values that more closely follow the trendline of the core. Results discussed in Wiesner (2024) further examine the ways in which XRD and magnetic susceptibility data could support the potential subdivision of the "Squaw Bay Formation."

Further research into the "Squaw Bay" is necessary to definitively locate the boundary between it and the Norwood Member, and is also necessary to determine how the formation could be subdivided. More detailed data collection and analysis specifically in geochemical fields, like XRD, could be useful in these determinations.

ACKNOWLEDGEMENTS

This material is based upon work supported by the Keck Geology Consortium and the National Science Foundation under Grant No. 2050697. Additional thanks to the College of Wooster Geology Department; the Michigan Geological Repository for Research and Education; the Beloit College Geology Department; Drs. Shelley Judge, James Zambito, Peter Voice, and Meagen Pollock; my Keck internship group; and, my friends and family.

REFERENCES

Adducci, J.G., 2015, Geological Controls on Stratigraphy and Sedimentation of the Mississippian Marshal Formation, Michigan Basin, USA [M.S. Thesis]: Western Michigan University, 178 p.

Blakey, R.C., 2013, Deep Time MapsTM – Maps of Ancient Earth, https://deeptimemaps.com/ (accessed April 2022).

Currie, B.J., 2016, Stratigraphy of the Upper Devonian-Lower Mississippian Michigan Basin: Review and Revision with an Emphasis on the Ellsworth Petroleum System [M.S. Thesis]: Western Michigan University, 160 p.

Department of the Interior, 2021, Secretarial Order No. 3404: https://www.doi.gov/sites/doi.gov/files/elips/documents/so-3404-508.pdf (accessed September 2023).

Ells, G.D., 1979, Stratigraphic Cross Sections Extending from Devonian Antrim Shale to Mississippian Sunbury Shale in the Michigan Basin: Michigan Department of Natural Resources, Geological Survey Division Michigan Department of Natural Resources, Geological Survey Division, Report of Investigation 22, 186 p.

Gutschick, P.C., and Sandberg, C.A., 1991, Late Devonian history of Michigan Basin, in Catacosinos, P.A., and Daniels, P.A., Jr., eds., Early Sedimentary Evolution of the Michigan Basin: Geological Society of America, Special Paper 256, p. 181-202, https://doi.org/10.1130/SPE256-p181.

Howell, P., and van der Pluijm, B., 1999, Structural sequences and styles of subsidence in the Michigan Basin: Geological Society of America Bulletin, v. 111, no.7, p. 974-991.

Keck Geology Consortium, 2023, The History of Keck Geology Consortium: https://keckgeology.org/history/ (accessed September 2023).

Mastalerz, M., Drobniak, A., Ames, P., and McLaughlin, P.I., 2019, Application of pXRF

elemental analysis and organic petrography in correlation of Pennsylvanian strata: An example from the Indiana part of the Illinois Basin, USA: International Journal of Coal Geology, v. 216, https://doi.org/10.1016/j.coal.2019.103342.

McGregor, D.J., 1954, Stratigraphic Analysis of Upper Devonian and Mississippian Rocks in Michigan Basin: Bulletin of the American Association of Petroleum Geologists, v. 38, no.11, p. 2324-2356.

North American Commission on Stratigraphic Nomenclature, 2021, North American Stratigraphic Code: Stratigraphy, v. 13, p. 153-204, https://doi.org/10.29041/strat.18.3.01.

Warthin, A.S., and Cooper, G.A., 1935, New formation names in the Michigan Devonian: Journal of the Washington Academy of Sciences, v. 25, no. 12, p. 524-526, http://www.jstor.org/stable/24530378.

Western Michigan University, 2023, Michigan Geological Repository for Research and Education (MGRRE): https://wmich.edu/michigangeologicalrepository (Accessed September 2023).

Wiesner, A., 2024, An Analysis of Stratigraphic, Paleoecologic, and Geochemical Variability in the "Squaw Bay Formation," Michigan Basin [B.S. thesis]: The College of Wooster, 101 p.

Zambito, J.J., McLaughlin, P.I., Haas, L.D., Stewart, E.K., Hurth, M.J., and Bremmer, S.E., 2016, Sampling Methodologies and Data Analysis Techniques for Geologic Materials Using Portable X-Ray Fluorescence (pXRF) Elemental Analysis: Wisconsin Geological and Natural History Survey, Open-File Report WOFR2016-02, 5 appendices, 12 p.

Zambito IV, J.J., and Voice, P.J., this volume, Integrated stratigraphic and paleoenvironmental study of the Middle-Late Devonian carbonate to black shale transition in the Michigan Basin.

KECK Geology Consortium
Learning Science Through Research
Published by the Keck Geology Consortium
Short Contributions
Keck Geology Consortium
Volume 36
May 2024
doi: 10.18277/AKRSG.2024.36.15

GEOCHEMICAL ANALYSIS OF THE MIDDLE TO UPPER DEVONIAN ANTRIM SHALE, KROCKER 1-17 CORE, MICHIGAN BASIN

MIKAYLA C. GIEHLER, Macalester College
Project Advisor: Kelly R. MacGregor

INTRODUCTION

The Middle to Upper Devonian is distinguished by global biotic events attributed to marine anoxia (black shale) and perturbations in the carbon cycle (Becker et al. 2020). While previous studies had documented these events in the North American Appalachian Basin (see House, 2002), less attention has been directed toward discerning analogous global events within the neighboring Michigan Basin. This investigation aims to reconstruct the paleoredox conditions and organic matter production and preservation within the Antrim Shale from the Krocker 1-17 drill core located in the north-central Michigan Basin. Since black shale organic matter is derived from a combination of marine and terrestrial sources, this study utilizes elemental proxies for sedimentation and paleoredox to distinguish terrestrial organic matter input to the basin from primary marine organic matter accumulation.

METHODS

This study focuses on the Krocker 1-17 core (core location and detailed geologic setting provided in Zambito and Voice, this volume). Core measurements and detailed lithological observations were made at the Michigan Geological Repository for Research and Education (MGRRE). A Dremel equipped with a diamond-tipped drill bit (model 7123) was used to cleanse the exterior of the core (to mitigate potential contamination introduced during the coring process). A total of 96 powdered samples from the Krocker 1-17 core were collected (~3 to 4 ft. apart) using a Dremel tool with a tungsten carbide drill bit (model 9906).

Portable x-ray fluorescence (pXRF) analysis was conducted at the Beloit College Department of Geology to discern the elemental composition of the samples obtained from both cores utilizing the Thermo Fisher Scientific Niton XL3t GOLDD+ Handheld XRF Analyzer (see methods in Zambito et al. 2016). Uranium (U), molybdenum (Mo), silicon (Si), and aluminum (Al) were collected by pXRF analysis. Borehole log data including total gamma, potassium (K) and thorium (Th) spectral gamma, as well as Total Organic Carbon (TOC) were provided by MGRRE. U and Mo are used as paleoredox proxies given their tendency to attach to organic matter, which is preserved under low oxygen conditions (Tribovillard et al. 2006). The Si/Al ratio is used as a proxy for detrital sediment input to the study area, with higher values indicating increased quartz influx (Sageman et al. 2003).

RESULTS AND DISCUSSION

As shown in Figure 1, total gamma, U, TOC, and Mo show consistent patterns through the Antrim Shale. For all of these profiles, higher values are observed in the Norwood and Lachine members of the Antrim Shale, while lower values occur in the Paxton Member. In contrast, both K and Th are relatively consistent through the Antrim Shale. The profile of Si/Al shows elevated values in the Norwood Member and consistently low values in the Paxton, similar to the gamma log and concentrations of U, TOC, and Mo; however, whereas the gamma log and concentrations of U, TOC, and Mo all show decreasing trends through the Lachine Member, the Si/Al trend shows an increase. The values of Mo observed, which range well above 200 ppm in the Norwood Member, suggest anoxic conditions on the seafloor (Tribovillard et al.

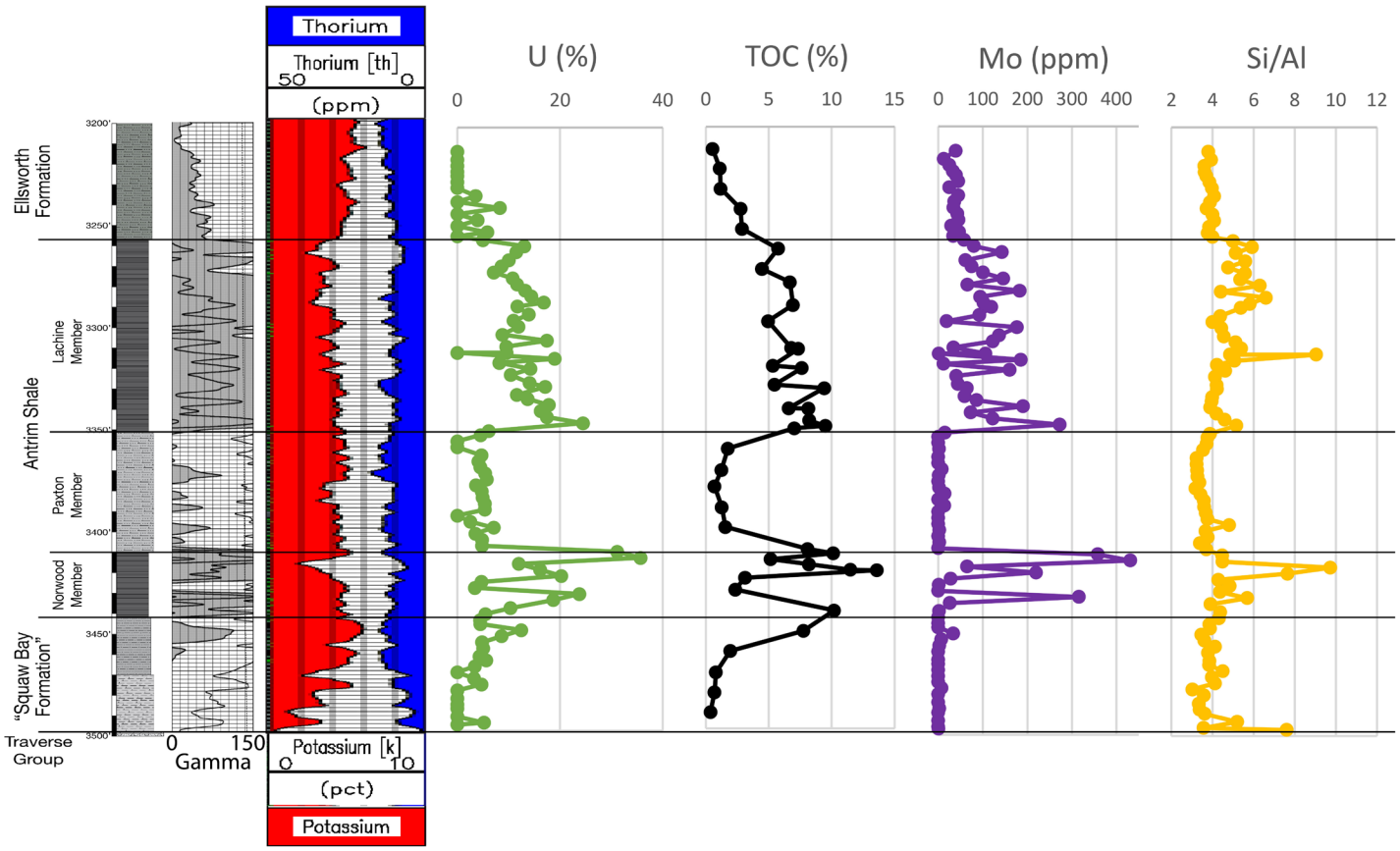

Figure 1. Well logs and geochemical results from the Krocker 1-17 core.

2006).

The similarity of the gamma log and concentrations of U, TOC, and Mo indicate that the gamma log pattern is related to the natural radioactivity of U, and not K and Th in this succession. Correspondence of the concentrations of U, TOC, and Mo is interpreted to suggest that the U and Mo are preserved attached to organic matter (see Tribovillard et al. 2006). The elevated value of Si/Al in the Norwood, which corresponds to elevated TOC values, and slight decrease in values of K when Si/Al is highest is interpreted to represent an interval of high productivity and silica accumulation via the skeletons of radiolarians rather than sediment influx to the basin; indeed, radiolarians are known from this stratigraphic interval (Gutschick and Sandberg, 1991). The increasing trend observed in Si/Al through the Lachine Member coincident with decreasing TOC values may indicate that marine organic matter accumulation is being diluted through this part of the succession due to increased detrital sediment input, though it is unclear if terrestrial organic matter is fluxing to the basin with the detrital sediment. Future analysis of this core will include organic carbon isotopic analysis to analyze sources of organic matter within the basin.

CONCLUSIONS

This study demonstrated that in the Michigan Basin, organic matter preservation is closely associated with anoxic sea floor conditions and because of seafloor geochemical conditions, U and Mo patterns are closely associated with that of TOC. The data set presented herein suggests that most organic matter in the Antrim Shale was likely derived from marine sources, but further isotopic work is necessary to confirm this.

ACKNOWLEDGEMENTS

This material is based upon work supported by the Keck Geology Consortium and the National Science Foundation under Grant No. 20250697. Access to drill core and samples was provided by the Michigan Geological Repository for Research and Education (MGRRE) at Western Michigan University. Special appreciation goes to all contributors to the Keck

2023-2024 research project, including advisors Peter Voice and James Zambito. Additional thanks goes out to Tiffany Barker-Edwards, Jack Gugino, and Isabel Johnson for assistance in pXRF data collection.

REFERENCES

Becker, R. T., Marshall, J. E. A., Da Silva, A.-C., Agterberg, F. P., Gradstein, F. M., and Ogg, J. G., (2020) The Devonian Period. In Gradstein, F. M., Ogg, J. G., Schmitz, M. D., and Ogg, G. M. (Eds.) Geologic Time Scale 2020. Elsevier, p. 733-810

Gutschick, R. C., & Sandberg, C. A. (1991). Upper Devonian biostratigraphy of Michigan Basin. In Catacosinos, P. A. and Daniels, P. A., Jr. (Eds.), Early Sedimentary Evolution of the Michigan Basin, Geological Society of America Special Paper, 256:155–180. https://doi.org/10.1130/spe256-p155

House, M.R. (2002) Strength, timing, setting and cause of mid-Paleozoic extinctions. Palaeogeography, Palaeoclimatology, Palaeoecology, 181(1-3):5-25 https://doi.org/10.1016/S0031-0182(01)00471-0

Sageman, B. B., Murphy, A. E., Werne, J. P., Ver Straeten, C. A., Hollander, D. J., & Lyons, T. W. (2003). A tale of shales: The relative roles of production, decomposition, and dilution in the accumulation of organic-rich strata, Middle-Upper Devonian, Appalachian Basin. Chemical Geology, 195(1–4), 229–273. https://doi.org/10.1016/s0009-2541(02)00397-2

Tribovillard, N., Algeo, T.J., Lyons, T., and Riboulleau, A. (2006) Trace metals as paleoredox and paleoproductivity proxies: An update. Chemical Geology, 232(1–2), 12-32 https://doi.org/10.1016/j.chemgeo.2006.02.012

Zambito IV, J.J., and Voice, P.J., this volume, Integrated stratigraphic and paleoenvironmental study of the Middle-Late Devonian carbonate to black shale transition in the Michigan Basin.

Zambito, J.J., McLaughlin, P.I., Haas, L.D., Stewart, E.K., Hurth, M.J., and Bremmer, S.E., 2016b, Sampling Methodologies and Data Analysis Techniques for Geologic Materials Using Portable X-Ray Fluorescence (pXRF) Elemental Analysis: Wisconsin Geological and Natural History Survey, Open-File Report WOFR2016-02, 5 appendices, 12 p.

KECK Geology Consortium
Learning Science Through Research
Published by the Keck Geology Consortium
Short Contributions
Keck Geology Consortium
Volume 36
May 2024
doi: 10.18277/AKRSG.2024.36.16

EXPLORING THE SUITABILITY OF THE MIDDLE-LATE DEVONIAN ANTRIM SHALE, MICHIGAN BASIN, FOR ORGANIC CARBON ISOTOPIC ANALYSIS

JACK P. GUGINO, Miami University
Project Advisor: Brian S. Currie

INTRODUCTION

Motivation

The Middle-Late Devonian is distinguished by widely acknowledged biotic phenomena attributed to marine anoxia and perturbations in the carbon cycle (Berner et al., 1995). While these events have been extensively documented in strata of the North American Appalachian Basin (Sageman et al, 2003; Zambito et al., 2016a), more attention needs to be directed toward discerning analogous global biotic occurrences within the neighboring Michigan Basin. To accomplish this, stable isotope geochemistry, more specifically organic carbon isotopes (^{12}C and ^{13}C), can be applied to establish periods of global warming and cooling (Mackensen et al, 2019). During photosynthesis, ^{12}C and ^{13}C are fractionated as plants convert CO_2 and sunlight into energy. It requires less energy for a plant to incorporate an atom of the lighter isotope ^{12}C than it does an atom of ^{13}C; therefore, the $\delta^{13}C$ ratio of materials such as carbonate and organic matter can be used to reconstruct changes to the carbon cycle. However, before such experimental techniques are pursued, the carbon fluxes within an isotope system must be understood. This investigation aims to determine the suitability of $\delta^{13}C$ values from organic carbon in Middle-Late Devonian black shale deposits within the Antrim Formation for carbon cycle reconstruction. Since black shale organic matter (OM) is possibly a combination of marine and terrestrial sources, the first step is to utilize elemental proxies for sedimentation to understand terrestrial OM input to the basin. Ultimately, a detailed understanding of local detrital fluxes into the Michigan Basin and potential terrestrial organic carbon input to marine settings is necessary to place the Michigan Basin carbon isotopic profile within the global framework.

Background

Black shales are fine-grained, dark-colored, organic carbon-rich sedimentary rocks that are generally composed of clay minerals, quartz silt, organic matter, and kerogen. Most black shales are found in marine settings (Potter et al., 1980), but they can also form in lacustrine depositional systems (Bohacs et al., 2000). Their black color is due to the presence and abundance of organic matter and pyrite; therefore, the reducing environments where pyrite forms suggest black shales require anoxic water column conditions (Sageman et al., 2003). Moreover, carbonates precipitate either directly or indirectly by organic processes. For instance, direct precipitation occurs when animals or plants secrete lime skeletons, while indirect precipitation happens when biochemical changes in water precipitate carbonate as individual crystals (Selley, 2005). Most ancient carbonate deposition takes place in shallow water depths (<10-20 m) as lime-producing organisms require photosynthesis in oxic environments. Additionally, deposition generally arises in environments with low abundances of siliciclastic input as high abundances disrupt light penetration into waters.

The identified transitions between black shales and carbonates across the Michigan Basin indicate changes between these anoxic (black shales) and oxic (carbonates) environmental conditions. Furthermore, depositional transitions between black shales and carbonates are not exclusive to the Michigan Basin, as the Appalachian Basin underwent similar changes in lithologies associated with marine sequences (Brett

and Baird, 1996). While the primary factors directing these cycles are a matter of debate, they are commonly related to eustatic variations, including glacial melt and growth prompted by global climate changes (Johnson et al., 1985). The research undertaken by Gutschick and Sandberg (1991a and 1991b) summarizes the biostratigraphy and depositional history of the Middle-Late Devonian sequence within the Michigan Basin. These studies suggest that depositional events in the Michigan Basin are linked to Devonian eustatic sea-level fluctuations, aligning with Acadian orogenic tectophases and the deposition of the Catskill Delta in the Appalachian Basin.

GEOLOGIC SETTING

The overall stratigraphy of the Michigan Basin is attributed to a failed rift that occurred ~1.1 bya (Hinze and Chandler, 2020). This process caused weakening in the surrounding lithosphere, and as time progressed, sediment deposition resulted in mass subsidence initiating the formation of the basin. The Late Devonian Michigan Basin emerged as one of several local depressions within the Eastern Interior seaway (Gutschick and Sandberg, 1991a). This body of water occupied the North American craton between the Acadian Mountains and the Transcontinental Arch (Fig. 1). Subsequent basin construction began toward the end of the Middle Devonian due to subsidence driven by the Traverse Group carbonates. The Middle-Late Devonian is characterized by anoxic events associated with perturbations in the global carbon cycle as increased organic carbon production overwhelms the oxygenation of seawater developing organic-rich mud that lithifies to black shale (He et al., 2022). Consequently, units of carbonates and shales transition across the basin and vary in thickness due to accommodation and surrounding terrestrial input (Howell and van der Pluijm, 1999).

This research focuses on the description of the State Chester Welch 18 core within the Middle-Late Devonian Traverse Group and Antrim Formation strata, deposited in the Michigan Basin during the Givetian, Frasnian, and Famennian stages (approximately 385.3 to 359.3 million years ago; Becker et al., 2020). Extracted from the northcentral region of the basin (Fig. 2), the depth of the core

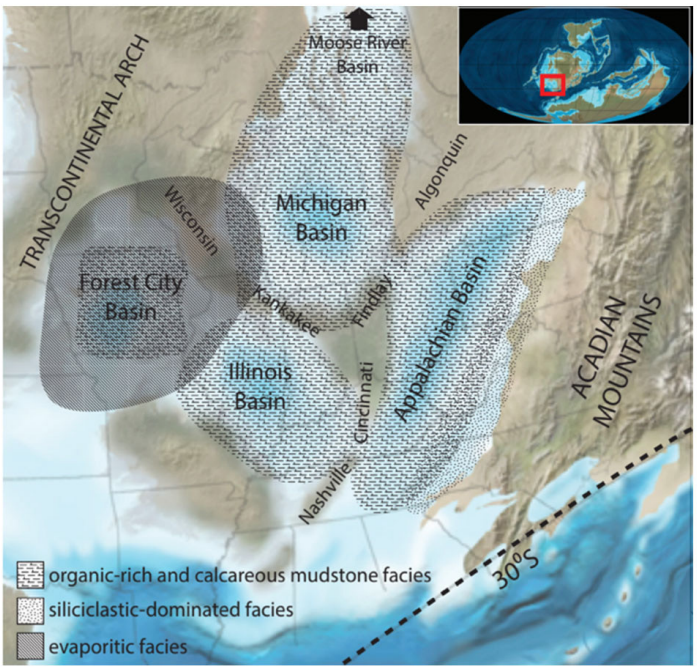

Figure 1. Paleoenvironmental map of the Middle-Late Devonian showcasing various lithologies and depositional locations of the Michigan Basin and surrounding areas. Paleogeographic maps are adapted from Blakey (2013) and Zambito and Voice (this volume).

interval studied ranges from 1,435.1 feet to 1,684.15 feet, with a total length of 249.05 feet.

METHODS

Lithology

Core measurements and detailed lithological observations were made at the Michigan Geological Repository for Research and Education (MGRRE). The description of the State Chester Welch 18 involved examination at the macroscopic level, refined to a scale of one-tenth of a foot. Subsequent analysis focused on delineating facies based on criteria including color, effervescence, fossil abundance, mineral assemblage, bioturbation, and diagenetic features. Following this initial characterization, the core was sampled at three-foot (approximately 1 meter) intervals. A Dremel equipped with a diamond-tipped drill bit (model 7123) operating at ~2,000 revolutions per minute (rpm) was employed to cleanse the core's exterior to mitigate potential contamination introduced during the coring process. A total of 79 samples from the State Chester Welch 18 were systematically extracted from the pre-determined locations along the core using a Dremel outfitted with

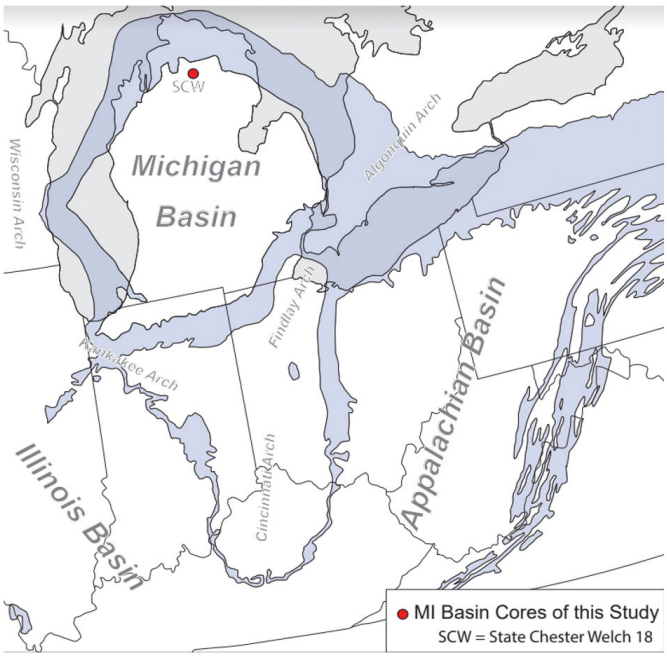

Figure 2. Location of the State Chester Welch 18 drill core used in this study. Purple-gray areas represent the Devonian outcrop belt. Adapted from Zambito and Voice (this volume).

a tungsten carbide drill bit (model 9906) operating at ~5,000 rpm and carefully packaged in 2.0mL plastic vials to preserve their integrity for further analytical procedures.

Geochemistry

Portable x-ray fluorescence (pXRF) analysis was conducted at the Beloit College Department of Geology to discern the elemental composition of the samples obtained from the core utilizing the Thermo Fisher Scientific Niton XL3t GOLDD+ Handheld XRF Analyzer (see methods in Zambito et al., 2016b). To ensure accurate measurements, calibration of the elemental compositions of each sample was executed following the protocol outlined in Rowe et al. (2012) using standards from the pXRF manufacturer, NIST, and the USGS. Elemental proxies for siliciclastic influx (Si, Si/Al, and K) were used to understand changes in detrital influx through time. Individual powdered samples were prepared at Beloit College for future determination of total organic carbon (TOC) and organic stable carbon isotope ratio ($\delta^{13}C$).

RESULTS

Lithology

The stratigraphy of St. Chester Welch 18 core consists of ~249.05 ft of marine sediments transitioning between black shale and carbonate lithologies (Fig. 3). The sequence begins with ~10 ft of the light gray Traverse Group limestone which hosts many fossils (e.g., corals, crinoids, bryozoan, brachiopods, and stromatoporoid) along with various degrees of bioturbation. The Traverse Group's contact with the "Squaw Bay Formation" is at ~1,674.75 ft. The "Squaw Bay" lithology is represented by shifts between light and dark gray where light gray shales host minor evidence of bioturbation and fossils, few pyrite inclusions, and silt laminations. At ~1,645.5 ft, the "Squaw Bay Formation" transitions into the Antrim Shale. The Antrim Shale in this core is further separated into three members: Norwood, Paxton, and Lachine members. The Norwood Member extends for ~44.35 ft and it is the first of the black shales to be observed. This member is very black in color, has trace amounts of pyrite, and exhibits minor interbedded silt laminations. The contact of the Norwood Member with the Paxton Member is at ~1,601.15 ft. This lithology is generally light gray in color with minor transitions between dark gray, has pyrite inclusions, concretions, small bioturbations, and silt laminations. The contact of the Paxton Member with the Lachine Member is at ~1,560 ft. The Lachine Member is mostly black in color with a slight transition into dark grey towards the top of the member. Throughout the member, there are pyrite inclusions, silt laminations, and a minor bioturbated interval. The contact of the Lachine Member with the Ellsworth Formation is at ~1,478 ft. The Ellsworth Formation is light to dark grey, has abundant silt laminations, and transitions to a dark brown towards the end.

Geochemistry

Elemental analysis was performed on all 79 powdered core samples at approximately three-foot intervals across the "Squaw Bay Formation", Antrim Shale (Norwood, Paxton, and Lachine), and Ellsworth Formation. Concentrations of elements of interest (Silicon, Aluminum, and Potassium) collected using pXRF were used to make graphs for sedimentation rate proxies, while Total Organic Carbon (TOC) was originally measured and provided by Dellapenna

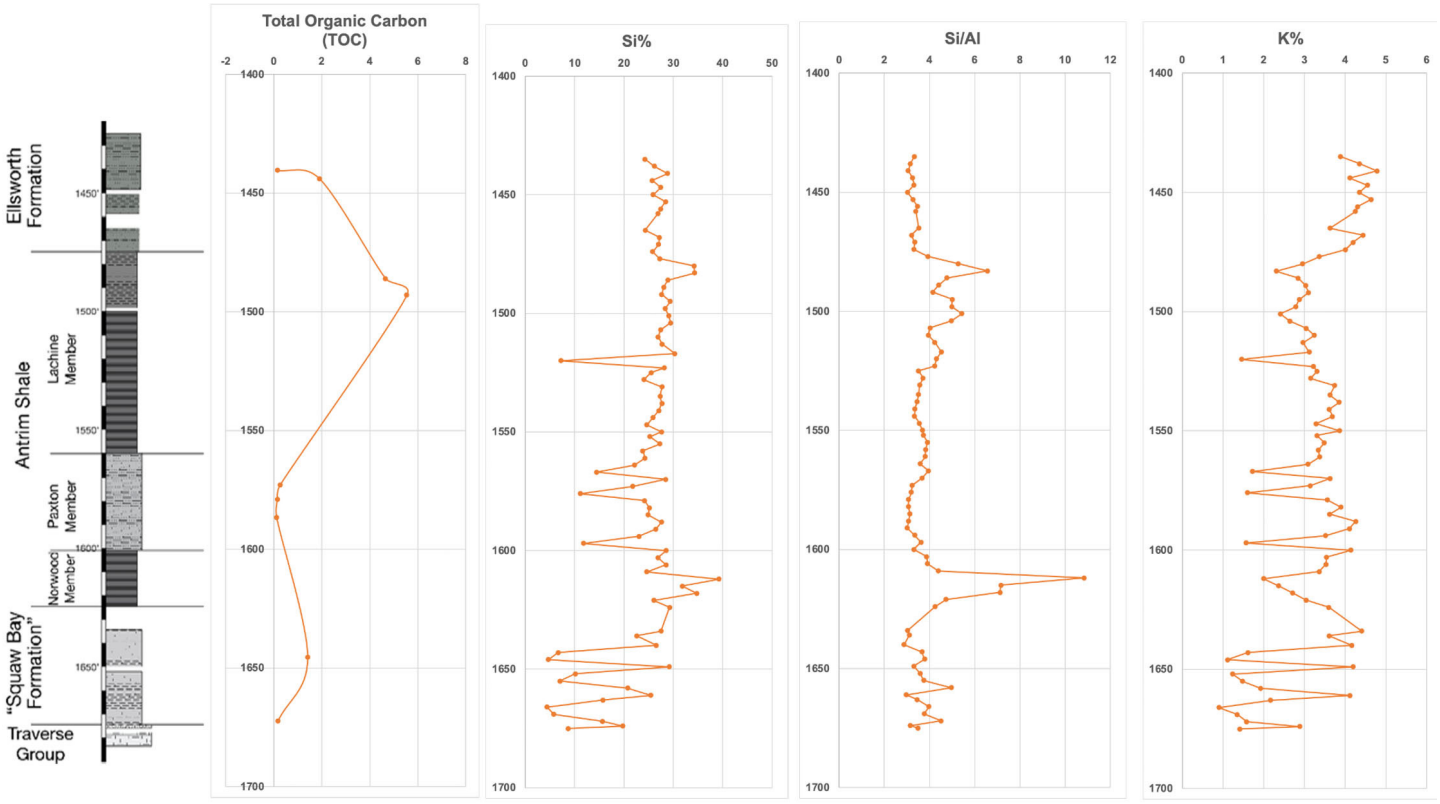

Figure 4. Lithostratigraphy after Zambito and Voice (this volume), Total Organic Carbon (TOC) from Dellapenna (1991), and pXRF trends of the State Chester Welch 18 core showing Si%, Si/Al, and K%.

(1991) as shown in Figure 3. In the "Squaw Bay Formation", TOC initially increases then gradually decreases around 1%, Si% readily fluctuates between 5% and 30% with an increasing trend overall, Si/Al has minor fluctuations confined to ~3 and 4, and K% has many fluctuations between 1% and 5% with a sharp decrease at the end. In the Norwood Member, TOC decreases gradually, Si% increases to 40% then sharply decreases to ~25%, Si/Al spikes to ~11 and drops back down to 4, and K% decreases to 2% before rapidly increasing to ~4%. In the Paxton Member, TOC continues to decrease until 0% and begins to increase, Si% fluctuates between 10% and 30%, Si/Al is consistently between 3 and 4, and K% fluctuates between 1.5% and 4.25%. In the Lachine Member, TOC continues to increase to ~6% before decreasing, Si% remains relatively consistent between 25% and 30% with a spike down to ~8%, Si/Al stays consistently between 3 and 4 as it increases to ~6.5 and sharply decreases to ~3, and K% has minor fluctuates as it decreases to ~2% with one spike down to 1.5% In the Ellsworth Formation, TOC continues to decrease before reaching ~0%, Si% is consistently 25% with slight fluctuations, Si/Al is relatively stable around 3, and K% increases to ~4.5% and continue to have slight fluctuations between 3.5% and 5%.

DISCUSSION

St. Chester Welch 18 is one of two drill cores analyzed both lithologically and geochemically for organic carbon isotope analytical suitability: the second being the Krocker 1-17 (Giehler et al., this volume). Identical lithological and geochemical methodologies were conducted on the Krocker 1-17 samples. Utilizing the same elemental proxies for detrital input dynamics, initial pXRF analysis shows similar trends in sedimentation rate proxies between the two core locations, suggesting that basin-fill dynamics are spatially consistent.

First, TOC provides context on the depositional environment and the conditions under which sediments were deposited. Second, silica content (Si%) provides a measure of the overall abundance of silicate minerals present (e.g., quartz, feldspar, clay). Third, silica to aluminum ratio (Si/Al) is useful for determining the source rock composition and weathering conditions. For instance, aluminum is commonly found in feldspars and clays, which are

susceptible to weathering, while silica is resistant to weathering. Therefore, high Si/Al ratios suggest minimal weathering and a primary source of silicate material, whereas low ratios suggest intense weathering and removal of aluminum-rich minerals. Fourth, potassium content (K%) gives insight into the overall abundance of potassium-bearing minerals in the detrital sediment (e.g., feldspars). Together, these proxies provide valuable insight into the detrital input dynamics of the Michigan Basin further to identify the suitability of organic carbon isotopic analysis.

In the Norwood, Si%, Si/Al, and K% mostly correspond suggesting predominantly clay mineral deposition, though an anomalously high interval of Si%, Si/Al, and TOC (and low K%) is interpreted as high paleoproductivity and biogenic silica production (radiolarians). In the Paxton, all elemental proxies for sedimentation are relatively consistent through time, indicating minimal detrital flux changes. This suggests that the Paxton is an ideal unit to conduct organic carbon isotopic analysis because of the relative stability of detrital influx within that unit as it does not experience any spikes. This stability facilitates distinguishable differences in future isotope ratio analysis as detrital influx does not contaminate the marine signal.

In the Lachine, the overall trend of increasing Si% and Si/Al and corresponding decreasing K and TOC suggests increased detrital input through time. pXRF data highlights different sources of detrital influx between the Lachine and Ellsworth units. This difference was also noticeable in lithologic results, with a visible difference in color and composition between the two units- the Lachine being a darker, pyritic shale and the Ellsworth having thick, interfingering bands of coarser-grained material. Consistent trends in both cores indicate these patterns are similar across the basin, therefore, this study is more reproducible using additional cores. Ultimately, these trends provide the necessary baseline for future work interpreting organic carbon isotopic data.

FUTURE WORK

The preliminary lithological and geochemical investigation of the St. Chester Welch 18 core compared with the Krocker 1-17 core in the Michigan Basin show detrital input dynamics are consistent across time and space. These patterns provide a promising baseline for interpreting organic carbon isotopic data and necessitate further analysis. Ultimately, future work will utilize Total Organic Carbon (TOC) and stable organic carbon isotopes for further assessment of both the Krocker 1-17 and State Chester Welch 18, by conducting isotope ratio mass spectrometry at UC Davis Stable Isotope Facility.

ACKNOWLEDGMENTS

This material is based upon work supported by the Keck Geology Consortium and the National Science Foundation under Grant No. 2050697. Access to drill core and samples was provided by the Michigan Geological Repository for Research and Education (MGRRE) at Western Michigan University. Special appreciation goes to all contributors to the Keck 2023-2024 Michigan Basin research project, including advisors Peter Voice and James Zambito. Additional thanks go out to Tiffany Barker-Edwards, Mikayla Giehler, and Isabel Johnson for assistance in pXRF data collection.

REFERENCES

Becker, R. T., Marshall, J. E. A., Da Silva, A.-C., Agterberg, F. P., Gradstein, F. M., and Ogg, J. G., (2020) The Devonian Period. In Gradstein, F. M., Ogg, J. G., Schmitz, M. D., and Ogg, G. M. (Eds.) Geologic Time Scale 2020. Elsevier, p. 733-810

Berner, R. & Maynard, J. & Scheckler, Stephen. (1995). Late Devonian oceanic anoxic events and biotic crises: "Rooted" in the evolution of vascular plants. GSA Today. 5. 45, 64-66.

Blakey, R.C., 2013, Deep Time MapsTM – Maps of Ancient Earth, https://deeptimemaps.com/ (accessed April 2022).

Bohacs, K. M., Carroll, A. R., Neal, J. E., & Mankiewicz, P. J. (2000). Lake-basin type, source potential, and hydrocarbon character: An integrated sequence-stratigraphic–geochemical framework. In Gierlowski-Koredesch, E. H. and Kelts, K. R. (Eds.) Lake basins through space and time, AAPG Studies in Geology, 46: 3-34.

Brett, C. E., & Baird, G. C. (1996). Middle Devonian sedimentary cycles and sequences in the Northern Appalachian Basin. In Witzke, B. J., Ludvigson, G. A., and Day, J. (Eds.) Paleozoic Sequence Stratigraphy; Views from the North American Craton. Geological Society of America Special Paper, 306: 213-241. https://doi.org/10.1130/0-8137-2306-x.213

Dellapenna, T. M. (1991) Sedimentological, structural, and organic geochemical controls on natural gas occurrence in the Antrim Formation in Otsego County, Michigan. Unpublished MS thesis, Western Michigan University, 147 p.

Giehler, M.C., this volume, Lithological and geochemical analysis of the Middle to Upper Devonian Antrim Shale, Krocker 1-17 Core, Michigan Basin.

Gutschick, R. C., & Sandberg, C. A. (1991a). Upper Devonian biostratigraphy of Michigan Basin. In Catacosinos, P. A. and Daniels, P. A., Jr. (Eds.), Early Sedimentary Evolution of the Michigan Basin, Geological Society of America Special Paper, 256:155–180. https://doi.org/10.1130/spe256-p155

Gutschick, R. C., & Sandberg, C. A. (1991b). Late Devonian history of Michigan Basin.In Catacosinos, P. A. and Daniels, P. A., Jr. (Eds), Early Sedimentary Evolution of the Michigan Basin, Geological Society of America Special Paper, 256:181–202. https://doi.org/10.1130/spe256-p181

He, R., et al. (2022) Devonian upper ocean redox trends across Laurussia: Testing potential influences of marine carbonate lithology on bulk rock I/Ca signals. Frontiers in Marine Science 9: 874759.

Hinze, W. J. and Chandler, V. W. 2020, Reviewing the Configuration and Extent of the Midcontinent Rift, Precambrian Research, 342, 105688, doi: 10.1016/j.precamres.2020.105688.

Howell, Paul D., and Ben A. Van Der Pluijm. (1999) Structural sequences and styles of subsidence in the Michigan Basin. Geological Society of America Bulletin 111(7) 1999: 974-991

Johnson, J.G., Klapper, G., & Sandberg, C. A. (1985). Devonian eustatic fluctuations in Euramerica. Geological Society of America Bulletin, 96(5), 567-587. https://doi.org/10.1130/0016-7606(1985)96<567:defie>2.0.co;2

Mackensen, A., & Schmiedl, G. (2019). Stable carbon isotopes in paleoceanography: Atmosphere, oceans, and sediments. Earth-Science Reviews, 197, 102893. https://doi.org/10.1016/j.earscirev.2019.102893

Potter, P. E., Maynard, J. B., & Pryor, W. A. (1980). Sedimentology of Shale. Springer-Verlag, Berlin, 313 p. https://doi.org/10.1007/978-1-4612-9981-3

Rowe, H., Hughes, N., and Robinson, K. (2012). The quantification and application of handheld energy-dispersive x-ray fluorescence (ED-XRF) in mudrock chemostratigraphy and geochemistry. Chemical Geology 324: 122-131.

Sageman, B. B., Murphy, A. E., Werne, J. P., Ver Straeten, C. A., Hollander, D. J., & Lyons, T. W. (2003). A tale of shales: The relative roles of production, decomposition, and dilution in the accumulation of organic-rich strata, Middle-Upper Devonian, Appalachian Basin. Chemical Geology, 195(1–4), 229–273. https://doi.org/10.1016/s0009-2541(02)00397-2

Selley, R. C. (2005). Sedimentary rocks | limestones. In Selley, R. C., Cocks, R. M., and Plimer, I. R. (Eds.) Encyclopedia of Geology, 107–113. https://doi.org/10.1016/b0-12-369396-9/00305-1

Zambito, J. J., Joachimski, M. M., Brett, C. E., Baird, G. C., & Sarah Aboussalam, Z. (2016a). A carbonate carbon isotope record for the Late Givetian (Middle Devonian) global Taghanic Biocrisis in the type region (Northern Appalachian Basin). In Becker, R. T., Königshof, P., and Brett, C. E. (Eds Devonian Climate, Sea Level and Evolutionary Events, Geological Society, London, Special Publications, 423: 223–233. https://doi.org/10.1144/sp423.7

Zambito, J.J., McLaughlin, P.I., Haas, L.D., Stewart, E.K., Hurth, M.J., and Bremmer, S.E., 2016b, Sampling Methodologies and Data Analysis Techniques for Geologic Materials Using Portable X-Ray Fluorescence (pXRF) Elemental Analysis: Wisconsin Geological and Natural History Survey, Open-File Report WOFR2016-02, 5 appendices, 12 p.

Zambito IV, J.J., and Voice, P.J., this volume, Integrated stratigraphic and paleoenvironmental study of the Middle-Late Devonian carbonate to

black shale transition in the Michigan Basin.

KECK Geology Consortium
Learning Science Through Research
Published by the Keck Geology Consortium
Short Contributions
Keck Geology Consortium
Volume 36
May 2024
doi: 10.18277/AKRSG.2024.36.17

MAGNETIC SUSCEPTIBILITY OF SEDIMENTARY STRATA IN THE LATE DEVONIAN ANTRIM FORMATION OF THE MICHIGAN BASIN

TIFFANY BARKER-EDWARDS, University of Texas at San Antonio
Project Advisors: Peter J. Voice and James J. Zambito IV

INTRODUCTION

This study utilizes the magnetic susceptibility (MS) of sedimentary strata to correlate the Late Devonian Antrim Formation black shale and calcareous mudstone across the Michigan Basin as well as with a previously published MS profile from contemporaneous, shale-dominated strata from the Illinois Basin. MS can be used as a proxy for changes in material composition, which is linked to paleoclimate-controlled sediment fluxes and depositional environments.

The Devonian Period of Earth's history contains many geological events of environmental instability, often tied to sea-level fluctuations (Becker at al., 2020). The cores interpreted in this study include strata from the Middle-Upper Devonian, specifically the Givetian, Frasnian, and Famennian stages.The studies of Gutschick and Sandberg (1991a,b) provide the basis for much of our understanding of the biostratigraphy and depositional history of the Middle-Late Devonian succession in the Michigan Basin, including repeated transgressive-regressive cycles.

The Acadian Orogeny is a major Devonian mountain-building event in eastern North America, resulting from the collision of the eastern margin of Laurentia with a series of landmasses (Fig. 1; Ver Straeten, 2010). In the Appalachian Basin, the alternating sediment types (carbonate versus siliciclastic) record a cyclic series of sedimentary basin responses to tectonic events (tectophases) in the Acadian Orogeny (Ver Straeten, 2010). Subsidence during the Acadian Orogeny created a deep anoxic sea floor depositional environment within the Appalachian Basin; anoxic

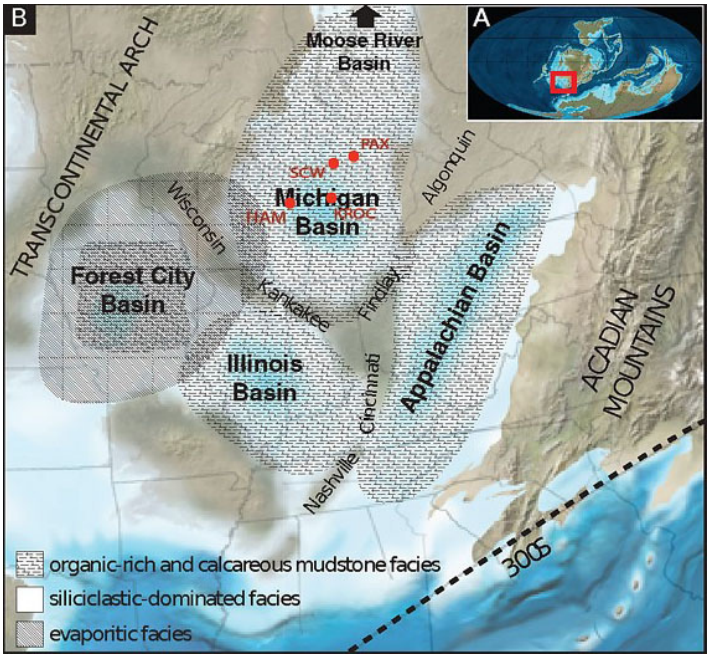

Figure 1. A) Global paleogeographic map for the Devonian (red box is location of panel B). Paleogeographic map of a portion of North America. Location of four rock cores analyzed in this study, the Krocker (KROC), Paxton Quarry (PAX), State Chester Welsch (SCW), and State Hamlin (HAM). Paleogeographic maps are adapted from Blakey (2013) and Zambito and Voice (this volume)

deposits (black shale) are also seen in the Michigan Basin at this time, though Michigan Basin subsidence was not necessarily tectonic (Zambito and Voice, this volume). These periods of black shale deposition align with major global events and can be used to create an event stratigraphic framework (Becker et al., 2020). Paleoclimate-controlled sediment fluxes and depositional environments are influenced by sea level changes (local and those related to global events) and therefore have the potential to record global events. For more information on the geological setting of the study area, see Zambito and Voice (this volume).

METHODS

Data Collection

The magnetic susceptibility of sediment is related to the concentration of detrital-dominated paramagnetic and ferrimagnetic minerals and is therefore a proxy for detrital influx (Ellwood et al. 2011). Significant magnetic minerals are either in the iron-titanium-oxygen (FeTiO) group or the iron-sulfur (FeS) group; each mineral or rock has a different average susceptibility (SI) value based on its composition. There are two basic sources of magnetic minerals in carbonates, authigenic and detrital minerals. Authigenic magnetic minerals are commonly magnetite, hematite, siderite, etc. The occurrence and concentrations of these minerals are related to the local sedimentary setting (Zhang et al., 2000). Detrital magnetic minerals come from the erosion and accumulation of rock fragments, sediment, or other materials. The occurrence and concentration of these minerals is therefore related to the sediment already present within the sedimentary environment.

The Terraplus KT-10R v2 Magnetic Susceptibility Meter was used to collect data approximately every foot along a flat surface of the cores. The measurement sequence is as follows; a free air measurement followed by a sample measurement then the final free air measurement. The sample measurement involves placing the oscillator coil directly on to the surface of the core being measured. The complete sequence takes 7 seconds to complete after which the SI unit appears on the screen. Excel was used to plot the data collected with the Terraplus MS Meter, as the device maintains an excel file with the values recorded.

Converting MS Data

The Terraplus KT-10R v2 Magnetic Susceptibility Meter outputs magnetic susceptibility as volume susceptibility based on the diameter of core input into the instrument. Ellwood et al (2011) suggest presenting magnetic susceptibility data as δMS, which is dimensionless and allows direct comparison to other datasets. To convert volume susceptibility (k) data to mass susceptibility ($\chi\rho$) data for conversion to δMS, the following formula is used: $\chi\rho = k/\rho$, where ρ = density (g/cm^3). The following density values were used when converting MS values, based on the average density for the strata studied from previously collected density values from drill plug analysis: lower, calcareous Squaw Bay (ρ = 2.734, n = 10); upper Squaw Bay (ρ = 2.605, n = 9); Norwood (ρ = 2.458, n = 12); Paxton (ρ = 2.654, n = 19); Lachine (ρ = 2.479, n = 32); and Ellsworth (ρ = 2.689, n = 15).

RESULTS

The magnetic susceptibility data was collected from rock cores taken from three different areas within the Michigan Basin; in this paper, only the data from the Krocker 1-17 core is presented (Fig. 2). The stratigraphic succession studied in the Krocker (KROC) core is 280 ft thick. In ascending order, there are the Traverse Group, the "Squaw Bay Formation", the Antrim Shale (which includes the Norwood, Paxton, and Lachine Members), and the lower Ellsworth Formation. As seen in Figure 3, the "Squaw

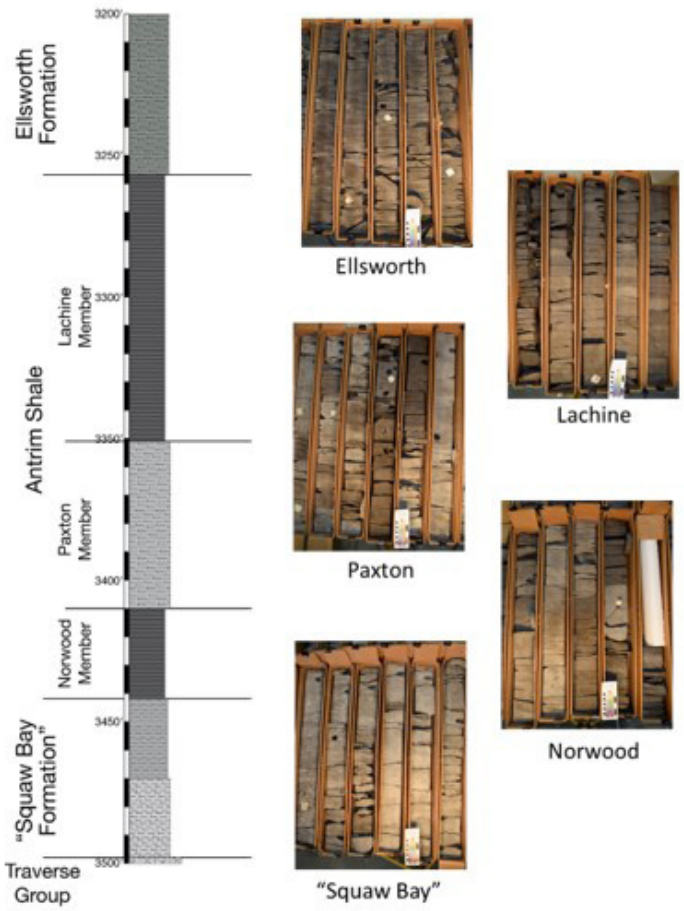

Figure 2. Stratigraphic section of the Krocker Core showing unit thicknesses, changes in lithology, and stratigraphic units. Pictures of the rock core were taken at the Michigan Geological Repository for Research and Education.

Bay Formation" and Norwood have δMS values which occur in the -0.4 to 0.4 range. The Paxton has δMS values which are slightly higher than the Norwood and around 0.0 to 0.6. The Lachine typically has δMS values in the 0.0 to 0.4 range. The Ellsworth has δMS values which occur in the 0.4 to 0.8 range.

DISCUSSION

Visual characteristics of rock cores can also be analyzed to understand the history of each formation (Fig. 2). Gray shales are typically more fossiliferous and have intense bioturbation, consistent with rock found within the "Squaw Bay Formation", Paxton Member of the Antrim Shale, and the Ellsworth Formation. During these times, relatively more clastic sediment was deposited into the basin. These units tend to have higher MS values indicating a decrease in sea level during time of deposition and increased detrital influx (Fig. 3). Darker shales present in the Norwood and Lachine members illustrate times of sea level rise and typically display lower MS values (Fig. 3). During these times there was an increase in organic matter preservation and less detrital clastic input. Shifts seen along the magnetic susceptibility profiles align with boundaries of lithostratigraphic units, suggesting abrupt changes in detrital influx at unit boundaries.

Using the converted MS data makes comparison of the Michigan Basin Krocker 1-17 core with previously published data from the "Bullitt County Core" from Kentucky (Over et al., 2019) in the southern Illinois Basin possible. The magnetic susceptibility basinal profiles of the Michigan and Illinois basin cores appear to show similar MS patterns within biostratigraphically correlated stratigraphic intervals. Both basins likely received sediment input from the Acadian Orogeny but have a slight difference in proximity to the source (Fig. 1).

CONCLUSION

In the Michigan Basin, a MS profile through the basinal Krocker 1-17 core shows that MS patterns correspond to lithostratigraphic units. For some of these units the MS patterns are similar among the cores, though not for all units. Preliminary

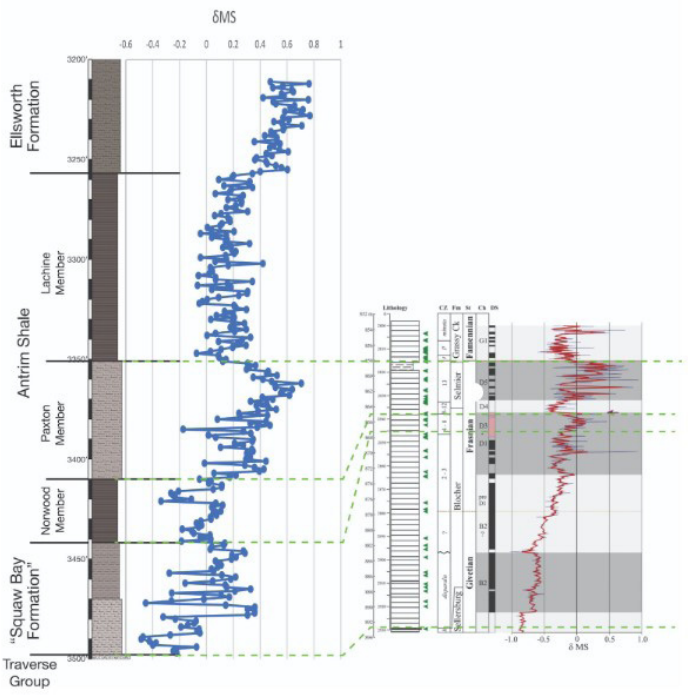

Figure 3. Location of the State Chester Welch 18 drill core used in this study.The converted MS data of the Krocker 1-17 core plotted next to MS data from the Bullitt County Core located in the Illinois Basin (Over, et al., 2019). Corresponding biostratigraphic intervals are denoted with green dashed lines.

interpretation is that MS patterns are a result of proximity to sediment source (Acadian Orogeny versus Transcontinental Arch) as well as intrabasinal early diagenetic processes (pyrite mineralization). Furthermore, the lithostratigraphic units in these cores may not be chronostratigraphically equivalent.

This study also compares the Michigan Basin MS basinal profile (Krocker 1-17 core) with previously published data from the "Bullitt County Core" from Kentucky, in the southern Illinois Basin (Over et al., 2019). Within a biostratigraphic framework, the Michigan and Illinois Basin cores express similar MS patterns. This is possibly because sediment input to these two locations is primarily sourced from the Acadian Orogeny, and the depositional environment and therefore early diagenetic processes, are similar. Future work could combine mineralogical analysis with the MS profiles to decipher the source of magnetic susceptibility, currently hypothesized to be driven by ilmenite concentration.

ACKNOWLEDGEMENTS

This material is based upon work supported by the

Keck Geology Consortium and the National Science Foundation under Grant No. 2050697. Access to drill core and samples provided by the Michigan Geological Repository for Research and Education (MGRRE) at Western Michigan University. I would like to thank Jay Zambito and Peter Voice for advising this project, as well as student colleagues M. Giehler, J. Gugino, I. Johnson, H. O'Bryan, C. Quiroz, L. Trong, A. Wiesner, and M. Winget for their encouragement and friendship during the project.

REFERENCES

Becker, R.T., Marshall, J.E.A., Da Silva, A.-C., Agterberg, F.P., Gradstein, F.M., and Ogg, J.G., 2020, The Devonian Period, in Gradstein, F.M., Ogg, J.G., Schmitz, M.D., and Ogg, G.M. eds., Geologic Time Scale 2020, Elsevier, p. 733–810, doi:10.1016/B978-0-12-824360-2.00022-X.

Blakey, R.C., 2013, Deep Time MapsTM – Maps of Ancient Earth, https://deeptimemaps.com/ (accessed April 2022).

Ellwood, B., Tomkin, J., El Hassani, A., Bultynck, P., Brett, C., Schindler, E.& Feist, R., and Bartholomew, A., 2011, A climate-driven model and development of a floating-point time scale for the entire Middle Devonian Givetian Stage: A test using magnetostratigraphy susceptibility as a climate proxy. Palaeogeography Palaeoclimatology Palaeoecology. 304. 85-95. doi:10.1016/j.palaeo.2010.10.014.

Gutschick, R. and Sandberg, C. 1991a, Late Devonian history of Michigan Basin. Early Sedimentary Evolution of the Michigan Basin. GSA Special Papers. doi:10.1130/SPE256-p181.

Gutschick, R. and Sandberg, C. 1991b, Upper Devonian biostratigraphy of Michigan Basin. Early Sedimentary Evolution of the Michigan Basin. GSA Special Papers. doi:/10.1130/SPE256-p155

Over, D., Hauf, E., Wallace, J., Chiarello, J., Gilleaudeau, G., and Song, Y., 2019, Conodont biostratigraphy and magnetic susceptibility of Upper Devonian Chattanooga Shale, eastern United States: Evidence for episodic deposition and disconformities. Palaeogeography, Palaeoclimatology, Palaeoecology. 524. doi:10.1016/j.palaeo.2019.03.017.

Ver Straeten, C.A., 2010, Lessons from the foreland basin: Northern Appalachian basin perspectives on the Acadian orogeny, From Rodinia to Pangea: The Lithotectonic Record of the Appalachian Region, Richard P. Tollo, Mervin J. Bartholomew, James P. Hibbard, Paul M. Karabinos (251-282) doi: 10.1130/2010.1206(12).

Zambito IV, J.J., and Voice, P.J., this volume, Integrated stratigraphic and paleoenvironmental study of the Middle-Late Devonian carbonate to black shale transition in the Michigan Basin.

Zhang, S., Wang, X., and Zhu, H., 2000, Magnetic Susceptibility Variations of Carbonate Controlled by Sea-Level Changes. Sci. China Ser. D-Earth Sci. 43, 266–276. doi.org/10.1007/BF02906822.

KECK Geology Consortium
Learning Science Through Research
Published by the Keck Geology Consortium
Short Contributions
Keck Geology Consortium
Volume 36
May 2024
doi: 10.18277/AKRSG.2024.36.18

CHARACTERIZING THE SEDIMENT SOURCE OF THE ELLSWORTH FORMATION OF THE MICHIGAN BASIN USING LITHOSTRATIGRAPHY AND CHEMOSTRATIGRAPHY

ISABEL R. JOHNSON, Beloit College
Project Advisor: James J. Zambito IV

INTRODUCTION

This study aims to litho- and chemostratigraphically characterize the Ellsworth Formation in the Michigan Basin. The stratigraphic relationship between the alternating green-gray silty shale of the Ellsworth Formation and the underlying black shale of the Antrim Formation varies in the literature (Fig. 1; Gutschick and Sandberg, 1991; Catacosinos et al., 2000; Currie, 2016). The differences in proposed relationships are substantial, with implications for chronostratigraphy in the Michigan Basin. This project uses litho- and chemostratigraphy to define the base of the Ellsworth in one core from the north-central Michigan Basin, as well as the amount of lithologic and chemostratigraphic variation within the Ellsworth. These analyses were used to characterize the sediment source in order to better understand and constrain the Ellsworth Formation.

Geologic Setting

This study focuses on the Late Devonian (Fammenian) Ellsworth Formation and upper portion of the Antrim Formation which contains the Lachine and Upper Members, which were deposited approximately 365 mya (Palmer, 1983; Gutschick and Sandberg, 1991). As shown in Figure 1, the green-gray silty shale of the Ellsworth Formation has previously been interpreted as being deposited contemporaneously with the black shale of the upper member of the Antrim Formation (Gutschick and Sandberg, 1991), as a unit that occurs stratigraphically above both the Lachine and the Upper Antrim (Catacosinos, 2000), or as a unit that occurs between the black shales of the Lachine and Upper Antrim and extends into the eastern half of the Lower

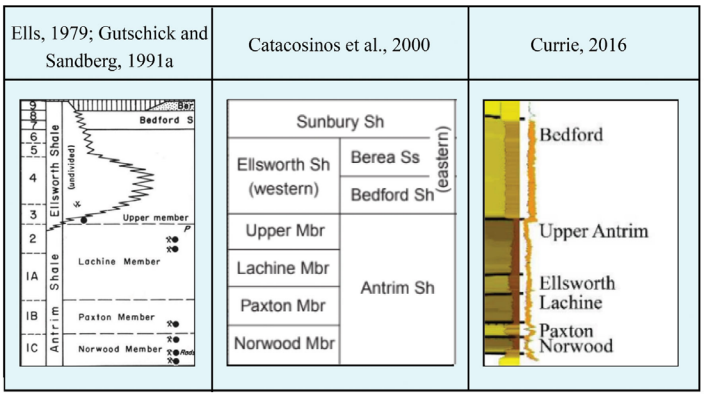

Figure 1. Differing interpretations in the literature of the stratigraphic relationships between the Lachine Member, Ellsworth Formation, and Upper Antrim Member. Modified from Gustchick and Sandberg, (1991), Catacosinos and others (2000), and Currie (2016).

Peninsula (Currie, 2016). The Antrim Shale Formation of the Michigan Basin is generally known as a period of slow accumulating hemipelagic sediments in an oxygen-starved basin, high in organic material and with no evidence of upwelling (Gutschick and Sandberg, 1991). In the later parts of the Famennian, a shift in sedimentation began, marked by the appearance of the Ellsworth Formation silty shales prograding into the basin. The green-gray silty shale of the Ellsworth Formation deltaic sediments were transported from west to east, originating from the Wisconsin Arch (Ells, 1979; Gutschick and Sandburg, 1991).

Previous Stratigraphic Studies

Gutschick and Sandberg (1991) describe the Antrim and Ellsworth as deposited contemporaneously and intertonguing at this time (Fig. 1). They describe the Ellsworth being thickest in the west and thinning to the east but not reaching the easternmost side of the

Michigan Basin, as the Antrim Shale is deposited around the Ellsworth wedge (Fig. 1). In the late Famennian, the Ellsworth Delta retreated and the slow accumulation of anoxic, organic-rich clay sediments that make up the Upper Antrim resumed across most of the basin according to Gutschick and Sandberg (1991) as shown in Figure 1.

However, the most recent stratigraphic column produced by the Michigan Geological Survey presents a different stratigraphic interpretation. The chart constructed by Catacosinos et al. (2000) placed the Antrim Shale Formation, including the Upper Antrim Member, to be stratigraphically under the Ellsworth Shale Formation (Fig. 1). This suggests that the Antrim Shale was completely deposited before the Ellsworth Formation prograded into the basin and the Antrim and Ellsworth do not interfinger (Catacosinos et al., 2000) as shown in Figure 1.

More recently, Currie (2016) suggested that the Ellsworth Formation occurs stratigraphically above the Lachine Member, and uniformly thins to the east but reaches the easternmost edge of the basin (Fig. 1). Currie (2016) places the Upper Antrim Member as being deposited on top of the Ellsworth (Fig.1).

METHODS

Johnson (2024) studied two cores from the Michigan Geological Repository for Research and Education (MGRRE). Herein, results are summarized using only one core: St. Chester Welch #18 (see Fig. 3 of Zambito and Voice, this volume). The St. Chester Welch #18 core provides sequences characteristic of shallower depositional systems during the Late Devonian. Using this core allows for the characterization of the sediment that would have been deposited closer to the source that fed the Ellsworth Delta. It should be noted that this core does not show the upper contact of the Ellsworth Formation and overlying units, so the succession in this study reaches an indeterminable portion within the Ellsworth Formation.

For a detailed lithologic analysis, Ellsworth siltstone laminae thicknesses were measured. For elemental and mineralogical analyses of these two cores, pXRF and XRD were used, respectively. For further details and information on methods used in this study, see Johnson (2024).

RESULTS

Lithology

The Lachine Member in the St. Chester Welch #18 core is a dark, black homogenous shale in which laminations were visible with a hand lens (Fig. 2). The transition from the Lachine Member into the Ellsworth becomes highly interbedded with siltstone and shale laminae almost immediately at the contact (Fig. 2). Up section, the siltstone laminae are a light green-gray color and the shale laminae are a dark gray to gray color (Fig. 2). The green-gray siltstone laminations rarely exceeded 1.5 cm. thick, but the thickest observed were 3 cm and 9.1 cm (Fig. 3). The siltstone laminae in this core were thicker near the contact with the Lachine Member, and become thinner upsection (Fig. 3). These thick laminae seemed to occur in intervals, with several feet of thin laminae between the next thick laminae interval (Fig. 3). For detailed laminae thicknesses see Appendix B in Johnson (2024).

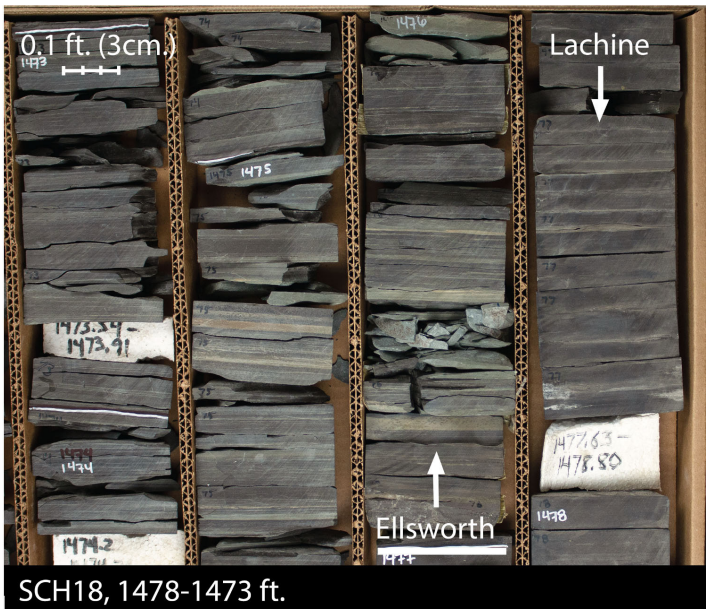

Figure 2. Photograph of the succession of the St. Chester Welch #18 (SCH18) core where the contact between the Lachine Member of the Antrim Formation and the Ellsworth Formation occurs. Photograph shows the St. Chester Welch #18 core from 1478 ft - 1473 ft, and the contact between the Lachine Member and the Ellsworth Formation occurs at 1477 ft (indicated by arrows).

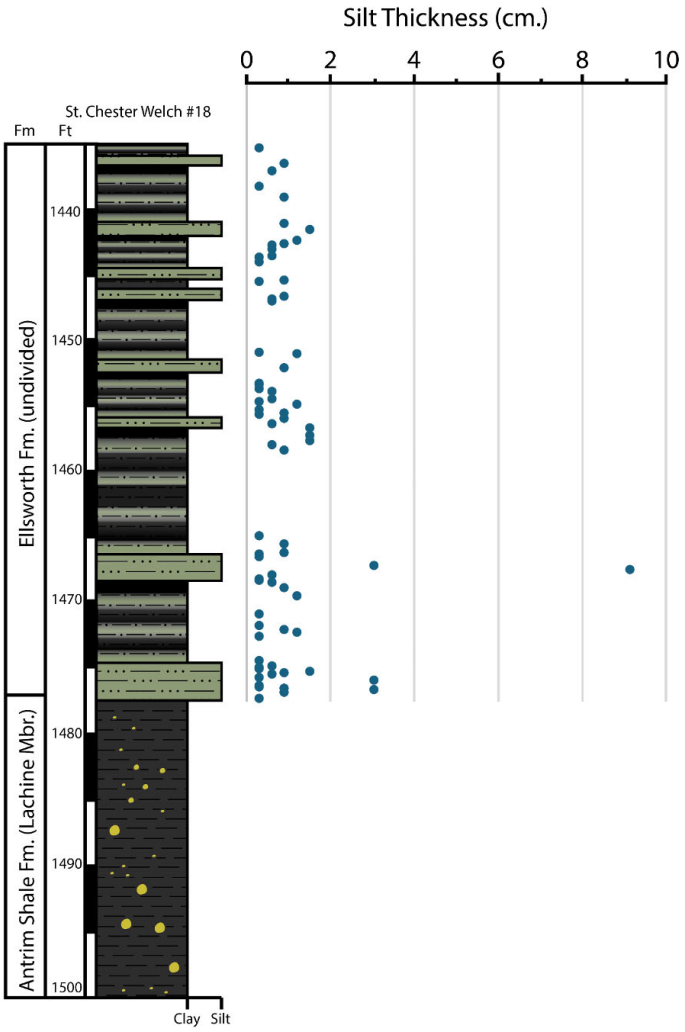

Figure 3. Measured siltstone laminae thickness in the St. Chester Welch #18 core next to a stratigraphic column. It should be noted that only the thickest siltstone laminae were measured, and any laminations less than 0.3 cm (3 mm) are not represented herein.

Elemental and Mineralogical Analysis

In the St. Chester Welch #18 core, K% and Al% covary, with concentrations increasing from the Lachine Member into the Ellsworth Formation (Fig. 4). Si% and Si/Al covary in the Lachine, but Si% maintains elevated concentrations in the Ellsworth and Si/Al shifts to consistently lower values, therefore covariation is difficult to observe visually (Fig. 4). A similar pattern to Si/Al and Si% is seen in Ti% and Ti/Al (Fig. 4). However, Zr/Al and Zr% covary throughout both units, but Zr% exceeds Zr/Al in the Ellsworth (Fig. 4). It should be noted that covariation within the Ellsworth is not consistent (Fig. 4). Additional chemostratigraphic data is available in Johnson (2024).

Minerals detected in this core included quartz, K-feldspar, plagioclase, calcite, dolomite, pyrite, apatite, halite, illite and mica, and other clay minerals (Fig. 4). The Lachine Member contained about 12% clay minerals with a high value of 25% at 1492.5 ft, and the Ellsworth Formation contained 18-25% clay minerals (Fig. 4). Both the Lachine and Ellsworth contained a non-clay mineralogy between 75 and 90%, with the majority being quartz (Fig. 4). The Lachine Member contained 45-70% quartz, with a decrease at the contact with the Ellsworth which contained 30-40% (Fig. 4). K-Feldspar percentages decrease in the Lachine approaching the contact with Ellsworth, and then increase within the Ellsworth Formation (Fig. 4). Additional mineralogic data is available in Johnson (2024).

DISCUSSION

Lithology

The St. Chester Welch #18 core has siltstone-shale interbeds appearing at the contact with the Lachine Member, with the siltstone laminae getting thinner upsection (Figs. 2 and 3). These observations indicate that sedimentation rate and in the St. Chester Welch #18 core was greater near the contact with the Lachine, and gradually decreased through time. This also suggests that the orientation of the delta that sourced Ellsworth Formation sediments likely changed through time (Fig. 5). Initially, due to the thick siltstone laminae at the contact with the Lachine, the Ellsworth Delta reached the St. Chester Welch #18 core in which deposition was high and the core was in the direct trajectory of the delta (Fig. 5). During this time, both hypothesized wind direction and fluvial influx came from the modern day northwest, with the delta prograding into the basin eastward (Fig. 5). However, the gradual rate of laminae becoming thinner upsection suggests that there was a change in sedimentation rate through time, which could be due to the migration of the delta as it prograded into the basin (Fig. 5). However, using just the St. Chester Welch #18 core makes it difficult to determine the lobe migration direction, therefore the area of migration is distinguished by a dashed line herein (Fig. 5).

Sediment Characterization

Si% and Si/Al covary in the Lachine, but Si% exceeds

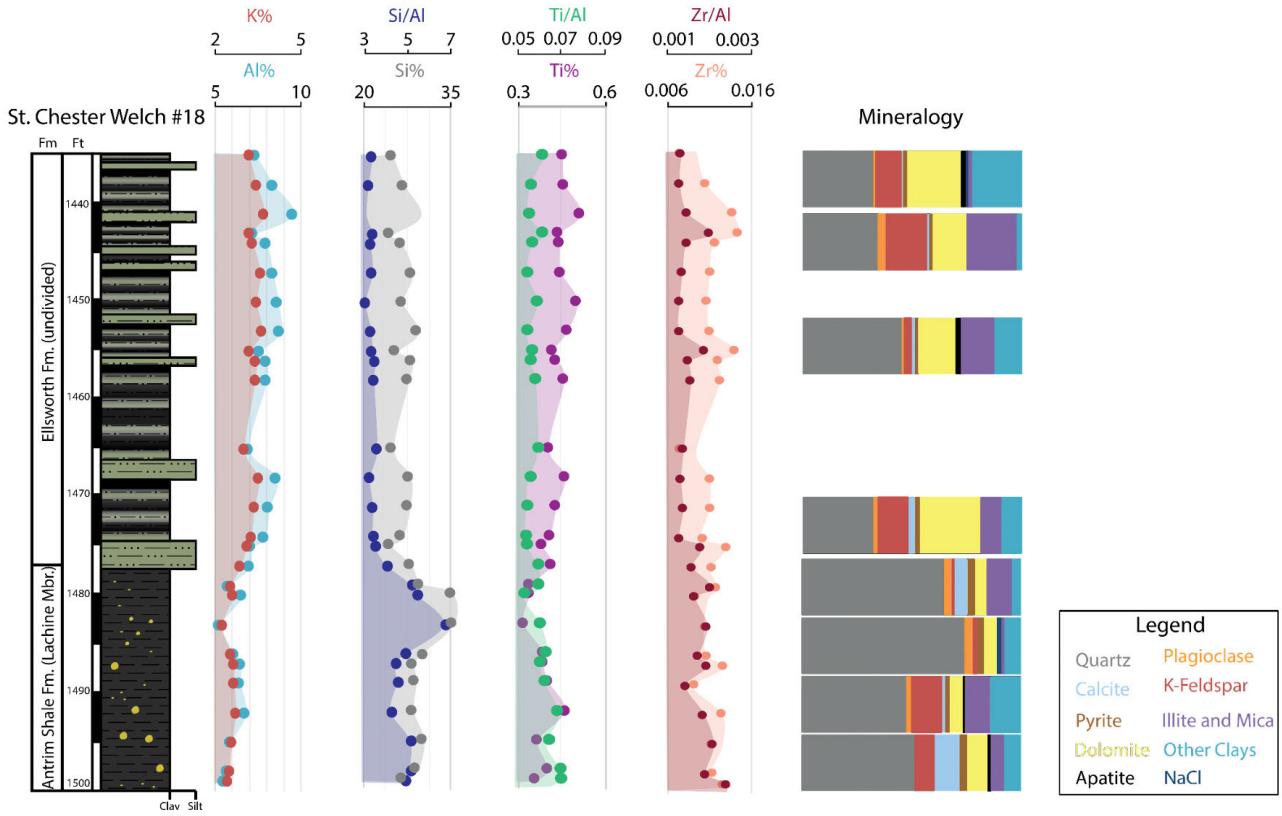

Figure 4. Lithostratigraphy, elemental chemostratigraphy, and mineralogy of the St. Chester Welch #18 core.

Si/Al in the Ellsworth (Fig. 4). This elevation in Si% suggests that clay minerals as well as detrital quartz grains are sourced similarly and coming into the basin together, whereas the Ellsworth delta is receiving more clay minerals and less quartz due to a different siliciclastic source than that which fed the Lachine Member. Non-clay sources of silicon could potentially be sand and silt-sized quartz grains, or silicified microfossils which have been identified in previous studies (Hathon, 1979). The variety of minerals present in the St. Chester Welch #18 core possibly corresponds to the proximity of the core to the Ellsworth Delta, indicating that this core represents an area close to the mouth of the river delta (Figs. 4 and 5).

The Lachine Member of the Antrim Formation also hosts atypical percentages of quartz compared to other black shales (Hathon, 1979). It would be unusual for a black shale to contain such high percentages of quartz sourced from siliciclastic input, so previous studies have speculated that this quartz is authigenic (Hathon, 1979). This authigenic quartz may have precipitated in situ, and may be diagenetic precipitation from pore fluids (Hathon, 1979). Quartz in the Antrim could also be biogenic (Gutchick and Sandberg, 1991). However, the source of the unusual amount of quartz present in the Antrim shale is still debated (Churchman et al., 1976; Hathon, 1979).

Sediment Sources

Because Ti/Al and Zr/Al are proxies for silt-sized grains, and since Ti/Al and Zr/Al are consistently elevated in both cores, the source for some of these silt grains in the Ellsworth could be coming from a combination of fluvial and wind-blown silt as part of the Ellsworth Delta System (Figs. 4 and 5). It is not uncommon for the finest-grained aeolian-sourced loess to be deposited in lakes and seas, and these grains can be transported great distances into these basins (Soreghan et al., 2023 and references therein). Deep-time wind-blown silt deposits show that the lithification of these units can often be preserved as siltstones and mudstones in which the silt-dominated units can have clay components (Soreghan et al., 2023 and references therein). These deep-time aeolian-marine deposits have been observed in Ordovician, Devonian, and Mississippian aged rock (Soreghan et al., 2023 and references therein). In units that occur in these periods, it is likely that if the units being studied were deposited by fluvial systems and contain

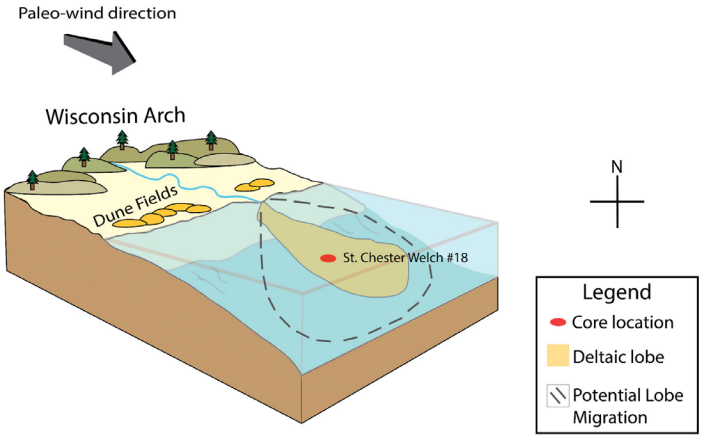

Figure 5. Reconstruction of the progradation of the Ellsworth Delta into the Michigan Basin. The St. Chester Welch #18 core records initial delta deposition, occurring in the center of the deltaic lobe. The dashed outline represents possible directions of migration based on the changes in silt laminae thicknesses recorded throughout the Ellsworth Formation succession. Reconstructions of potential dune fields on the edge of the basin, the river carrying sediment from the Wisconsin Arch, hypothesized paleo-wind direction, and a compass rose pointing to modern-day North are also included. Note that features are not to scale.

silt-sized grains, the silt presence among them could partially be composed of wind-blown silt (Soreghan et al., 2023 and references therein). Since the Ellsworth Formation is prograding into the Michigan Basin as a deltaic lobe fed from fluvial systems (Gutschick and Sandberg, 1991), the siltstone laminae present in the formation could be wind-blown in addition to fluvial sourced. This would indicate that the paleotopographic high of which the loess was sourced had to have been somewhat arid.

However, previous studies have listed the Michigan Basin as being located at a sub-tropical latitude of around 30 degrees south of the equator that receives high rainfall (see Fig. 3 in Zambito and Voice, this volume; Scotese, 1986; Gutschick and Sandberg, 1991). Conversely, 30 degrees north and south latitude are common places to find arid and semi-arid landscapes due to the divergence of the Westerly and Easterly Trade Winds (Walker, 1992). It has been previously suggested that laterally extensive facies of Devonian detrital silt-sized fractions that occur at the subtropical arid belt have a high likelihood of their silt deposits being aeolian-marine (Soreghan et al., 2023 and references therein). So, while the Michigan Basin would have been paleogeographically located in a sub-tropical latitude, it is possible that there could have been a semi-arid transcontinental arch sourcing a combination of fluvial and wind-blown silt-sized grains into the Ellsworth delta system and the basin itself (Fig. 5; Scotese, 1986; Gutchick and Sandberg, 1991). This, combined with the fluvial sediment feeding the delta, could have resulted in the closely interbedded siltstone and shale of the Ellsworth Formation.

ACKNOWLEDGEMENTS

This material is based upon work supported by the Keck Geology Consortium and the National Science Foundation under Grant No. 2050697. Additionally, thank you to Dr. James Zambito and Dr. Peter Voice for their support and mentorship throughout this project.

REFERENCES

Catacosinos, P.A., Harrison, W.B., Reynolds, R.F., Westjohn, D.B., and Wollensak, M.S., 2000, Stratigraphic Nomenclature for Michigan: Michigan Department of Environmental Quality and Geological Survey Division, and Michigan Basin Geological Society.

Churchman, G.J., Clayton, R.N., Sridhar, K., and Jackson, M.L., 1976: Oxygen Isotopic Composition of Aerosol Size Quartz in Shales: Journal of Geophysical Research, v. 81, no. 3, p. 381-386.

Currie, B., 2016, Stratigraphy of the Upper Devonian-Lower Mississippian Michigan Basin: Review and Revision with an Emphasis on the Ellsworth Petroleum System [M.S. thesis]: Western Michigan University, 148 p.

Ells, G. D., 1979, Stratigraphic cross sections extending from Devonian Antrim Shale to Mississippian Sunbury Shale in the Michigan Basin: Michigan Department of Natural Resources, Geological Survey Division Report of Investigation 22, 186 p.

Gutschick, R.C., and Sandberg, C.A., 1991, Late Devonian history of Michigan Basin: Geological Society of America Special Papers, v. 256, p. 181–202, doi:10.1130/SPE256-p181.

Hathon, C.P., 1979, The origin of the quartz in the Antrim Shale [M.S. Thesis]: Michigan State University, 31 p.

Johnson, I.R., 2024, Characterizing the Ellsworth Formation of the Michigan Basin using lithostratigraphy and chemostratigraphy [B.S. thesis]: Beloit College, 80 p.

Palmer, A. R., 1983, The Decade of North American Geology 1983 geological time scale: Geology, v. 11, p. 503-504.

Scotese, C. R., 1986, Early Famennian (367 Ma) equatorial world view, in Roy, S., ed., The Devonian; A portfolio of maps 1978-1986: Anchorage, Alaska Pacific University, The Devonian Institute, Plate 12.

Soreghan, G.S., Heavens, N.G., Pfiefer, L.S., and Soreghan, M.J., 2023, Dust and loess as archives and agents of climate and climate change in the late Paleozoic Earth system: Geological Society, London, Special Publications, v. 535, n. 1, p. 195-223, doi:10.1144/SP535-2022-208.

Walker, A.S., 1992, Deserts: Geology and Resources: U.S. Department of the Interior/U.S. Geological Survey, 60 p.

Zambito IV, J.J., and Voice, P.J., this volume, Integrated stratigraphic and paleoenvironmental study of the Middle-Late Devonian carbonate to black shale transition in the Michigan Basin.

KECK Geology Consortium
Learning Science Through Research
Published by the Keck Geology Consortium
Short Contributions
Keck Geology Consortium
Volume 36
May 2024
doi: 10.18277/AKRSG.2024.36.19

MODELING MARINE PALEOENVIRONMENTS OF THE ELLSWORTH PRODELTA DURING THE LATE DEVONIAN IN THE MICHIGAN BASIN

CONNOR J. QUIROZ, California State University, Monterey Bay
Project Advisors: Peter J. Voice and James J. Zambito IV

ABSTRACT

The Antrim Formation is an organic-rich black shale that was deposited in the Michigan Basin during the Devonian. The overlying Ellsworth Formation is a turbiditic prodelta deposit of a river system draining from the nearby Wisconsin Arch. Although turbidite deposits in the distal part of an alluvial fan are expected to follow a binomial distribution, there is no data to visualize the sediment sorting in the Ellsworth Formation. This study modeled the paleoenvironments of the Ellsworth Formation in the St. Chester Welch #18 core (see Figure 3 of Zambito and Voice, this volume) by characterizing the lithologic and geochemical properties to delineate grain size variations at fine scale. Generalized linear models were used to evaluate high resolution lithologic and geochemical trends throughout the Ellsworth Formation, elucidating an overall coarsening upward sequence within the core consisting of smaller scale cyclicity at the millimeter scale. Elemental data collected using portable X-Ray Fluorescence (pXRF) was used as a proxy for clastic input. Characterizing the Ellsworth Formation provides new insights into how prodeltas formed during the Devonian.

INTRODUCTION

During the Devonian, substantial plate tectonic activity occurred with the collision of Avalonia and other microplates colliding with the eastern margin of North America during the Acadian Orogeny (Murphy and Keppie 2005). The Late Devonian was relatively warm, with higher CO_2 levels in the atmosphere and was associated with high sea levels and large organic deposits on anoxic seafloors which lithified into black shales (Brugger et al. 2019). The black shale deposited during the Upper Devonian consists of silt and clay sized sediment, and composed of minerals including quartz and clay minerals. The Michigan Basin, one of four depocenters in the northeast and upper Midwest United States, contains Late Devonian black shale of the Antrim Shale deposited under low-oxygen conditions.

The Ellsworth Shale interfingers with the Antrim Shale in the Michigan Basin and is a lesser studied marine formation that has had its stratigraphic position debated (Dellapenna et al. 1991; Gutschick and Sandberg 1991; Currie 2016). The Ellsworth is currently not assigned to any geologic group and consists of a silty gray and green shale. Deposited near the end of the Late Devonian, it represents the turbiditic deposits of a prodelta of a river system that drained into the Michigan Basin (Gutschick and Sandberg 1991). In a turbidite system, sediments are deposited from turbidity currents that flow down the delta slope into the basin. The sediments of turbidite systems are expected to follow binomial distributions, especially in more distal prodelta (Chen and Hiscott 1999). While Gutschick and Sandberg (1991) defined the depositional environment of the Ellsworth as a prodelta and Currie (2016) used pXRF to describe the Ellsworth's lithology, there is no existing high resolution lithostratigraphic data describing the historical development of the Ellsworth Prodelta.

METHODS

Lithostratigraphy

The core used in this study is the State Chester

Welch #18, (permit number #33875, Otsego Co., MI, latitude: 44.9091388, longitude: -84.49979) housed at the Michigan Geological Repository for Research and Education (MGRRE). The Ellsworth Formation is present between depths of 1,435 to 1,476 ft (437.4 and 449.9 m) as shown in Figure 1. There were visible laminations between dark colored clay and lighter silt throughout the core, so the thickness of each lamination was measured down to 0.01 ft (0.003m) using an engineering ruler. When there was difficulty discerning grain size visually, the grain size was estimated by rubbing the sediment to infer whether it was silty or clay-rich. The four classifications used along the core were clay (0), silt (1), unidentifiable rubble (2), if the rock was too shattered to determine the grain size, or missing (x) if there was missing core.

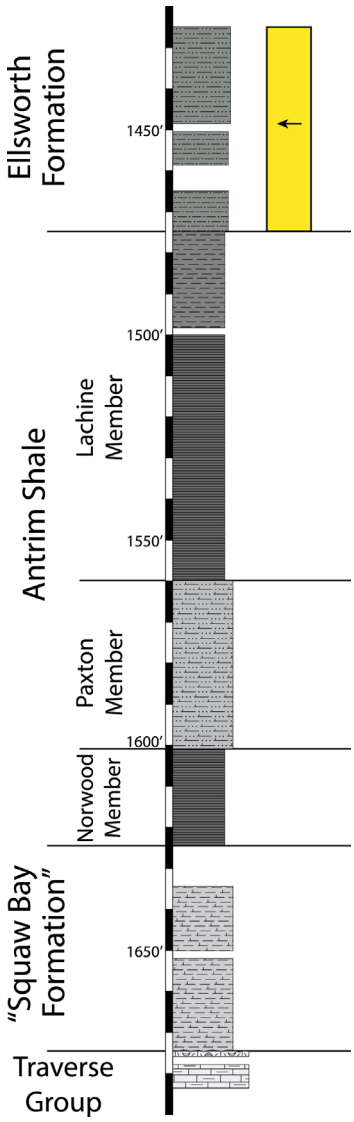

Figure 1. Stratigraphic column of the St. Chester #18 Welch Core with stratigraphic units labeled (adapted from Zambito and Voice, this volume). The yellow bar represents the interval of interest in this study.

Figure 2. More clay than silt is observed throughout the Ellsworth Formation within the St. Chester Welch #18 Core.

Statistical Analysis

Statistical Analysis was undertaken in the statistics software, R. A total of 415 laminations were recorded over the 42 ft (12.8m) core. Of these measurements, 22.22 ft (6.8m) were made up of clay, 7.9 ft (2.41m) were made up of silt, 0.12 ft were core too broken up to determine laminations, and 11.76 ft (3.58m) were missing. The rubble was excluded because of the small amount of clay and silt.

To observe the amount of clay and depth across the core, a bar plot was created of the proportion of footage depth to account for the missing data (Fig. 2). To measure the change in clay and silt amounts, a clay to silt (c/s) ratio variable, cs_ratio, was derived by dividing the clay amount by the silt amount, per foot. If the c/s ratio was greater than 1, there was more clay found at a given depth, and if the c/s ratio was less than 1, then there was less clay. A linear regression was modeled between c/s ratio and the well depth.

To measure how the frequency of laminations changed with depth, a variable, num_oscilations, was created that summed the total changes from silt to clay per foot and modeled a Quasi-Poisson regression to predict the number of oscillations with well depth. A Poisson regression was also modeled to find patterns in the frequency of larger sediments (>0.04 in) associated with depth (Fig. 3).

Geochemical Analysis

To identify the presence of clastic sediments, pXRF data was used to detect elemental composition changes throughout the Ellsworth. The elemental data was

Table 1. Elemental relationships in Ellsworth, indicated with positive and negative directions.

Elemental comparison	Relationship (+/-)	P-value ($\alpha = 0.05$)	R^2
Si/Al & Ti	-	0.001	0.760
Si/Al & K	-	0.018	0.413
Si/Al & Ca	+	0.007	0.499

collected using a Thermo Fisher Scientific Niton XL3t GOLDD+ Handheld XRF Analyzer at Beloit College. The elements measured were aluminum and silicon as a proxy for quartz and clay minerals, calcium as a proxy for carbonates, and zirconium and titanium as proxies for detrital continental sediments (Tribovillard et al. 2006). Elements were analyzed to observe how they corresponded with depth, the relationship between other elements, and how the quantity of one element varied between the Ellsworth and underlying Lachine Member (Tables 1 and 2).

RESULTS

Lithostratigraphic Analysis

There were observable patterns from an empirical analysis of the Ellsworth Formation. The laminations alternated between clay and silt laminations with a coarsening upward sequence throughout the column and there was more clay found than silt in the Ellsworth. There was also an observable color shift from darker clay to lighter, green silts and that the frequency of laminations also decreased in the upper Ellsworth. There were also thick widths of silt at 1444 ft (440.13m) and 1467 ft (447.14m) in depth. When there were uniform grain sizes, there were still color variations in the clay (Figure 3).

Statistical Analysis

There were noticeable trends using the lithologic data from the Ellsworth Formation (Fig. 3). Looking at grain size distributions, there was a decreasing trend in the c/s ratio up section, meaning there was more silt present in the upper Ellsworth (coarsening upward). There was an increase in the number of laminations up section, meaning there were more shifts from clay to silt.

The geochemical data provided insights for the mineralogic composition of the Ellsworth. Using the pXRF data of the Ellsworth Formation, silicon normalized to aluminum (Si/Al) ratio had a negative relationship with titanium and potassium, and positive relationship with calcium (Table 1). The aluminum, potassium, and silicon to aluminum ratio amounts were each greater in the Ellsworth than in the underlying Lachine Member, but the titanium, calcium, and silicon amounts did not differ (Table 2).

DISCUSSION

While characterizing rocks by their sediment sorting, grain size, color, and mineral composition is important for lithostratigraphic description, running statistical analyses are also important to learn more about depositional environments (Steiner, 1966). This exploratory data provides observations to how the St. Chester Welch #18 samples from the Ellsworth Formation were deposited in a submarine prodelta. The pXRF data showed that higher values of silicon and titanium present in younger portions of the Ellsworth suggest higher siliciclastic, continental input into the prodelta setting (Tribovillard et al. 2006). There was less quartz present when the rock exhibited higher concentrations of titanium and potassium. The decrease in calcium with younger rock is inferred as less calcium carbonate present up section. Including higher resolution data for the pXRF may help to elucidate geochemical trends and refine the Ellsworth's chronostratigraphic framework (Morgan, 2022). The pXRF powder samples were taken along 3 ft (0.91m) intervals, which may not have accounted

Table 2. Elements that are more abundant in the Ellsworth than the underlying Lachine.

Element	P-value ($\alpha = 0.05$)
Al	1.945e-06
K	1.046e-10
Si/Al	2.274e-07

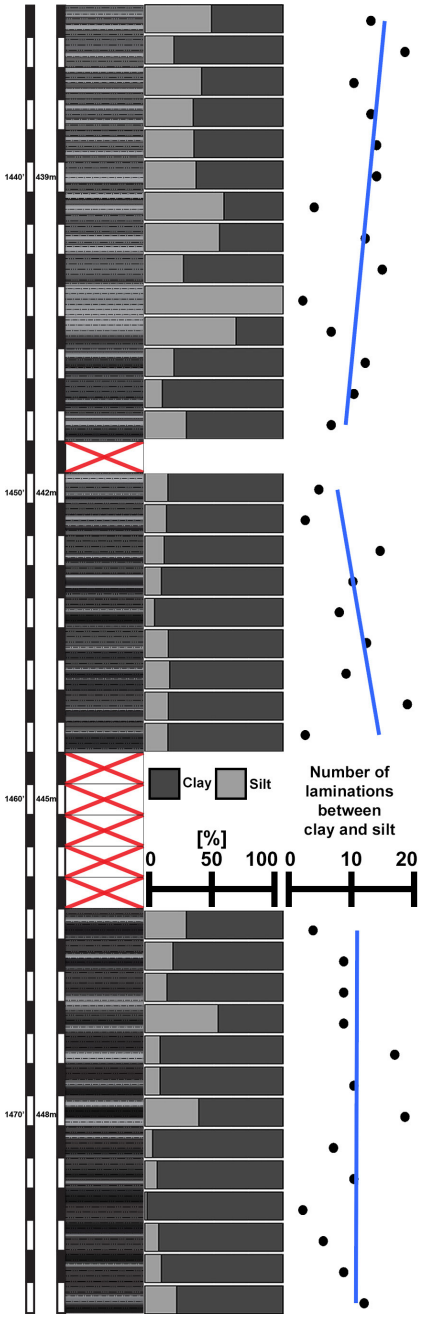

Figure 3. Reconstruction of the progradation of the Ellsworth delta into the MHigh resolution stratigraphic column of the studied interval of the St. Chester Welch #18 Core. Center track shows the percentage of rock present at each depth (middle), and number of laminations between clay and silt are seen on the right.

for geologic events occurring at higher resolutions.

Examination of crushed samples of the Ellsworth Formation using a low power binocular microscope showed that there were microlaminations present with thicknesses smaller than could be resolved with visual examination of the cores (Johnson, 2024). Future work could statistically analyze these microlaminations to better understand whether these microlaminations represent varves or tidally influenced deposits, which would provide higher resolution analysis for how prodeltas form.

CONCLUSIONS

The prodelta, as observed in the Ellsworth, prograded from the west to the east and included many environmental shifts through its development. A coarsening upward sequence within the succession studied was observed. This stratigraphic data presented herein can be used to inform research scientists and land managers for how prodeltaic environments developed during the Devonian and to understand how present deltaic environments may change.While only one well was measured at high resolution for this project, future work would require examination of other cores to show lateral variability in the Ellsworth deltaic system.

ACKNOWLEDGEMENTS

This material is based upon work supported by the Keck Geology Consortium and the National Science Foundation under Grant No. 2050697.

REFERENCES

Brugger J, Hofmann M, Petri S, Feulner G. 2019. On the Sensitivity of the Devonian Climate to Continental Configuration, Vegetation Cover, Orbital Configuration, CO2 Concentration, and Insolation. Paleoceanography and Paleoclimatology. 34(8):1375–1398. doi:https://doi.org/10.1029/2019pa003562.

Chen C, Hiscott RN. 1999. Statistical analysis of turbidite cycles in submarine fan successions; tests for short-term persistence. Journal of Sedimentary Research. 69(2):486–504.

Currie B. 2016. Stratigraphy of the Upper Devonian-Lower Mississippian Michigan Basin: Review and Revision with an Emphasis on the Ellsworth Petroleum System. Unpublished MS Thesis, Western Michigan University, Kalamazoo, MI.

Dellapenna, T. M., Twynham, M., and Harrison, W. B., III, 1991, New stratigraphic nomenclature for the Antrim Group, Michigan Basin, In Reed, R. C., Rarick, A., Bricker, M., McComb-Elowski,

P., Espinosa, L., Pothacamury, I., Skillings, C., Vugrinovich, R., and Wilson, S. E. (Eds.) Michigan: Its Geology and Geologic Resources, A Second Symposium 1991, p.8-9.

Gutschick, R.C. & Sandberg, C.A. (1991) Late Devonian History of Michigan Basin. In: Early Sedimentary Evolution of the Michigan Basin (Ed. by P. A. Catacosinos & P. A. Daniels, Jr.), Geological Society of America Special Paper, 256, 181-202. Geological Society of America (GSA), Boulder, CO, Boulder, CO, United States (USA).

Johnson, I.R., 2024, Characterizing the Ellsworth Formation of the Michigan Basin using lithostratigraphy and chemostratigraphy [B.S. thesis]: Beloit College, 80 p.

Katano I, Negishi JN, Minagawa T, Doi H, Kawaguchi Y, Kayaba Y. 2021. Effects of sediment replenishment on riverbed environments and macroinvertebrate assemblages downstream of a dam. Scientific Reports. 11(1):7525.

Morgan D. 2022 May 1. High-resolution trace element geochemistry and sequence stratigraphy of the Middle-Late Devonian (Givetian-Frasnian) Frasnes crisis. Unpublished MS Thesis, Texas Tech University, Lubbock, TX. https://ttu-ir.tdl.org/handle/2346/89401.

Murphy JB, Keppie JD. 2005. The Acadian Orogeny in the Northern Appalachians. International Geology Review. 47(7):663–687. doi:https://doi.org/10.2747/0020-6814.47.7.663.

Steiner J. 1966. Depositional environments of the Devonian rocks of the Eden-Merrimbula area, New South Wales. Unpublished Ph.D. Dissertation, The Australian National University, Canberra, Australia.

Tribovillard N, Algeo TJ, Lyons T, Riboulleau A. 2006. Trace metals as paleoredox and paleoproductivity proxies: An update. Chemical Geology. 232(1-2):12–32.

Zambito IV, J.J., and Voice, P.J., this volume, Integrated stratigraphic and paleoenvironmental study of the Middle-Late Devonian carbonate to black shale transition in the Michigan Basin.

KECK Geology Consortium
Learning Science Through Research
Published by the Keck Geology Consortium
Short Contributions
Keck Geology Consortium
Volume 36
May 2024
doi: 10.18277/AKRSG.2024.36.20

GEOLOGIC MAPPING OF ALPENA COUNTY, MICHIGAN

LAM T. TRUONG, California State Long Beach University
Project Advisors: Peter J. Voice and James J. Zambito IV

INTRODUCTION

The purpose of this project is to produce multiple geologic maps of the Devonian-Mississippian strata in Alpena County, Michigan with a focus on delineating the members of the Antrim Shale. The resulting maps will be useful for resource (aggregate and natural gas) and natural hazard (sinkholes) assessment. These refined Alpena bedrock maps provide the community with a better assessment of where natural resources are present and the susceptibility of natural hazards in the area for urban planning. Alpena historically has been a site of quarrying (limestone, shale) operations and hydrocarbon exploration from units including the Traverse Group. Carbonate-dominated intervals in the Traverse Group are susceptible to karsting and sinkholes are present in northern Alpena County. Understanding the risk of karsting assists in mitigating groundwater contamination from septic tanks and other sources of contamination.

GEOLOGIC SETTING

The Michigan Basin was a depocenter during the Devonian Period that is filled with a thick package of sediment. Alpena County is located in the northeastern Lower Peninsula of Michigan. This county is underlain predominantly by shale and limestone bedrock. The most recent geologic map of Alpena (Milstein, 1987 available on Geowebface, https://www.egle.state.mi.us/geowebface/) generalizes the Traverse Group as a single unit instead of identifying the ten formations mapped in the Alpena-area Traverse Group outcrop belt (Ehlers and Kesling, 1970). In addition, the Antrim and Ellsworth shales are mapped as a single unit as shown in Figure 1. Despite featuring similar lithologic characteristics, the deposition of Ellsworth occurs from the west whereas the rest of the

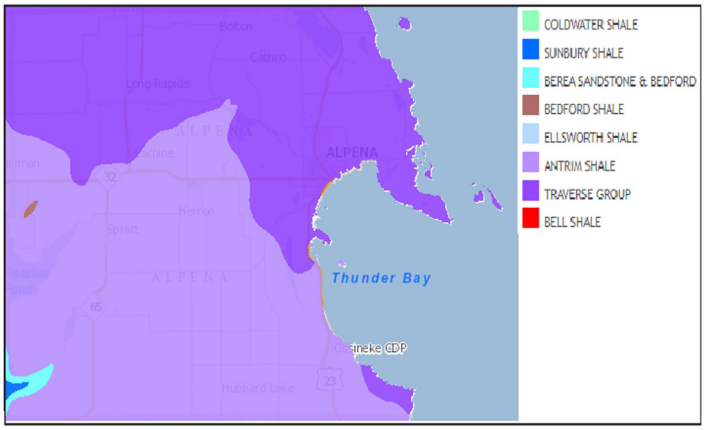

Figure 1. The Geowebface bedrock map (after Milstein, 1987) lumps the members of the Antrim and Ellsworth Formation as the Antrim Shale. Berea, Bedford, Coldwater (not shown on map) and Sunbury lithostratigraphic units only occur in the very southwesternmost portion of the county (a small outlier of Bedford also occurs in the western portion of the map area).

Mississippian and Devonian rocks were sourced from the east. Milstein (1987) also interpreted the younger Mississippian rocks to have limited exposures in far southwestern Alpena County. With recent driller's logs that are readily available for public use, a more detailed and accurate map can be produced. Exposed subsurface units that are featured in this county from youngest to oldest are Coldwater Shale, Sunbury Shale, Bedford-Berea formations, upper Antrim member, Ellsworth Formation, the Lachine, Paxton, and Norwood Members of the Antrim Shale, the "Squaw Bay Formation", and the Traverse Group.

The geography of the northern portion of Alpena County is blanketed by less than 50 feet thick of glacial drift, clays, gravels, and lake-shore deposits. The Wisconsin glaciation affected the fluctuation of land and lake elevations resulting in karsting of carbonates in the Traverse Group (Black, 1977) leading to possible sinkholes. Karst is a significant concern in this region of the state where homes have individual water wells and septic tank fields. In

addition, agricultural and industrial contamination may be readily moved through karst conduits.

The purpose of this research is to produce geologic maps of Alpena County by refining the contacts between bedrock units using the large volumes of well data that have become available since the Milstein (1987) map was compiled. It is important that the members of the Antrim Formation are subdivided further for clarity and gives better recognition of the distribution and scale of these members. The "Squaw Bay Formation" is undergoing efforts to rename and redescribe the unit due to 1) the name of the unit uses a derogatory term for Native American women, and 2) the unit has a long history of misuse in the subsurface (Fisher, 1969; Gutschick and Sandberg, 1991). The "Squaw Bay Formation" is sometimes lumped in with the Traverse Group and mapping its distribution will help with separating the interval from the underlying Traverse Group strata. A bedrock geologic map provides subsurface natural resource information that will be useful to regional planners, regulators, and other geologists. More specifically, it can be used for applications such as locating groundwater, oil and gas, and mineral resources.

METHODS

Oil/gas and water well logs were analyzed for formation tops and bedrock elevation in order to construct three maps using ArcGIS Pro: bedrock geologic, bedrock topography, and glacial drift thickness maps. The well distribution provided an interesting difficulty in constraining the geology of Alpena County. The southern half of the county has an extensive subsurface dataset from Antrim Shale gas wells which provided excellent constraints on bedrock elevations and formation tops. The northern half of the county by contrast has a paucity of oil and gas wells. Water wells provided constraints on the bedrock surface but the lack of detailed lithologic descriptions made interpreting the bedrock formations in this portion of the county challenging.

To better understand the units, a core from the Paxton Quarry (central Alpena County) was described and photographed in order to define the strata of the "Squaw Bay Formation", Antrim Shale, and Ellsworth Shale in the map area. After examining the core, subsurface datasets from the Michigan Geological Repository for Research and Education's archives were analyzed. The first dataset was composed of oil and gas drillers reports, documents prepared by the company drilling the well under state regulations. Drillers reports include information on the location of the well (surface location, surface elevation), the depth drilled to, and formation tops and lithologic information from units intercepted during drilling. An Excel spreadsheet was constructed from this dataset that included 1) the location of each well, 2) the surface elevation of the well, 3) the elevation of the bedrock surface, and 4) formation tops of each unit drilled through down to the Dundee Formation. In some cases, the drillers reports were validated using wireline logs.

Southern Alpena County has a significant distribution of oil and gas wells, but the rest of the county required using a second database, water well records from Michigan Wellogic. Water well drilling companies are also required by state regulations to submit drillers reports, unfortunately, these logs usually do not include information on stratigraphic units drilled through, but rather generalized descriptions of lithologic material encountered while drilling. A second Excel spreadsheet was generated from the water well reports that included the following information: 1) surface location of the well, 2) surface elevation of the well, 3) bedrock elevation,

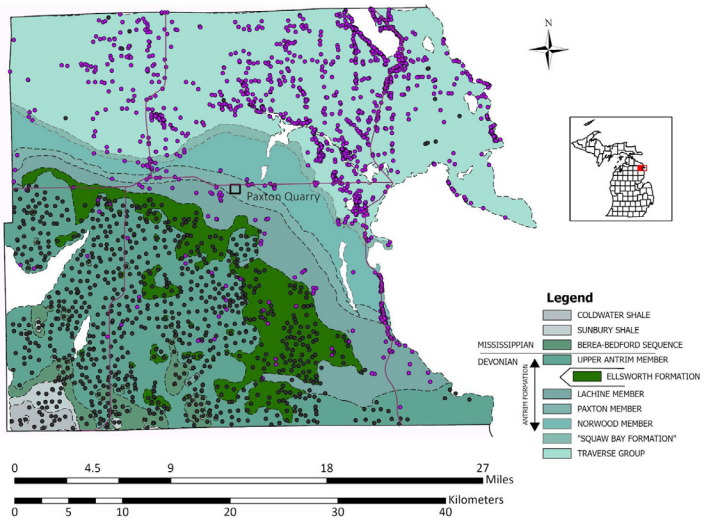

Figure 2. The current study's version of the bedrock map of Alpena County showing the subcrop pattern of the geologic map. A database of 886 oil and gas wells and 1361 water wells logs was used to create this map.

and 4) lithology of bedrock. Total of 886 oil and gas and 1361 water well logs from the database were imported into ArcGIS Pro. ArcGIS Pro was used to generate geologic maps. Wells were coded for the shallowest bedrock unit and mapped to show the distribution of these units (Fig. 2). ArcGIS Pro was used to draw polygons representing geologic units. The bedrock elevation map was drawn by contouring bedrock elevation data from the two well datasets (Fig. 3). Glacial drift thickness was calculated from the difference between the surface elevation and the bedrock surface in each well, followed by contouring these thicknesses across the county to generate a glacial drift thickness map (Fig. 4).

RESULTS

Lithologic Description

In the Paxton Quarry core, the upper Traverse Group is gray microcrystalline and fossiliferous limestone. In the subsurface, the Traverse Group consists of limestone, dolostone, argillaceous limestones, and calcareous shales (Ehlers and Kesling, 1970). Overlying the Traverse Group, the "Squaw Bay Formation" consists of fossiliferous gray shale with pyrite concretions in the Paxton Quarry Core. At the type locality (also in Alpena County), the "Squaw Bay Formation" consists of 1) *Zoophycos*-bearing, dolomitic limestones, and 2) Molluscan limestones (Gutschick and Sandberg, 1991). The oldest member of the Antrim Shale, the Norwood, is dark gray to black, laminated shale characterized by high gamma radiation emissions as shown in Figure 5. The Paxton Member is a light to gray laminated shale with pyrite inclusions and emitting lower gamma radiation. Above the Paxton Member, is the Lachine Member, which consists of gray-black laminated to bioturbated shale with a high gamma radiation signature. While Gutschick and Sandberg (1991) do not recognize the Ellsworth Formation in Alpena County, Currie (2016) has interpreted, from wireline log analysis, a thin interval of Ellsworth Formation between the Lachine and upper Antrim members of the Antrim Shale. The Ellsworth Formation is gray to green interbedded siltstone and shale. Returning to the fourth member of the Antrim Shale, the upper Antrim member consists of gray-black laminated shale.

No early Mississippian bedrock units are found in the Paxton Quarry Core and are cited from observations recorded on drillers reports. The Bedford-Berea composite stratigraphic unit is a moderate to gray compact sandstone-shale unit. The Sunbury Shale is a dark brown-black fissile and brittle shale. The youngest subsurface bedrock unit, the Coldwater Shale, is a gray micaceous and compact shale.

Geologic Maps

The bedrock geologic map produced in this study shows a structural pattern of the margin of a

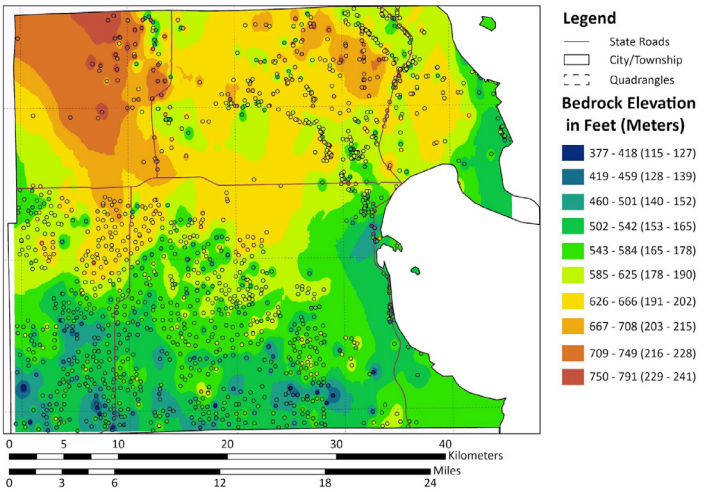

Figure 3. The bedrock surface map for Alpena County generated by this study. Note that bedrock elevations are higher in the northern part of the county and lower in Alpena County. Contour interval approximately 41 feet.

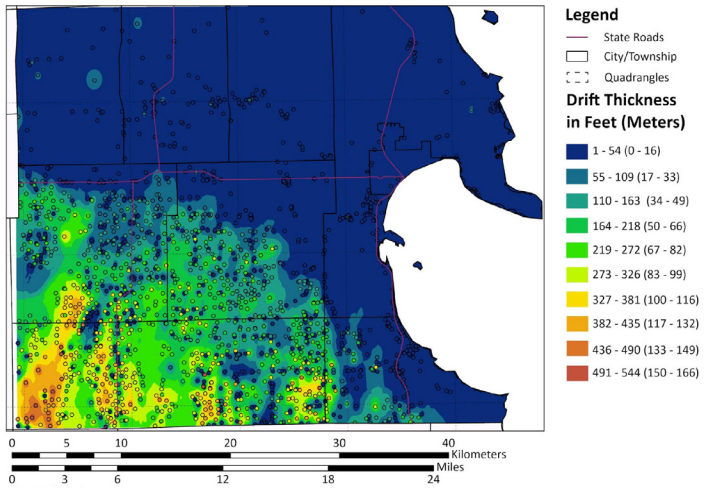

Figure 4. Drift thickness map was produced from oil/gas and water well logs where both the surface elevation and the depth to the bedrock surface were recorded. Note that the drift is thicker to the south and west in Alpena County. Contour interval approximately 54 feet.

depositional basin as shown in Figure 2. Stratigraphic units are younger to the southwest. The southern part of the county is dominated by the the upper Antrim member with significant subcrops of the Ellsworth Formation interfingered with the upper Antrim. The central portion of the county is underlain by the older members of the Antrim Shale (Norwood, Paxton, and Lachine Members) and the "Squaw Bay Formation" marking the transition to the older carbonates to the north and northeast. The northern portion of the county is mainly underlain by the undifferentiated Traverse Group.

The glacial drift thickness map indicates that glacial drift thickens towards the south. In northern Alpena County, the drift thickness above the Lachine Member, "Squaw Bay Formation", and Traverse Group ranges from 0 to 54 feet thick, which places glacial drift over carbonate rocks as shown in Figure 4. The Bedrock Elevation Map (Fig. 3) shows a different trend than the glacial drift thickness map - the bedrock elevation increases to the northwest. The topography of the bedrock elevation surface shows a mix of highs and lows in southeastern Alpena County suggesting the presence of glacially eroded valleys.

DISCUSSION

Geology

Bedrock units form arcuate belts from northwest to southeast in Alpena County and range from the Lower Mississippian units in the far southwest (Bedford-Berea, Sunbury, and Coldwater formations) to Devonian units across the majority of the county (Traverse Group, "Squaw Bay Formation", Antrim Shale, and Ellsworth Shale). The youngest unit is in the southwest and oldest unit in the northeast of Alpena County. This age distribution follows the regional dip of the Michigan Basin. The Traverse Group in northeastern Alpena County is characterized by interbedded carbonates and shales. The paucity of oil and gas wells (with detailed drillers logs) required using drillers reports from water wells. The observations from the water wells suggest a complex mosaic of shale and carbonates in northern Alpena County and the current study was unable to differentiate the ten formal formations in the

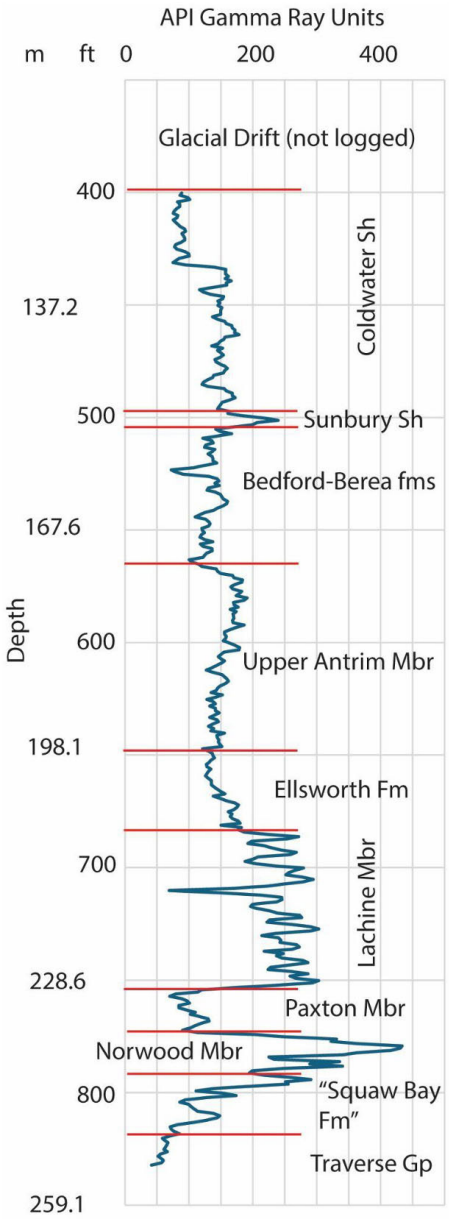

Figure 5. Gamma ray log from the Linn Operating Inc. Log Cabin Hunting Club #D2-24 well (Permit number 49295) in SW Alpena Co. The log shows the gamma ray signatures characteristic of each unit - note that the Norwood and Lachine Members of the Antrim Shale are characterized by high gamma radiation, while other units generally exhibit less gamma radiation. API – American Petroleum Institute, Fm – Formation, Fms – Formations, Gr – Group, Mbr – Member, Sh – Shale.

Traverse Group that had been mapped from outcrops; indeed, Ehlers and Kesling (1970 and references therein) lament the difficulty of correlation in the Traverse Group due to the lack of exposed contacts between formations in outcrops and the small size and scattered locations of available outcrops. As this study focused on subsurface data, no attempt was made to integrate the outcrop data from Black (1979) and Ehlers and Kesling (1970). The "Squaw

Bay Formation" was inferred to be present in the subsurface as a thin belt between the Traverse Group subcrop and the Norwood Member of the Antrim Shale. The "Squaw Bay Formation" does outcrop on the southern shore of Partridge Point on Birdsong Bay [Birdsong Bay is the revised name for "Squaw Bay" that is currently pending with the USGS] (Gutschick and Sandberg, 1991). The individual members of the Antrim Shale defined by Gutschick and Sandberg (1991) are geologically distinct and mappable across the county, suggesting that these units may be better treated as formal formations of an Antrim Group. The Ellsworth Formation outcrops in a belt between the Lachine Member of the Antrim Shale and the upper Antrim member of the Antrim Shale and further confirms the hypothesis of Currie (2016) for a thin Ellsworth Formation being present across the entire eastern Lower Peninsula in the subsurface. Drillers have identified the Bedford and Berea formations, the Sunbury Shale, and the Coldwater Shale in the southwesternmost portion of Alpena County. No attempt was made to subdivide the Bedford and Berea formations due to their gradational nature (Ells, 1979). Glacial incision during the Pleistocene has carved significant paleovalleys on this bedrock surface, with valleys trending NE-SW in Alpena County. Glacial drift thickens to the south and southwest in Alpena County.

Comparison to Published Maps

The updated geologic map is broadly similar to the Milstein (1987) bedrock map in Geowebface, while differing by providing more detail for the Antrim Shale and the Ellsworth Shale in central Alpena County. The high density of oil and gas wells in southern Alpena County allow for mapping of the members of the Antrim Formation. The only caveat is that where the Antrim Formation is less than 100 ft thick above hydrocarbon bearing zones, oil and gas wells were not drilled due to state regulations (W. Harrison, personal communication, 2024). This impacts the mapping of the boundaries of the Antrim members in the northern and eastern portions of their range where fewer wells were drilled.

The overall distribution of the Traverse Group is also similar to the Milstein (1987) bedrock map in Geowebface and like the previous map, we did not attempt to subdivide the Traverse Group into formations. While the density of water wells in northern Alpena County is also high, it was difficult to define the individual formations of the Traverse Group. Since the Traverse Group in this geographic region contains a range of lithologies including argillaceous limestone, shales, limestones, and dolostones, water well drillers did not identify specific units but instead described the lithologies at the bedrock surface. Factors such as this contribute to the uncertainty of the contact locations of the bedrock units for not only water well logs but oil/gas logs as well.

Natural Hazards

Portions of Alpena County underlain by the Traverse Group are prone to dissolution and collapse. The thinness of the drift over the Traverse Group allows infiltrating precipitation to widen fractures through dissolution (Holst and Foote, 1981) eventually leading to collapse and formation of sinkholes (Black, 1977). These sinkholes can be significant hazards during collapse events especially in the Thunder Bay area. Wells that are within sinkholes run the risk of water pollution as the karst act as conduits for contaminants and contamination of the aquifer from sewage is possible due to sinkholes. With the increasing pollution rate from active karst features, dangers of contamination from sewage may infiltrate residential areas affecting residents (Black, 1977).

CONCLUSIONS

Our maps broadly match the previously published map (Milstein, 1987) available on Geowebface, though this study demonstrates that the members of the Antrim Shale are readily mapped in Alpena County subsurface. The Ellsworth Formation is present as a thin unit between the Lachine Member and upper Antrim member of the Antrim Shale. The Traverse Group was mapped as undifferentiated Traverse as the quality of the water well records in northern Alpena County were too poor to divide the unit. In southwestern Alpena County, the area underlain by the Bedford and Berea formations, Sunbury Shale, and Coldwater Shale is mapped more precisely than in previous efforts. Karst is a significant hazard in

northeastern Alpena County where thin glacial drift overlies carbonates of the Traverse Group.

ACKNOWLEDGEMENTS

This material is based upon work supported by the Keck Geology Consortium and the National Science Foundation under Grant No. 2050697. We appreciate Greg Anderson's assistance and advice with Arc GIS.

REFERENCES

Black, T. J. 1977, Bedrock Topography and Overburden Thickness of Northeastern Alpena and Eastern Presque Isle Counties, Michigan, Unpublished MS thesis, Department of Geology, Kansas State University, Manhattan, KS.

Currie, B. J. 2016, Stratigraphy of the Upper Devonian-Lower Mississippian Michigan Basin: Review and revision with an emphasis on the Ellsworth Petroleum System, Unpublished MS thesis, Western Michigan University, Kalamazoo, MI.

Ehlers, G. M. and Kesling, R. V. 1970, Devonian strata of Alpena and Presque Isle counties, Michigan, in Stonehouse, H. B. (Ed.), Michigan Basin Geological Society and Geological Society of North America North Central Section, 130 p.

Ells, G.D., 1979, Stratigraphic Cross Sections Extending from Devonian Antrim Shale to Mississippian Sunbury Shale in the Michigan Basin: Michigan Department of Natural Resources, Geological Survey Division Michigan Department of Natural Resources, Geological Survey Division, Report of Investigation 22, 186 p.

Fisher, J. C. 1969, The distribution and characteristics of the Traverse Formation of Michigan, Unpublished MS thesis, Department of Geology, Michigan State University, East Lansing, MI.

Gutschick, R. C. and Sandberg, C. A. 1991, Late Devonian history of Michigan Basin, in Catacosinos, P. A. and Daniels, P. A., Jr. (Eds.), Early Sedimentary Evolution of the Michigan Basin, Geological Society of America Special Paper, 256, 181-202, Geological Society of America, Boulder, Co.

Holst, T. B.and Foote, G. R. 1981, Joint Orientation in Devonian Rocks in the Northern Portion of the Lower Peninsula of Michigan, Geological Society of America Bulletin, 92, 85-93.

Milstein, M. L. 1987, Bedrock Geology of Southern Michigan, Michigan Department of Natural Resources, BG-01, 1:500,000.